At the cutting edge of atomic force microscopy

Edited by Thilo Glatzel, Peter Grutter, Omur Dagdeviren and Shigeki Kawai

Imprint

ReactorAFM/STM – dynamic reactions on surfaces at elevated temperature and atmospheric pressure

Tycho Roorda[*1], Hamed Achour[1], Matthijs A. van Spronsen[2], Marta E. Cañas-Ventura[2], Sander B. Roobol[2,3], Willem Onderwaater[2], Mirthe Bergman[2], Peter van der Tuijn[2], Gertjan van Baarle[4], Johan W. Bakker[2], Joost W. M. Frenken[2] and Irene M. N. Groot[*1]

Abstract

Previous work has shown the ReactorSTM and ReactorAFM, capable of studying materials under industrially relevant conditions. Here we show current developments of the ReactorAFM/STM, implementing a qPlus sensor to add the ability of combining atomic force microscopy (AFM) and scanning tunneling microscopy (STM) techniques to study the geometric and electronic structure of materials under reaction conditions. We demonstrate this by imaging a Pd(100) single crystal at 450 K with combined AFM/STM. The surface is compared under ultrahigh vacuum and under 0.5 bar O_2 pressure showing a notable increase in RMS current, which we attribute to oxidation. Also, we study cobalt nanoparticle catalysts on an aluminum oxide support, industrially relevant in the Fischer–Tropsch synthesis. The catalysts are imaged before and after reaction at 430 K as the current maximum temperature of the qPlus sensor used falls just below the reaction temperature. Quadrupole mass spectrometry data show the reaction taking place by monitoring product gases during heating and cooling of the sample under CO and H_2 gas pressures of 2 bar. The monitored gases include H_2O as byproduct and the hydrocarbons ethane ($m/z = 30$), propane ($m/z = 44$), and hexane ($m/z = 86$), which all show increases in counts while between 490 and 550 K. The added ability to scan various surfaces with combined AFM/STM while monitoring the reaction products demonstrates the versatility offered by the ReactorAFM/STM to study catalysts under realistic industrial conditions.

Introduction

Operando catalysis is the field of research that monitors the structure, composition, and morphology of a catalyst while simultaneously investigating its activity, reactivity, and selectivity under industrially relevant conditions. While much research has been conducted at room temperatures (or below) and under ambient to ultrahigh vacuum (UHV) conditions, industrial conditions expose catalysts to 1000 K and beyond in pressures ranging from ambient to 100 bar [1,2]. This difference in pressure, which influences whether a given catalyst becomes reactive, is referred to as the pressure gap. To provide an interpretive framework for catalysts under industrial conditions, new experimental and theoretical analysis tools are required. While recent years have witnessed a tremendous effort in this direction [3], many of these techniques are photon-based [4-9]. Even though they provide valuable insights, the development of surface-sensitive techniques that can image the catalyst at the atomic scale under high-pressure and high-temperature conditions remains crucial.

In attempting to close the pressure gap, a high-pressure ReactorSTM has been developed [10,11]. The pressures in the scanning tunneling microscopy (STM) reactor are orders of magnitude above UHV (up to several bar), rendering gas–catalyst interactions very significant and leading to differences in reaction mechanisms [12-15]. Alongside the pressure gap, the existence of the materials gap refers to the complexity and heterogeneity of real catalysts. Such catalysts are compounds that possess a special complex mixture consisting essentially of metals, oxides, and promoters, supported on refractory oxides. The requirement of a conductive substrate limits STM techniques in relevant industrial applications involving such more complex catalysts. For this reason, an atomic force microscopy (AFM) version of the high-pressure STM employing a quartz tuning fork (QTF) was introduced to overcome this limitation [16]. Unlike STM, which uses the electric tunneling effect, AFM probes the forces of the tip–sample interaction. This makes AFM independent of surface conductivity and therefore a powerful tool to bridge the materials gap. The drawback of this high-pressure AFM setup is that it could not be combined with STM. While STM provides insights of the electronic state and structure of the surface, AFM offers structural and electrostatic information. Therefore, combining AFM with STM brings the best of both techniques together and offers a more precise understanding of catalytic systems.

In this paper, we present the design of a combined AFM/STM integrated in a high-pressure gas flow reactor. The combined technique is based on the state-of-the-art tuning fork sensor in a qPlus configuration with three contacts, two for AFM and one for STM [17]. In order to illustrate the applicability of the technique, operando oxidation of Pd(100) under 0.5 bar of oxygen at 450 K was carried out using nc-AFM while simultaneously recording the electrical current signal of the formed oxide. Furthermore, we show high-temperature and high-pressure images just below our current temperature limit for an industrially relevant catalyst undergoing Fischer–Tropsch synthesis (FTS).

Challenges while applying a tuning fork as force sensor

A drawback of the QTF as a force sensor is that its temperature sensitivity increases with increasing temperatures; in fact, it can even serve as a micro temperature sensor [18]. As a result, temperature fluctuations while scanning cause shifts in resonance frequency, which could be misinterpreted as a force signal. A QTF's resonance frequency changes with temperature according to the following equation:

$$\frac{\Delta f}{f_0} = 1 - c\left(T - T_0\right)^2,$$ (1)

where Δf is the shift in resonance frequency, f_0 is the natural resonance frequency of the tuning fork (with tip glued on, at T_0), c refers to the parabolic temperature coefficient, T is the temperature, and T_0 refers to the maximum where the tuning fork is designed to be the least temperature-dependent. Since tuning forks have originally been mass-produced for time keeping in watches, T_0 is designed to be at room temperature (RT). Using a QTF as a force sensor implies that temperature fluctuations can be interpreted as height features and ultimately results in losing contact with the surface when these fluctuations exceed the setpoint of the scanner. When scanning at temperatures farther from T_0, this effect becomes larger.

The QTF's resonance frequency depends on pressure according to the following equation:

$$\frac{\Delta f}{f_0} = -\frac{1}{2}\frac{\mu}{\rho A},$$ (2)

where μ is the added mass due to the interaction with surrounding gas molecules, ρ is the density of the quartz tuning fork, and A is the area of the cross section [19]. Basically, the pressure dependence is due to dampening of the prong with respect to the gas molecules around it. While we do encounter reductions in scanning quality with increasing pressure, this effect is less prominent than the limitations caused by increased temperatures.
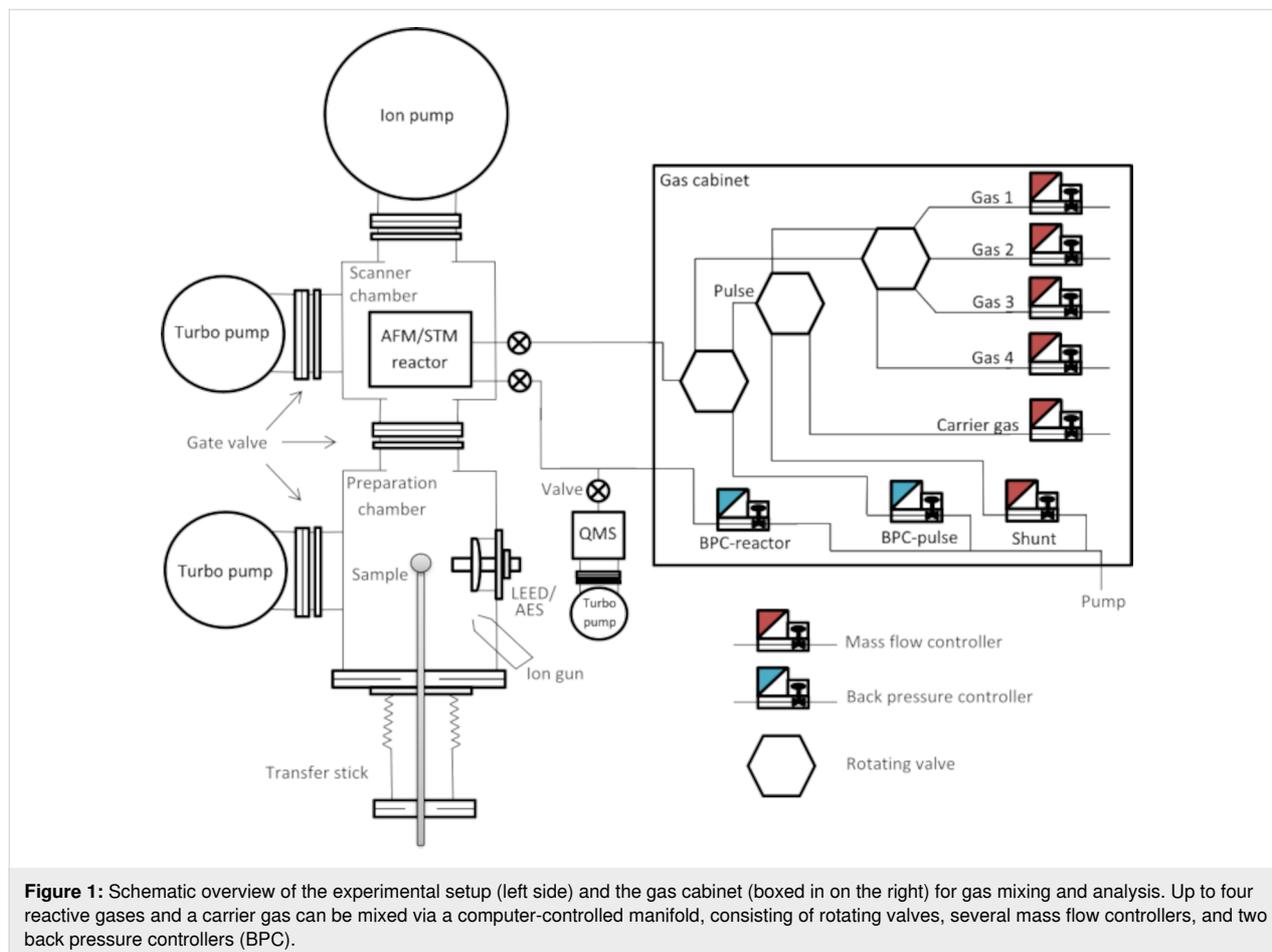
Experimental setup
Overview

A simplified diagram of the experimental setup is shown in Figure 1. The apparatus is composed of two chambers maintained at UHV conditions and separated by a gate valve. The preparation chamber is devoted to sample preparation and characterization, while the other accommodates the AFM/STM reactor. The sample can be introduced into the setup by means of a load lock and transferred throughout the chambers with a transfer stick. The preparation chamber accommodates standard surface preparation techniques including an ion sputter gun, an e-beam evaporator, a quadrupole mass spectrometer, as well as a combined low-energy electron diffraction/Auger electron spectroscopy system to verify the cleanliness, structure, and composition of the surface. The UHV system is supported by four pneumatic air legs resting on a concrete slab, which is separated from the foundation of the building, and isolated from the main floor in an ultramicroscopy hall.

The AFM/STM is contained in a high-pressure cell and sealed off from the UHV chamber by a Kalrez elastomer seal, which exhibits outstanding thermal stability and chemical resistance

together with improved sealing performance in both high-pressure and high-temperature environments. Being in direct contact with the sample surface, the seal's maximum temperature poses a reaction temperature limitation of 600 K [11]. The vacuum is maintained by a corrosion-resistant turbo pump as well as an ion pump. A gas cabinet for gas mixing, consisting of several rotating valves, mass flow controllers, and back pressure controllers, is connected to the AFM/STM reactor, permitting pressures of up to 20 bar. Four gases plus a carrier gas can be mixed and transported to and from the reactor by capillaries at gas mixing ratios ranging from 1:1 up to 1:100 with a flow up to 40 mL/min controlled via a Python script. A separate quadrupole mass spectrometer (QMS) at the exhaust of the reactor chamber is equipped with its own turbo pump allowing for a direct correlation between surface morphology and catalytic properties by measuring the gases that leave the reactor.

AFM/STM reactor

The main objective in the design of the AFM/STM reactor is the possibility to observe the structural and electronic properties of the surface at high gas pressures and temperatures, independent of its conductivity. The extension from STM-only and

Figure 1: Schematic overview of the experimental setup (left side) and the gas cabinet (boxed in on the right) for gas mixing and analysis. Up to four reactive gases and a carrier gas can be mixed via a computer-controlled manifold, consisting of rotating valves, several mass flow controllers, and two back pressure controllers (BPC).

AFM-only to the combined AFM/STM reactor is an ongoing development of the existing ReactorSTM and ReactorAFM [11,16]. Therefore, in this section we will only go briefly through the main aspects of the reactor setup. The AFM/STM insert, as shown in Figure 2a,b, demonstrates the following configuration:

- The microscope (highlighted in red in Figure 2a is suspended by springs and eddy current damping for vibration isolation.
- The sample holder (highlighted in blue in Figure 2a is inserted by locking the spring mechanism with the locking bellow and then fixed to the microscope by inflating the "reactor" bellow.
- The substrate can be heated from behind by electron bombardment using a tungsten heating filament.
- The qPlus sensor is mounted to a three-contact slider and controlled by a piezotube. The piezotube is outside of the reactor volume.
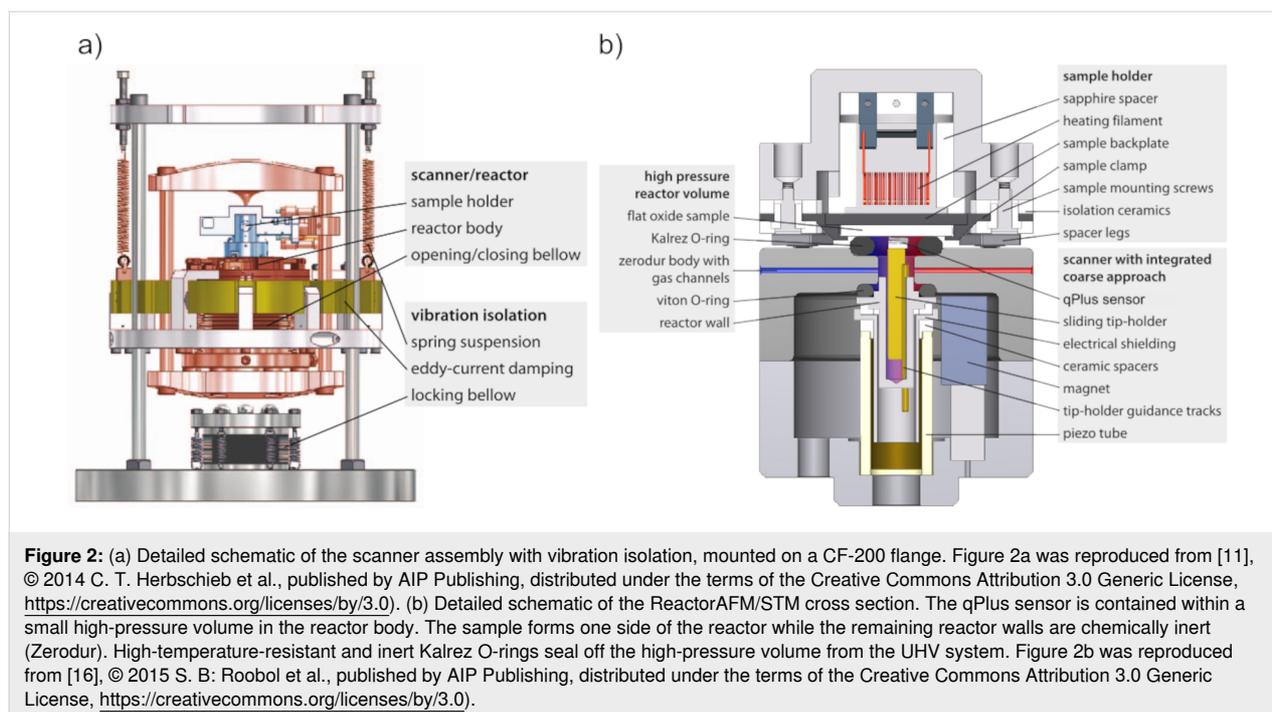
Figure 2b shows a schematic cross section of the AFM/STM reactor together with the sample holder. For high-pressure experiments, the reactor volume needs to be sealed off from the UHV surrounding. This is achieved by inflating the upper bellow with pressurized air against the Kalrez O-ring, which is located on top of the reactor body sealing off the sample. This ensures that only the AFM/STM sensor and its holder are inside the reactor, while the other microscope components, such as the piezoelement, are under UHV conditions. The reactor volume is
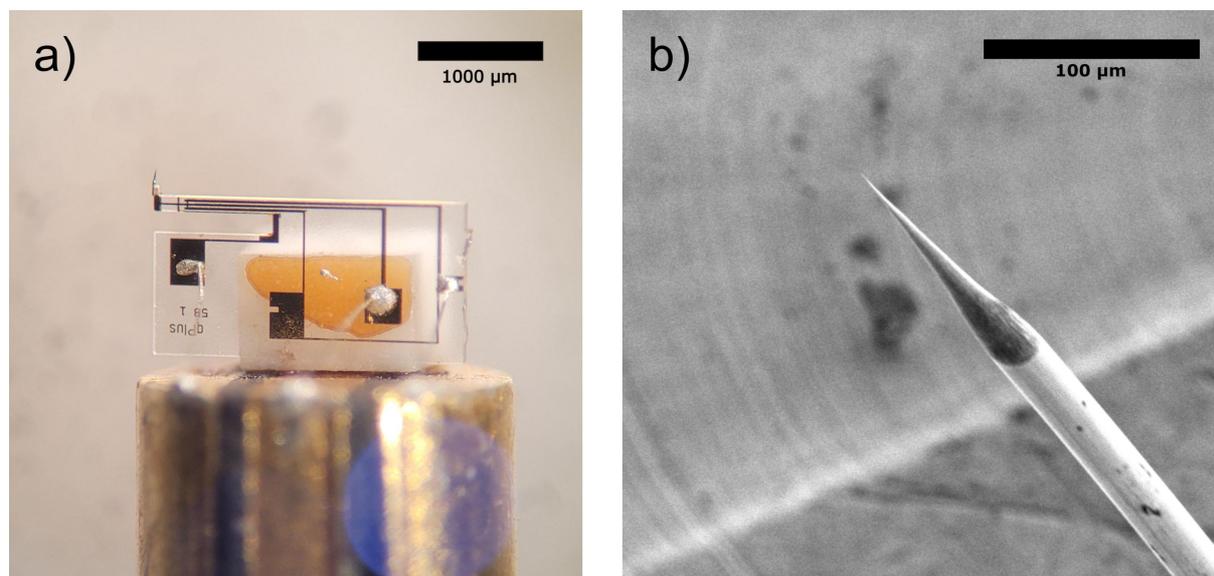
connected to two gas capillaries that transport gas in and out of the sealed reactor. The gas is then analyzed during the reaction by means of a QMS, which is directly connected to the exit channel of the reactor. In order to make the setup catalytically inert, the materials that make up both the reactor and the sample holder have been chosen to be chemically inert. For further details of the STM and AFM reactor design and performance, we refer to [16,20].

qPlus-sensor-based AFM/STM

The core of our AFM/STM scanner incorporates a third-generation QTF in a qPlus configuration with one prong fixed and the other one carrying a metallic tip positioned at the very end [17]. The main reasons for employing this kind of sensor are its very high sensitivity to short-range forces, simultaneous acquisition of the tunneling current, and its small oscillation amplitudes (10 pm to 100 nm) [16]. The fundamental limits of the quartz tuning fork as a force sensor in scanning probe microscopy have been discussed in detail by Grober and colleagues [21]. Moreover, conventional AFM requires an optical detection method with a laser diode, which is not compatible with the design limitations of a reactor volume of 95 μL.

Figure 3a shows a zoomed-in image of a third-generation M5B qPlus sensor (purchased from Nanosurf). The sensor has four gold electrodes of which three are used for AFM drive and readout, and current signal. The fourth electrode (on the back) is connected to one of the AFM contacts. The sensor is glued to a ceramic block with a non-conductive glue (EpoTek H770E),

Figure 2: (a) Detailed schematic of the scanner assembly with vibration isolation, mounted on a CF-200 flange. Figure 2a was reproduced from [11], © 2014 C. T. Herbschieb et al., published by AIP Publishing, distributed under the terms of the Creative Commons Attribution 3.0 Generic License, https://creativecommons.org/licenses/by/3.0). (b) Detailed schematic of the ReactorAFM/STM cross section. The qPlus sensor is contained within a small high-pressure volume in the reactor body. The sample forms one side of the reactor while the remaining reactor walls are chemically inert (Zerodur). High-temperature-resistant and inert Kalrez O-rings seal off the high-pressure volume from the UHV system. Figure 2b was reproduced from [16], © 2015 S. B: Roobol et al., published by AIP Publishing, distributed under the terms of the Creative Commons Attribution 3.0 Generic License, https://creativecommons.org/licenses/by/3.0).

Figure 3: (a) M5B qPlus sensor mounted to and connected through a 3-contact slider for AFM drive, AFM readout, and STM readout. (b) Scanning electron microscopy image of a 25 μm wide chemically etched Pt/Ir wire tip.

which is mounted on the slider. The slider is made of a high-speed steel rod, which is partitioned in three and isolated by non-conductive epoxy. The metallic sections are then coated with gold to ensure catalytic inertness and slide over tracks that serve as electrical feedthrough. The wiring from the QTF electrodes to the holder is made with 25 μm-diameter gold wire glued with conductive epoxy (EpoTek H20E). The holder with the QTF is magnetically held inside the piezotube that consists of a single tube and performs both the coarse approach and the fine scanning motion. The piezoelement, made of lead zirconate titanate, is placed outside the reactor and rests on an aluminum tube, which is part of the reactor wall and serves as a protection against the high-pressure gases, as well as a shield from high piezovoltages. The scanner range can go up to 3.6 μm × 3.6 μm and does not have a coarse range in the *x* and *y* directions.

Tip preparation

Tips are fabricated by electrochemical etching of a 25 μm Pt/Ir wire immersed in a $CaCl_2$ electrolytic solution ($CaCl_2$ 5 g, H_2O 30 mL, acetone 2 mL). An alternating current (AC) voltage (50 Hz, 1–10 V) is applied between the tip and a gold ring electrode with the etching solution in suspension resulting in a sharp tip, which serves as the probe. In a second step, the etched Pt/Ir tip is washed with isopropanol, then by Milli-Q water and dried with pure nitrogen gas. In the third step, the etched tip is cut to length and glued on by hand with silver epoxy to the free end of the tuning fork prong. Tip lengths are cut to approximately 200 μm to prevent unwanted potential lateral tip displacement and vibration modes that might occur for tip heights longer than

400 μm [22]. A Pt/Ir tip is chosen such that it does not oxidize in reaction conditions.

Electronics and data acquisition

The tunneling current is collected using a preamplifier (DLPCA-200 preamp, Femto Messtechnik GmbH, Germany) with the bias applied to the sample. The tuning fork is driven by an AC voltage, and its deflection is measured by the resultant current. The qPlus signal preamplification is provided by a Femto HQA-15M-10T high-frequency charge amplifier with a high gain of 10 V/pC, before it is fed to the signal analyzer. The tip motion and the feedback loop are controlled by electronics from RHK technology. A phase-locked loop is employed for locking the phase between the AC drive signal to the QTF and the signal input. When the phase is locked, the resonance frequency of the tuning fork will shift as the tip interacts with the surface. Amplitude, frequency, and phase are measured. These signals are then fed into the electronics for monitoring and feedback options. The RHK software (R9 plus) allows for various user controls, that is, setpoint (frequency shift for AFM feedback or current for STM feedback), amplitude, and phase as well as the current images can be recorded separately or in several combined modes and compared in real time.
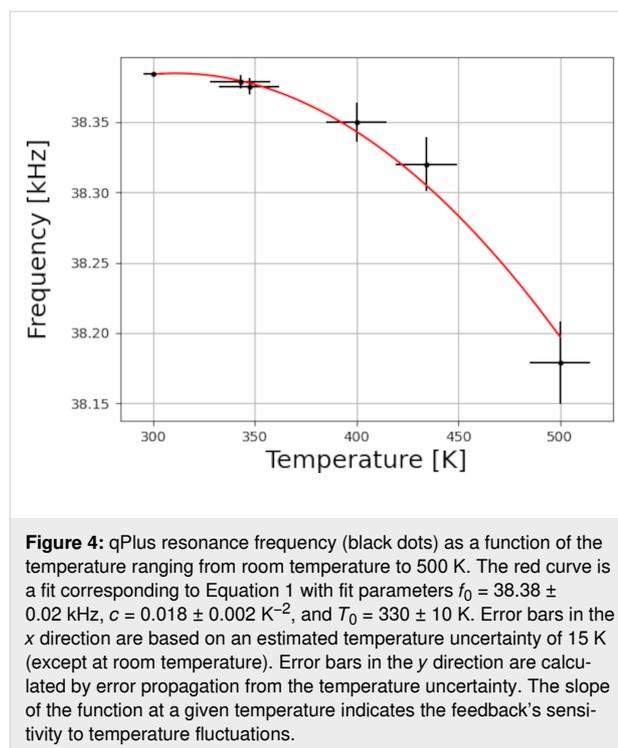
Results and Discussion

To demonstrate the capabilities of the combined ReactorAFM/STM, we show results from two different types of experiments. In the first, we show operando combined AFM/STM images of a clean Pd(100) single crystal that undergoes oxidation of the

surface. The oxidation happens at 450 K under 0.5 bar of oxygen atmosphere. The second experiment is a FTS experiment, where we show AFM images of catalytic cobalt nanoparticles. The nanoparticles are deposited on an oxide layer representing realistic and relevant industrial catalysts. Here, the reaction conditions exceed the temperature limit of the qPlus sensor used in that measurement. Therefore, we show AFM images taken below the reaction temperature, before and after the reaction takes place, with QMS data of the product gases during reaction. In this experiment, the substrate is an aluminum oxide layer through which electrons cannot tunnel and, thus, cannot be studied by STM methods. Before presenting these high-temperature, high-pressure experiments, we show the temperature dependence of the qPlus sensor used in these experiments.

Figure 4 shows the resonance frequency of the qPlus sensor as a function of the temperature. The thermocouple used to measure this temperature is intended to indicate the substrate temperature on the sample holder. This means that it is situated at a certain distance from the qPlus sensor and that we cannot be certain of the sensor's exact temperature. For this reason, we attribute a rough 15 K temperature uncertainty to these measurements, which is represented in the *x* error bars. Typically, after increasing the temperature, a minimum wait of 4 h is required for the resonance frequency to stabilize because of temperature fluctuations. The error bars in the *y* direction are calculated by error propagation on the temperature uncertainty to demonstrate the spread in resonance frequency shifts while the temperature stabilizes. The purpose of this graph is to determine the temperature range at which we can operate the tuning fork and to illustrate the degree of difficulty while scanning at high temperature. Beyond 500 K, no resonance was measured for this specific sensor as the signal became too weak. The fitted function follows Equation 1 with fitting parameters $f_0 = 38.38 \pm 0.02$ kHz, $c = 0.018 \pm 0.002$ K^{-2}, and $T_0 = 330 \pm 10$ K. The slope of the curve at a given temperature indicates the sensor's sensitivity to temperature fluctuations. Near room temperature, where the slope is 0, it is relatively insensitive to temperature fluctuations, while at increasing (and decreasing [23]) temperatures, the slope is steeper; hence, it becomes more important to have a stable temperature while scanning. The data in this graph were collected under UHV conditions; increasing the pressure will affect the Q-factor [19] and, in turn, the signal-to-noise ratio.

To demonstrate the performance of the AFM/STM reactor, we show in Figure 5 images of an as-prepared Pd(100) single crystal, taken at 450 K under UHV conditions (Figure 5a) and under oxidation reaction conditions (Figure 5b). Scanning at high temperature and pressure is performed with the same feedback settings as in UHV and at RT; however, long waiting

Figure 4: qPlus resonance frequency (black dots) as a function of the temperature ranging from room temperature to 500 K. The red curve is a fit corresponding to Equation 1 with fit parameters $f_0 = 38.38 \pm 0.02$ kHz, $c = 0.018 \pm 0.002$ K^{-2}, and $T_0 = 330 \pm 10$ K. Error bars in the *x* direction are based on an estimated temperature uncertainty of 15 K (except at room temperature). Error bars in the *y* direction are calculated by error propagation from the temperature uncertainty. The slope of the function at a given temperature indicates the feedback's sensitivity to temperature fluctuations.

times are required and feedback might be lost because of the higher sensitivity to fluctuations in pressure and temperature while scanning. The images were taken in combined nc-AFM/STM mode using the frequency shift d*F* as feedback, while recording the tunneling current simultaneously (Figure 5c,d). Consequently, the tip–sample distance will be maintained throughout the image while the current signal will be a direct indication of the conductivity of the surface. The Pd(100) surface has been prepared using the standard recipe of repeated cycles of Ar-ion sputtering (3 µA, 1 kV, 30 min) at room temperature followed by annealing at 1000 K for 5 min.

In Figure 5a,c, taken at 450 K under UHV conditions, we recognize steps in the vertical direction, which correspond to the Pd(100) steps. In the current signal image, the same steps are visible and defined more distinctly than in the topographic image. After the introduction of 0.5 bar oxygen in the reactor, and once the qPlus sensor had stabilized (with a 30 Hz drop in resonance frequency), the tip was re-approached to the surface and scanning was started, as shown in Figure 5b with the corresponding current signal in Figure 5d. At a different field of view, we observe Pd(100) steps angled slightly off the vertical direction and less well-defined than under UHV conditions. Most notably is the appearance of high-density, insulating islands illustrated in the current signal image (appearing as dark spots with the same color contrast as in Figure 5c). By observing the root-mean-squared (RMS) surface roughness (R_q) under UHV conditions of 0.17 nm in topography and 50 pA in
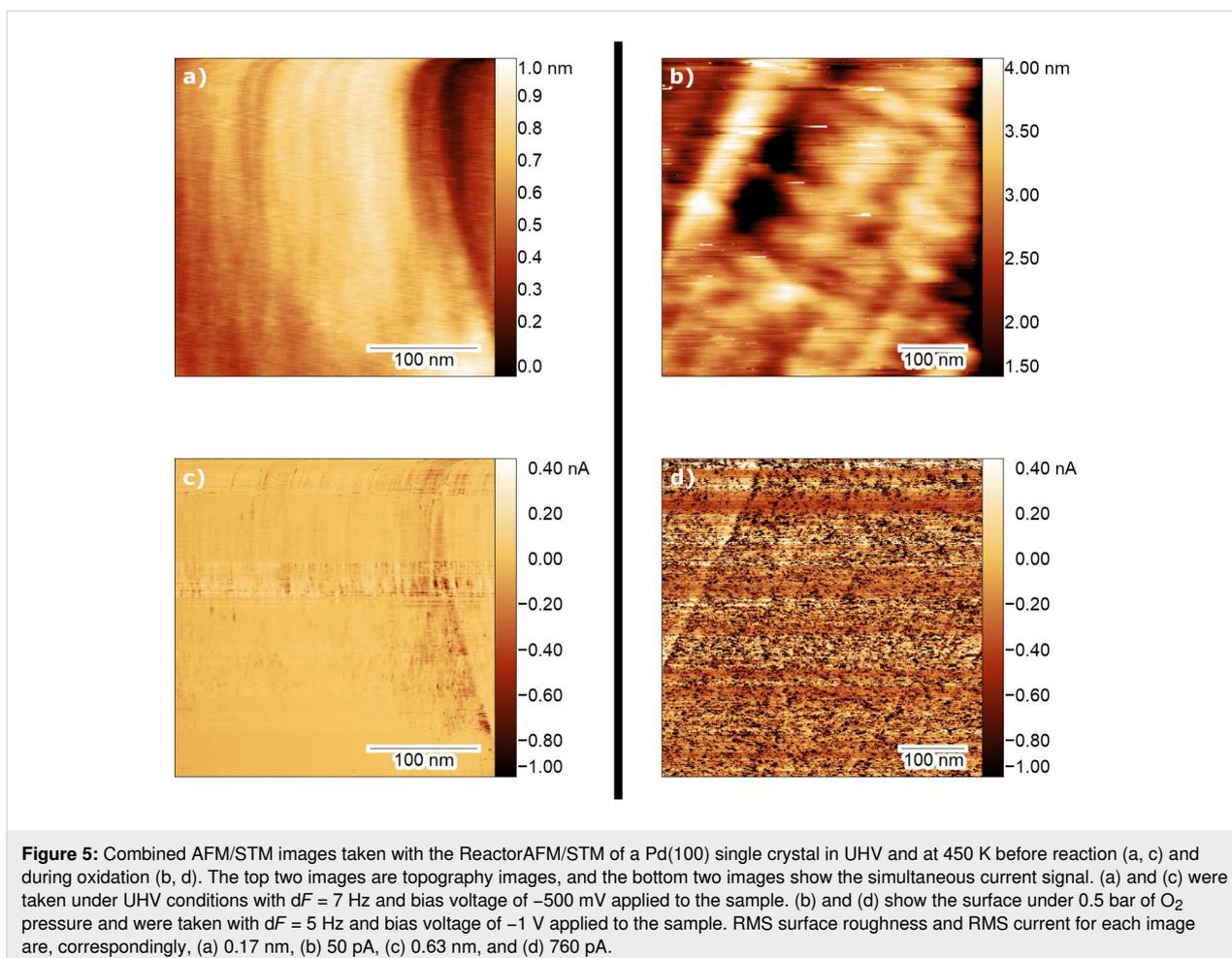
Figure 5: Combined AFM/STM images taken with the ReactorAFM/STM of a Pd(100) single crystal in UHV and at 450 K before reaction (a, c) and during oxidation (b, d). The top two images are topography images, and the bottom two images show the simultaneous current signal. (a) and (c) were taken under UHV conditions with dF = 7 Hz and bias voltage of –500 mV applied to the sample. (b) and (d) show the surface under 0.5 bar of O_2 pressure and were taken with dF = 5 Hz and bias voltage of –1 V applied to the sample. RMS surface roughness and RMS current for each image are, correspondingly, (a) 0.17 nm, (b) 50 pA, (c) 0.63 nm, and (d) 760 pA.

the current signal, we determine that the surface is rather smooth and flat. In contrast, under oxidation conditions, the surface roughness in topography is increased to 0.63 nm because of the more challenging scanning conditions. However, the current signal surface roughness increases by an order of magnitude to 760 pA with respect to Figure 5c. This significant increase in surface roughness, which can be observed as the appearance of dark spots, is due to the formation of islands with reduced conductivity, which we attribute to oxidation of the surface.

To further demonstrate the ReactorAFM/STM capabilities, we show results from a FTS investigation. FTS is a series of reactions where CO and H_2 gas react to form various hydrocarbons C_nH_{2n+2}, with water as byproduct [24]. We have investigated the reaction on Co nanoparticles deposited on an Al_2O_3 support, grown on a NiAl(110) single crystal. The NiAl(110) surface has been prepared by repeated cycles of Ar-ion sputtering (3 µA, 1 kV, 30 min) at room temperature followed by annealing at 1000 K for 5 min. The oxide is deposited ex situ (in a nearby setup, transfer is done in air) by physical vapor deposition using

an aluminum oxide sputter target and NiAl(110) as substrate. The deposition was performed at a 10^{-3} mbar argon pressure for a duration of 40 min. Once placed back in the main setup, the sample is annealed at 800 K in 10^{-6} mbar of O_2 to remove carbon impurities and replenish the oxygen in the oxide layer. The composition of the surface was verified by AES (not shown here). The cobalt nanoparticles were deposited by e-beam evaporation with a Co rod, an emission current of 6 mA, and beam energy of 2 kV for 7 min. Figure 6a shows an AFM image at room temperature and high vacuum ($\approx 10^{-7}$ mbar) of the prepared surface in the closed reactor. The Co nanoparticles appear as bright dots on the surface with an average diameter of $\approx$20 nm.

Figure 6b shows the surface at 430 K under 2 bar of CO and H_2. Due to significant changes in temperature, the tip had to be retracted and re-approached after recording the image in Figure 6a, which means that we have a new field of view. We observe that the surface otherwise looks similar to Figure 6a with respect to the density and size distribution of the particles. While maintaining the gas flow, the sample's temperature was
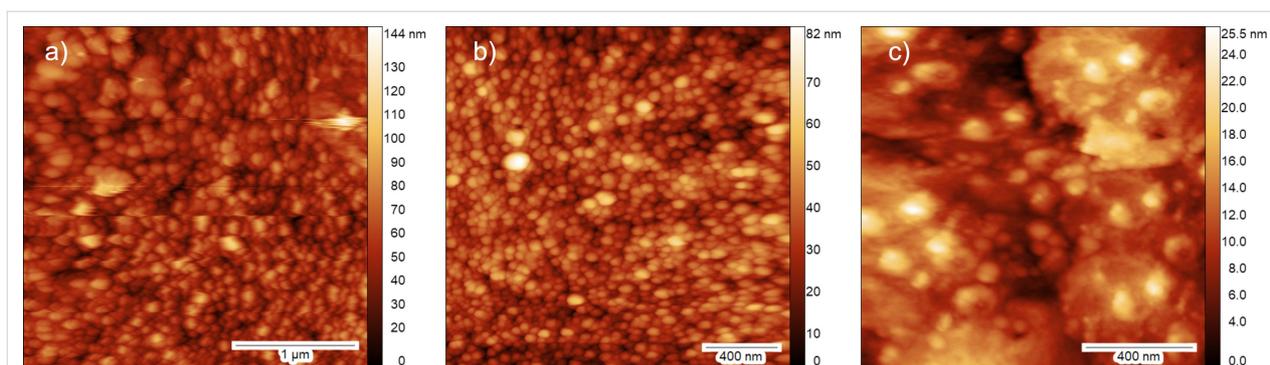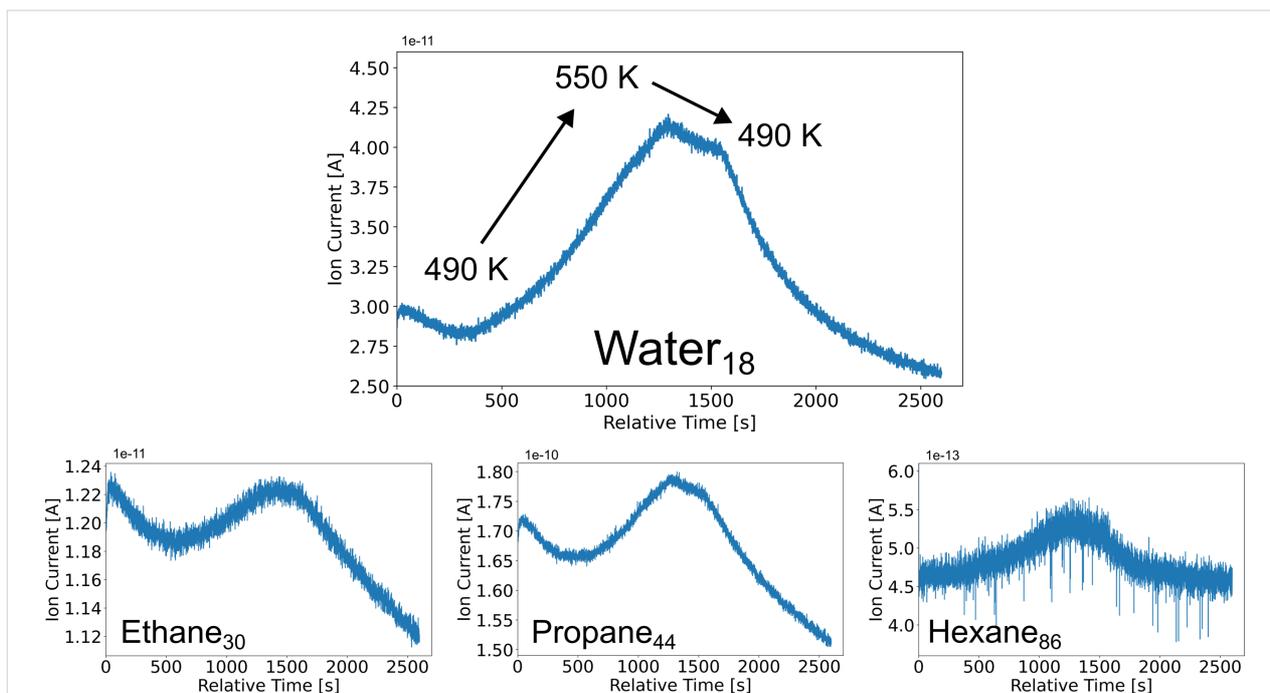
Figure 6: AFM images of cobalt nanoparticles on a thick (50 nm) Al_2O_3 film taken (a) before reaction, at RT and high vacuum, (b) at 430 K and 2 bar CO and H_2 pressure before reaction, and (c) after reaction has occurred, at 430 K and 2 bar pressure of CO and H_2. (a) and (c) were taken in constant signal mode of the RHK controller with setpoint 40 and 58 pA respectively, (b) is taken in constant drive mode with setpoint dF = 3 Hz.

increased with a rate of 1 K per 10 s up to 550 K; at this temperature FTS takes place. This is outside the possible temperature window of scanning with our tuning fork, as explained above. Therefore, we were only able to scan at 430 K before (Figure 6b) and after the reaction occurred (Figure 6c). As can be seen, the surface has undergone a change due to the reaction. The particle size distribution has changed; it appears that smaller particles are no longer visible and that there is an increase in larger particle sizes.

Despite not being able to image the surface during the FTS reaction at 550 K, it was possible to measure possible reaction products using QMS at higher temperatures, as shown in Figure 7. During the heating process, at around 490 K, we observe a strong increase in the counts of water (m/z 18) indicating that the FTS reaction has started. After ≈1200 seconds, the water signal reaches a maximum. Hereafter, the temperature decreases, until reaching 490 K, where the reaction completely stops and the number of counts starts to significantly decrease. At 490 K, at which point the Co catalyst ceases its reactivity, the reaction stops. Furthermore, we observe maxima in masses of m/z 30, 44, and 86, representing ethane, propane, and hexane, respectively, in the same time frame as that for the observation of water formation.

Figure 7: Operando QMS data of various product gases as a function of time during heating and cooling cobalt nanoparticles on a 50 nm thick Al_2O_3 film. Data shown for masses of m/z 18, 30, 44, and 86, which correspond to water (as byproduct), ethane, propane, and hexane, respectively.

Conclusion

The developments in the ReactorAFM/STM design prove it to be an instrumental tool to study (catalyst) materials under industrially relevant conditions. We show that at present, we can operate the qPlus sensor at temperatures of up to 500 K while exposing the surface to reactive gases of a few bars. With combined AFM/STM, we were able to visualize the electronic structure changes of the surface under reaction conditions. Variations in the root-mean-squared current signal verifies that the surface is undergoing oxidation. Furthermore, with an industrially relevant example of cobalt nanoparticles on an oxide support, we were able to image the catalyst before and after reaction at high temperature and pressure. Quadrupole mass spectrometry data of H_2O as byproduct and the hydrocarbons ethane (m/z 30), propane (m/z 44), and hexane (m/z 86), confirmed that Fischer–Tropsch synthesis has occurred and demonstrated the abilities of the setup.

Further developments of the ReactorAFM/STM could benefit from increasing the temperature range of the quartz tuning forks. This could be achieved by further investigating the temperature limitation and considering one designed with a higher T_0, offering greater stability at elevated temperatures. Additionally, exploring the effects of varying support thicknesses and materials, as well as size distributions of metallic nanoparticles, and identifying which product gases are favored under specific reaction conditions, could extend our understanding of FTS.

Funding

ORCID® iDs

Tycho Roorda - https://orcid.org/0000-0001-9137-0215
Matthijs A. van Spronsen - https://orcid.org/0000-0002-5136-2816
Mirthe Bergman - https://orcid.org/0009-0000-2729-9629
Joost W. M. Frenken - https://orcid.org/0000-0002-2486-7720
Irene M. N. Groot - https://orcid.org/0000-0001-9747-3522

Data Availability Statement

Data generated and analyzed during this study is available from the corresponding author upon reasonable request.

References

1. Somorjai, G. A.; Li, Y. *Introduction to surface chemistry and catalysis;* John Wiley & Sons, 2010.
2. Ertl, G.; Knözinger, H.; Weitkamp, J., Eds. *Handbook of heterogeneous catalysis;* VCH Weinheim, 1997; Vol. 2. doi:10.1002/9783527619474
3. Frenken, J.; Groot, I., Eds. *Operando Research in Heterogeneous Catalysis;* Springer Series in Chemical Physics; Springer International Publishing: Cham, Switzerland, 2017. doi:10.1007/978-3-319-44439-0
4. Zaera, F. *Chem. Soc. Rev.* **2014,** *43,* 7624–7663. doi:10.1039/c3cs60374a
5. Salmeron, M.; Schlögl, R. *Surf. Sci. Rep.* **2008,** *63,* 169–199. doi:10.1016/j.surfrep.2008.01.001
6. Grass, M. E.; Karlsson, P. G.; Aksoy, F.; Lundqvist, M.; Wannberg, B.; Mun, B. S.; Hussain, Z.; Liu, Z. *Rev. Sci. Instrum.* **2010,** *81,* 053106. doi:10.1063/1.3427218
7. Nguyen, L.; Tang, Y.; Li, Y.; Zhang, X.; Wang, D.; Tao, F. *Rev. Sci. Instrum.* **2018,** *89,* 054103. doi:10.1063/1.5022738
8. Tardif, S.; Pavlenko, E.; Quazuguel, L.; Boniface, M.; Maréchal, M.; Micha, J.-S.; Gonon, L.; Mareau, V.; Gebel, G.; Bayle-Guillemaud, P.; Rieutord, F.; Lyonnard, S. *ACS Nano* **2017,** *11,* 11306–11316. doi:10.1021/acsnano.7b05796
9. van Rijn, R.; Ackermann, M. D.; Balmes, O.; Dufrane, T.; Geluk, A.; Gonzalez, H.; Isern, H.; de Kuyper, E.; Petit, L.; Sole, V. A.; Wermeille, D.; Felici, R.; Frenken, J. W. M. *Rev. Sci. Instrum.* **2010,** *81,* 014101. doi:10.1063/1.3290420
10. Rasmussen, P. B.; Hendriksen, B. L. M.; Zeijlemaker, H.; Ficke, H. G.; Frenken, J. W. M. *Rev. Sci. Instrum.* **1998,** *69,* 3879–3884. doi:10.1063/1.1149193
11. Herbschleb, C. T.; van der Tuijn, P. C.; Roobol, S. B.; Navarro, V.; Bakker, J. W.; Liu, Q.; Stoltz, D.; Cañas-Ventura, M. E.; Verdoes, G.; van Spronsen, M. A.; Bergman, M.; Crama, L.; Taminiau, I.; Ofitserov, A.; van Baarle, G. J. C.; Frenken, J. W. M. *Rev. Sci. Instrum.* **2014,** *85,* 083703. doi:10.1063/1.4891811
12. Navarro, V.; van Spronsen, M. A.; Frenken, J. W. M. *Nat. Chem.* **2016,** *8,* 929–934. doi:10.1038/nchem.2613
13. van Spronsen, M. A.; Frenken, J. W. M.; Groot, I. M. N. *Nat. Commun.* **2017,** *8,* 429. doi:10.1038/s41467-017-00643-z
14. van Spronsen, M. A.; van Baarle, G. J. C.; Herbschleb, C. T.; Frenken, J. W. M.; Groot, I. M. N. *Catal. Today* **2015,** *244,* 85–95. doi:10.1016/j.cattod.2014.07.008
15. Böller, B.; Durner, K. M.; Wintterlin, J. *Nat. Catal.* **2019,** *2,* 1027–1034. doi:10.1038/s41929-019-0360-1
16. Roobol, S. B.; Cañas-Ventura, M. E.; Bergman, M.; van Spronsen, M. A.; Onderwaater, W. G.; van der Tuijn, P. C.; Koehler, R.; Ofitserov, A.; van Baarle, G. J. C.; Frenken, J. W. M. *Rev. Sci. Instrum.* **2015,** *86,* 033706. doi:10.1063/1.4916194
17. Giessibl, F. J. *Rev. Sci. Instrum.* **2019,** *90,* 011101. doi:10.1063/1.5052264
18. Ma, J.; Xu, J.; Duan, J.; Xu, H. *Res. J. Appl. Sci., Eng. Technol.* **2013,** *5,* 1232–1237. doi:10.19026/rjaset.5.4855
19. Christen, M. *Sens. Actuators* **1983,** *4,* 555–564. doi:10.1016/0250-6874(83)85067-7
20. Herbschleb, C. T. ReactorSTM: imaging catalysts under realistic conditions. Ph.D. Thesis, Faculty of Science, Leiden University, 2011.
21. Grober, R. D.; Acimovic, J.; Schuck, J.; Hessman, D.; Kindlemann, P. J.; Hespanha, J.; Morse, A. S.; Karrai, K.; Tiemann, I.; Manus, S. *Rev. Sci. Instrum.* **2000,** *71,* 2776–2780. doi:10.1063/1.1150691

22. Melcher, J.; Stirling, J.; Shaw, G. A. *Beilstein J. Nanotechnol.* **2015,** *6,* 1733–1742. doi:10.3762/bjnano.6.177

23. Hembacher, S.; Giessibl, F. J.; Mannhart, J. *Appl. Surf. Sci.* **2002,** *188,* 445–449. doi:10.1016/s0169-4332(01)00976-x

24. Steynberg, A. P. *Introduction to Fischer-Tropsch technology; Studies in surface science and catalysis*, Vol. 152; Elsevier: Amsterdam, Netherlands, 2004; pp 1–63. doi:10.1016/s0167-2991(04)80458-0

Nanoscale capacitance spectroscopy based on multifrequency electrostatic force microscopy

Pascal N. Rohrbeck[1,2], Lukas D. Cavar[1,3], Franjo Weber[1,2], Peter G. Reichel[1], Mara Niebling[1,3] and Stefan A. L. Weber[*1,3,4]

Full Research Paper

Address:
[1]Max Planck Institute for Polymer Research, Ackermannweg 10, 55128 Mainz, Germany, [2]Department of Chemistry, University of Mainz, Duesbergweg 10-14, 55128 Mainz, Germany, [3]Department of Physics, University of Mainz, Staudingerweg 7, 55128 Mainz, Germany and [4]Institute for Photovoltaics, University of Stuttgart, Pfaffenwaldring 47, 70569 Stuttgart, Germany

Email:
Stefan A. L. Weber[*] - Stefan.Weber@ipv.uni-stuttgart.de

* Corresponding author

Abstract

We present multifrequency heterodyne electrostatic force microscopy (MFH-EFM) as a novel electrostatic force microscopy method for nanoscale capacitance characterization at arbitrary frequencies above the second cantilever resonance. Besides a high spatial resolution, the key advantage of the multifrequency approach of MFH-EFM is that it measures the second-order capacitance gradient at almost arbitrary frequencies, enabling the measurement of the local dielectric function over a wide range of frequencies. We demonstrate the reliable operation of MFH-EFM using standard atomic force microscopy equipment plus an external lock-in amplifier up to a frequency of 5 MHz, which can in principle be extended to gigahertz frequencies and beyond. Our results show a significant reduction of signal background from long-range electrostatic interactions, resulting in highly localized measurements. Combined with refined tip–sample capacitance models, MFH-EFM will enhance the precision of quantitative studies on dielectric effects in nanoscale systems across materials science, biology, and nanotechnology, complementing established methods in the field.

Introduction

Technological progress in fields including electronics, energy storage, photonics, and biomedical devices would not have been possible without the development of new materials. Progress in these areas requires a detailed understanding of material properties, particularly at the nanoscale, where phenomena such as quantum confinement, interface effects, and defect dynamics

play a critical role. Innovations in characterization techniques have enabled researchers to explore these properties with unprecedented precision, paving the way for the design of materials with tailored functionalities [1-6].

Dielectric properties are fundamental for understanding the behavior and performance of various material systems, as they directly influence charge storage, polarization, and energy dissipation mechanisms. For instance, in microelectronic devices, high-κ dielectric materials such as HfO_2 and ZrO_2 are critical for minimizing leakage currents and enhancing gate capacitance in transistors [7-9]. In energy storage systems, the dielectric constants of polymer–ceramic composites determine the efficiency and reliability of capacitors [10]. Similarly, in next-generation photovoltaic devices, the dielectric properties of absorber layers, such as lead-halide perovskites, affect carrier recombination and electric field distribution, thereby influencing power conversion efficiency [11].

At the nanoscale, the importance of dielectric properties becomes even more pronounced. Many advanced materials exhibit nanoscale structural heterogeneity, where quantum confinement, phase composition, and interfacial effects cause significant deviations in dielectric behavior compared to bulk materials [12,13]. These nanoscale variations influence key properties such as charge transport, polarization dynamics, and defect distributions, directly impacting the performance of microelectronic and energy systems [14,15]. Understanding these effects requires correlating nanoscale dielectric properties with structural and morphological features.

Scanning probe techniques have revolutionized nanoscale material characterization. Since the invention of scanning tunneling microscopy (STM) [16] and atomic force microscopy (AFM) [17], various electric force-based methods, called electrostatic force microscopy (EFM) methods, have emerged to study materials such as perovskite solar cells [18-20] and Li-ion batteries [21-23]. AFM enables simultaneous acquisition of topographic and electronic data by applying AC or DC voltages across the tip–sample gap, allowing for the detection of capacitive forces [24,25] or contact potential difference (CPD) [18]. Its exceptional spatial resolution, ranging from sub-micrometer [24,26] to atomic scales [27,28], makes AFM a powerful tool for nanoscale analysis.

Scanning probe-based capacitance mapping methods can be divided into two categories: Methods measuring the tip–sample capacitance directly are referred to as scanning capacitance microscopy (SCM) [29-54], whereas methods measuring the capacitive tip–sample force are referred to as scanning capacitance force microscopy (SCFM) [24,25,55-73]. Compared to

optical ellipsometry or reflectance spectroscopy, SCM and SCFM can map surface properties such as film thickness [35,39] and dielectric constants [35,74], with superior spatial resolution. However, in particular, SCM techniques face limitations due to nonlocal stray capacitances [40] from cantilever, tip cone, and the electrical connection, which hamper precise measurements and decrease resolution [55,61].

The advantage of SCFM methods is that capacitive forces depend on the first- or higher-order capacitance gradients with respect to the tip–sample distance, automatically canceling out the background capacitance caused by electrical connections and – to some degree – by the cantilever and the tip cone [24,25,55-73]. For example, Cherniavskaya et al. and Crider et al. laid the groundwork for EFM-based nanoscale dielectric measurements such as SCFM [68,69]. Generally, EFM methods using higher-order capacitance gradients exhibit superior lateral resolution [75].

An interesting extension of SCM and SCFM is the possibility to vary the electrostatic excitation frequency, enabling broadband dielectric nanospectroscopy experiments. While it is relatively straightforward to measure the frequency-dependent capacitance in SCM [29,54,76,77], force-based SCFM measurements are usually coupled to the cantilever resonances, limiting the available frequency space. Single-pass second-harmonic EFM in the attractive regime has been used to detect the cantilever response at the second harmonic of the electrostatic force (2ω) [68-70,72] generated when $\Delta\omega_e$ spans the range from 8 kHz to 2 MHz [70]. SCFM in the megahertz regime has been implemented [70,71] as well as a heterodyne-based EFM mode [59,72,73,78]. By using a low-frequency modulation of a high-frequency electrostatic drive, the response can be picked up either via a frequency shift or by an electrostatic response at one of the cantilever's resonance frequencies. Thus, the dielectric response can be studied at almost arbitrary frequencies. Using this method, Gramse et al. have demonstrated broadband spectroscopy of dielectric layers in air [72] and water [59].

Building on this idea, we propose a novel, multifrequency AFM-based method for nanoscale capacitance characterization at arbitrary frequencies above the second cantilever resonance. Our approach measures the second capacitance gradient, enhancing localization by minimizing stray capacitance contributions [65]. This method enables high-frequency capacitance gradient spectroscopy without requiring specialized equipment beyond a lock-in amplifier (LIA).

The following sections introduce the theoretical framework of multifrequency EFM, demonstrate its resolution enhancement experimentally, and validate its spectroscopic capabilities by

measuring nanoscale dielectric properties of microfabricated SiO_2 samples. Finally, we compare its performance with established techniques through capacitance imaging of a model microcapacitor system and a perfluoroalkyl-alkane $F(CF_2)_{14}(CH_2)_{20}H$ (F14H20) sample.

Theory
Multifrequency electrostatic force microscopy
The electrostatic force F_{ES} between tip and sample can be understood in terms of the gradient of the energy, W_C, stored in the tip–sample capacitor C with respect to the tip–sample separation z, as given by

$$F_{ES} = \frac{\partial W_C}{\partial z} = \frac{1}{2} \cdot \frac{\partial C}{\partial z} \cdot V_{tip-sample}^2, \tag{1}$$

where $V_{tip-sample}$ specifies the electrical voltage across the tip–sample gap. In conventional EFM with single-frequency excitation, $V_{tip-sample}$ is given by Equation 2 [18]:

$$V_{ES} = V_{DC} - V_{CPD} + V_{AC} \cdot \sin(\omega_e \cdot t), \tag{2}$$

with V_{DC} the DC voltage offset applied to the tip, V_{AC} the AC voltage amplitude with the frequency ω_{AC} at a certain time t and V_{CPD} the CPD, which corresponds to the difference in tip and sample work function [18]. Inserting Equation 2 into Equation 1, we obtain the following expression:

$$F_{ES} = \frac{1}{2} \frac{\partial C}{\partial z} \left((V_{DC} - V_{CPD})^2 + \frac{V_{AC}^2}{2} \right) \tag{3}$$

$$+ \frac{\partial C}{\partial z} (V_{DC} - V_{CPD}) V_{AC} \sin(\omega_e t) \tag{4}$$

$$+ \frac{\partial C}{\partial z} \frac{V_{AC}^2}{4} \cos(2\omega_e t). \tag{5}$$

Alongside a static component in Equation 3, the electrostatic force has periodic time-dependent components at frequencies ω_e and $2\omega_e$, which correspond to Equation 4 and Equation 5, respectively. In the case of an oscillating AFM tip, the tip–sample distance z and, thereby, the tip–sample capacitance and its gradients are changing periodically. This periodic fluctuation of the capacitance gradient $C'(t) = \frac{\partial C}{\partial z}(t)$ adds an additional dynamic component to Equations Equation 3–Equation 5. Using a Fourier expansion for the capacitance gradient $C'(t) = \frac{\partial C}{\partial z}(t)$ yields [18]:

$$C'(t) = C'(z_0) + C''(z_0) \cdot A_m \cdot \cos(\omega_m t) + \dots \tag{6}$$

By inserting Equation 6 into Equations Equation 3–Equation 5, we find that frequency mixing between $C'(t)$ and the electrostatic excitation leads to sidebands at frequencies $\omega_{SB,1} = (\omega_m \pm \omega_{AC})$ and $\omega_{SB,2} = (\omega_m \pm 2\omega_{AC})$ besides the mechanical oscillation at ω_m[18]. The amplitude of the first harmonic frequency components is used in conventional amplitude modulation (AM) and sideband or heterodyne Kelvin probe force microscopy (KPFM) [18,26,79]. The second harmonic signals are proportional to the local capacitance gradients, providing information about the local tip–sample capacitance. To ensure a sufficient signal-to-noise ratio, the resulting frequencies should coincide with one of the cantilever's resonance frequencies, limiting the choice of excitation frequencies.

We can avoid this limitation by using a multifrequency excitation approach. With a double-frequency excitation, we can write the tip–sample voltage as

$$V_{tip-sample} = V_{AC,1} \cdot \sin(\omega_{e,1}t) + V_{AC,2} \cdot \sin(\omega_{e,2}t). \tag{7}$$

In the case of two drives with identical amplitude $V_{AC,1} = V_{AC,2} = \frac{V_{AC}}{2}$, Equation 7 can be rearranged as

$$V_{tip-sample} = V_{AC} \cdot \sin\left(\frac{\omega_{e,1} - \omega_{e,2}}{2}t\right) \cdot \sin\left(\frac{\omega_{e,1} + \omega_{e,2}}{2}t\right). \tag{8}$$

Thus, the waveform can be viewed as a high-frequency oscillation at $(\omega_{e,1} + \omega_{e,2})/2 = \omega_{mod}/2$ with a low-frequency amplitude modulation at frequency $(\omega_{e,1} - \omega_{e,2})/2 = \Delta\omega_e/2$. This effect is also known as "beating" and is utilized in the AFM context for example in intermodulation AFM [80-83].

By inserting Equation 6 and Equation 8 in Equations Equation 3–Equation 5, we obtain the full expression for the electrostatic force. Here, we will focus on the DC force component in Equation 3 and set $V_{DC} - V_{CPD} = \Delta$:

$$F_{DC} = \frac{1}{2}\left(C' + C''A_m \sin(\omega_m t) + \dots\right) \cdot \left[\Delta^2 + \frac{V_{AC}^2}{2}\sin^2\left(\frac{\Delta\omega_e}{2}t\right)\right] \tag{9}$$

$$= \frac{1}{2}C'\left[\Delta^2 + \frac{V_{AC}^2}{4}\right] + \frac{1}{8}C'V_{AC}^2 \cos(\Delta\omega_e t) \tag{10}$$

$$+\frac{1}{2}C''A_m\left[\Delta^2+\frac{V_{AC}^2}{4}\right]\sin\left(\omega_m t\right)+\frac{1}{16}C''A_m V_{AC}^2 \sin\left[\left(\omega_m\pm\Delta\omega_e\right)t\right].\ (11)$$

In addition to a static force term identical to Equation 3, Equation 10 contains a term proportional to C' at frequency $2\omega_{mod}=\Delta\omega_e$. This force has been used for AM-based dielectric spectroscopy [63,69,74,84-88]. The second term, Equation 11, contains a force component at the mechanical drive frequency ω_m and at a sideband frequency $\omega_m\pm 2\omega_{mod}$. The latter one is independent of the local CPD, making it interesting for dielectric measurements. As the magnitude of this force component depends on C'', we can expect a superior lateral resolution through a reduction of long-range force contributions from tip cone and cantilever. As in the case of conventional EFM, signal-to-noise is greatly improved by choosing $\Delta\omega_e$ such that one of the induced sidebands falls on one of the cantilever's mechanical resonances. We call this method multifrequency heterodyne electrostatic force microscopy (MFH-EFM).

To calculate the second capacitance gradient, we need to calculate the electrostatic force from the detected amplitude signal, A_{det}, taking into account the cantilever's frequency-dependent spring constant or transfer function, $k(\omega)$:

$$\frac{\partial^2 C}{\partial z^2}=C''=\frac{16A_{det}\cdot k\left(\omega\right)}{A_m\cdot V_{AC}^2}. \quad (12)$$

Interestingly, the forces in Equation 11 only depend on the frequency difference, $\Delta\omega_e$, of the electrical drive frequencies.
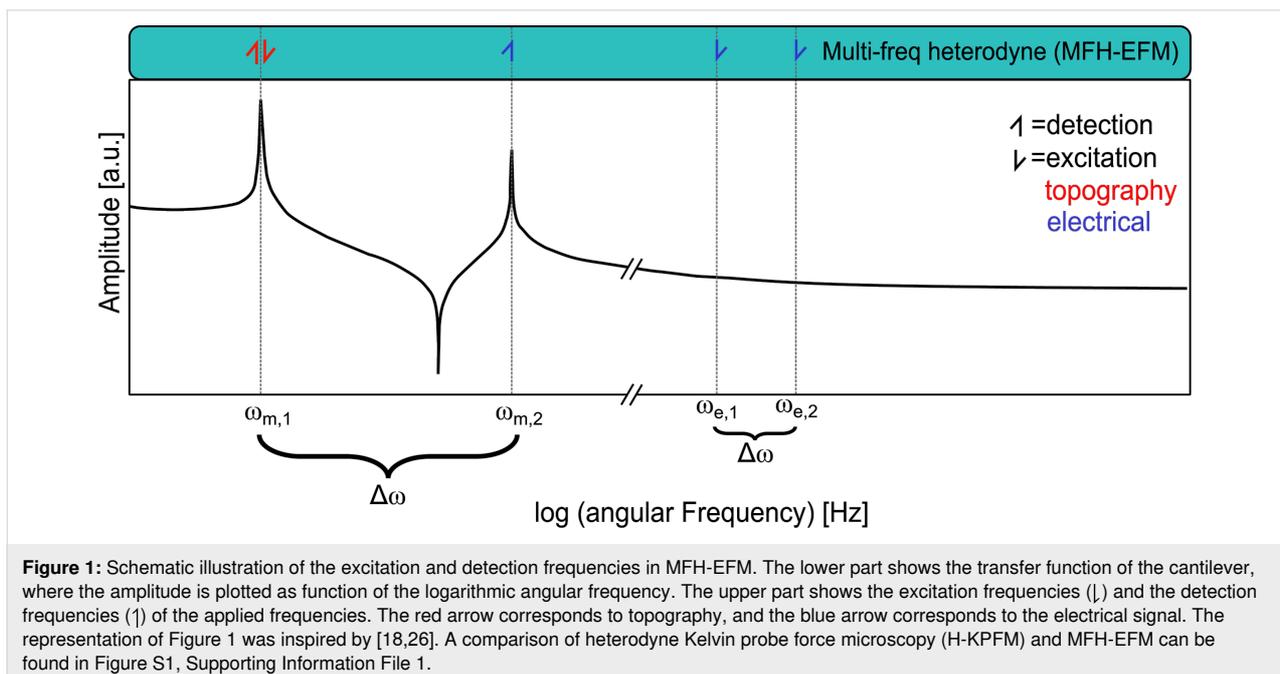
Thus, the experiments can be performed at almost arbitrarily high AC frequencies. The lower limit for the frequency range is given by the second resonance of the cantilever. Towards higher frequencies, the impedance of the electrical connection will introduce a damping of the excitation signal that has to be considered in Equation 12. By using appropriate means of coupling the electrical excitation into the tip–sample gap, experiments at microwave or even at optical frequencies are possible. In our setup, the two excitation frequencies can be varied in frequency from ≈600 kHz up to at least 50 MHz, limited by the bandwidth of the LIA. To reach a nanoscale-sensitive measurement of the dielectric constant in media besides air, a detection at higher excitation frequencies in the megahertz regime is strictly necessary [59].

The indirect detection of local capacitance variations by means of an electrostatic force has the advantage that it does not require additional devices for the measurement except for the LIA similar to that in the work of Gramse and colleagues [56]. Nevertheless, quantifying the total tip–sample capacitance will require varying the distance, for example, by force–distance spectroscopy.

Methods
Multifrequency heterodyne electrostatic force microscopy to measure the second capacitive gradient C''

We perform MFH-EFM using a conductive AFM cantilever in tapping mode with a mechanical drive near the fundamental

Figure 1: Schematic illustration of the excitation and detection frequencies in MFH-EFM. The lower part shows the transfer function of the cantilever, where the amplitude is plotted as function of the logarithmic angular frequency. The upper part shows the excitation frequencies (↓) and the detection frequencies (↑) of the applied frequencies. The red arrow corresponds to topography, and the blue arrow corresponds to the electrical signal. The representation of Figure 1 was inspired by [18,26]. A comparison of heterodyne Kelvin probe force microscopy (H-KPFM) and MFH-EFM can be found in Figure S1, Supporting Information File 1.

cantilever eigenmode $\omega_{m,1}$ with a mechanical amplitude A_m. Additionally, we apply two high-frequency electrical excitations of identical magnitude ($V_{AC,1} = V_{AC,2}$) at the frequencies $\omega_{e,1}$ and $\omega_{e,2}$ (see Equation 7). A schematic of the excitation frequencies is shown in Figure 1.

We select the excitation frequencies at the *n*-th and the ($n + 1$)-th multiple of the frequency gap $\Delta\omega = (\omega_{m,2} - \omega_{m,1})$ (see Figure 1). Note that the use of integer multiples is a technical limitation coming from our LIA. In principle, any combination of frequencies with $\Delta\omega = (\omega_{m,2} - \omega_{m,1})$ would work. We then use lock-in detection to measure the induced mechanical excitation exactly at the second mechanical resonance of the cantilever ($\omega_{m,2}$).

Single-frequency electrostatic force microscopy to measure the first capacitive gradient C'

To obtain a quantitative comparison of the signal contributions to the signals based on the first and the second capacitance gradient, we performed single-frequency excitation EFM (SF-EFM) measurements as comparison to the multifrequency approach described above. In the fixed-frequency configuration, we use lock-in amplification to detect the second harmonic force component at $2\omega_e$ induced by a single-frequency (ω_E) stimulus (see Equation 5).
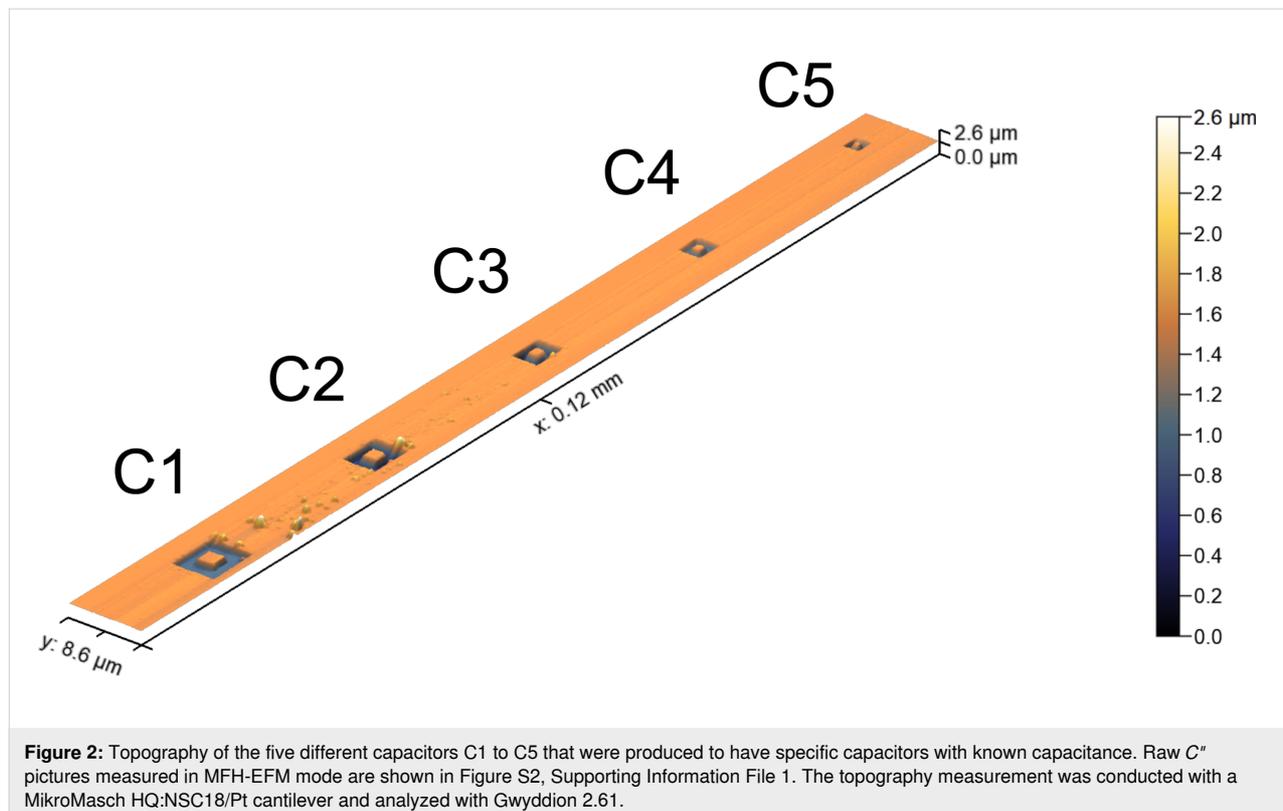
To enhance the signal, we select ω_E such that $2\omega_E$ coincides with the second resonance of the cantilever ($2\omega_E = \omega_{m,2}$). We connect the numerical value of the capacitance gradient to the detected amplitude using the cantilever's frequency-dependent transfer function or spring constant $k(\omega)$ by

$$\frac{\partial C}{\partial z} = C' = \frac{4 A_{det} \cdot k(\omega)}{V_{AC}^2}. \tag{13}$$

For the variable-frequency detection of C', we apply two AC voltages of the same magnitude ($V_{AC,1} = V_{AC,2}$) at frequencies n and ($n + 1$) times the second resonance frequency $\omega_{m,2}$. According to Equation 10, this will excite an oscillation at $\omega_{m,2}$ with an amplitude proportional to C'.

Silicon microcapacitors

To generate structures with a defined dielectric response, we prepared a series of microcapacitors. We used these structures to compare the C' and C'' distance dependencies from several force–distance curves with model calculations using tip–sample models from the literature, as well as for dielectric nanospectroscopy experiments. The microcapacitors were produced by focused ion beam (FIB) milling on a silicon wafer with a 300 nm layer of SiO_2 and a 14 nm sputtered layer of Pt on it (Figure 2).

Figure 2: Topography of the five different capacitors C1 to C5 that were produced to have specific capacitors with known capacitance. Raw C'' pictures measured in MFH-EFM mode are shown in Figure S2, Supporting Information File 1. The topography measurement was conducted with a MikroMasch HQ:NSC18/Pt cantilever and analyzed with Gwyddion 2.61.

Results and Discussion

To investigate whether the C''-sensitive detection leads to an improved spatial resolution of MFH-EFM as compared to conventional methods, we calculate the distance dependence of the first- and second-order capacitance gradients in an ideal cantilever. We compare our calculations to experimentally obtained force–distance curves. We then show the first practical examples of high-frequency capacitive spectra obtained by this method on etched SiO_2 microcapacitors, along with high-resolution high-frequency capacitance images obtained over self-assembled molecular F14H20.

Tip–sample capacitance

The total capacitance between sample and cantilever consists of contributions from tip apex, tip cone, lever, and some additional stray capacitance caused by the signal cables in the AFM head (Figure 3). In the case of a dielectric sample, the tip-, apex- and lever-surface capacitors are connected in series with capacitors formed by the sample dielectric layer. The exact configuration for these capacitors depends strongly on the local electric field distribution around tip apex, tip cone, and cantilever. Whereas the apex capacitance contains the desired local information, the stray capacitance from cone, lever, and cables produces a background signal that effectively reduces the lateral resolution of the local capacitance measurement. Practically, these signal contributions can be discerned by their respective distance dependence.
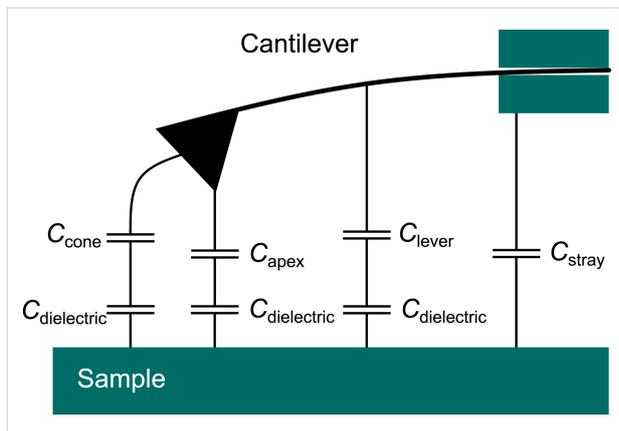

Figure 3: Schematic illustration of tip apex, tip cone, lever, and stray capacitances. The contribution of the tip apex contains the most localized part of the overall capacitance signal. The mesoscopic tip cone and the macroscopic cantilever, in contrast, contribute to the long-range stray capacitance, effectively delocalizing the signal.

To further investigate this distance dependence, we compare experimental force–distance spectra to analytical and numeric models from the literature. In particular, we combine the models for the apex contribution of Hudlet et al. [89] with the cone and lever contributions from Colchero and colleagues

[90,91]. The full equations for the force together with the resulting capacitance used here are given in the Appendix section (see Equations Equation 16–Equation 21 and Figure 10 below).

In Figure 4, we compare the respective contributions to the first and second capacitance gradients together with the corresponding electrostatic forces during a typical AFM experiment as functions of tip–sample distance z. For the force calculations, we used Equation 12 together with the parameters of a regular EFM cantilever (NuNano SPARK 70 Pt) and an electrical drive of $V = 2$ V and a mechanical amplitude of $A_m = 10$ nm. Comparing the graphs, we can immediately see that the total C' signal retains a significant long-range contribution even at a tip–sample separation of 3000 nm (Figure 4a). In contrast, the C'' signal drops more rapidly over a short distance z (Figure 4b), indicating a reduced influence of long-range contributions to the force signals.
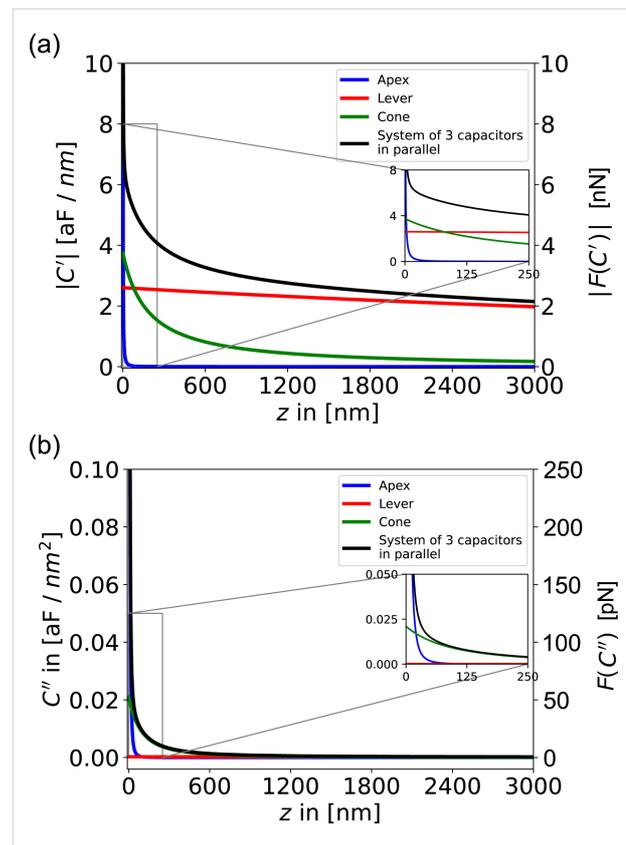
Figure 4: Contributions of the respective components to the (a) first numeric derivative C' and (b) second numeric derivative C'' of the capacitance as functions of the distance z between tip and sample. Additionally, the respective forces (a) $F(C')$ and (b) $F(C'')$ were plotted as functions of z. A NuNano SPARK 70 Pt cantilever ($w = 30$ μm, $l = 225$ μm, $\alpha = 11°$, $h = 12$ μm, $\theta = 25°$, $r = 18$ nm, and $\delta = 3.7 \cdot 10^{-7}$) was used for the calculations with an mechanical amplitude of $A_m = 10$ nm, an excitation voltage of $V_{AC} = 2$ V, and a total amount of calculated points of 100,000. The blue line marks the apex, the green line the cone, the red line the lever, and the black line marks the entire system of the three components in parallel.

A measure of how much the signal is disturbed by non-local long-range contributions is the apex contribution to the total signal at a given distance *z*. At a typical tip–sample separation of 10 nm, the apex signal makes up more than 82% of the complete *C″* signal, while the apex contribution to the first capacitance gradient only makes up less than 10% of the total *C′* signal. In closer proximity of 1 nm distance to the sample, the apex contribution to the *C″* signal increases to 99.8%, whereas the *C′* signal still contains a significant amount of non-local signal contributions with 62% apex vs 38% cone and lever signal. Another way to quantify the "locality" of a force signal is to investigate the tip–sample separation at which the tip apex contribution surpasses the lever-plus-cone contributions within Figure 4. This is true in Figure 4a for distances smaller than ≈3 nm, while in Figure 4b, this is the case even for distances smaller than ≈20 nm. Comparing the absolute values of the forces, however, we see that MFH-EFM yields much weaker forces: At a tip–sample distance of 10 nm, the AM-based operation leads to a force of $F_{ES}(C') = 6.7$ nN, as compared to $F_{ES}(C'') = 280$ pN for MFH-EFM. Hence, the resulting electrostatic force and, thereby, the expected force is by more than a factor of 24 lower for MFH-EFM. Thus, the improved lateral resolution comes at the price of a reduced signal-to-noise ratio.

To reproduce these findings experimentally, we performed force–distance spectroscopy on the etched microcapacitors shown in Figure 2. The resulting curves of the *C′* and *C″* signals qualitatively reproduced the simulation results (Figure 5). Whereas the *C″* signal only emerged from the noise at distances of less than 500 nm, the *C′* signal shows a monotonic decrease over the full 3 μm of vertical travel. Compared to the simulations, the experimental *C′* signal shows a slower decrease, indicating a stronger influence from the tip cone. The direct comparison of the model and the data of the second and first capacitance gradients can be found in Figure S16 and Figure S17, Supporting Information File 1, respectively. These results clearly show that the MFH-EFM method produced an electrostatic force signal that is highly local with suppressed stray contributions from cone and lever.

Dielectric nanospectroscopy

The advantage of the multifrequency excitation approach of MFH-EFM is that we can choose arbitrary frequencies above the detection frequency for the electrostatic excitation. As the tip–sample capacitance is influenced by the dielectric properties of the material in the tip–sample gap (see Figure 3), the frequency-dependent electrostatic force represents the local dielectric function. To demonstrate the feasibility of dielectric nanospectroscopy, we performed MFH-EFM frequency spectroscopy at three different locations on the microcapacitor sample. The first spectrum was recorded on one of the microcapacitors (*C3*, see Figure 2). Then, we measured in one of the FIB-etched trenches around the capacitors. Here, we assume that the bare silicon surface is covered by a thin native oxide layer (Si). Last, we measured on a particle of unknown origin (Dirt, visible in Figure 2). The frequency sweeps were performed by keeping the tip position and amplitude fixed, varying the two heterodyne excitation frequencies while keeping their separation
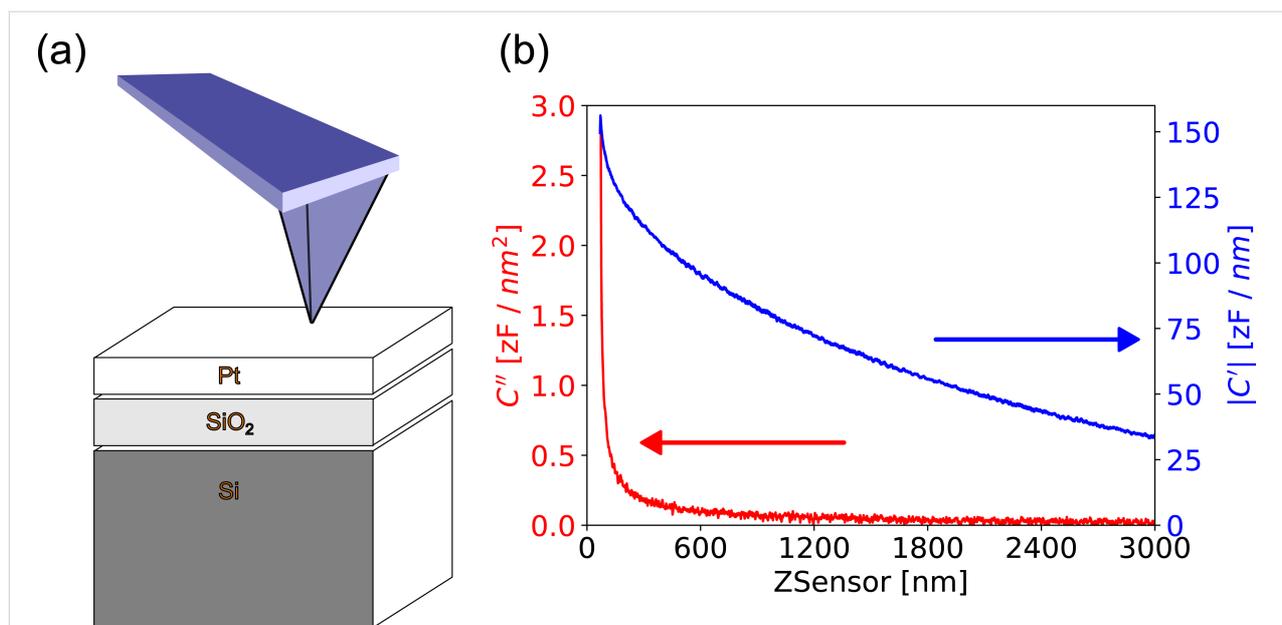
Figure 5: Comparison of the *C″* and the *C′* single force curves (b) of a microcapacitor (a) while doing MFH-EFM (see Equation 11 and Equation 12) and compared with the detection of 2ω (see Equation 5 and Equation 13). The measurement was conducted with a NuNano SPARK 70 Pt cantilever.

fixed, and recording the resulting excitation amplitude at the second mechanical resonance. All spectra were normalized against a reference spectrum recorded on the bare substrate far away from the capacitors to compensate any frequency response arising from the stray capacitance in the signal paths and cantilever. The electrostatic signal of the capacitor C3 showed a drop at around 2 MHz in Figure 6. When considering the capacitance of C3 of 183 ± 1 aF and the drop-off frequency ω_d of the capacitance at 1.7 MHz, we can calculate the resistance R via the RC time ($RC = 1/\omega_d$) as $R \approx 3200$ MΩ. This value is much smaller compared to the calculated value of the resistance of SiO_2, which is $25 \cdot 10^{21}$ Ω, taking into account the electrical resistivity of silicon dioxide of $\rho_{SiO_2} = 25 \cdot 10^{16}$ Ωm [92] and a thickness of the SiO_2 layer of 300 nm on an area of 9 µm². The observed discrepancy may be attributed to the increased conductivity of the microcapacitors, which is a result of the incorporation of Ga^+ ions into the SiO_2 layer.

Figure 6: Comparison of the normalized C'' (red colors on top) and normalized C' (blue colors at the bottom) frequency sweep on one of the capacitors (C3, see Figure 2, cross symbols), on milled silicon (Si, triangle symbols), and on a particle of unknown origin (Dirt, square symbols). This experiment was conducted with a MikroMasch HQ:NSC18/Pt cantilever. The non-normalized data, as well as normalized data over a wider frequency range, can be viewed in Figures S3–S6 and S9–S12, Supporting Information File 1.

The C'' signal of the bare Si was stable over the whole range of excitation frequencies and only dropped at a much higher frequency around 24 MHz (see Figure S5, Supporting Information File 1). The dielectric response of the undefined particle was significantly lower compared to the response of the capacitor structures. In the frequency response, we found little to no signal response, even at low excitation frequency. A rise of the signal at around 6 MHz could be observed in all the C'' signals at that frequency (see Figure S3, Supporting Information File 1), which we attribute to a capacitive singularity in the electrical connection to the sample. We observed a similar be-

havior in the frequency range between 5 and 10 MHz and around 17 MHz. We want to point out that we used standard AFM equipment with no special means to control the impedance of the electrical connections. To obtain more trustworthy data in the frequency range above 5 MHz, specialized sample and cantilever holders with coaxial electric connections will be required.

To compare these results with the conventional AM-based EFM approach, we repeated the spectroscopy experiments for the C' signal based on the second term in Equation 10 (Figure 6, non-normalized data in Figures S9–S11, Supporting Information File 1). In comparison to the MFH-EFM data, the C' frequency sweep looked very similar on the different structures. We think that this reduction in contrast is caused by the stronger influence of the long-range interactions from tip cone and cantilever in the C' signal. Thus, the overall impact of the local surface dielectric properties under the tip apex is reduced as compared to the impact of the dielectric properties probed by tip cone and cantilever (see Figure 3).

Imaging C′ versus C″

To demonstrate the capabilities of MFH-EFM as an imaging method, we performed experiments on self-assembled nanostructures consisting of the amphiphilic molecule F14H20 (Figure 7). F14H20 exhibits a strong dipole moment of 3.1 D oriented along the chains consisting of fluorinated and hydrogenated parts [93], leading to a strong nanoscale contrast in the dielectric signal.

On the silicon substrate, F14H20 formed groups of spherical particles with a diameter of 40 ± 5 nm (Figure 7a) [94,95]. Simultaneously with the topography, we recorded the C'' amplitude and phase at electrical excitation frequencies of 1.59 and 1.98 MHz. In the dielectric spectroscopy images, we see a sharp contrast between the F14H20 particles and the silicon substrate, both in C' (Figure 7b,c) and C'' (Figure 7d,e). Within all images, the particles exhibit a lower amplitude signal than the surroundings [95]. The latter is formed by a thin fluoroalkane layer with molecules lying along the sample surface [95]. The contrast within the particles correlates with variations of dielectric permittivity, and the latter is related to averaged dipole values [95]. Similar work [96] indicated that the response increases with an increase of sample permittivity [95,96]. We measured a CPD difference between Si and F14H20 of −0.72 ± 0.08 V (see Figure S15, Supporting Information File 1), which is close to the literature value of −0.8 V [97].

Interestingly, the image of the C' signal (Figure 7c,e) showed a more blurry structure (compare the insets in Figure 7b,c). Another effect that can be observed in the C' phase images is
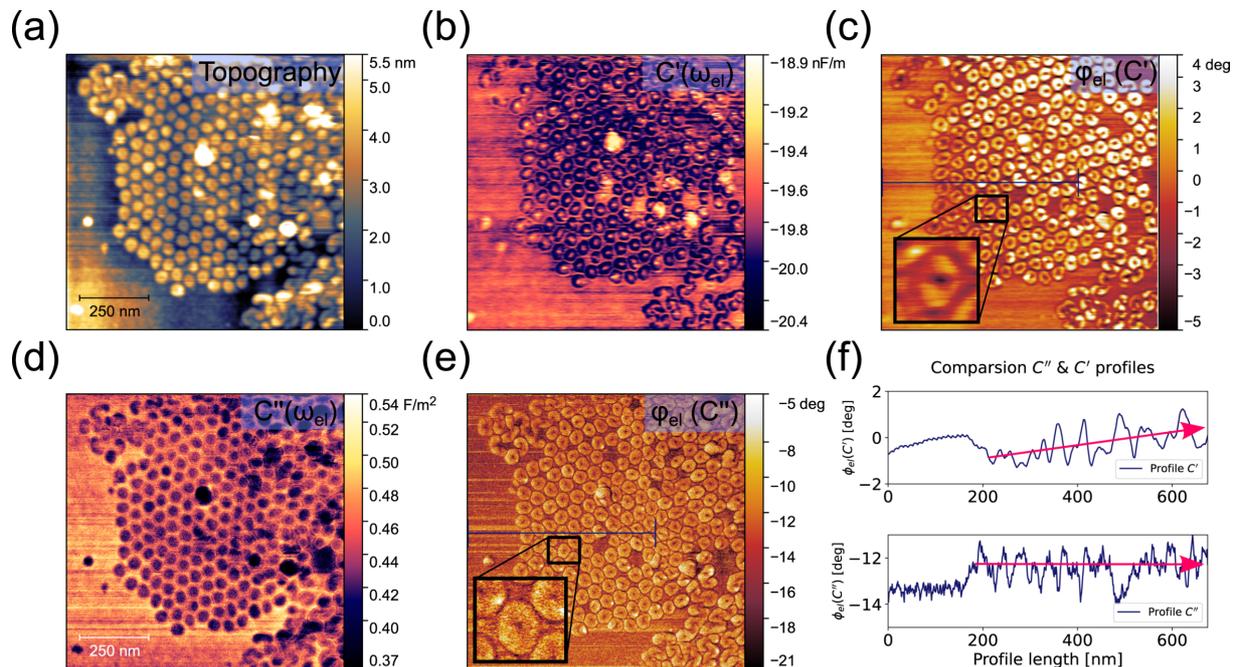
Figure 7: MFH-EFM images taken on F14H20. (a) Topography image. (b) C' image detected at $\omega_{m,2}$ under excitation at 235.579 kHz. (c) Electric phase φ_{el} of the C' signal detected at $\omega_{m,2}$ under excitation at 235.579 kHz. (d) C'' image detected at $\omega_{m,2}$ under excitation at frequencies of 1.59 and 1.98 MHz. (e) Electric phase φ_{el} of the C'' signal detected at $\omega_{m,2}$ under excitation at frequencies of 1.59 and 1.98 MHz. (f) Profiles of the phase images shown in (c) and (e) with 128 pixels width and the same resolution. The full picture can be found in Figure S15, Supporting Information File 1. The measurements were conducted with a MikroMasch HQ:NSC18/Pt cantilever.

that the individual contrast on the particles changes when going towards the center of the particle agglomerate (upper graph in Figure 7f). While there is only a very shallow contrast for the first two to five particles, both the contrast and the baseline signals increased towards the center of the agglomerate. In the C'' images, however, the dielectric contrast remained the same across the particle agglomerate, demonstrating once more that MFH-EFM provides more local information and is less affected by long-range electrostatic effects.

Conclusion

We have presented a novel method for high-resolution nanoscale capacitance characterization based on multifrequency electrostatic force microscopy, complementing established methods in the field. The key advantage of the multifrequency approach of MFH-EFM is that it allows for measurements of higher-order tip–sample capacitance gradients at almost arbitrary frequencies above the second cantilever resonance, enabling the measurement of the local dielectric function over a wide range of frequencies. In comparison to many existing SCM operation modes, MFH-EFM leads to a significant reduction of signal background, which results in higher locality of the measurements with less cross talk. This is due to the fact that the second capacitance gradient is less affected by long-range

interactions, such as those from tip cone and lever. We demonstrate the reliable operation using standard AFM equipment together with an external LIA up to a frequency of 5 MHz. At higher frequencies (up to 50 MHz in our case), the signals were dominated by impedance effects from the signal connections. Thus, to move towards reliable measurements at higher frequencies, specialized high-frequency equipment with coaxial signal connections will be required.

Our analytical simulations of the distance-dependent tip–sample capacitance showed that current models are not able to fully simulate the experimental data. Thus, to enable quantitative measurements of the tip–sample capacitance, further measures such as improved tip–sample models or full numerical simulations will be required. Here, the suppression of long-range electrostatic interactions in MFH-EFM could simplify the simulations. Thus, MFH-EFM could further improve quantitative studies on dielectric effects in nanoscale systems across materials science, biology, and nanotechnology.

Experimental
Polymer blend samples
We used F14H20 samples that we bought from SPM Labs LLC, Tempe, AZ, USA.

Microcapacitors

Si wafers "CZ" were bought from "Si-Mat" with a diameter of 150 mm, $\langle 100 \rangle$ surface orientation, a thickness of 675 ± 20 μm, a resistivity of 1.5–4.0 Ωcm, and with p-type doping with B atoms. These wafers were thermally oxidized with 300 nm SiO_2. A compact coating unit 010/LV with the sputter head SP010 was used to sputter 14 nm of Pt on top of the wafer. The microcapacitors were then milled out of the surface using a FEI Nova600 Nanolab FIB apparatus with a dual Ga^+ ion beam.

Multifrequency heterodyne electrostatic force microscopy

MFH-EFM was measured on an Oxford Instruments/Asylum Research MFP-3D Infinity AFM in a nitrogen glovebox (level of humidity below 0.3%, level of oxygen below 0.1%). The typical resonance frequency of the Pt/Ir-coated conductive cantilevers (NuNano SPARK-150Pt and MikroMasch HQ:NSC18/Pt) was ≈75 kHz; the levers had a spring constant of 2–3 N·m^{-1}, a tip radius of 18 nm, and a tip height of 10–18 μm. The topography feedback measurements were performed with amplitude modulation on the first eigenmode $\omega_{m,1}$, and the oscillation amplitude was kept to 70–90 nm for all measurements. The force spectroscopy measurements were done with a z rate of 0.2 Hz and a force distance of 8 μm for all samples.

We used a Zurich Instruments HF2 LIA for all experiments. The electric drive amplitude of the $V_{AC,1} = V_{AC,2}$ signal varied

between 3 and 5 V, depending on the obtained signal from the sample. We grounded the sample via the sample holder with an external wire to ground level of the LIA. The V_{AC} was applied to the tip directly, while the AFM head connections were switched off. The setup of the AFM is shown in Figure 8. The electrical connection from the LIA to the cantilever with the two excitation voltages was realized by using a direct cable connection.

Focused ion beam milling

FIB milling of the cantilever was conducted using a LEO Gemini instrument from Zeiss. It was used with an acceleration voltage of 3 kV.

Appendix
Equations to calculate the C'' and C' signal from the voltages

Equation 14 shows a detailed expression of Equation 12. The detected amplitude from the LIA, A_{det}, contains the voltage from the LIA ($V_{MFH-EFM}$) and $\Xi_{amp,d2C}$, the amplification factor of this voltage from the LIA in MFH-EFM mode. The frequency-dependent spring constant $k(\omega)$ in Equation 12 contains the inverse optical lever sensitivity (InvOLS) of the second harmonic (InvOLS$_2$), the spring constant of the second resonance (k_2), and the Q-factor shown in Equation 14. It is important to note that the InvOLS and the spring constant on the

Figure 8: Schematic setup of the MFH-EFM apparatus. Additionally to a regular AFM, two different voltages with different frequencies are applied to the cantilever.
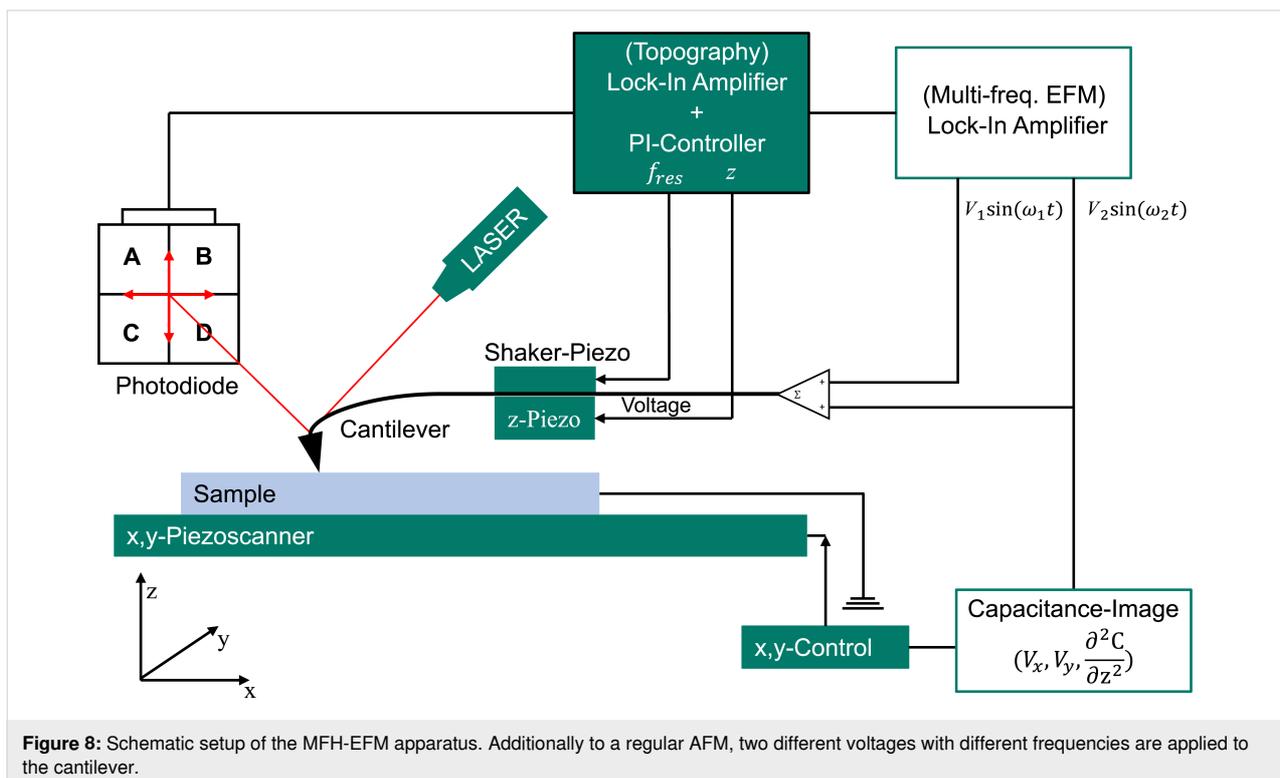
second resonance are not the same as measured on the first resonance by the method of Sader and colleagues [98]. It is rather necessary to calculate the properties of the cantilever for the respective eigenmodes [99].

$$\frac{\partial^2 C}{\partial z^2}(\omega) = C''(\omega) = \frac{16 \cdot V_{\text{MFH-SCM}}(\omega) \cdot InvOLS_2(\omega) \cdot k_2(\omega)}{A_{\text{m}} \cdot V_{\text{AC}}^2 \cdot \Xi_{\text{amp,d2C}} \cdot Q} \quad (14)$$

Equation 15 shows a detailed expression of Equation 13. Again, the expression A_{det} contains the detected voltage from the LIA ($V_{\text{SF–EFM}}$) and an amplification factor $\Xi_{\text{amp,dC}}$ of the signal captured with the LIA in SF-EFM mode. The frequency-dependent spring constant $k(\omega)$ is the same as above and consists of $InvOLS_2$, k_2, and the Q-factor.

$$\frac{\partial C}{\partial z}(\omega) = C'(\omega) = \frac{4 \cdot V_{\text{SF-EFM}}(\omega) \cdot InvOLS_2(\omega) \cdot k_2(\omega)}{V_{\text{AC}}^2 \cdot \Xi_{\text{amp,dC}} \cdot Q} \quad (15)$$

## Full double excitation force equations

This section gives a full overview of the electric amplitude contributions at various frequencies while activating the MFH-EFM mode. For simplicity, we will use the following substitutions: $\omega_{\text{m}}^1 t = O$, $\omega_e t = E$, $\omega_{\text{mod}} t = M$, $V_{\text{CPD}} - V_{\text{DC}} = \Delta$, $\hat{V}_{\text{AC}} = V$, and $A_{\text{m}}^1 = A$. Table 1 shows the overview of the force components at various frequencies for the resulting static ω and 2ω force components acting on the cantilever.

Table 1: Overview of the components of the multifrequency electrostatic force microscopy.

Frequency	Amplitude
DC	1/2 C' [$\Delta^2 + U^2/4$]
2M	1/8 $C'U^2$
O	1/2 $C''A[\Delta^2 + U^2/4]$
O ± 2M	1/16 $C''AU^2$
E ± M	1/2 $C'U\Delta$
O ± (E ± M)	1/4 $C''AU\Delta$
2E	1/8 $C'U^2$
2(M ± E)	1/16 $C'U^2$
O ± 2E	1/16 $C''AU^2$
O ± 2(E ± M)	1/32 $C''AU^2$

Tip–sample capacitance model

We used the model of Hudlet et al. [89] for the tip apex and, in addition, used the sum of cone and lever distribution of Colchero and colleagues [90,91]. The cantilever can be modeled as a tilted plate capacitor with a truncated cone at the end of the cantilever and with a sharp round tip apex at the end of the tip cone. This is shown schematically in Figure 9.
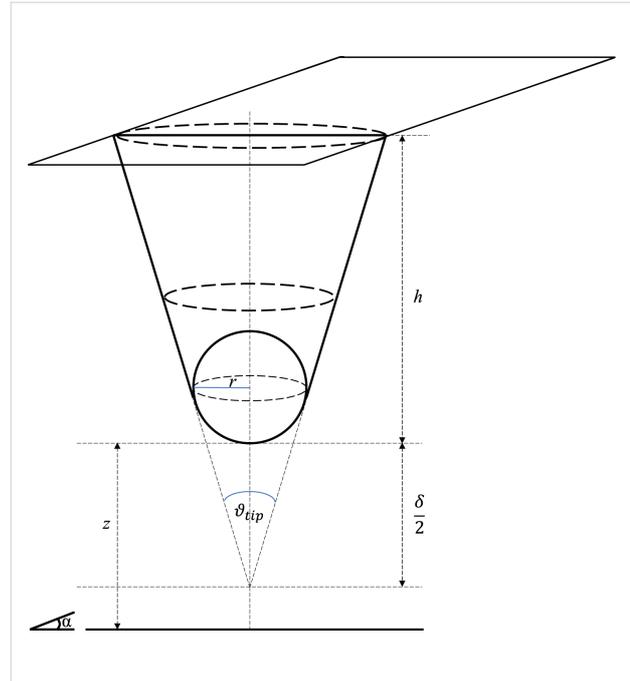
Figure 9: Sketch of the capacitance model of the truncated cone with spherical apex. Here h is the height of the tip, r is the radius of the sphere, ϑ_{tip} is the opening angle of the tip, δ is the truncated part of the cone, and z is the distance between sample and tip apex with respect to the surface normal of the sample. α is the angle between the surface and the lever of the cantilever.

In this case, the electrostatic force for the lever is given by Equation 16[90,91]:

$$F_{\text{lever}}(z) = \frac{2 \tan^2\left(\frac{\alpha}{2}\right)}{\alpha^2} \varepsilon_0 V_{\text{tip–sample}}^2 \frac{lw}{h^2}$$
$$\cdot \frac{1}{\left[\left(1 + \frac{z}{h}\right) \cdot \left(1 + \frac{z + 2l\tan\left(\frac{\alpha}{2}\right)}{h}\right)\right]} \cdot \quad (16)$$

Integration taking into account Equation 1 yields:

$$C_{\text{lever}}(z) = \frac{2 \tan^2\left(\frac{\alpha}{2}\right)}{\alpha^2} \varepsilon_0 V_{\text{tip–sample}}^2 \frac{lw}{h^2}$$
$$\cdot \frac{h^2 \cot\left(\frac{\alpha}{2}\right)\left\{\ln(h+z) - \ln\left[\cos\left(\frac{\alpha}{2}\right)(h+z) + 2l\sin\left(\frac{\alpha}{2}\right)\right]\right\}}{2l}, \quad (17)$$

where ε_0 is the dielectric constant of the vacuum. The dimensions of the lever are given by its width w, its length l, and the height of the tip cone h. The lever is tilted by the angle $\alpha = \vartheta_{\text{lever}}$.

The tip cone can be approximated by a truncated cone (Figure 9). The electrostatic force as a function of the distance between tip cone and sample is given by Equation 18[90,91]:

$$F_{\text{cone}}(z) = \frac{4\pi}{\left(\pi - \vartheta_{\text{tip}}\right)^2} \varepsilon_0 V_{\text{tip−sample}}^2$$

$$\cdot \left[\ln\left(\frac{z - \frac{\delta}{2} + h}{z + \frac{\delta}{2}} \right) - \sin\left(\frac{\vartheta_{\text{tip}}}{2} \right) \frac{h - \delta}{z - \frac{\delta}{2} + h} \cdot \frac{z - \frac{\delta}{2}}{z + \frac{\delta}{2}} \right], \quad (18)$$

with the open angle of the tip cone (ϑ_{tip}) and the height of the truncated part of the cone ($\delta = r/\tan^2(\vartheta_{\text{tip}}/2)$) [90,91]. Integration of this equation to obtain the capacitance yields

$$C_{\text{cone}}(z) = 2\frac{4\pi\varepsilon_0}{\left(\vartheta_{\text{tip}} - \pi\right)^2}$$

$$\cdot \left\{ \sin\left(\frac{\vartheta_{\text{tip}}}{2} \right) \left[h\ln(2f_1) - \delta\ln f_2 \right] + f_1 \ln\left(\frac{f_2}{2f_1} \right) + (\delta - h)\ln f_2 \right\}, \quad (19)$$

where $f_1 = z - \dfrac{\delta}{2} + h$ and $f_2 = 2z + \delta$.

The tip apex is approximated as a sphere over an infinite surface (Figure 9). The corresponding electrostatic force between a tip apex and the surface is given by Equation 20[89]:

$$F_{\text{apex}}(z) = \pi\varepsilon_0 r^2 V_{\text{tip−sample}}^2 \left(\frac{1 - \sin\left(\frac{\vartheta_{\text{tip}}}{2} \right)}{z\left\{ z + r\left[1 - \sin\left(\frac{\vartheta_{\text{tip}}}{2} \right) \right] \right\}} \right). \quad (20)$$

Hence, the capacitance is given by

$$C_{\text{apex}}(z) = 2\pi\varepsilon_0 r \ln\left\{ \frac{z + r\left[1 - \sin\left(\frac{\vartheta_{\text{tip}}}{2} \right) \right]}{z} \right\}. \quad (21)$$

When the capacitance of the cantilever is plotted as function of the distance between the tip and the sample, z, Figure 10 is obtained. The parameters were taken from the website of the producer of the NuNano SPARK 70 Pt cantilever: $w = 30$ μm, $l = 225$ μm, $\alpha = 11°$, $h = 12$ μm, $\vartheta_{\text{cone}} = 25°$, $r = 18$ nm, and $V_{\text{AC}} = 2$ V.

In order to get the first, C', and second capacitance gradient, C'', of the relevant parts of the cantilever, we used the onward and
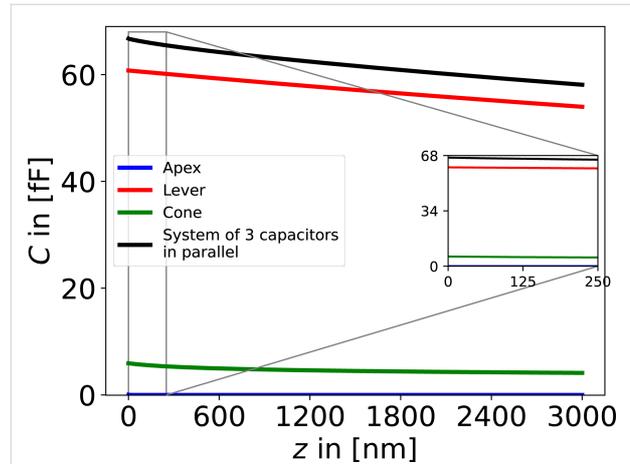
Figure 10: Contributions of the respective components to the numeric capacitance C as a function of the distance z between tip and sample. The properties of the NuNano SPARK 70 Pt cantilever ($w = 30$ μm, $l = 225$ μm, $\alpha = 11°$, $h = 12$ μm, $\theta = 25°$, $r = 18$ nm, and $\delta = 3.7 \cdot 10^{-7}$) with a mechanical amplitude of $A_{\text{m}} = 10$ nm, an excitation voltage of $V_{\text{AC}} = 2$ V, and a total number of 100,000 calculated points, were used for the calculations. The blue line marks the apex, the green line the cone, the red line the lever, and the black line marks the entire system of the three components in parallel.

backward differentiation given in Equation 22 and the central differential quotient of the second order given in Equation 23, respectively. The step size was chosen to be $1\cdot10^{-10}$ m with a total number of 1,000,000 steps. Models of the first and the second capacitance gradient can be found in Figure 4a and Figure 4b, respectively.

$$f'(x) = \frac{f(x+h) - f(x-h)}{2h} \quad (22)$$

$$f''(x) = \frac{f(x+h) - 2f(x) + f(x-h)}{h^2} \quad (23)$$

Supporting Information

Supporting information features a comparison of the working principles of H-KPFM and MFH-EFM, all the raw and normalized data of the MFH-EFM frequency spectroscopy measurements, the full comparison of the MFH-EFM, SF-EFM, and H-KPFM images on the F14H20 structures, and finally a comparison of the model data and the measured data on the microcapacitors.

Supporting Information File 1
Additional experimental data.
[https://www.beilstein-journals.org/bjnano/content/supplementary/2190-4286-16-49-S1.pdf]

Acknowledgements

Author Contributions

Pascal N. Rohrbeck: conceptualization; data curation; formal analysis; investigation; methodology; project administration; resources; software; validation; visualization; writing – original draft; writing – review & editing. Lukas D. Cavar: resources; software; writing – review & editing. Franjo Weber: software. Peter G. Reichel: investigation. Mara Niebling: resources; software. Stefan A. L. Weber: conceptualization; funding acquisition; resources; supervision; validation; writing – original draft; writing – review & editing.

ORCID® iDs

Pascal N. Rohrbeck - https://orcid.org/0000-0002-1514-6008

Data Availability Statement

Data generated and analyzed during this study is available from the corresponding author upon reasonable request.

Preprint

A non-peer-reviewed version of this article has been previously published as a preprint: https://doi.org/10.3762/bxiv.2024.72.v1

References

1. Elayarani, P.; Sumathi, T.; Sivakumar, G.; Pragadeswaran, S.; Suthakaran, S.; Sathiyamurthy, S.; Seshadhri, J.; Ayyar, M.; Arularasu, M. V. *Z. Phys. Chem.* **2024,** *238,* 1019–1042. doi:10.1515/zpch-2023-0531
2. Majid, F.; Bashir, M.; Bibi, I.; Ayub, M.; Khan, B. S.; Somaily, H. H.; Al-Mijalli, S. H.; Nazir, A.; Iqbal, S.; Iqbal, M. *Z. Phys. Chem.* **2023,** *237,* 1345–1360. doi:10.1515/zpch-2022-0097
3. Iqbal, Z.; Imran, M.; Latif, S.; Nazir, A.; Ibrahim, S. M.; Ahmad, I.; Iqbal, M.; Iqbal, S. *Z. Phys. Chem.* **2023,** *237,* 1139–1152. doi:10.1515/zpch-2022-0113
4. Ali, F.; Safdar, A.; Younas, U.; Sillanpaa, M.; Pervaiz, M.; Nazir, A.; Naeem, M.; Iqbal, M.; Al-Kahtani, A. A.; Tighezza, A. M. *Z. Phys. Chem.* **2023,** *237,* 599–616. doi:10.1515/zpch-2022-0098
5. Nazir, A.; Alam, S.; Alwadai, N.; Abbas, M.; Bibi, I.; Ali, A.; Ahmad, N.; Al Huwayz, M.; Iqbal, M. *Z. Phys. Chem.* **2023,** *237,* 1733–1751. doi:10.1515/zpch-2023-0331
6. Arif, H.; Yasir, M.; Ali, F.; Nazir, A.; Ali, A.; Al Huwayz, M.; Alwadai, N.; Iqbal, M. *Z. Phys. Chem.* **2023,** *237,* 689–705. doi:10.1515/zpch-2023-0224
7. Sahoo, K. K.; Pradhan, D.; Ghosh, S. P.; Gartia, A.; Kar, J. P. *Phys. Scr.* **2024,** *99,* 025934. doi:10.1088/1402-4896/ad196b
8. Zhu, C.; Liu, A.; Liu, G.; Jiang, G.; Meng, Y.; Fortunato, E.; Martins, R.; Shan, F. *J. Mater. Chem. C* **2016,** *4,* 10715–10721. doi:10.1039/c6tc02607a
9. Paily, R.; DasGupta, A.; DasGupta, N.; Bhattacharya, P.; Misra, P.; Ganguli, T.; Kukreja, L. M.; Balamurugan, A. K.; Rajagopalan, S.; Tyagi, A. K. *Appl. Surf. Sci.* **2002,** *187,* 297–304. doi:10.1016/s0169-4332(01)01040-6
10. Robertson, J. *Rep. Prog. Phys.* **2006,** *69,* 327–396. doi:10.1088/0034-4885/69/2/r02
11. Werner, F.; Babbe, F.; Elanzeery, H.; Siebentritt, S. *Prog. Photovoltaics* **2019,** *27,* 1045–1058. doi:10.1002/pip.3196
12. Barsoukov, E.; Macdonald, J. R., Eds. *Impedance Spectroscopy;* John Wiley & Sons: Hoboken, NJ, USA, 2005. doi:10.1002/0471716243
13. Shi, N.; Ramprasad, R. *J. Comput.-Aided Mater. Des.* **2007,** *14,* 133–139. doi:10.1007/s10820-006-9034-9
14. Pang, H.-S.; Xu, H.; Tang, C.; Meng, L.-K.; Ding, Y.; Xiao, J.; Liu, R.-L.; Pang, Z.-Q.; Huang, W. *Org. Electron.* **2019,** *65,* 275–299. doi:10.1016/j.orgel.2018.09.025
15. Yalcinkaya, Y.; Rohrbeck, P. N.; Schütz, E. R.; Fakharuddin, A.; Schmidt-Mende, L.; Weber, S. A. L. *Adv. Opt. Mater.* **2024,** *12,* 2301318. doi:10.1002/adom.202301318
16. Binnig, G.; Rohrer, H.; Gerber, C.; Weibel, E. *Phys. Rev. Lett.* **1982,** *49,* 57–61. doi:10.1103/physrevlett.49.57
17. Binnig, G.; Quate, C. F.; Gerber, C. *Phys. Rev. Lett.* **1986,** *56,* 930–933. doi:10.1103/physrevlett.56.930
18. Axt, A.; Hermes, I. M.; Bergmann, V. W.; Tausendpfund, N.; Weber, S. A. L. *Beilstein J. Nanotechnol.* **2018,** *9,* 1809–1819. doi:10.3762/bjnano.9.172
19. Hermes, I. M.; Best, A.; Winkelmann, L.; Mars, J.; Vorpahl, S. M.; Mezger, M.; Collins, L.; Butt, H.-J.; Ginger, D. S.; Koynov, K.; Weber, S. A. L. *Energy Environ. Sci.* **2020,** *13,* 4168–4177. doi:10.1039/d0ee01016b
20. Rohrbeck, P. N. Untersuchung von lokalen Aufladungsdynamiken an Perowskit-Korngrenzen mit zeitaufgelösten KPFM Methoden. Master thesis, Johannes Gutenberg University Mainz, 2021.
21. Bergmann, V. W.; Weber, S. A. L.; Javier Ramos, F.; Nazeeruddin, M. K.; Grätzel, M.; Li, D.; Domanski, A. L.; Lieberwirth, I.; Ahmad, S.; Berger, R. *Nat. Commun.* **2014,** *5,* 5001. doi:10.1038/ncomms6001
22. Weber, S. A. L.; Hermes, I. M.; Turren-Cruz, S.-H.; Gort, C.; Bergmann, V. W.; Gilson, L.; Hagfeldt, A.; Graetzel, M.; Tress, W.; Berger, R. *Energy Environ. Sci.* **2018,** *11,* 2404–2413. doi:10.1039/c8ee01447g
23. Zhu, C.; Fuchs, T.; Weber, S. A. L.; Richter, F. H.; Glasser, G.; Weber, F.; Butt, H.-J.; Janek, J.; Berger, R. *Nat. Commun.* **2023,** *14,* 1300. doi:10.1038/s41467-023-36792-7
24. Martin, Y.; Abraham, D. W.; Wickramasinghe, H. K. *Appl. Phys. Lett.* **1988,** *52,* 1103–1105. doi:10.1063/1.99224
25. Abraham, D. W.; Williams, C.; Slinkman, J.; Wickramasinghe, H. K. *J. Vac. Sci. Technol., B: Microelectron. Nanometer Struct.–Process., Meas., Phenom.* **1991,** *9,* 703–706. doi:10.1116/1.585536
26. Garrett, J. L.; Munday, J. N. *Nanotechnology* **2016,** *27,* 245705. doi:10.1088/0957-4484/27/24/245705
27. Eaton, P.; West, P. *Atomic Force Microscopy;* Oxford University Press: Oxford, UK, 2010. doi:10.1093/acprof:oso/9780199570454.001.0001
28. Biberger, R.; Benstetter, G.; Goebel, H.; Hofer, A. *Microelectron. Reliab.* **2010,** *50,* 1511–1513. doi:10.1016/j.microrel.2010.07.052
29. Jaensch, S.; Schmidt, H.; Grundmann, M. *Phys. B (Amsterdam, Neth.)* **2006,** *376-377,* 913–915. doi:10.1016/j.physb.2005.12.227

30. Tran, T.; Oliver, D. R.; Thomson, D. J.; Bridges, G. E. Sub-zeptofarad sensitivity scanning capacitance microscopy. In *IEEE CCECE2002. Canadian Conference on Electrical and Computer Engineering. Conference Proceedings (Cat. No.02CH37373),* 2002; pp 455–459. doi:10.1109/ccece.2002.1015268

31. Raineri, V.; Giannazzo, F. *Solid State Phenom.* **2001,** *78–79,* 425. doi:10.4028/www.scientific.net/ssp.78-79.425

32. Barrett, R. C.; Quate, C. F. *J. Appl. Phys.* **1991,** *70,* 2725–2733. doi:10.1063/1.349388

33. Goto, K.; Hane, K. *Rev. Sci. Instrum.* **1997,** *68,* 120–123. doi:10.1063/1.1147749

34. Fumagalli, L.; Ferrari, G.; Sampietro, M.; Casuso, I.; Martínez, E.; Samitier, J.; Gomila, G. *Nanotechnology* **2006,** *17,* 4581–4587. doi:10.1088/0957-4484/17/18/009

35. Gomila, G.; Toset, J.; Fumagalli, L. *J. Appl. Phys.* **2008,** *104,* 024315. doi:10.1063/1.2957069

36. Fumagalli, L.; Ferrari, G.; Sampietro, M.; Gomila, G. *Nano Lett.* **2009,** *9,* 1604–1608. doi:10.1021/nl803851u

37. Matey, J. R.; Blanc, J. *J. Appl. Phys.* **1985,** *57,* 1437–1444. doi:10.1063/1.334506

38. Arakawa, H.; Nishitani, R. *J. Vac. Sci. Technol., B: Microelectron. Nanometer Struct.–Process., Meas., Phenom.* **2001,** *19,* 1150–1153. doi:10.1116/1.1379796

39. Lee, D. T.; Pelz, J. P.; Bhushan, B. *Nanotechnology* **2006,** *17,* 1484–1491. doi:10.1088/0957-4484/17/5/054

40. Lee, D. T.; Pelz, J. P.; Bhushan, B. *Rev. Sci. Instrum.* **2002,** *73,* 3525–3533. doi:10.1063/1.1505655

41. Isenbart, J.; Born, A.; Wiesendanger, R. *Appl. Phys. A: Mater. Sci. Process.* **2001,** *72* (Suppl. 2), S243–S251. doi:10.1007/s003390100793

42. Kopanski, J. J.; Mayo, S. *Appl. Phys. Lett.* **1998,** *72,* 2469–2471. doi:10.1063/1.121397

43. Casuso, I.; Fumagalli, L.; Gomila, G.; Padrós, E. *Appl. Phys. Lett.* **2007,** *91,* 063111. doi:10.1063/1.2767979

44. Biberger, R.; Benstetter, G.; Schweinboeck, T.; Breitschopf, P.; Goebel, H. *Microelectron. Reliab.* **2008,** *48,* 1339–1342. doi:10.1016/j.microrel.2008.06.013

45. Smoliner, J.; Basnar, B.; Golka, S.; Gornik, E.; Löffler, B.; Schatzmayr, M.; Enichlmair, H. *Appl. Phys. Lett.* **2001,** *79,* 3182–3184. doi:10.1063/1.1415044

46. Brezna, W.; Schramboeck, M.; Lugstein, A.; Harasek, S.; Enichlmair, H.; Bertagnolli, E.; Gornik, E.; Smoliner, J. *Appl. Phys. Lett.* **2003,** *83,* 4253–4255. doi:10.1063/1.1628402

47. Giannazzo, F.; Raineri, V.; Mirabella, S.; Impellizzeri, G.; Priolo, F.; Fedele, M.; Mucciato, R. *J. Vac. Sci. Technol., B: Microelectron. Nanometer Struct.–Process., Meas., Phenom.* **2006,** *24,* 370–374. doi:10.1116/1.2151907

48. Brezna, W.; Fischer, M.; Wanzenboeck, H. D.; Bertagnolli, E.; Smoliner, J. *Appl. Phys. Lett.* **2006,** *88,* 122116. doi:10.1063/1.2189030

49. Futscher, M. H.; Lee, J. M.; McGovern, L.; Muscarella, L. A.; Wang, T.; Haider, M. I.; Fakharuddin, A.; Schmidt-Mende, L.; Ehrler, B. *Mater. Horiz.* **2019,** *6,* 1497–1503. doi:10.1039/c9mh00445a

50. Kopanski, J. J.; Marchiando, J. F.; Lowney, J. R. *Mater. Sci. Eng., B* **1997,** *44,* 46–51. doi:10.1016/s0921-5107(96)01797-7

51. Kopanski, J. J.; Marchiando, J. F.; Lowney, J. R. *J. Vac. Sci. Technol., B: Microelectron. Nanometer Struct.–Process., Meas., Phenom.* **1996,** *14,* 242–247. doi:10.1116/1.588455

52. Goto, K.; Hane, K. *J. Appl. Phys.* **1998,** *84,* 4043–4048. doi:10.1063/1.368617

53. de Voogd, J. M.; van Spronsen, M. A.; Kalff, F. E.; Bryant, B.; Ostojić, O.; den Haan, A. M. J.; Groot, I. M. N.; Oosterkamp, T. H.; Otte, A. F.; Rost, M. J. *Ultramicroscopy* **2017,** *181,* 61–69. doi:10.1016/j.ultramic.2017.05.009

54. Hiranaga, Y.; Cho, Y. *Rev. Sci. Instrum.* **2019,** *90,* 083705. doi:10.1063/1.5097906

55. Kobayashi, K.; Yamada, H.; Matsushige, K. *Appl. Phys. Lett.* **2002,** *81,* 2629–2631. doi:10.1063/1.1510582

56. Gramse, G.; Casuso, I.; Toset, J.; Fumagalli, L.; Gomila, G. *Nanotechnology* **2009,** *20,* 395702. doi:10.1088/0957-4484/20/39/395702

57. Fumagalli, L.; Gramse, G.; Esteban-Ferrer, D.; Edwards, M. A.; Gomila, G. *Appl. Phys. Lett.* **2010,** *96,* 183107. doi:10.1063/1.3427362

58. Fumagalli, L.; Esteban-Ferrer, D.; Cuervo, A.; Carrascosa, J. L.; Gomila, G. *Nat. Mater.* **2012,** *11,* 808–816. doi:10.1038/nmat3369

59. Gramse, G.; Edwards, M. A.; Fumagalli, L.; Gomila, G. *Appl. Phys. Lett.* **2012,** *101,* 213108. doi:10.1063/1.4768164

60. Gramse, G.; Dols-Perez, A.; Edwards, M. A.; Fumagalli, L.; Gomila, G. *Biophys. J.* **2013,** *104,* 1257–1262. doi:10.1016/j.bpj.2013.02.011

61. Kimura, K.; Kobayashi, K.; Yamada, H.; Matsushige, K. *Appl. Surf. Sci.* **2003,** *210,* 93–98. doi:10.1016/s0169-4332(02)01486-1

62. Henning, A. K.; Hochwitz, T. *Mater. Sci. Eng., B* **1996,** *42,* 88–98. doi:10.1016/s0921-5107(96)01688-1

63. Checa, M.; Neumayer, S. M.; Susner, M. A.; McGuire, M. A.; Maksymovych, P.; Collins, L. *Appl. Phys. Lett.* **2021,** *119,* 252905. doi:10.1063/5.0078034

64. Li, Z.-Y.; Gu, B.-Y.; Yang, G.-Z. *Phys. Rev. B* **1998,** *57,* 9225–9233. doi:10.1103/physrevb.57.9225

65. Gil, A.; Colchero, J.; Gómez-Herrero, J.; Baró, A. M. *Nanotechnology* **2003,** *14,* 332–340. doi:10.1088/0957-4484/14/2/345

66. Fukuzawa, R.; Takahashi, T. *Rev. Sci. Instrum.* **2020,** *91,* 023702. doi:10.1063/1.5127219

67. Izumi, R.; Miyazaki, M.; Li, Y. J.; Sugawara, Y. *Beilstein J. Nanotechnol.* **2023,** *14,* 175–189. doi:10.3762/bjnano.14.18

68. Cherniavskaya, O.; Chen, L.; Weng, V.; Yuditsky, L.; Brus, L. E. *J. Phys. Chem. B* **2003,** *107,* 1525–1531. doi:10.1021/jp0265438

69. Crider, P. S.; Majewski, M. R.; Zhang, J.; Oukris, H.; Israeloff, N. E. *Appl. Phys. Lett.* **2007,** *91,* 013102. doi:10.1063/1.2753539

70. Cadena, M. J.; Sung, S. H.; Boudouris, B. W.; Reifenberger, R.; Raman, A. *ACS Nano* **2016,** *10,* 4062–4071. doi:10.1021/acsnano.5b06893

71. Riedel, C.; Arinero, R.; Tordjeman, P.; Lévêque, G.; Schwartz, G. A.; Alegria, A.; Colmenero, J. *Phys. Rev. E* **2010,** *81,* 010801. doi:10.1103/physreve.81.010801

72. Gramse, G.; Schönhals, A.; Kienberger, F. *Nanoscale* **2019,** *11,* 4303–4309. doi:10.1039/c8nr05880f

73. Gramse, G.; Kölker, A.; Škereň, T.; Stock, T. J. Z.; Aeppli, G.; Kienberger, F.; Fuhrer, A.; Curson, N. J. *Nat. Electron.* **2020,** *3,* 531–538. doi:10.1038/s41928-020-0450-8

74. Fumagalli, L.; Ferrari, G.; Sampietro, M.; Gomila, G. *Appl. Phys. Lett.* **2007,** *91,* 243110. doi:10.1063/1.2821119

75. Söngen, H.; Rahe, P.; Neff, J. L.; Bechstein, R.; Ritala, J.; Foster, A. S.; Kühnle, A. *J. Appl. Phys.* **2016,** *119,* 025304. doi:10.1063/1.4939619

76. Tran, T.; Oliver, D. R.; Thomson, D. J.; Bridges, G. E. *Rev. Sci. Instrum.* **2001,** *72,* 2618–2623. doi:10.1063/1.1369637

77. Moertelmaier, M.; Huber, H. P.; Rankl, C.; Kienberger, F. *Ultramicroscopy* **2014,** *136,* 67–72. doi:10.1016/j.ultramic.2013.07.011

78. Millan-Solsona, R.; Checa, M.; Fumagalli, L.; Gomila, G. *Nanoscale* **2020,** *12,* 20658–20668. doi:10.1039/d0nr05723a

79. Sugawara, Y.; Kou, L.; Ma, Z.; Kamijo, T.; Naitoh, Y.; Jun Li, Y.
    Appl. Phys. Lett. **2012,** *100,* 223104. doi:10.1063/1.4723697
80. Platz, D.; Tholén, E. A.; Pesen, D.; Haviland, D. B. *Appl. Phys. Lett.*
    2008, *92,* 153106. doi:10.1063/1.2909569
81. Borgani, R.; Forchheimer, D.; Bergqvist, J.; Thorén, P.-A.; Inganäs, O.;
    Haviland, D. B. *Appl. Phys. Lett.* **2014,** *105,* 143113.
    doi:10.1063/1.4897966
82. Garrett, J. L.; Leite, M. S.; Munday, J. N. *ACS Appl. Mater. Interfaces*
    2018, *10,* 28850–28859. doi:10.1021/acsami.8b08097
83. Dobryden, I.; Borgani, R.; Rigoni, F.; Ghamgosar, P.; Concina, I.;
    Almqvist, N.; Vomiero, A. *Nanoscale Adv.* **2021,** *3,* 4388–4394.
    doi:10.1039/d1na00319d
84. Labardi, M.; Prevosto, D.; Nguyen, K. H.; Capaccioli, S.; Lucchesi, M.;
    Rolla, P.
    J. Vac. Sci. Technol., B: Microelectron. Nanometer Struct.–Process., Meas., Phenom. **2010,** *28,* C4D11–C4D17. doi:10.1116/1.3368597
85. Schwartz, G. A.; Riedel, C.; Arinero, R.; Tordjeman, P.; Alegría, A.;
    Colmenero, J. *Ultramicroscopy* **2011,** *111,* 1366–1369.
    doi:10.1016/j.ultramic.2011.05.001
86. Miccio, L. A.; Kummali, M. M.; Schwartz, G. A.; Alegría, Á.;
    Colmenero, J. *Ultramicroscopy* **2014,** *146,* 55–61.
    doi:10.1016/j.ultramic.2014.06.006
87. Miccio, L. A.; Kummali, M. M.; Schwartz, G. A.; Alegría, Á.;
    Colmenero, J. *J. Appl. Phys.* **2014,** *115,* 184305.
    doi:10.1063/1.4875836
88. Miccio, L. A.; Schwartz, G. A. *AIP Conf. Proc.* **2014,** *1599,* 150–153.
    doi:10.1063/1.4876800
89. Hudlet, S.; Saint Jean, M.; Guthmann, C.; Berger, J. *Eur. Phys. J. B*
    1998, *2,* 5–10. doi:10.1007/s100510050219
90. Colchero, J.; Gil, A.; Baró, A. M. *Phys. Rev. B* **2001,** *64,* 245403.
    doi:10.1103/physrevb.64.245403
91. Law, B. M.; Rieutord, F. *Phys. Rev. B* **2002,** *66,* 035402.
    doi:10.1103/physrevb.66.035402
92. Halpern, A.; Erlbach, E. *Schaum's outline of theory and problems of
    beginning physics II: waves, electromagnetism, optics, and modern
    physics;* McGraw-Hill: New York, NY, USA, 1998.
93. Lyubchenko, Y. L., Ed. *Nanoscale Imaging;* Springer: New York, NY,
    USA, 2018. doi:10.1007/978-1-4939-8591-3
94. Mourran, A.; Tartsch, B.; Gallyamov, M.; Magonov, S.; Lambreva, D.;
    Ostrovskii, B. I.; Dolbnya, I. P.; de Jeu, W. H.; Moeller, M. *Langmuir*
    2005, *21,* 2308–2316. doi:10.1021/la048069y
95. Magonov, S.; Alexander, J. *Beilstein J. Nanotechnol.* **2011,** *2,* 15–27.
    doi:10.3762/bjnano.2.2
96. Sugimura, H.; Ishida, Y.; Hayashi, K.; Takai, O.; Nakagiri, N.
    Appl. Phys. Lett. **2002,** *80,* 1459–1461. doi:10.1063/1.1455145
97. Abed, A. E.; Fauré, M.-C.; Pouzet, E.; Abillon, O. *Phys. Rev. E* **2002,**
    65, 051603. doi:10.1103/physreve.65.051603
98. Sader, J. E.; Chon, J. W. M.; Mulvaney, P. *Rev. Sci. Instrum.* **1999,** *70,*
    3967–3969. doi:10.1063/1.1150021
99. Labuda, A.; Kocun, M.; Lysy, M.; Walsh, T.; Meinhold, J.; Proksch, T.;
    Meinhold, W.; Anderson, C.; Proksch, R. *Rev. Sci. Instrum.* **2016,** *87,*
    073705. doi:10.1063/1.4955122

The impact of tris(pentafluorophenyl)borane hole transport layer doping on interfacial charge extraction and recombination

Konstantinos Bidinakis[1] and Stefan A. L. Weber[*1,2]

Full Research Paper

Address:
[1]Max Planck Institute for Polymer Research, Ackermannweg 10, 55128 Mainz, Germany and [2]Institute for Photovoltaics, University of Stuttgart, Pfaffenwaldring 47, 70569 Stuttgart, Germany

Email:
Stefan A. L. Weber[*] - stefan.weber@ipv.uni-stuttgart.de

* Corresponding author

Abstract

Selective charge transport layers have a strong influence on the overall efficiency and stability in perovskite solar cell devices. Specifically, the charge extraction and recombination occurring at the interfaces between the perovskite and these materials can be a limiting factor for performance. A lot of effort has been put into improving the conductivity of selective contacts, as well as the junction quality and energetic alignment with the absorber. On the hole extracting side, organic semiconductors have been extensively used due to their flexibility and favorable properties. Two of such compatible materials that have yielded high performing devices are the small molecule 2,2',7,7'-tetrakis[*N,N*-di(4-methoxyphenyl)amino]-9,9'-spirobifluorene (spiro-OMeTAD) and the polymer poly[bis(4-phenyl)(2,4,6-trimethylphenyl)amine] (PTAA). In this work, we investigate the impact of hole transport layer doping on the performance and potential distribution in solar cells based on these materials. To do so on operating solar cells, we created samples with exposed cross-sections and examined their potential profile distributions with Kelvin probe force microscopy (KPFM), implementing our comprehensive measurement protocol. Using the Lewis acid tris(pentafluorophenyl)borane (BCF), we enhanced the hole extracting material/perovskite junction quality in spiro-OMeTAD and in PTAA based devices. Measurements under illumination show that the improvement is caused by a reduced recombination rate at the perovskite/hole transporter interface.

Introduction

Perovskite solar cells (PSCs) are a promising class of photovoltaic material that exhibits high power conversion efficiencies and relies on a low-cost solution-processed fabrication method [1-4]. At the core of their success lies the perovskite absorber material, which exhibits impressive bulk properties, such as long carrier lifetimes and low recombination rates [5-8].

However, the granular nature of perovskites and the layered structure of their solar cells, introduce complications such as grain boundaries and interfacial defect states that hinder performance. Specifically, since the interaction of adjacent layers at the interfaces of a solar cell is an important limiting factor for its operation, there is a need for dedicated studies regarding interfacial behavior. Kelvin probe force microscopy (KPFM) is an important tool for conducting such studies, enabling the measurement of the perovskite's surface potential by monitoring the electrostatic force between the surface and a conductive probe (See Supporting Information File 1, Section 1). This measurement can provide insights about charge generation and transport within the absorber material, as well as charge extraction to the relevant interfaces [9-12].

The details of interfacial electronic carrier extraction at the junctions of the perovskite with the electron and hole transport layers (ETL, HTL) define the ability of a solar cell to generate electrical current effectively. Particularly, the relative capability of the two interfaces to properly extract and block charges is critical, since issues such as energetic misalignment, trap states, and interfacial recombination may lead to an uneven extraction and therefore a charge accumulation within the perovskite. Initial studies suggested that this asymmetrical charge carrier behavior indicates an unfavorable hole extraction and a promoted electron extraction [9,13,14], but the migration and interaction of mobile ions (such as I^- ions interacting with 2,2',7,7'-tetrakis[*N*,*N*-di(4-methoxyphenyl)amino]-9,9'-spirobifluorene (spiro-OMeTAD) [15,16] and Li^+ ions interacting with TiO_2 [17,18]) has also been proposed to explain the asymmetrical distribution of charges within the perovskite [19,20].

Many research endeavors involve the optimization of ETLs in terms of passivation, post-fabrication treatment, and choice of optimal materials [21-23], leaving research on HTL optimization vastly overlooked. In regular n-i-p architecture devices mostly two organic semiconductors have been used as HTL in the past: spiro-OMeTAD and poly[bis(4-phenyl)(2,4,6-trimethylphenyl)amine] (PTAA) [24]. These compounds exhibit favorable solubility, reasonable energetic alignment with most perovskites, and an amorphous nature. The main issues that arise from their usage involve poor conductivity and mechanical stability [25], the existence of pinholes, and a poor adhesion with the adjacent perovskite. There have been many studies trying to address these points and advance PSC performance through HTL optimization, with conventional approaches mainly focusing on the doping strategies applied to these two materials [26-29].

The organic semiconductors spiro-OMeTAD and PTAA are traditionally doped with the ionic p-dopant bis(trifluoro-methane)sulfonimide lithium salt (LiTFSI) and 4-tertbutylpyridine (tBP). In the case of spiro-OMeTAD, in presence of oxygen, LiTFSI promotes its oxidation reaction by stabilizing its radical cation, resulting in the generation of mobile holes [30-32]. For PTAA, under illumination, a similar mechanism is proposed, whereby the oxidation of PTAA raises the conductivity of the polymer [33]. For both HTLs, the inclusion of tBP promotes a better distribution of the HTL on the perovskite, preventing organic semiconductor/LiTFSI phase segregation [34], thus leading to an improved morphology and uniformity of the resulting layer. However, its unfavorable long-term impact on stability indicates that new doping strategies might be required in the future [35,36]. For this, there have been efforts for finding cheap hydrophobic acidic substances with good solubility in solvents orthogonal to the underlying perovskite active layer. Such an alternative compound is tris(pentafluorophenyl)borane (BCF), which is an electrophilic Lewis acid that interacts with the organic semiconductor and increases its conductivity.

Here, we performed a dedicated study for the HTL/perovskite interface, in order to evaluate the effects of dopants such as BCF on the interfacial potential landscape in working devices. In this work we chose four HTL doping configurations that have been reported for high-performing solar cells [24,37,38]: (i) spiro-OMeTAD doped with LiTFSI and tBP, (ii) spiro-OMeTAD doped with BCF, (iii) PTAA doped with LiTFSI and tBP, and (iv) PTAA doped with BCF. All the cells from all the batches were nominally identical, except for the HTL. We examined the potential distribution in all configurations via KPFM. We cleaved the devices and prepared smooth cross-sections by means of argon ion polishing. To get results that closely simulate the operation of working devices, we used a comprehensive static KPFM measurement protocol (See Supporting Information File 1, Section 2) and measured potential profiles across all layers while applying a voltage or under illumination. Our results indicate that the inclusion of BCF has a passivating effect on iodide defects within the devices. Particularly, a major improvement on the diode character of the HTL/perovskite interface was observed, in both spiro-OMeTAD and PTAA cells. The details of device fabrication, ion milling parameters, and KPFM procedure are reported in the Experimental Section.

Results and Discussion
Efficiency characterization

Whilst BCF (Figure 1) has an advantageous impact on the conductivities of both spiro-OMeTAD and PTAA, when similar dopant concentrations are used, the effect on PTAA is more pronounced, which implies dissimilarities in the underlying doping mechanisms (See Supporting Information File 1, Section

Figure 1: The structures of (a) spiro-OMeTAD, (b) PTAA and (c) BCF.
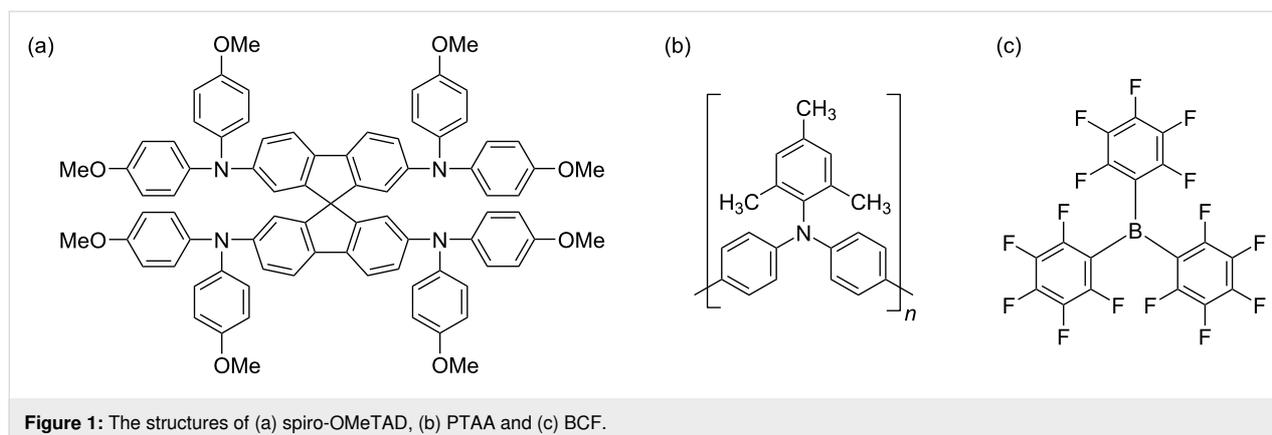
3). Nevertheless, we decided that for our BCF batches the best approach was to dope both spiro-OMeTAD and PTAA solely with BCF and forgoing using further additives LiTFSI and tBP. This was in order to more directly evaluate the effect of BCF compared to the more traditional doping path of LiTFSI and tBP. The BCF concentration used in both cases was 8 wt % with respect to the polymer repeating unit (PTAA), or molecular weight (spiro-OMeTAD).

To confirm the beneficial effect of the doping of the HTL with BCF, we initially characterized the photovoltaic performance of each of the four solar cell batches with a solar simulator under 1 Sun irradiation (1000 W/m^2). The corresponding parameters are reported in Table 1 and they refer to a statistical analysis of backward scans from ten devices of each batch. A slow scan rate of 60 mV/s was used for the current density–voltage (*J–V*) curves so as the ion distribution within the cell is under quasi-equilibrium [39].

We notice that BCF had a beneficial effect on both spiro-OMeTAD and PTAA in terms of photovoltaic parameters. Whilst the positive effect on short-circuit current (J_{sc}) and open-circuit voltage (V_{oc}) is marginal, the increase on the fill factor (FF) is more substantial, and is reflected on the elevated average power conversion efficiencies (PCE) of the batches. The average increased efficiency observed in the cells of batches that incorporated BCF can be attributed to the im-

proved conductivity of the HTL material, as well as the passivation of mobile ionic defects. Specifically, these defects are prevented from drifting and accumulating at the interfaces of the perovskite and giving rise to non-radiative recombination sites, which diminish the HTL/perovskite junction quality [40,41]. To investigate the microscopic origins of these effects at the interfaces, we performed cross-sectional KPFM.

A well-performing solar cell was selected from each batch and after cleaving, it was subjected to argon ion milling in order to get a smooth cross-section. This is useful for getting stable KPFM images, without electrostatic cross-talk. At every step of this procedure, the current–voltage characteristics were being monitored, as shown in Figure 2. By carefully selecting the parameters of the ion milling, we can ensure that the exposed interfacial structure is not damaged and the cells remain operational. Additionally, in order to more accurately interpret interfacial measurements, a precise characterization of the positions of the different solar cell layers is required. We identified the thickness and uniformity of the layers by comparing scanning electron microscopy (SEM) and atomic force microscopy (AFM) images (See Supporting Information File 1, Section 4). The lateral resolution for both AFM and SEM measurements is a few nanometers. The AFM channel that exhibited the clearest contrast between the layers was the amplitude error signal during the amplitude modulation topography scan. Supporting Information File 1, Figure S4 and Table S1, show the layered

Table 1: Solar cell device photovoltaic parameters employing different HTL doping strategies.

HTL doping strategy	J_{sc} (mA/cm^2)	V_{oc} (V)	FF (%)	PCE (%)
Batch 1: spiro-OMeTAD without BCF	22.3 ± 0.3	0.98 ± 0.15	74.1 ± 0.8	16.2 ± 0.3
Batch 2: spiro-OMeTAD with BCF	23.0 ± 0.8	1.04 ± 0.16	75.6 ± 2.6	17.3 ± 0.4
Batch 3: PTAA without BCF	23.3 ± 0.7	1.00 ± 0.14	75.4 ± 0.9	17.6 ± 0.4
Batch 4: PTAA with BCF	23.6 ± 0.6	1.01 ± 0.12	78.5 ± 0.2	18.7 ± 0.2
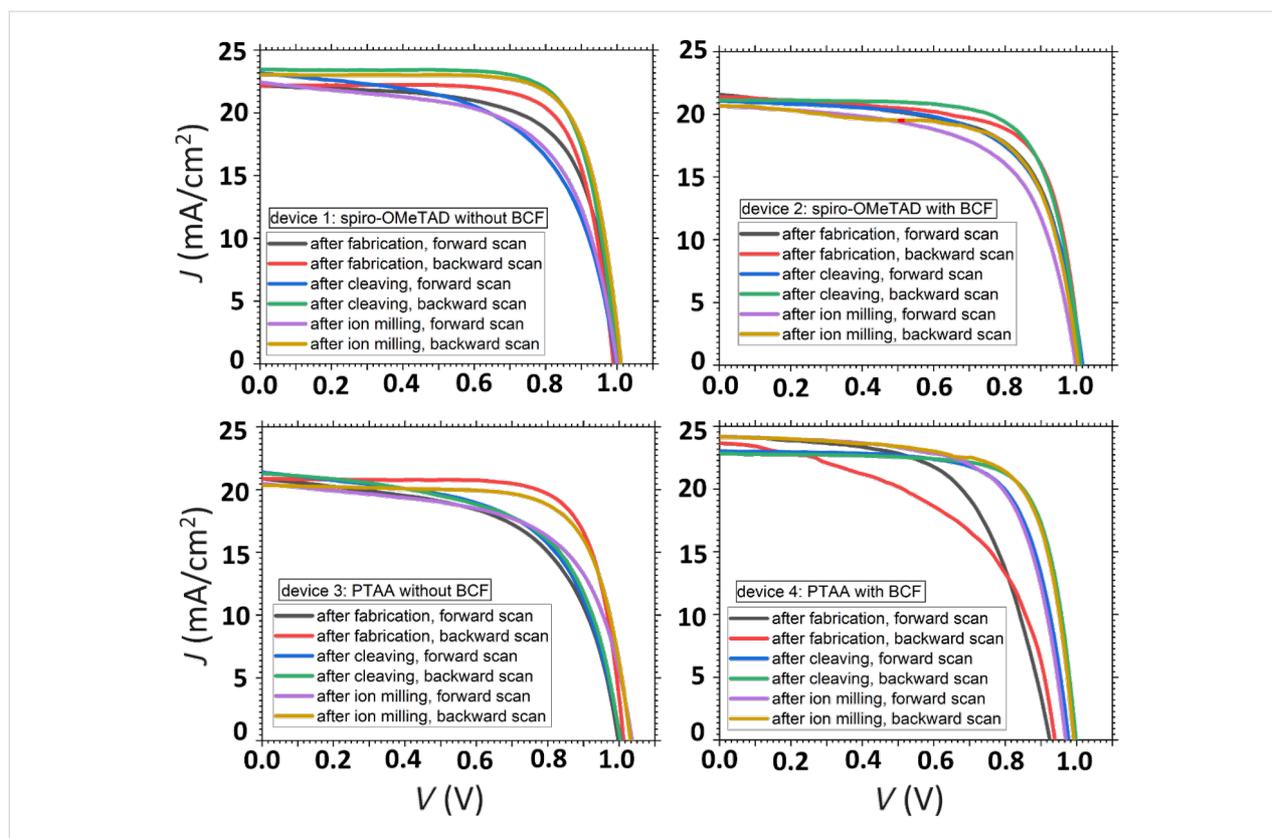
Figure 2: Current–voltage characteristics for the four solar cells that were chosen to be cleaved and polished for cross-sectional KPFM measurements. The plots show that the cells (that were ultimately measured with cross-sectional KPFM), survived both cleaving and consecutive ion milling without significant alteration to their performance. The paradoxically improved performance that is seen in some cleaved or ion milled cells can be attributed to either the well-documented self-healing of PSCs [42], or to difficulties accurately determining the active area of a cleaved solar cell.

structure and layer thickness for each of the ion polished devices from the four batches. An important note that is highlighted by these measurements is that the optimal HTL thickness indicated by most spiro-OMeTAD PSC recipes is 200–370 nm, whereas that number for PTAA layers is much lower, around 40 nm [24]. The reduced bulk series resistance that comes with a thinner layer is reflected in superior J_{sc} values of PTAA cells. On the other hand, thinner HTLs pose a greater challenge in avoiding shunts, which makes device characterization via SEM essential.

To study the effect of different HTLs on the HTL/perovskite interfaces and how their choice affects charge extraction and recombination in our solar cells, we employed cross-sectional KPFM, more specifically our measurement protocol for static KPFM, which allows us to evaluate the response of our cells under both applied voltages and under illumination.

Kelvin probe force microscopy characterization with an applied voltage

When charges get generated, they drift to the sides of the device to externally recombine, or in the case of open circuit, to accu-

mulate, leading to forward biasing of the solar cell. Therefore, the surface potential profile of a forward biased device can be correlated with the potential distribution under illumination and open circuit [43-45] (See Supporting Information File 1, Section 2). By forward biasing, we bypass the open-circuit conditions and have a continuous charge flow within our devices, which operate with an external source of voltage. Consequently, charge transport can be studied, which depends on the diode characteristics of the interfaces. By biasing our devices with a voltage value close to V_{oc}, we can plot the potential distribution across the layers of our solar cells and evaluate the charge extraction at their interfaces.

The CPD profile graphs under dark and short circuit depend on the relative work function of the materials comprising the different layers of the devices. In particular, the CPD value of the perovskite layer is influenced by the composition and the doping of the perovskite [15,46]. In Figure 3, the potential profiles plotted for the four devices exhibit features that deviate from the ideal profiles of a p-i-n junction (See Supporting Information File 1, Section 1), with voltage drops and rises being apparent because of the band bending introduced by mobile

Figure 3: (a–d) SEM images showing the position of the hole and electron transport layers (HTL, ETL). (e–h) The CPD results of the cross-sectional KPFM measurement under dark/short circuit (black curves) and with an applied voltage of +1 V on the Au side (red curves, FTO side grounded). We apply +1 V because $V_{oc} \approx 1$ V. (i–l) The electric field difference built-up at the perovskite interfaces induced by the applied voltage.

ions or surface defect states caused by the cleaving. Furthermore, the CPD decrease (black curves) on the HTL side relative to the perovskite when BCF is included in both cases reveals the p-doping of the HTL by the Lewis acid [47], whilst the increase of the perovskite CPD indicates an indirect n-doping induced by BCF. When subjecting the devices to a forward bias of 1 V (red curves), which is approximately the value of the open-circuit voltage, we were able to observe potential profile distributions indicative of p-i-n junctions in all devices, with a lower CPD on the ETL side where the electrons accumulate under bias. Subtracting the first measurement from the second, we filter out all information from the data that does not pertain to potential changes due to charge separation and accumulation at the perovskite junctions because of the applied bias (like the aforementioned defect-state and relative work function contributions).

Consequently, we use these bias-induced potential profiles (that result from the aforementioned subtraction of CPD profiles) to plot electric field profiles (Figure 3i–l) that reflect the junction quality of the perovskite absorber with its adjacent transport layers. We chose to present the results as electric field differences and not as bias-induced voltage profiles, since the electric field peaks provide a more intuitive way of immediately identifying the position of the built-in fields that enable charge separation. These profiles that are being referred to as "electric field difference" are presented in Figure 3i–l.

To extract the electric field difference profiles, we applied the following equation:

$$E = -\frac{\mathrm{d}V}{\mathrm{d}x}.$$

Here, E is the electric field difference, V is the measured potential under 1 V bias minus the potential at dark/short-circuit conditions and x is the distance.

For these measurements, we applied +1 V to the Au electrode to forward bias the device (Figure 3e–h and Supporting Information File 1, Section 5). The resulting magnitude of the electric field difference profile reflects the relative competition of the two junctions on either side of the perovskite to efficiently extract charges [48], as described by our model in Figure 4.

By applying a forward bias of approximately V_{oc}, we bring our cell into the same configuration as the open-circuit and illuminated case and we have a sufficient diffusive current flowing through the two junctions, but smaller in magnitude compared to the current flowing through an ohmic contact. Therefore, the junction exhibiting the more pronounced rectifying behavior will still limit the current flow. For our model, the influence of the resistance of the active layer is omitted, as it remains the same for all devices tested. If the rectifying capability of the
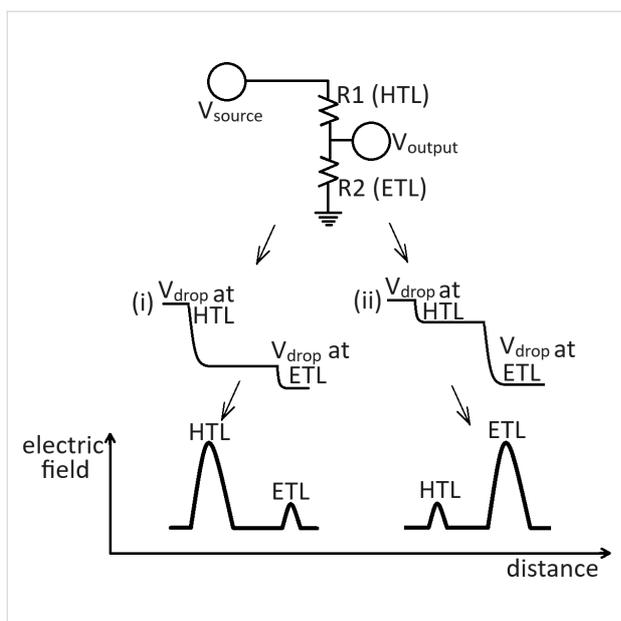
Figure 4: A schematic depicting a simple representation of the two interfacial resistances of the perovskite diode-junctions, as resistors in a voltage divider. Whilst KPFM is a more complex experiment, we can juxtapose the two measurements because they both result in quantifying the potential characteristics of a system, where current flows through resistive elements. A resistor represents the ability of a diode junction to efficiently block current in reverse bias. (i) If R1 > R2 (here: HTL shows better rectifying properties and a better diode quality than ETL), the voltage mostly drops at R1 (HTL). (ii) If R1 < R2 (here: HTL exhibits a more ohmic behavior than ETL due to a decreased charge extraction and more interfacial recombination), the voltage mostly drops at R2 (ETL). Given the identical ETLs of the four device batches we fabricated, we can directly compare the four different HTLs we used. The potential profiles are measured with cross-sectional KPFM and the electric field profiles are derived by the equation $E = -dV/dx$, since electrostatic fields are conservative.

HTL/perovskite junction is poor, then under the applied bias, more current will readily flow through it and the voltage will mainly drop on the ETL interface, where the diode quality is better and less saturation current flows. This larger voltage drop corresponds to a larger electric field difference magnitude on the ETL side (Figure 4).

Any improvement in charge extraction at one interface does not necessarily increase the total (bias-induced or photo-) voltage, but rather, it redistributes how this voltage is shared between the HTL and ETL interfaces (for the following explanation bias-induced voltage and photovoltage can be thought of as equivalent, as explained in Supporting File 1, Section 2). That is because under open-circuit conditions, the total photovoltage across the device is fundamentally limited by the quasi-Fermi level splitting (QFLS) in the perovskite absorber, meaning that the overall voltage is mainly constrained by the recombination processes in the absorber. An improved interfacial behavior cannot overcome bulk recombination limits, even though poor alignment at defective interfaces creates additional losses that

compound the problem. Our results show that under equilibrium, an improved HTL (better energy alignment with the perovskite, reduced interfacial recombination) only has a secondary effect on QFLS, which means that bulk recombination predominantly defines the V_{oc}.

Since our data (Table 1) indicates that V_{oc} remains mainly unchanged after replacing the original HTLs with BCF including ones, this suggests that the total QFLS does not increase with the inclusion of BCF, in both the spiro-OMeTAD and PTAA cases. However, the improved FF in both types of cells (Table 1) reveals that BCF doping plays a critical role in improving the charge transport and interfacial properties of the devices. Firstly, by increasing the conductivity of the organic compound it is doping, BCF reduces the series resistance of the HTL and improves charge transport to the terminal. Furthermore, as a strong Lewis acid, BCF passivates mobile iodide defects at the perovskite/HTL interface, which act as recombination centers, thus reducing non-radiative recombination losses and improving hole extraction efficiency. These beneficial effects lead to a redistribution of the voltage drops at the HTL and ETL junctions, with them being increased and decreased respectively, while the total voltage drop is maintained around the value of V_{oc}. All the above become apparent when plotting the electric field difference profiles (Figure 3i–l), by differentiating the bias-induced voltage profiles, where the aforementioned voltage drops are now expressed as electric field peaks.

For the interpretation of the electric field peaks, both their widths and their heights should be taken into consideration, as they both define the area under the peaks, which corresponds to the total voltage drop across the interfaces of the perovskite layer. Specifically, the peak widths depend on the span of the voltage drop, which depends on the thickness of the transport layers, which is variable along the cell, (as can be seen in Figure S4 and Supporting Information File 1, Section 6). Since our graphs refer to just a specific line across the cell layers, that might be a source of inconsistency for the plotted peak width. Correspondingly, that affects the peak height, since a broader voltage drop would give a smaller height of electric field for the same drop magnitude. Therefore, for a complete understanding of the electric field difference plots (Figure 3), an analysis of their integrals which take into account both the peak heights and widths is required (see Supporting Information File 1, Section 7). Results show that the areas under the electric field peaks of the HTL side are smaller than those on the ETL side for devices 1 and 3, whereas the peaks of the HTL side shows a larger area than that of the ETL side for devices 2 and 4. This shows that, given that the ETLs remained the same, the BCF dopant had a beneficial effect on the rectifying properties of the HTL/perovskite junction, in accordance with our proposed explana-

tion regarding the improvement of the HTL properties when BCF is added.

Another problem may arise from the fact that the perovskite layers do not adhere completely smoothly and uniformly to the transport layers, so whilst they have statistically similar widths in the four devices, for a specific measurement, the junction distances may vary between the four solar cells. Also, whilst the electric field peaks are indicative of the diode junction positions, these may not coincide with the two perovskite interfaces, since the exact position where charge extraction takes place might be affected by factors such as ion accumulation. In a previous study, we demonstrated that the position of the potential drop can be significantly shifted into the transport layers, due to ionic interactions [15].

In the case of the cells incorporating spiro-OMeTAD, from the *J–V* characterization, we expect the potential profiles of the cells with BCF to reflect the increased efficiency compared to the ones with LiTFSI/tBP. Indeed, from Figure 3i,j we can see that in the spiro-OMeTAD cell without BCF, the ETL/perovskite junction exhibits a marginally better diode quality relative to that of the HTL/perovskite interface. This is due to the fact that even though its peak is comparatively smaller in magnitude, the area under that peak is slightly larger, as shown in Supporting Information File 1, Figure S7. However, the situation reverses in the cell from the BCF batch. A diode with higher quality at the HTL side leads to a more efficient charge extraction/charge blocking on that interface relative to the other. Therefore, there is a larger and broader electric field difference peak due to the higher value of extracted charges at that interface. A similar circumstance arises in the PTAA solar cell when LiTFSI/tBP is replaced by BCF. Then, we notice a strong increase in the HTL field strength relative to the ETL, which reflects the improvement in the HTL/perovskite diode quality when BCF is incorporated (Figure 3k,l and Supporting Information File 1, Figure S7). This result is associated with improved charge transport properties and a reduction in the number of trap states at that interface. We propose that BCF, as a Lewis acid electron acceptor, efficiently coordinates with under-coordinated iodide defects and passivates them, increasing junction quality, promoting p-doping, and diminishing recombination at the HTL interface. This, in conjunction with the superior PTTA/perovskite interaction and the favorable morphological properties of PTTA, leads to a considerable increase in the voltage drop at the hole extracting side of the device.

We also noted the iodide passivation as a main source for the discrepancy between the CPD profiles of devices 1–2 and 3–4 in Figure 3e–h, as the existence of iodide ions and their accu-

mulation at the interfaces has an effect on the measured potential profiles.

Kelvin probe force microscopy characterization under illumination and open circuit

To study the quality of the HTL interfaces regarding recombination of photo-generated charge carriers, we illuminated the solar cell under open-circuit conditions and subtracted the dark/short-circuit profile, in order to extract the photo-carrier voltage. The resulting profile is independent from effects coupled to the built-in field, as well as from the aforementioned contributions of the relative work functions of the materials and possible surface defect states created from cleaving (See Supporting Information File 1, Sections 8 and 10). This time, the voltage is generated within the active area of the solar cell and the charge carriers are induced by the illumination. Unlike the previous experiment, where we considered charge transport as the reason for our results, we now force our devices to operate in open circuit under a net zero charge flow condition. Therefore, charge recombination becomes the limiting factor that defines V_{oc} and device performance.

For devices 1 and 3 (without BCF), we can identify two diode junctions on either side of the perovskite absorber, which are almost equal in magnitude, whereas in devices 2 and 4 (with BCF) the HTL/perovskite junction clearly becomes the dominant one, as shown in Supporting Information File 1, Figure S10. Judging from the photo-charge built-up at the interfaces of the perovskite layer, for the solar cells that incorporate LiTFSI and tBP, there is not a single operation defining voltage drop, but rather both perovskite interfaces are approximately equal in their voltage drop magnitude and therefore contribute equally to charge extraction. Devices that exhibit two charge separating junctions are more prone to charge recombination compared to devices with just one junction [46]. On the contrary, devices that incorporate BCF-doped HTLs, exhibit one large drop at the perovskite/HTL interface, indicative of the dominant diode junction that exists there. In order to further understand charge separation within the solar cells, we can use these photopotential profiles in order to examine charge extraction and accumulation within the solar cells.

By plotting charge density profiles we can more clearly point out the sum of photo-charge that has been extracted at the perovskite interfaces and accumulated under open-circuit conditions. Unlike the measurements under bias, here we excited a large number of charges within the absorber, which diffuse, get extracted, and aggregate at the interfaces, giving rise to a large charge density magnitude we can plot. In order to generate the

photo-carrier density profiles, we applied the Poisson's equation:

$$\rho_{photo}(x) = -\varepsilon_0\varepsilon\frac{d^2}{dx^2}V_{photo}(x).$$

Here, ε_0 is the permittivity of free space, ε is the relative permittivity of the perovskite material, and V_{photo} is the photopotential profile measured with KPFM.

Under open-circuit conditions, photo-generated free carriers are generated within the absorber material and diffuse to their corresponding side of the cell: electrons towards the ETL interface and holes towards the HTL interface. The relative ability of these interfaces to efficiently extract (and block) charges depends on the energetic alignment with the perovskite and the defect-induced interfacial recombination that occurs there. These factors determine the charge density that will ultimately accumulate on the cell edges under open-circuit conditions.

In Supporting Information File 1, Figure S11a–d we can identify that in the case of the spiro-OMeTAD cell, there is an increase in the perovskite dark CPD, indicative of n-type doping, indirectly induced by the BCF additive. For the PTAA cell, the perovskite dark CPD also exhibited an increase relative to the CPD of the HTL. When the illumination is turned on, the BCF-doped spiro-OMeTAD cell exhibits a linear CPD, indicative of a homogeneous electric field within the perovskite and a p-i-n junction, where charges can drift inside the perovskite to the corresponding interfaces. We have reported

such uniform potentials, without significant local variations, in a previous study [15]. In the case of the PTAA cell, the CPD within the perovskite remained flat, indicating that the charge carriers have to diffuse to the interfaces and separate under the influence of the local fields there. In addition, when BCF was introduced in both spiro-OMeTAD and PTAA cells, the open-circuit photovoltage built up more strongly at the HTL/perovskite interface. This indicates the increased charge separation potency of the junction due to decreased charge recombination rates (Supporting Information File 1, Figure S10).

In Figure 5a–d we again identified the charge separating junctions in each cell, as calibrated by the AFM and SEM images (Supporting Information File 1, Figure S4). In the cells that use spiro-OMeTAD as HTL, we can identify that positive charges get separated at the HTL/perovskite interface, whereas negative charges get separated within the mesoporous TiO_2. In the traditionally doped cell, we notice that on the HTL side there is a comparable amount of electrons and holes on each side of the junction. On the ETL side, however, there are more positive charges on the perovskite side than ETL-extracted negative charges, which leads to a positive charging of the perovskite. On the contrary, when BCF is added in the spiro-OMeTAD precursor solution, the HTL/perovskite interface extracts charges more efficiently and becomes the dominant junction relative to the one on the ETL side. A previous study of our group [15] has associated the charging within the perovskite absorber under open-circuit conditions with unbalanced recombination rates of electrons and holes at its two interfaces. More specifically, a positive charging of the perovskite was connected with a preferential recombination of electrons at the HTL side. The elimina-
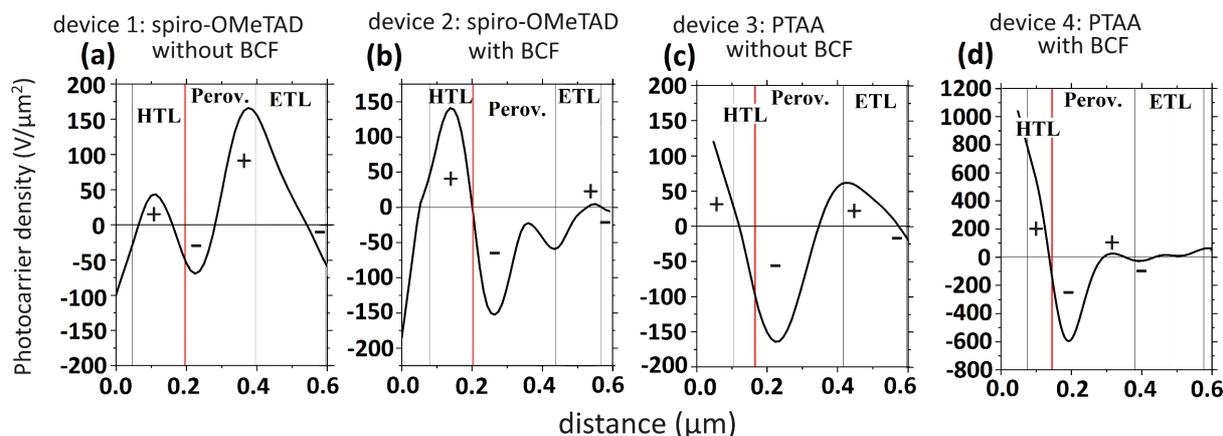
Figure 5: (a–d) Plots of the photo-charge density profiles ($\rho_{photo}(x)/\varepsilon_0\varepsilon$) across the three inner device layers (HTL, perovskite, and ETL), with notations for positive and negative charge accumulation under open-circuit conditions. The full graphs are presented in Supporting Information File 1, Figure S11.

tion of this magnitude of positive built-up indicates that BCF has improved the junction quality in terms of charge carrier leakage. In addition, it has diminished defect-induced interfacial recombination by passivating iodide interstitials within the perovskite, which can transport to the interfaces and act as non-radiative recombination centers [49,50].

In the cells that use PTAA/BCF as HTL, we noticed a large increase in the number of charges that get separated at the HTL junction compared to the ETL junction (in relation with the traditionally doped PTAA cell). This indicates an improvement in the junction quality on the HTL side enabled by the BCF. Again, we propose that BCF is forming a Lewis adduct with under-coordinated halide ions that have migrated towards the HTL side and passivates them, diminishing interfacial recombination and increasing charge extraction [51,52]. In both cases of spiro-OMeTAD and PTAA cells, the charge magnitude at the HTL interface overtook that at the ETL interface, which is proof of the increased HTL/perovskite junction quality and reduced recombination rates when BCF is included as additive.

Moreover, in the past, our group proposed the existence of an interlayer between HTL and perovskite, created by spiro-OMeTAD – iodide complex formation, which reduced the efficiency of solar cells [15]. Results showed that this was visible in cross-sectional KPFM results by way of a slight shift (≈70 nm) of the interfacial electron blocking layer into the spiro-OMeTAD. This interaction was said to de-dope spiro-OMeTAD and introduce a resistive layer that acted as a barrier for charge extraction. Such interaction between spiro-OMeTAD and iodide ions, as well as PTAA and iodide ions has also been reported elsewhere in the literature [53,54]. In Figure 5a–d (vertical red lines) we can see that both devices that do not include BCF exhibit this shift of the electron blocking interface (≈40 nm for the spiro-OMeTAD device, ≈45 nm for the PTAA device), which indicates the negative interaction of the mobile iodide defects that have diffused towards the hole extracting interface. On the contrary, the devices that incorporated BCF do not exhibit such shift, which suggests the successful passivation of iodide defects by the Lewis acid. We note that the spatial resolution of cross-sectional KPFM is sensitive enough to distinguish these slight shifts of tens of nanometers. This microscopically observed result translates to the macroscopic efficiency characterization, specifically the increased FF, which directly relates to a decrease in series resistance close to the HTL side of the corresponding devices.

Conclusion

In conclusion, we incorporated BCF, an electrophilic substance with passivating properties, in the two most popular HTL semi-conductors for PSCs. Current–voltage characterization indicated that the inclusion of BCF had a beneficial effect on the performance of both spiro-OMeTAD and PTAA cells. By applying our comprehensive static cross-sectional KPFM measurement protocol, we showed an increased junction quality and a reduced recombination rate for the HTL/perovskite interface of the selected characteristic devices from the batches that included BCF, compared to the ones from the batches that used the traditional doping method. Furthermore, for the devices that incorporated BCF, there is strong indication that the Lewis acid has a passivating effect on iodide defects, which accentuates the positive impact of BCF as an HTL additive for PSC performance enhancement. Cross-sectional KPFM provides a valuable tool for locally evaluating that impact and our set of measurements can act as a standard for evaluating devices for individual layer optimization.

Experimental
Solution and device preparation

For device fabrication, we mainly used the recipe of Klasen et al. [21]. We patterned fluorine-doped tin oxide (FTO) substrates on thin (1.1 mm) glass from Ossila (11–13 Ω/cm^2) with Zn powder and a 2 M HCl solution. Then, we brushed it thoroughly using a liquid alkaline concentrate (Hellmanex), followed by a 30 min argon plasma cleaning (200-G TePla Plasma System, Technics Plasma GmbH, at 0.14 mbar and 280 W). Consequently, we deposited a compact layer of TiO_2 via an aqueous 0.75 M $TiCl_4$ solution (Sigma-Aldrich, 99.99% trace metal basis). A volume of 80 μL of the solution was spin-coated at 5000 rpm for 30 s, and the resulting films were annealed at 500 °C for 30 min. Afterwards, we deposited a mesoporous TiO_2 layer from a (transparent) titania paste solution (Aldrich, 16.67 wt % in ethanol) via spin coating and annealed it (same parameters as in the previous step). After each of these titania deposition steps, we subjected the films to a UV-ozone cleaning step (FHR UVO 150) for 30 min, with an oxygen flow of 10 L/min. Then, a 1 M methylammonium lead iodide (MAPI) precursor solution was prepared (lead iodide 99.99% trace metals basis from TCI, methylammonium iodide >99.99% from Greatcell solar) with the materials dissolved in a DMF/DMSO (4:1) solvent and spin-coated using a two-step deposition method (500 rpm for 10 s and 4000 rpm for 25 s). A volume of 150 μL of toluene was used as anti-solvent 10 s into the second step. The perovskite was crystalized during a 100 °C annealing step for 30 min. For the cells that incorporated spiro-OMeTAD, we used a solution containing 72.3 mg spiro-OMeTAD, 28.8 μL tBP, and 17.5 μL LiTFSI solution (520 mg in 1 mL acetonitrile), all dissolved in 1 mL chlorobenzene (or BCF in chlorobenzene at an 8% mol ratio with spiro-OMeTAD, for the corresponding devices) and spin coated 80 μL at 4000 rpm for 30 s. For the cells that incorporated PTAA, we used a solution

containing 15 mg PTAA, 7.5 µL, LiTFSI solution (170 mg in 1 mL acetonitrile), and 7.5 µL tBP solution (1:1 in acetonitrile), dissolved in 1 mL toluene. For the BCF batch, instead of LiTFSI and tBP, BCF was added in at an 8% mol ratio to PTAA. After the HTL deposition, an Au electrode was evaporated as a back contact under vacuum (Edwards FL 400 Au evaporator). The devices were characterized in terms of efficiency with a solar simulator (Abet Technologies, SunLite) under AM1.5 illumination.

Cross-section preparation

To create solar cells with exposed cross-sections, we mechanically cleaved the solar cells along the direction perpendicular to their active layers, thus exposing their interfaces for direct measurement. In order to get a smooth cross-section, we employed argon ion milling (Hitachi IM4000, discharge current: 130 µA, acceleration voltage: 2.5 kV, discharge voltage: 0.75 kV). Since argon is inert and the process occurs under vacuum, we minimized the possibility for chemical contamination of our solar cells.

Kelvin probe force microscopy

Mapping the surface potential of the samples was conducted via an Asylum Research MFP3D microscope (Oxford Instruments) and an HF2LI-MOD lock-in amplifier (Zurich Instruments), in an argon atmosphere glove box (less than 1% ppm O_2 and negligible humidity). The cantilever used was SCM PIT V2 (resonance frequency: 75 kHz, spring constant: 3 N/m, Bruker). The scan rate of the measurement was 0.5 Hz. To increase the reliability of our data, we employed heterodyne-KPFM [55], whereby we mechanically excited the cantilever at its first resonant frequency, f_1, and electrically excited at a frequency of (f_2–f_1), where f_2 is the second resonant frequency [56]. Frequency mixing between the mechanical vibration at f_1 and the electrostatic force generates a sideband signal at frequency f_2, which is used as input for the KPFM feedback loop. For the extraction of the electric field and photocarrier density profiles from the surface potential data, we applied the definitional voltage equation for a conservative electric field and the Poisson equation, respectively. The profiles were smoothed with a 30 point adjacent-averaging method, to get smooth derivative curves with negligible noise.

Supporting Information

Supporting Information File 1
Additional information.
[https://www.beilstein-journals.org/bjnano/content/supplementary/2190-4286-16-52-S1.pdf]

Funding

Author Contributions

Konstantinos Bidinakis: conceptualization; data curation; formal analysis; investigation; methodology; project administration; resources; software; validation; visualization; writing – original draft; writing – review & editing. Stefan A. L. Weber: conceptualization; data curation; formal analysis; funding acquisition; investigation; methodology; project administration; resources; software; supervision; validation; visualization; writing – original draft; writing – review & editing.

ORCID® iDs

Konstantinos Bidinakis - https://orcid.org/0009-0007-5131-3399
Stefan A. L. Weber - https://orcid.org/0000-0003-3052-326X

Data Availability Statement

Data generated and analyzed during this study is available from the corresponding author upon reasonable request.

Preprint

A non-peer-reviewed version of this article has been previously published as a preprint: https://doi.org/10.3762/bxiv.2024.53.v1

References

1. Kojima, A.; Teshima, K.; Shirai, Y.; Miyasaka, T. *J. Am. Chem. Soc.* **2009**, *131*, 6050–6051. doi:10.1021/ja809598r
2. Green, M. A.; Ho-Baillie, A.; Snaith, H. J. *Nat. Photonics* **2014**, *8*, 506–514. doi:10.1038/nphoton.2014.134
3. Al-Ashouri, A.; Köhnen, E.; Li, B.; Magomedov, A.; Hempel, H.; Caprioglio, P.; Márquez, J. A.; Morales Vilches, A. B.; Kasparavicius, E.; Smith, J. A.; Phung, N.; Menzel, D.; Grischek, M.; Kegelmann, L.; Skroblin, D.; Gollwitzer, C.; Malinauskas, T.; Jošt, M.; Matič, G.; Rech, B.; Schlatmann, R.; Topič, M.; Korte, L.; Abate, A.; Stannowski, B.; Neher, D.; Stolterfoht, M.; Unold, T.; Getautis, V.; Albrecht, S. *Science* **2020**, *370*, 1300–1309. doi:10.1126/science.abd4016
4. Yang, L.; Feng, J.; Liu, Z.; Duan, Y.; Zhan, S.; Yang, S.; He, K.; Li, Y.; Zhou, Y.; Yuan, N.; Ding, J.; Liu, S. *Adv. Mater. (Weinheim, Ger.)* **2022**, *34*, 2201681. doi:10.1002/adma.202201681
5. Stranks, S. D.; Eperon, G. E.; Grancini, G.; Menelaou, C.; Alcocer, M. J. P.; Leijtens, T.; Herz, L. M.; Petrozza, A.; Snaith, H. J. *Science* **2013**, *342*, 341–344. doi:10.1126/science.1243982
6. Dong, Q.; Fang, Y.; Shao, Y.; Mulligan, P.; Qiu, J.; Cao, L.; Huang, J. *Science* **2015**, *347*, 967–970. doi:10.1126/science.aaa5760
7. Shi, D.; Adinolfi, V.; Comin, R.; Yuan, M.; Alarousu, E.; Buin, A.; Chen, Y.; Hoogland, S.; Rothenberger, A.; Katsiev, K.; Losovyj, Y.; Zhang, X.; Dowben, P. A.; Mohammed, O. F.; Sargent, E. H.; Bakr, O. M. *Science* **2015**, *347*, 519–522. doi:10.1126/science.aaa2725
8. Johnston, M. B.; Herz, L. M. *Acc. Chem. Res.* **2016**, *49*, 146–154. doi:10.1021/acs.accounts.5b00411

9. Chang, J.; Xiao, J.; Lin, Z.; Zhu, H.; Xu, Q.-H.; Zeng, K.; Hao, Y.; Ouyang, J. *J. Mater. Chem. A* **2016,** *4,* 17464–17472. doi:10.1039/c6ta05350e

10. Garrett, J. L.; Tennyson, E. M.; Hu, M.; Huang, J.; Munday, J. N.; Leite, M. S. *Nano Lett.* **2017,** *17,* 2554–2560. doi:10.1021/acs.nanolett.7b00289

11. Yang, C.; Du, P.; Dai, Z.; Li, H.; Yang, X.; Chen, Q. *ACS Appl. Mater. Interfaces* **2019,** *11,* 14044–14050. doi:10.1021/acsami.8b21774

12. Noel, N. K.; Habisreutinger, S. N.; Pellaroque, A.; Pulvirenti, F.; Wenger, B.; Zhang, F.; Lin, Y.-H.; Reid, O. G.; Leisen, J.; Zhang, Y.; Barlow, S.; Marder, S. R.; Kahn, A.; Snaith, H. J.; Arnold, C. B.; Rand, B. P. *Energy Environ. Sci.* **2019,** *12,* 3063–3073. doi:10.1039/c9ee01773a

13. Edri, E.; Kirmayer, S.; Mukhopadhyay, S.; Gartsman, K.; Hodes, G.; Cahen, D. *Nat. Commun.* **2014,** *5,* 3461. doi:10.1038/ncomms4461

14. Bergmann, V. W.; Weber, S. A. L.; Javier Ramos, F.; Nazeeruddin, M. K.; Grätzel, M.; Li, D.; Domanski, A. L.; Lieberwirth, I.; Ahmad, S.; Berger, R. *Nat. Commun.* **2014,** *5,* 5001. doi:10.1038/ncomms6001

15. Hermes, I. M.; Hou, Y.; Bergmann, V. W.; Brabec, C. J.; Weber, S. A. L. *J. Phys. Chem. Lett.* **2018,** *9,* 6249–6256. doi:10.1021/acs.jpclett.8b02824

16. Weber, S. A. L.; Hermes, I. M.; Turren-Cruz, S.-H.; Gort, C.; Bergmann, V. W.; Gilson, L.; Hagfeldt, A.; Graetzel, M.; Tress, W.; Berger, R. *Energy Environ. Sci.* **2018,** *11,* 2404–2413. doi:10.1039/c8ee01447g

17. Hou, W.; Ma, Y.; Kang, J.; Xiao, Y.; Han, G. *Adv. Mater. Interfaces* **2022,** *9,* 2201259. doi:10.1002/admi.202201259

18. Li, Z.; Xiao, C.; Yang, Y.; Harvey, S. P.; Kim, D. H.; Christians, J. A.; Yang, M.; Schulz, P.; Nanayakkara, S. U.; Jiang, C.-S.; Luther, J. M.; Berry, J. J.; Beard, M. C.; Al-Jassim, M. M.; Zhu, K. *Energy Environ. Sci.* **2017,** *10,* 1234–1242. doi:10.1039/c7ee00358g

19. Tress, W.; Marinova, N.; Moehl, T.; Zakeeruddin, S. M.; Nazeeruddin, M. K.; Grätzel, M. *Energy Environ. Sci.* **2015,** *8,* 995–1004. doi:10.1039/c4ee03664f

20. Yu, H.; Lu, H.; Xie, F.; Zhou, S.; Zhao, N. *Adv. Funct. Mater.* **2016,** *26,* 1411–1419. doi:10.1002/adfm.201504997

21. Klasen, A.; Baumli, P.; Sheng, Q.; Johannes, E.; Bretschneider, S. A.; Hermes, I. M.; Bergmann, V. W.; Gort, C.; Axt, A.; Weber, S. A. L.; Kim, H.; Butt, H.-J.; Tremel, W.; Berger, R. *J. Phys. Chem. C* **2019,** *123,* 13458–13466. doi:10.1021/acs.jpcc.9b02371

22. Kim, S.; Zhang, F.; Tong, J.; Chen, X.; Enkhbayar, E.; Zhu, K.; Kim, J. *Sol. Energy* **2022,** *233,* 353–362. doi:10.1016/j.solener.2022.01.053

23. Li, F.; Shen, Z.; Weng, Y.; Lou, Q.; Chen, C.; Shen, L.; Guo, W.; Li, G. *Adv. Funct. Mater.* **2020,** *30,* 2004933. doi:10.1002/adfm.202004933

24. Rombach, F. M.; Haque, S. A.; Macdonald, T. J. *Energy Environ. Sci.* **2021,** *14,* 5161–5190. doi:10.1039/d1ee02095a

25. Le Corre, V. M.; Stolterfoht, M.; Perdigón Toro, L.; Feuerstein, M.; Wolff, C.; Gil-Escrig, L.; Bolink, H. J.; Neher, D.; Koster, L. J. A. *ACS Appl. Energy Mater.* **2019,** *2,* 6280–6287. doi:10.1021/acsaem.9b00856

26. Cappel, U. B.; Daeneke, T.; Bach, U. *Nano Lett.* **2012,** *12,* 4925–4931. doi:10.1021/nl302509q

27. Burschka, J.; Kessler, F.; Nazeeruddin, M. K.; Grätzel, M. *Chem. Mater.* **2013,** *25,* 2986–2990. doi:10.1021/cm400796u

28. Nguyen, W. H.; Bailie, C. D.; Unger, E. L.; McGehee, M. D. *J. Am. Chem. Soc.* **2014,** *136,* 10996–11001. doi:10.1021/ja504539w

29. Watson, B. L.; Rolston, N.; Bush, K. A.; Taleghani, L.; Dauskardt, R. H. *J. Mater. Chem. A* **2017,** *5,* 19267–19279. doi:10.1039/c7ta05004f

30. Abate, A.; Leijtens, T.; Pathak, S.; Teuscher, J.; Avolio, R.; Errico, M. E.; Kirkpatrik, J.; Ball, J. M.; Docampo, P.; McPherson, I.; Snaith, H. J. *Phys. Chem. Chem. Phys.* **2013,** *15,* 2572–2579. doi:10.1039/c2cp44397j

31. Wang, S.; Yuan, W.; Meng, Y. S. *ACS Appl. Mater. Interfaces* **2015,** *7,* 24791–24798. doi:10.1021/acsami.5b07703

32. Hawash, Z.; Ono, L. K.; Qi, Y. *Adv. Mater. Interfaces* **2016,** *3,* 1600117. doi:10.1002/admi.201600117

33. Kim, Y.; Jung, E. H.; Kim, G.; Kim, D.; Kim, B. J.; Seo, J. *Adv. Energy Mater.* **2018,** *8,* 1801668. doi:10.1002/aenm.201801668

34. Juarez-Perez, E. J.; Leyden, M. R.; Wang, S.; Ono, L. K.; Hawash, Z.; Qi, Y. *Chem. Mater.* **2016,** *28,* 5702–5709. doi:10.1021/acs.chemmater.6b01777

35. Lamberti, F.; Gatti, T.; Cescon, E.; Sorrentino, R.; Rizzo, A.; Menna, E.; Meneghesso, G.; Meneghetti, M.; Petrozza, A.; Franco, L. *Chem* **2019,** *5,* 1806–1817. doi:10.1016/j.chempr.2019.04.003

36. Wang, S.; Huang, Z.; Wang, X.; Li, Y.; Günther, M.; Valenzuela, S.; Parikh, P.; Cabreros, A.; Xiong, W.; Meng, Y. S. *J. Am. Chem. Soc.* **2018,** *140,* 16720–16730. doi:10.1021/jacs.8b09809

37. Luo, J.; Xia, J.; Yang, H.; Chen, L.; Wan, Z.; Han, F.; Malik, H. A.; Zhu, X.; Jia, C. *Energy Environ. Sci.* **2018,** *11,* 2035–2045. doi:10.1039/c8ee00036k

38. Liu, J.; Liu, W.; Aydin, E.; Harrison, G. T.; Isikgor, F. H.; Yang, X.; Subbiah, A. S.; De Wolf, S. *ACS Appl. Mater. Interfaces* **2020,** *12,* 23874–23884. doi:10.1021/acsami.0c03660

39. Courtier, N. E.; Cave, J. M.; Foster, J. M.; Walker, A. B.; Richardson, G. *Energy Environ. Sci.* **2019,** *12,* 396–409. doi:10.1039/c8ee01576g

40. Ye, T.; Wang, J.; Chen, W.; Yang, Y.; He, D. *ACS Appl. Mater. Interfaces* **2017,** *9,* 17923–17931. doi:10.1021/acsami.7b02969

41. Ren, G.; Han, W.; Deng, Y.; Wu, W.; Li, Z.; Guo, J.; Bao, H.; Liu, C.; Guo, W. *J. Mater. Chem. A* **2021,** *9,* 4589–4625. doi:10.1039/d0ta11564a

42. Yu, Y.; Zhang, F.; Yu, H. *Sol. Energy* **2020,** *209,* 408–414. doi:10.1016/j.solener.2020.09.018

43. Chen, Q.; Mao, L.; Li, Y.; Kong, T.; Wu, N.; Ma, C.; Bai, S.; Jin, Y.; Wu, D.; Lu, W.; Wang, B.; Chen, L. *Nat. Commun.* **2015,** *6,* 7745. doi:10.1038/ncomms8745

44. Lan, F.; Jiang, M.; Tao, Q.; Li, G. *IEEE J. Photovoltaics* **2018,** *8,* 125–131. doi:10.1109/jphotov.2017.2762525

45. Lan, F.; Jiang, M.; Li, G. The characterization of defects states and charge injection barriers in perovskite solar cells. In *2017 IEEE 17th International Conference on Nanotechnology (IEEE-NANO),* Pittsburgh, PA, USA, July 25–28, 2017; IEEE, 2017; pp 379–382. doi:10.1109/nano.2017.8117404

46. Cai, M.; Ishida, N.; Li, X.; Yang, X.; Noda, T.; Wu, Y.; Xie, F.; Naito, H.; Fujita, D.; Han, L. *Joule* **2018,** *2,* 296–306. doi:10.1016/j.joule.2017.11.015

47. Marqués, P. S.; Londi, G.; Yurash, B.; Nguyen, T.-Q.; Barlow, S.; Marder, S. R.; Beljonne, D. *Chem. Sci.* **2021,** *12,* 7012–7022. doi:10.1039/d1sc01268a

48. Xiao, C.; Zhai, Y.; Song, Z.; Wang, K.; Wang, C.; Jiang, C.-S.; Beard, M. C.; Yan, Y.; Al-Jassim, M. *ACS Appl. Mater. Interfaces* **2023,** *15,* 20909–20916. doi:10.1021/acsami.2c22801

49. Zhang, X.; Turiansky, M. E.; Shen, J.-X.; Van de Walle, C. G. *Phys. Rev. B* **2020,** *101,* 140101. doi:10.1103/physrevb.101.140101

50. Wiktor, J.; Ambrosio, F.; Pasquarello, A. *J. Mater. Chem. A* **2018,** *6,* 16863–16867. doi:10.1039/c8ta06466k

51. Yang, Z.; Dou, J.; Kou, S.; Dang, J.; Ji, Y.; Yang, G.; Wu, W.-Q.;
    Kuang, D.-B.; Wang, M. *Adv. Funct. Mater.* **2020,** *30,* 1910710.
    doi:10.1002/adfm.201910710

52. Wang, S.; Wang, A.; Deng, X.; Xie, L.; Xiao, A.; Li, C.; Xiang, Y.; Li, T.;
    Ding, L.; Hao, F. *J. Mater. Chem. A* **2020,** *8,* 12201–12225.
    doi:10.1039/d0ta03957h

53. Kim, H.-S.; Seo, J.-Y.; Park, N.-G. *J. Phys. Chem. C* **2016,** *120,*
    27840–27848. doi:10.1021/acs.jpcc.6b09412

54. Gueye, I.; Shirai, Y.; Khadka, D. B.; Seo, O.; Hiroi, S.; Yanagida, M.;
    Miyano, K.; Sakata, O. *ACS Appl. Mater. Interfaces* **2021,** *13,*
    50481–50490. doi:10.1021/acsami.1c11215

55. Axt, A.; Hermes, I. M.; Bergmann, V. W.; Tausendpfund, N.;
    Weber, S. A. L. *Beilstein J. Nanotechnol.* **2018,** *9,* 1809–1819.
    doi:10.3762/bjnano.9.172

56. Garrett, J. L.; Munday, J. N. *Nanotechnology* **2016,** *27,* 245705.
    doi:10.1088/0957-4484/27/24/245705

Tendency in tip polarity changes in non-contact atomic force microscopy imaging on a fluorite surface

Bob Kyeyune, Philipp Rahe and Michael Reichling[*]

Abstract

We investigate the impact of tip changes on atomic-scale non-contact atomic force microscopy (NC-AFM) contrast formation when imaging a $CaF_2(111)$ surface. A change of the atomic contrast is explained by a polarity change of the tip-terminating cluster or by a polarity-preserving tip change via the re-arrangement of the foremost atoms. Based on the established understanding of the unique contrast patterns on $CaF_2(111)$, polarity-preserving and polarity-changing tip changes can be identified unambiguously. From analyzing a large set of images, we find that the vast majority of tip changes tend to result in negative tip termination. This analysis delivers hints for tip configurations suitable for stable imaging of $CaF_2(111)$ surfaces.

Introduction

Non-contact atomic force microscopy (NC-AFM) [1] is a surface science tool that has been used to atomically resolve surfaces of semiconductor and insulator materials in real space with unprecedented spatial resolution [2-6]. Besides high-resolution imaging of molecular structures [7], NC-AFM has demonstrated its ability to identify sublattices of atomic surfaces [8-10]. In these studies, the knowledge of the tip's atomic structure plays a vital role as the tip-terminating cluster uniquely interacts with the different surface atoms. At cryogenic temperatures, the use of functionalized tips such as as

CO-terminated tips [6,11], Xe-terminated tips [12-14] and O-terminated Cu tips [15-17] has become the state-of-the-art for structure elucidation and identification of surface sites.

However, this approach is presently not feasible for measurements performed at room temperature as the required control over the tip termination is challenged by thermal motion. For room-temperature measurements, it is common practice to bring the tip apex in slight contact with the surface under investigation to form a tip cluster yielding atomic contrast [18]. As struc-

ture and chemical composition of the resulting tip-terminating cluster are not known, the understanding of contrast formation with non-functionalized tips has been developed over many years based on theoretical simulations of NC-AFM data for a variety of plausible tip models [9,19-22]. Through further endeavors, a qualitative distance-dependent approach involving electrostatic interactions and Pauli repulsion has recently been exemplified on $CaF_2(111)$ [10]. As a central result, gradual atomic contrast transitions as a function of the tip–sample distance have been introduced as criteria for identifying a positively and a negatively terminated tip [10]. Still, a crucial aspect in sublattice identification studies is to distinguish between contrast changes caused by a change of the tip-terminating cluster (i.e., a tip change) and a distance-dependent contrast evolution for a stable tip. Tip changes are inevitable in NC-AFM experiments with non-functionalized tips, especially as commonly used silicon tips are very reactive and readily pick up various entities. This particularly concerns the transfer of surface species to the tip when the tip is subject to intentional or unintentional contact with the surface. Furthermore, ambient species like native oxides, hydrogen ions, or residual water can adsorb on the tip apex during scanning. Additionally, the foremost tip atom may rearrange to minimize the tip surface energy in response to increasing tip–sample interaction forces.

Here, we perform an experimental investigation of tip changes during NC-AFM imaging of a $CaF_2(111)$ surface with non-functionalized tips at both room temperature (RT) and low temperature (LT). We identify atomic contrast changes resulting either from a polarity change of the tip-terminating cluster or from a polarity-preserving tip change. Following the recently developed model for contrast formation on $CaF_2(111)$ surfaces [10], we adopt the contrast mode notations C_1, C_3, and C_4^* for a positively terminated tip and C_2 and C_4 for a negatively terminated tip. The distance-dependent contrast evolution [10] is summarized along the vertical columns in Figure 1. This figure additionally includes markers for tip changes as demonstrated in this work: Black solid arrows mark contrast changes exhibiting a change in tip polarity demonstrated in this work, while polarity-preserving tip changes are indicated by grey arrows. In addition, dashed arrows denote polarity changing tip changes that were observed during our experiments but are not discussed in the following as they represent the reverse direction of presented cases.

The contrast modes C_4 or C_4^* are cyclic members of the same contrast mode, as introduced in [10]. Consequently, the assignment of NC-AFM image data to these contrasts modes requires the acquisition of systematic distance-dependent measurements [10]. Without such distance-dependent data, the contrast mode assignment is questionable.

Figure 1: Distance-dependent contrast formation on $CaF_2(111)$ for positively and negatively terminated tips (vertical columns) as well as transitions between contrast modes due to tip changes. The contrast modes C_1, C_3, and C_4^* (C_2 and C_4) are assigned to a positive (negative) tip termination [10]. Solid black arrows indicate experimentally observed changes of the tip polarity, while grey arrows denote polarity-preserving tip changes. Dashed black arrows indicate tip changes that were observed but are excluded from the discussion herein.

Experimental

RT experiments were performed on a bulk CaF_2 crystal after preparing a clean $CaF_2(111)$ surface by cleaving the crystal in ultra-high vacuum (UHV) [23]. For the LT experiments, a $CaF_2/CaF/Si(111)$ thin film sample was used. The sample was prepared in situ by first degassing a p-type Si (B-doped) sample (Institute of Electronic Materials Technology, Warsaw, Poland) for several hours after introduction into the vacuum. Second, the Si(111)-(7 × 7) termination was formed by flash annealing cycles. Third, CaF_2 material (99.9% purity) was deposited on the Si(111)-(7 × 7) surface from an EFM3T e-beam sublimator (Focus GmbH, Huenstetten, Germany) at substrates temperatures of 550 °C. Under these conditions, a CaF interface layer is formed, which removes the Si (7 × 7) reconstruction and allows for growing multilayers of well-ordered $CaF_2(111)$ [24,25], see [26] for further preparation details.

RT experiments were performed with a UHV 750 AFM system (RHK, Troy, MI USA) operated at a base pressure of 7.0×10^{-11} mbar. An Ar^+ ion-sputtered silicon cantilever with an eigenfrequency of around 300 kHz and a quality factor of 22000 was used. The NC-AFM was operated in the frequency-modulation mode with an oscillation amplitude of 7.4 nm, and images shown herein were acquired in the quasi constant-height mode [18]. Frequency shift values printed in the respective images correspond to the setpoint of the feedback loop. LT experiments were performed at 77 K using a LT UHV STM/AFM (ScientaOmicron, Taunusstein, Germany) operated at a base pressure of 5×10^{-10} mbar. NC-AFM measurements were con-

ducted with a quartz cantilever based on a tuning fork [27] and a chemically etched tungsten tip attached to the end of the active prong. The tip was further prepared in situ using common STM-based approaches on the bare Si surface after introducing the sensor into the vacuum system [28]. The NC-AFM microscope was operated in the frequency-modulation mode with an oscillation amplitude of 60 pm, and images were acquired in the true constant-height mode using an atom-tracking and feed-forward system for instantaneous drift compensation [29].

All frequency shift (Δf) images are presented with regions of strong attractive tip–sample interaction depicted as 'bright' and regions of weak attractive or repulsive interaction reproduced as 'dark'. In NC-AFM, the frequency shift Δf is proportional to the weighted average of the tip–sample interaction force gradient [30]. Attractive forces mostly exhibiting a positive force gradient are considered as negative and yield a negative Δf according to a generally accepted convention. When acquiring data in the constant height mode, we invert Δf images so that a steeper force gradient appears as a brighter feature corresponding to an elevation in an image of the same feature taken in the constant frequency shift (topography) mode. Arrows in the upper right corner of Δf images represent the fast (horizontal) and slow (vertical) scan directions.
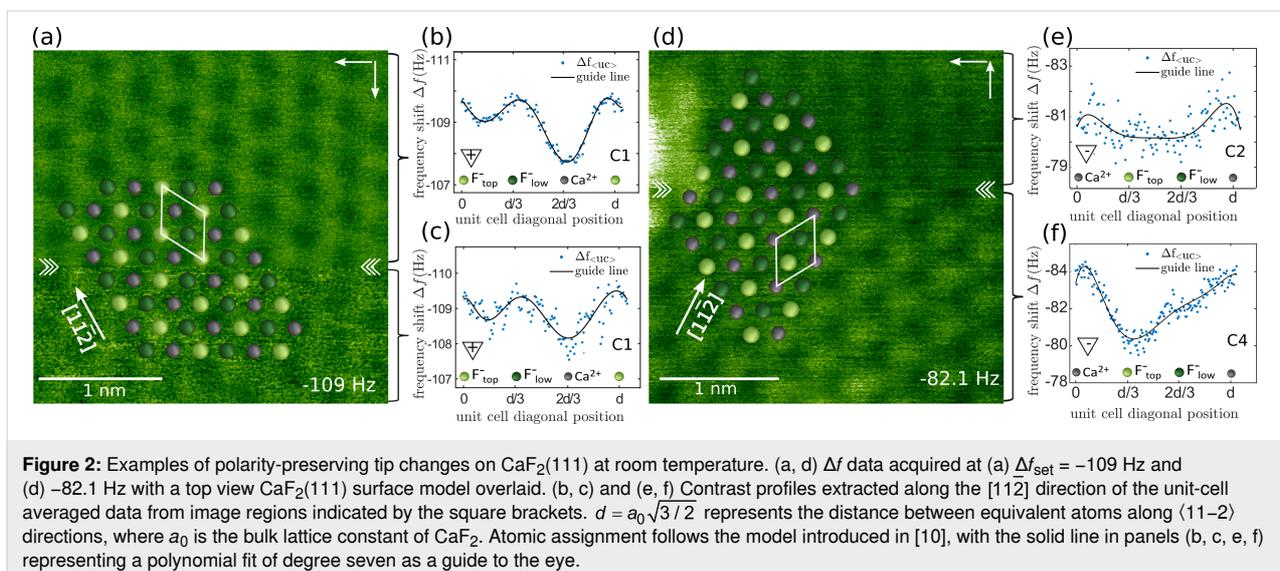
The surface directions for the bulk crystal exposing the (111) surface can be determined by cleaving the crystal along another surface from the {111} family [31]. For CaF_2 thin films grown on Si(111) surfaces, it has been established that the film grows in type-B epitaxy [24,25,32]. This implies that the $[11\bar{2}]$ direction of the silicon crystal surface points in opposite direction of the $[11\bar{2}]$ direction of the CaF_2 thin film. The $[11\bar{2}]$ direction of the pristine Si(111) (7 × 7) surface was determined by identi-

fying the faulted and unfaulted halves of the (7 × 7) reconstructed unit cell from STM imaging [33]. With the surface orientation established, the sublattices can be identified through a distance-dependent analysis of NC-AFM images [10], and corresponding model drawings of the CaF_2(111) surface geometry are superimposed on the image data.

To improve the signal-to-noise ratio of the Δf data in the RT experiments, unit cell averaging is performed as described in [10]. From the unit-cell averaged data, contrast profile lines $\Delta f_{\langle uc\rangle}$ are extracted along the diagonal of the unit cell in the $[11\bar{2}]$ direction, with the resulting data included as traces next to the respective NC-AFM images.

Results and Discussion

In Figure 2, we present RT data showing two examples of abrupt contrast changes where the polarity of the tip is maintained (polarity-preserving tip changes) but a different atomic contrast appears. The occurrences of tip changes are marked by the two chevron arrows framing the respective scan line. The nature of these changes as polarity preserving can be assessed from the contrast profiles shown in Figure 2b,c,e,f based on the conclusions in [10]. The image in Figure 2a maintains contrast mode C_1, yet with an abrupt change in intensity (see Figure 2b,c), while the contrast change present in Figure 2d represents a transition from contrast mode C_4 (see Figure 2f) to contrast mode C_2 (see Figure 2e). The assignment of the contrast mode C_4 follows a distance-dependent analysis of the data acquired prior to this image (data not shown). Positioning the CaF_2(111) surface models in Figure 2a and Figure 2d relative to the NC-AFM data is based on the sublattice analysis of the contrast profiles shown in Figure 2b,c and Figure 2e,f, respectively. This positioning indicates that there is no lateral

Figure 2: Examples of polarity-preserving tip changes on CaF_2(111) at room temperature. (a, d) Δf data acquired at (a) Δf_{set} = −109 Hz and (d) −82.1 Hz with a top view CaF_2(111) surface model overlaid. (b, c) and (e, f) Contrast profiles extracted along the $[11\bar{2}]$ direction of the unit-cell averaged data from image regions indicated by the square brackets. $d = a_0\sqrt{3/2}$ represents the distance between equivalent atoms along $\langle 11\text{–}2\rangle$ directions, where a_0 is the bulk lattice constant of CaF_2. Atomic assignment follows the model introduced in [10], with the solid line in panels (b, c, e, f) representing a polynomial fit of degree seven as a guide to the eye.

shift involved during the tip changes as the same lattice fits well before and after the tip changes. While this is true for the NC-AFM images shown here, images indicating a lateral shift upon a tip change are commonly observed. The assignment to a polarity-preserving tip change is based on the finding that for Figure 2a, the contrast mode C_1 is related to a positively terminated tip, whereas for Figure 2d, the contrast modes C_2 and C_4 are both explained by a negatively terminated tip.

Next, we discuss tip changes that modify the tip polarity with exemplary data for negative-to-positive and positive-to-negative transitions reproduced, respectively, in Figure 3a and Figure 3d. In particular, the image data in Figure 3a recorded at RT and the corresponding contrast profiles (Figure 3b,c) exemplify a contrast change from C_2 (associated with a negatively terminated tip) to C_3 (associated with a positively terminated tip). In contrast, the image data in Figure 3d acquired at LT and the corresponding contrast profiles (Figure 3e,f) show an abrupt change from contrast mode C_1 to C_4, implying a change from a positive to a negative tip termination. To maintain stable imaging, the tip was retracted by about 100 pm immediately after the tip change, explaining the abrupt change in image contrast. Based on the sublattice identification in the contrast profiles in Figure 3b,c and Figure 3e,f, we superimpose the $CaF_2(111)$ surface model to the data in Figure 3a and Figure 3d and furthermore find that the tip change clearly goes along with a change in polarity of the contrast forming tip cluster in both cases.

A tentative explanation for the positive-to-negative tip change is a pickup of a fluorine ion from the surface by the tip, resulting in a negative tip termination. As a consequence, the tip interacts strongly attractively with the surface Ca^{2+} ions, explaining the contrast enhancement induced by the tip change.

During the analysis of 213 images acquired at RT, we observed 32 tip changes, with repeated evidence for polarity changes in both directions. Among these, 72% resulted in negatively terminated tips, while 28% ended in positively terminated tips. Across all 213 analyzed images, 67% exhibited contrasts associated with negatively terminated tips and 33% with positively terminated tips. This consistent trend suggests that negative tip termination is the more stable configuration when imaging fluorite surfaces.

An intriguing example involving a sequence of tip changes to eventually arrive in contrast mode C_4 is shown in Figure 4. Images in Figure 4a–c and Figure 4g–i represent image data acquired while step-wise decreasing the frequency shift setpoint. Such a reduction of the tip–surface distance eventually triggers tip changes. Contrast profiles for identifying the respective contrast modes are shown in Figure 4d–f and Figure 4j–l. It is found that the tip first yields contrast C_1 (associated with a positively terminated tip) but experiences a polarity-changing tip change (Figure 4b) upon approach to the surface from contrast C_1 to C_2 (negatively terminated tip). Further approach reveals an unsteady C_2 contrast (Figure 4c) as evidenced by the difference in contrast strength of the contrast profiles in Figure 4f, whereby the C_2 contrast in the upper part (red contrast profile) is slightly weaker compared to that in the lower image half (blue contrast profile). A second polarity-preserving tip change is identified in the subsequent image in Figure 4g. Upon further decreasing the frequency shift setpoint, the C_2 contrast stabilizes in Figure 4g to Figure 4h and eventually develops to contrast C_4 (negatively terminated tip) in Figures 4i,l at further reduced tip–sample distance. While the evolution of contrast mode C_2 to C_4 is readily explained by the distance-dependence of imaging $CaF_2(111)$ with a negative tip [10], this series clearly shows the change from a previously pos-
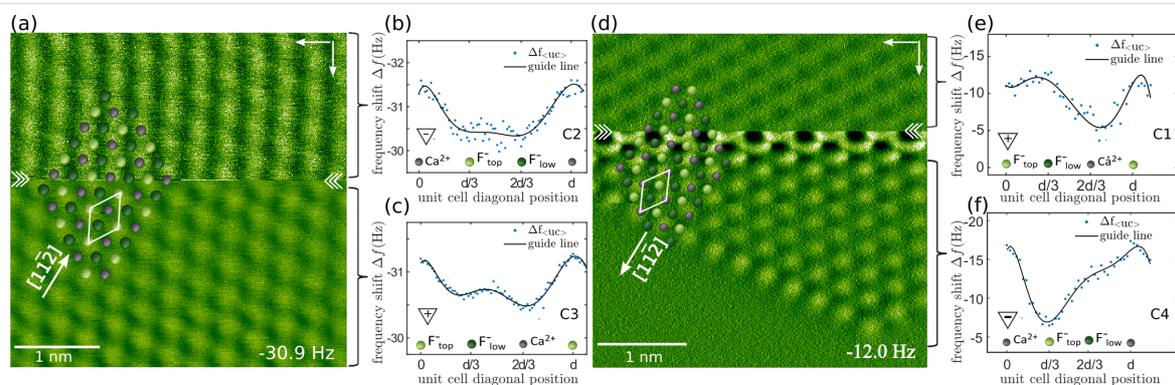
Figure 3: Examples of polarity-changing tip changes on $CaF_2(111)$. (a) Δf data acquired at Δf_{set} = −30.9 Hz (RT) and (d) Δf data acquired on a thin film sample at Δf_{set} = −12.0 Hz (77 K). Top-view $CaF_2(111)$ surface models are overlaid. (b, c) and (e, f) show line profiles extracted along the $[11\bar{2}]$ direction of the unit-cell averaged data in the regions indicated by the square brackets. $d = a_0\sqrt{3/2}$ represents the distance between equivalent atoms along $\langle 11\text{–}2 \rangle$ directions, where a_0 is the bulk lattice constant of CaF_2. Atomic assignment follows the model introduced in [10], with the solid line in panels (b, c, e, f) representing a polynomial fit of degree seven as a guide to the eye.

Figure 4: Tip changes leading to a successively stabilizing negative tip termination. (a–c) and (g–i) Δf data acquired while step-wise decreasing the tip–sample distance (Δf_{set} = −60.2 Hz to −78.0 Hz). (d–f) and (j–l) Line profiles extracted along the [11$\bar{2}$] direction of the unit-cell averaged data. $d = a_0\sqrt{3}/2$ represents the distance between equivalent atoms along ⟨11–2⟩ directions, where a_0 is the bulk lattice constant of CaF$_2$. Atomic assignment follows the model introduced in [10], with the solid line in panels (d–f) and (j–l) representing a polynomial fit of degree seven as a guide to the eye.
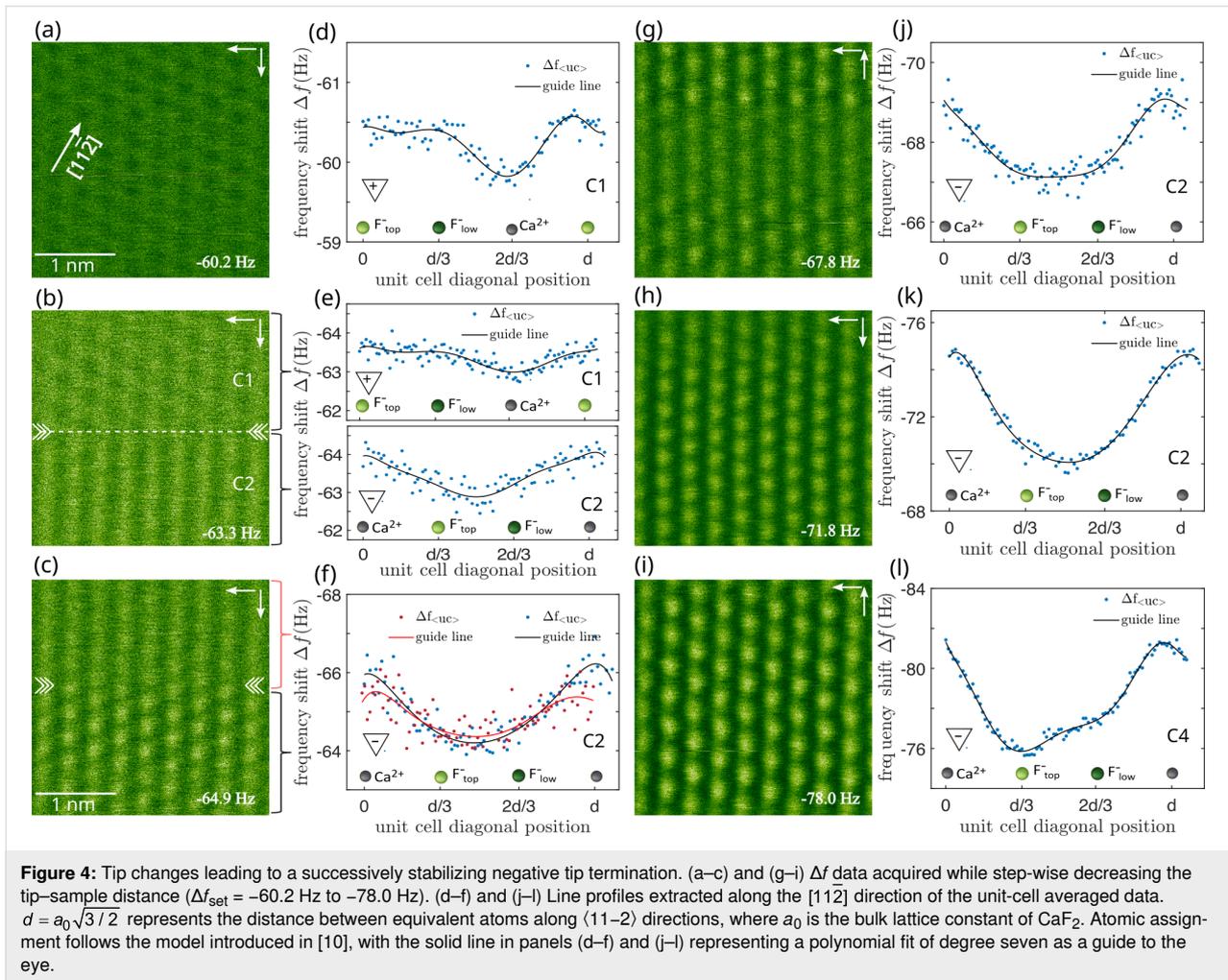
itively terminated tip to a negatively terminated tip finally attaining a stable configuration.

Unlike in the RT data, where we observe both polarity-preserving and polarity-changing tip changes, at low temperature, so far no polarity-preserving tip changes were observed. This is a plausible result as tip stability is generally considered a merit of LT measurements. However, conclusions drawn from LT data are based on a much smaller number of measurements than those for RT data, and we anticipate that polarity-preserving tip changes at low temperature would be found as rare events in a sample of measurements with higher statistical significance.

Conclusion

In conclusion, we present NC-AFM data demonstrating tip changes on a bulk CaF$_2$(111) surface at room temperature and on a CaF$_2$/CaF/Si(111) thin film surface at 77 K. We demonstrate the effect of tip changes on the contrast formation and find, as a key result, routes for a discrimination between

polarity-preserving tip changes and tip changes associated with a change in tip polarity. Experimental evidence of both cases is found, with a tendency for negative tip termination to be the more stable configuration. We tentatively interpret this finding as a result of picking up a surface fluorine ion by the tip.

Author Contributions

Bob Kyeyune: conceptualization; data curation; formal analysis; investigation; visualization; writing – original draft; writing – review & editing. Philipp Rahe: conceptualization; data cura-

tion; funding acquisition; investigation; resources; writing –
review & editing. Michael Reichling: conceptualization;
funding acquisition; project administration; resources; supervi-
sion; validation; writing – review & editing.

ORCID® iDs

Bob Kyeyune - https://orcid.org/0000-0001-9078-909X
Philipp Rahe - https://orcid.org/0000-0002-2768-8381
Michael Reichling - https://orcid.org/0000-0003-3186-9000

Data Availability Statement

Data generated and analyzed during this study is available from the corre-
sponding author upon reasonable request.

References

1. Albrecht, T. R.; Grütter, P.; Horne, D.; Rugar, D. *J. Appl. Phys.* **1991,**
   69, 668–673. doi:10.1063/1.347347
2. Morita, S.; Abe, M.; Yokoyama, K.; Sugawara, Y. *J. Cryst. Growth*
   2000, *210,* 408–415. doi:10.1016/s0022-0248(99)00720-4
3. Morita, S.; Sugimoto, Y.; Oyabu, N.; Nishi, R.; Custance, O.;
   Sugawara, Y.; Abe, M. *J. Electron Microsc.* **2004,** *53,* 163–168.
   doi:10.1093/jmicro/53.2.163
4. Schütte, J.; Rahe, P.; Tröger, L.; Rode, S.; Bechstein, R.; Reichling, M.;
   Kühnle, A. *Langmuir* **2010,** *26,* 8295–8300. doi:10.1021/la904706p
5. Rahe, P.; Schütte, J.; Kühnle, A. *J. Phys.: Condens. Matter* **2012,** *24,*
   084006. doi:10.1088/0953-8984/24/8/084006
6. Liebig, A.; Hapala, P.; Weymouth, A. J.; Giessibl, F. J. *Sci. Rep.* **2020,**
   10, 14104. doi:10.1038/s41598-020-71077-9
7. Pavliček, N.; Gross, L. *Nat. Rev. Chem.* **2017,** *1,* 0005.
   doi:10.1038/s41570-016-0005
8. Foster, A. S.; Barth, C.; Shluger, A. L.; Reichling, M. *Phys. Rev. Lett.*
   2001, *86,* 2373–2376. doi:10.1103/physrevlett.86.2373
9. Hoffmann, R.; Weiner, D.; Schirmeisen, A.; Foster, A. S. *Phys. Rev. B*
   2009, *80,* 115426. doi:10.1103/physrevb.80.115426
10. Kyeyune, B.; Olbrich, R.; Reichling, M.; Rahe, P. *Phys. Rev. B* **2024,**
    110, 155417. doi:10.1103/physrevb.110.155417
11. Liebig, A.; Peronio, A.; Meuer, D.; Weymouth, A. J.; Giessibl, F. J.
    New J. Phys. **2020,** *22,* 063040. doi:10.1088/1367-2630/ab8efd
12. Jiménez-Sánchez, M. D.; Nicoara, N.; Gómez-Rodríguez, J. M.
    Appl. Surf. Sci. **2021,** *542,* 148669. doi:10.1016/j.apsusc.2020.148669
13. Kawai, S.; Foster, A. S.; Björkman, T.; Nowakowska, S.; Björk, J.;
    Canova, F. F.; Gade, L. H.; Jung, T. A.; Meyer, E. *Nat. Commun.* **2016,**
    7, 11559. doi:10.1038/ncomms11559
14. Mohn, F.; Schuler, B.; Gross, L.; Meyer, G. *Appl. Phys. Lett.* **2013,** *102,*
    073109. doi:10.1063/1.4793200
15. Bamidele, J.; Kinoshita, Y.; Turanský, R.; Lee, S. H.; Naitoh, Y.;
    Li, Y. J.; Sugawara, Y.; Štich, I.; Kantorovich, L. *Phys. Rev. B* **2012,** *86,*
    155422. doi:10.1103/physrevb.86.155422
16. Mönig, H.; Amirjalayer, S.; Timmer, A.; Hu, Z.; Liu, L.; Díaz Arado, O.;
    Cnudde, M.; Strassert, C. A.; Ji, W.; Rohlfing, M.; Fuchs, H.
    Nat. Nanotechnol. **2018,** *13,* 371–375. doi:10.1038/s41565-018-0104-4
17. Wiesener, P.; Förster, S.; Merkel, M.; Schulze Lammers, B.; Fuchs, H.;
    Amirjalayer, S.; Mönig, H. *ACS Nano* **2024,** *18,* 21948–21956.
    doi:10.1021/acsnano.4c03155
18. Barth, C.; Foster, A. S.; Reichling, M.; Shluger, A. L.
    J. Phys.: Condens. Matter **2001,** *13,* 2061–2079.
    doi:10.1088/0953-8984/13/10/303
19. Hoffmann, R.; Kantorovich, L. N.; Baratoff, A.; Hug, H. J.;
    Güntherodt, H.-J. *Phys. Rev. Lett.* **2004,** *92,* 146103.
    doi:10.1103/physrevlett.92.146103
20. Foster, A. S.; Shluger, A. L.; Nieminen, R. M. *Nanotechnology* **2004,**
    15, S60–S64. doi:10.1088/0957-4484/15/2/013
21. Pou, P.; Ghasemi, S. A.; Jelinek, P.; Lenosky, T.; Goedecker, S.;
    Pérez, R. *Nanotechnology* **2009,** *20,* 264015.
    doi:10.1088/0957-4484/20/26/264015
22. Yurtsever, A.; Fernández-Torre, D.; González, C.; Jelínek, P.; Pou, P.;
    Sugimoto, Y.; Abe, M.; Pérez, R.; Morita, S. *Phys. Rev. B* **2012,** *85,*
    125416. doi:10.1103/physrevb.85.125416
23. Tröger, L.; Schütte, J.; Ostendorf, F.; Kühnle, A.; Reichling, M.
    Rev. Sci. Instrum. **2009,** *80,* 063703. doi:10.1063/1.3152367
24. Olmstead, M. A. Heteroepitaxy of Disparate Materials: From
    Chemisorption to Epitaxy in CaF₂/Si(111). In *Thin Films:
    Heteroepitaxial Systems;* Liu, W. K.; Santos, M. B., Eds.; Series on
    Directions in Condensed Matter Physics; World Scientific: Singapore,
    1999; pp 211–266. doi:10.1142/9789812816511_0005
25. Wollschläger, J. Resonant tunneling devices based on epitaxial
    insulator-semiconductor structures: growth and characterisation of
    CaF₂ films on Si(111). In *Recent Research Developments in Applied
    Physics;* Pandalai, S. G., Ed.; Transworld Research Network:
    Trivandrum, India, 2002; Vol. 5-II, pp 621–695.
26. Rahe, P.; Smith, E. F.; Wollschläger, J.; Moriarty, P. J. *Phys. Rev. B*
    2018, *97,* 125418. doi:10.1103/physrevb.97.125418
27. Giessibl, F. J. *Appl. Phys. Lett.* **1998,** *73,* 3956–3958.
    doi:10.1063/1.122948
28. Sweetman, A.; Stirling, J.; Jarvis, S. P.; Rahe, P.; Moriarty, P.
    Phys. Rev. B **2016,** *94,* 115440. doi:10.1103/physrevb.94.115440
29. Rahe, P.; Schütte, J.; Schniederberend, W.; Reichling, M.; Abe, M.;
    Sugimoto, Y.; Kühnle, A. *Rev. Sci. Instrum.* **2011,** *82,* 063704.
    doi:10.1063/1.3600453
30. Söngen, H.; Bechstein, R.; Kühnle, A. *J. Phys.: Condens. Matter* **2017,**
    29, 274001. doi:10.1088/1361-648x/aa6f8b
31. Kyeyune, B.; Olbrich, R.; Rahe, P.; Reichling, M. *Rev. Sci. Instrum.*
    2024, *95,* 023702. doi:10.1063/5.0182520
32. Wollschläger, J. *Appl. Phys. A: Mater. Sci. Process.* **2002,** *75,*
    155–166. doi:10.1007/s003390101064
33. Sugimoto, Y.; Yi, I.; Morita, K.-i.; Abe, M.; Morita, S. *Appl. Phys. Lett.*
    2010, *96,* 263114. doi:10.1063/1.3457997

Deep learning for enhancement of low-resolution and noisy scanning probe microscopy images

Samuel Gelman[‡1], Irit Rosenhek-Goldian[‡2], Nir Kampf[2], Marek Patočka[2], Maricarmen Rios[2], Marcos Penedo[3], Georg Fantner[3], Amir Beker[4], Sidney R. Cohen[*2] and Ido Azuri[*1]

Full Research Paper

Address:
[1]Department of Life Sciences Core Facilities, Weizmann Institute of Science, Rehovot, 7610001, Israel, [2]Department of Chemical Research Support, Weizmann Institute of Science, Rehovot, 7610001, Israel, [3]École Polytechnique Fédérale de Lausanne, Laboratory for Bio- and Nano-Instrumentation, CH1015 Lausanne, Switzerland and [4]Bina, Weizmann Institute of Science, Rehovot, 7610001, Israel

Email:
Sidney R. Cohen[*] - sidney.cohen@weizmann.ac.il; Ido Azuri[*] - ido.azuri@weizmann.ac.il

* Corresponding author   ‡ Equal contributors

Abstract

In this study, we employed traditional methods and deep learning models to improve resolution and quality of low-resolution AFM images made under standard ambient scanning. Both traditional methods and deep learning models were benchmarked and quantified regarding fidelity, quality, and a survey taken by AFM experts. The deep learning models outperform the traditional methods and yield better results. Additionally, some common AFM artifacts, such as streaking, are present in the ground truth high-resolution images. These artifacts are partially attenuated by the traditional methods but are completely eliminated by the deep learning models. This work shows deep learning models to be superior for super-resolution tasks and enables significant reduction in AFM measurement time, whereby low-pixel-resolution AFM images are enhanced in both resolution and fidelity through deep learning.

Introduction

The capability of atomic force microscopy (AFM) to achieve high resolution at the nanometer level in plane (xy) and at the angstrom level in height (z), on a variety of surfaces, is one of its major advantages. AFM topographical imaging enables high-resolution imaging of simple and complex surfaces that capture the sensitive features, details, and information of the surface structure.

Whereas many manifestations of AFM are in use, including remarkable sub-molecular resolution for specialized systems working under low temperatures and high vacuum [1], the majority use remains that performed on commercial instruments working in ambient (or liquid) environments using one of several operating modes [2,3]. Achieving high-resolution images in such cases is hampered by a few shortcomings. First,

the scanning speed of traditional AFM is slow, and several minutes are typically required for each scan. Second, AFM scans can contain inherent artifacts in the captured image due to the operating system settings or the sample and its interaction with the tip. In principle, tip–surface contact should be carefully controlled to avoid damage due to these interactions. Scanning distortions due to non-linearities in the scan are also trickier to correct and harder to avoid in fast scanning. Some of these artifacts can be eliminated or attenuated by image processing techniques [4-12]. Another resolution-limiting factor in AFM is the tip size. In the well-established algorithm of blind reconstruction [13], "certainty maps" are provided, showing clearly where the tip does and does not measure each point. The sharper the tip relative to surface features, the more points it can access. Having said that, blind reconstruction has been used to map the surface to scales below the measured image feature size by "erosion" [14]. It is also important to note that recently machine-learning based methods have been applied to blind reconstruction to reconstruct true surface images from AFM images experimentally broadened by the tip [15]. Although these methods can sharpen images and remove certain tip artifacts, they are not as general in that they cannot upscale the image pixel resolution. Neither these nor the methods presented in this work can provide absolutely true information on parts of the surface the tip does not access.

One approach to obtain high-resolution images and overcome the slow scanning times is to apply image manipulation techniques to upscale low-resolution images to high (pixel) resolution. In a set of studies [16-19], traditional methods and deep learning models were successfully used to reconstruct high-resolution AFM images. In those studies, fidelity metrics were applied to quantify the quality of the reconstructed images. The most common fidelity metrics include peak-signal-to-noise-ratio (PSNR), which is based on pixel-to-pixel differences of the reference and reconstructed images and structural similarity index measure (SSIM), which avoids pixel-to-pixel comparison but instead compares changes in structural information between the images. In the research reported here, in addition to image fidelity metrics, we also incorporate "no-reference image quality metrics" that in some cases may be better aligned with the human perception evaluation and can be even inversely related to fidelity metrics [20]. These metrics are based, for example on contrast, texture richness, and feature frequency. This is of heightened importance for AFM images that may suffer from ubiquitous artifacts and blurring effects in their reference images. Specifically, we calculated here the perceptual index (PI) [20], which combines no-reference image quality measures of Ma et al. [21], which relate to human subjective scoring of super-resolution (SR) images, and the Natural Image Quality Evaluator (NIQE) [22], a blind no-reference image quality

metric based on the collection of "quality aware" image statistical features. Note that we use the term super-resolution here, as it is accepted in ML terminology, to refer to upscaling of images by at least a factor of four as was done in the research reported here. This is different from the usage in microscopy where the term refers to resolution beyond the classical physical limitations. Importantly, these no-reference metrics do not use reference images, as the name suggests. It means that they can result in an optimal quality score but do not account for the fidelity of the generated image. For this reason, it is always important to combine metrics from both domains, to first assess the fidelity of the reconstructed image with respect to a reference image and then its quality when attempting to quantify the performance of the upscaling methods and models.

An important distinction between this work and other implementations of deep learning for image enhancement is that in many cases, high-resolution images that are obtained from AFM scans are used to generate low-resolution counterparts by down-sampling to images that then serve as input to traditional methods and deep learning models. This approach is widely used in the community, with the advantage that it saves time and resources. That said, low-resolution images formed in that way are not comprised of physically accessed measurement pixels, simplifying both the experimental and computational components, which may affect the reported metrics. Furthermore, deep leaning models, as a rule of thumb, perform better when they are trained on large data sets. Since we had a relatively small number of images, we opted out of training a custom model and instead chose to use state-of-the-art pre-trained deep learning models trained on a large data set of real-world high-quality images.

In this study, we collected data sets from two different relatively complex surfaces that contain unique but pseudo-repeating structures, which are typical of those seen over a wide range of images spanning common materials and biological surfaces. The data sets contain low-resolution images of 128×128 pixels each and their counterpart high-resolution images of 512×512 pixels, which serve as the ground truth (GT). Importantly, both low- and high-resolution images are real scans of the surface and neither of them were obtained by image manipulation of the other. Then, we applied a set of traditional methods and SR pre-trained deep learning models on the low-resolution AFM images to obtain their enhanced-resolution image pairs. We performed a comparative study between traditional methods and SR pre-trained deep learning models and quantified their validity and performance by fidelity and quality metrics that were further supported by a survey taken by AFM experts. We found that, overall, the pre-trained SR deep learning models accurately retain the information from the low-

resolution images when compared to the GT while also resulting in significantly higher image quality compared to the traditional methods. These findings were supported by appropriate statistical testing.

Importantly, some of the high-resolution GT images suffer from common AFM artifacts that rarely appear in their low-resolution counterparts. Hence, an important outcome of this work, besides resolution enhancement of low-resolution images with the SR deep learning models was the elimination of artifacts in

the resulting AFM images. This can serve as a non-destructive method to obtain high-quality SR images of sensitive and soft materials.

Results and Discussion

In this study, 4× upscaled images were obtained from real measured low-resolution AFM images of Celgard® 2400 membrane and high-roughness titanium film used for tip characterization (Figure 1 and Figure 2, respectively). 4× upscaling means upscaling both the *x* and *y* directions and transforming an

Figure 1: Low- and high-resolution fast-AFM scans of two different locations on a Celgard® 2400 membrane surface, as well as the upscaled images using a traditional method (bilinear interpolation) and a deep learning model (RCAN). The aligned cropped image (94 × 94 and 370 × 370 pixels for low and high resolution, respectively) is displayed along with a corresponding zoom (20 × 20 and 80 × 80 pixels for low and high resolution, respectively) below it (Detail), marked with the white square in the full image. The light blue scale bar in the top-left image corresponds to 0.9 and 0.23 μm on full image and detail, respectively. The red arrows highlight the AFM artifacts, that is, "streaks" in the GT image that may be attenuated in the traditional bilinear method and have been removed in the deep learning model.

Figure 2: Low- and high-resolution AFM scans of two different locations on a titanium film, as well as the upscaled images using a traditional method (bilinear interpolation) and a deep learning model (RCAN). The aligned cropped image (94 × 94 and 370 × 370 pixels for low and high resolution, respectively) is displayed along with a corresponding zoom (20 × 20 and 80 × 80 pixels for low and high resolution, respectively) below it (Detail), marked with the white square in the full image. The light blue scale bar in the top-left image corresponds to 0.9 and 0.23 μm on full image and detail, respectively.

image of 128 × 128 pixels to 512 × 512 pixels, amounting to 16 times the total number of pixels. We note here that for some modes, such as contact mode or intermittent contact mode, the data is collected continuously and there is no acquisition time price paid for increased pixels in the fast scan direction (here, x). However, in some modes, such as peak force and photothermal off-resonance tapping as used here, unless the data is significantly oversampled, decreasing the number of pixels in both x and y scan directions will lower acquisition time proportionately. We therefore sample here with equal number of pixels in both x and y. The 4× upscaled images were ob-

tained using traditional methods [23-25] (bilinear, bicubic, and Lanczos4 interpolations) and SR deep learning models [26]. Seven different SR deep learning models were chosen (NinaSR-B0, NinaSR-B1, NinaSR-B2, RCAN, CARN, RDN, and EDSR) [27-31]. The model architectures are built of residual convolutional neural network blocks while each of them integrates a unique algorithmic component (see "Methods", "Computational Pipeline" section: "Traditional methods and deep learning super-resolution models"). For each low-resolution image, a corresponding AFM high-resolution image was measured and served as the GT. This enabled us to evaluate the 4× upscaled

image fidelity with respect to its GT high-resolution AFM image. Due to drift between acquisition at the two different resolutions, it was often necessary to align and crop the images so that corresponding low- (or the model-reconstructed high-resolution image) and high-resolution GT images were perfectly aligned. In addition to reference-based fidelity methods, no-reference methods were used to assess the quality of the 4× upscaled images. In this study, we evaluated the image fidelity and quality obtained with each method and model.

Image fidelity

The fidelity of the upscaled images was assessed by using established metrics such as PSNR and SSIM (see further explanation in the Methods section). For both metrics, the 4× upscaled images were compared to the GT. There was no statistically significant difference between the performance of deep learning models compared to the traditional methods, as

shown by the p-value Tukey's range test matrix comparisons in Figure 3 (all p-values are bigger than 0.98, except for that of the bilinear method, which performed worse than the other traditional methods, as well as some of the deep learning models for the SSIM metric with the smallest p-value of 0.12. Importantly, although this value is conventionally considered statistically insignificant, in some cases it could be sufficient, depending on the stringency required). This is also evident from the metrics values in Table 1 and Table 2 for both data sets.

Both PSNR and SSIM are based on comparison between the 4× upscaled images and the GT. Since there is no significant statistical difference between the traditional methods and the deep learning models fidelity metrics, image quality metrics remain the key determining factor when comparing any given method or model.
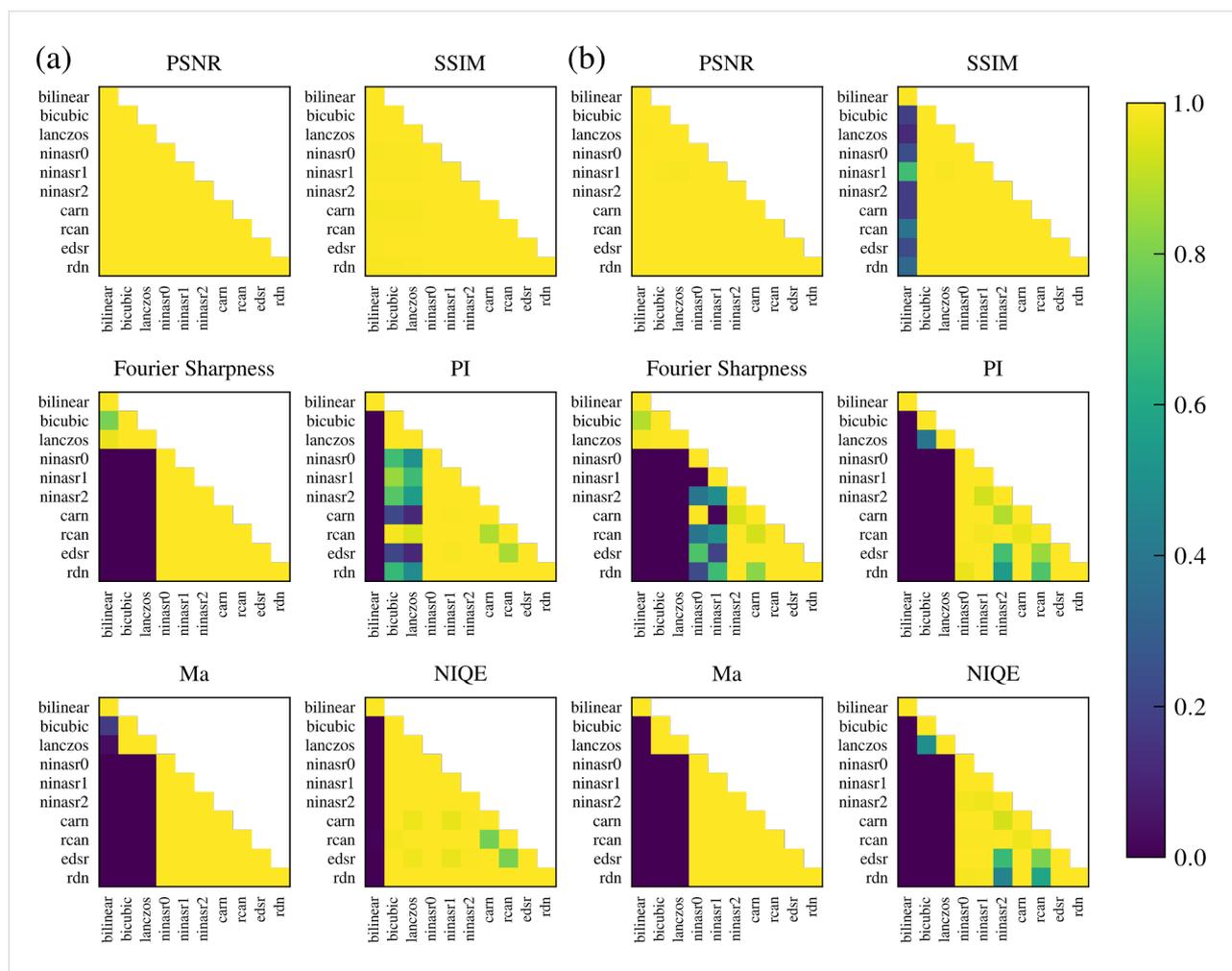
Figure 3: p-Values for six different metrics (PSNR, SSIM, Fourier Sharpness, PI, Ma, and NIQE) for the two data sets, (a) Celgard® 2400 membrane and (b) titanium film, generated using Tukey's range test. For clarity, only the lower triangular matrix values are presented as the matrices are symmetric. The diagonal represents a value with itself and is therefore always equal to one. Below the diagonal, values closer to zero (blue) represent statistically significant differences between the corresponding method/model performances.

Table 1: Comparison of method/model performance across metrics for the Celgard® 2400 membrane data set. Higher values indicate better performance, except for PI and NIQE, where lower values are better. Values in bold represent metrics for which SR deep learning models are statistically significantly better than all traditional methods. Values in parentheses are the range of standard deviation for each metric.

Method/Model	PSNR (4.30–4.76)	SSIM (0.054–0.068)	Fourier sharpness (0.11–0.19)	PI (0.42–0.97)	Ma (0.39–0.66)	NIQE (0.67–1.91)
Bilinear	29.02	0.901	5.194	9.990	2.217	12.20
Bicubic	28.90	0.900	5.246	9.161	2.533	10.85
Lanczos4	28.88	0.900	5.232	9.201	2.603	11.00
NinaSR0	28.58	0.888	**5.483**	8.885	**3.138**	10.91
NinaSR1	28.53	0.889	**5.489**	8.923	**3.173**	11.02
NinaSR2	28.60	0.890	**5.462**	8.896	**3.148**	10.94
CARN	28.57	0.888	**5.465**	8.776	**3.123**	10.67
RCAN	28.56	0.889	**5.485**	8.996	**3.149**	11.14
EDSR	28.57	0.889	**5.465**	8.771	**3.131**	10.67
RDN	28.52	0.887	**5.467**	8.871	**3.167**	10.91

Table 2: Comparison of method/model performance across metrics for the titanium film data set. Higher values indicate better performance, except for PI and NIQE, where lower values are better. Values in bold represent metrics for which SR deep learning models are statistically significantly better than all traditional methods. Values in parentheses are the range of standard deviation for each metric.

Method/Model	PSNR (2.22–2.82)	SSIM (0.016–0.022)	Fourier sharpness (0.09–0.16)	PI (0.16–0.25)	Ma (0.24–0.37)	NIQE (0.22–0.57)
Bilinear	32.43	0.915	5.323	9.316	2.892	11.52
Bicubic	33.11	0.93	5.382	7.964	3.6	9.53
Lanczos4	33.17	0.931	5.365	7.829	3.664	9.32
NinaSR0	32.76	0.929	**5.824**	**6.476**	**4.539**	**7.49**
NinaSR1	32.38	0.925	**5.997**	**6.447**	**4.592**	**7.49**
NinaSR2	32.71	0.93	**5.913**	**6.529**	**4.546**	**7.6**
CARN	32.83	0.93	**5.86**	**6.44**	**4.591**	**7.47**
RCAN	32.59	0.928	**5.914**	**6.515**	**4.561**	**7.59**
EDSR	32.65	0.929	**5.895**	**6.42**	**4.58**	**7.42**
RDN	32.61	0.928	**5.924**	**6.408**	**4.573**	**7.39**

A final comment on fidelity is that there are some cases where small features generated by the deep learning models do not appear in the ground truth. It is not always possible to assess whether these features are genuine or artifacts, as we note that ground truth is also not completely immune to artifacts. These questionable features can be treated as any potential artifact in microscopic images and benefit from verification by independent means, when possible. Minimally, sufficient statistics should be acquired to verify the existence of unusual, important features. A good protocol would be to zoom in and collect a small number of sample images at higher pixel resolution to see whether the features are properly interpreted by the upscaled images. Sometimes, as with all AFM work, it is beneficial to authenticate results using other microscopies such as electron microscopy, or spectroscopic techniques, where relevant.

Importantly, computationally, PSNR average values are very close to 30 for the Celgard® 2400 membrane surface and above 32 for the titanium film, putting them within the acceptable range of values to demonstrate the reliability of the suggested method.

Image quality

The image quality results show conclusively that the deep learning SR models outperform their traditional counterparts. Figure 1 and Figure 2 provide a comparison of the image

quality for both data sets along with the full image as well as image zoom details. These differences in quality between the images obtained with the deep learning models (RACN model) and those obtained with the traditional methods (Bilinear method) are clearly seen.

Quantitative metrics were also used to assess image quality. Natural images are composed of sharply delineated edges, whereas low-quality upscaled images are often characterized by blurred edges. Therefore, measuring the sharpness of an image can act as a proxy for image quality. One way to measure the sharpness is by measuring the gradient between neighboring pixel values.

Additionally, some methods exist that rely on extracting image features. These methods have become increasingly popular, and many variations of such methods have been published [20-22,32-34]. Several such methods were tested; the results were consistent across all of them and are given for PI, Ma, and NIQE. PI is a no-reference image quality metric [20] that incorporates the image feature extraction calculation of Ma and colleagues [21] as well as the NIQE metric [22]. The former relies on human subject studies of SR images and the latter is a blind, no-reference image quality metric based on the collection of "quality aware" image statistical features. PI is thus given by the formula PI = 0.5 × ((10 − Ma) + NIQE).

While Table 1 and Table 2 show the exact values of the different metrics for each method/model (values in bold represent metrics in which all SR deep learning models are statistically significantly better than all traditional methods), Figure 3 illustrates the statistically meaningful differences in performance between the methods/models with respect to image quality metrics, in favor of the deep learning models. While the metrics of the reference-based methods, PSNR and SSIM, show no statistically significant differences between the traditional methods and the deep learning models for image fidelity, the no-reference methods for image quality, Fourier Sharpness, PI, Ma, and NIQE exhibit such differences. Importantly, while for the titanium film data set, all SR deep learning models are statistically significantly better than the traditional methods for all of the no-reference image quality metrics, this is not the case for the Celgard® 2400 data set, for which only the Fourier Sharpness and Ma metrics are statistically significantly better for all SR deep learning models in comparison to the traditional methods. This could arise from the difference between fast and traditional AFM scanning as Celgard® 2400 was measured with fast AFM and titanium film with standard, slow AFM. The fast-scanning is often achieved at the expense of somewhat worse resolution or associated scanning artifacts. The better quality of the latter (titanium film) is reflected in better performance

metrics. Nevertheless, this highlights the utility of SR deep learning models for obtaining high-resolution and high-quality upscaled images from low-resolution AFM images. We should also note that the absolute values for PI, Ma, and NIQE are not optimal, since the metrics were designed and constructed for image populations different from AFM images. Nevertheless, the values are adequate for this comparative study.

Expert survey

AFM experts were presented with a blind test to assess both the fidelity and quality of samples generated using traditional methods and deep learning models (RCAN and RDN models) from both data sets. Figure 4 shows the mean results of the AFM experts and their standard deviations. The experts were asked to rank image fidelity and quality with discrete scores ranging between 1 (for low image fidelity and quality) and 6 (for high image fidelity and quality). The results agree with the other quantitative metrics in that the quality of the deep learning models ranked significantly higher than that of the traditional methods. Importantly, while there was no significant statistical difference in fidelity metrics calculated for the images obtained from traditional methods and deep learning models, in the field experts' evaluation, there is a statistically significant difference in favor of the deep learning models (with p-values below 2.9×10^{-7}).
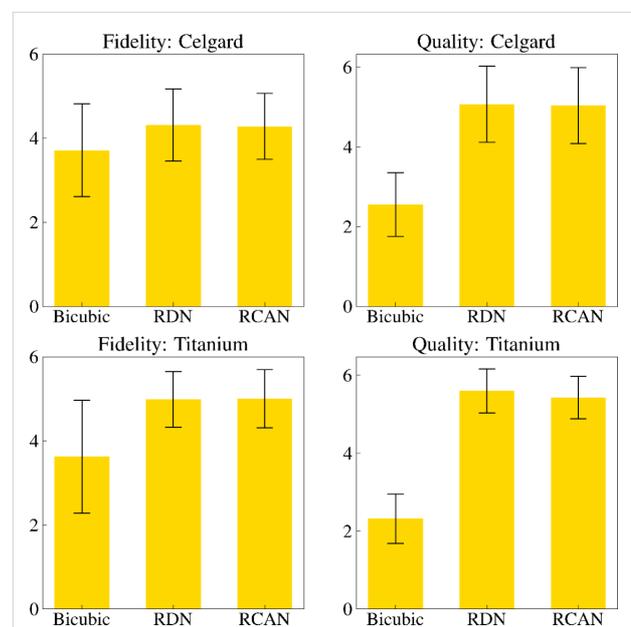
Figure 4: AFM expert survey results. Three experts were asked to judge a blind set of samples and to score each sample's fidelity and quality compared to the high-resolution ground truth image. The scores are discrete and in the range of 1 (low image fidelity and quality) and 6 (high image fidelity and quality). An example of a data set provided to the surveyors for each sample is presented below in Figure 5. Here, super-resolution models outperformed traditional methods in both quality and fidelity ratings by statistically significant amounts.

Pre-trained vs training and fine-tuning deep learning models

For best performance on new, unseen data, deep learning models usually require large amounts of data for training. To avoid this requirement, pre-trained models can be applied. A pre-trained model is a model that has been already trained on the data to perform a given task, here returning SR images from low-resolution images. Then, the pre-trained model can be used for inference without any further fitting procedure on new data such as that used in this research. This approach may work ideally when the target population is similar to the trained data population. Since it was not feasible here to obtain a large amount of data for training a deep learning model, we used pre-trained models supplied by the GitHub repository by Gabriel Gouvine [26]. Importantly, although the models were trained on natural images, which are different from the AFM population images, it yielded satisfactory results in terms of metrics values and AFM field experts. In addition, while EDSR is known to yield the most accurate results, it can be seen that for the pre-trained models, smaller models can yield better results than the EDSR for some of the metrics, as seen in Table 1 and Table 2. Finally, having a custom data set of a specific modality, such as AFM images, may result in an optimized trained or fine-tuned deep learning model which could outperform those employed here. Since our data sets were too small for this purpose, we did not examine this approach here but plan to address it in future work.

From low- to high-resolution artifact-free AFM images

Some of the high-resolution GT AFM images suffer from common artifacts as can be seen in Figure 1 (red arrows), in particular, in images that were captured at high scanning rates. These artifacts are almost invisible in the low-resolution images. It can be seen that these artifacts do not exist in the 4× upscaled deep learning models that excel in creating sharper natural images. This is in line with the reported ability of the RCAN SR deep learning model to recover images from artifacts [28]. When compared to the traditional methods, these artifacts may disappear as well, but, in some cases, they are only attenuated. This suggests another aspect in which the deep learning models are beneficial. Also, low-resolution images should contain enough information to capture the meaningful image features to ensure that the upscaled high-resolution images will be valid.

Conclusion

In this study, 4× upscaled high-resolution and high-quality images were obtained from low-resolution AFM images through the use of traditional methods and deep learning models. The effectiveness of these methods and models was then quantified using metrics to gauge the fidelity and quality of their outputs as well as through a survey taken by AFM experts. We found that the deep learning models yield better results in comparison to the traditional methods. In addition, common AFM artifacts such as streaking often appear in the GT high-resolution images. These artifacts are attenuated in the traditional methods while being fully eliminated in the deep learning models. These factors support our conclusion that deep learning models are the method of choice for upsampling low-resolution AFM images to yield high-resolution and high-quality images. Additionally, the application of the suggested procedure can greatly reduce AFM measurement time, enabling the introduction of a faster and more effective procedure into the AFM-based pipeline.

Methods

The Methods section is composed of Experimental and Computational Pipeline sections.

Experimental
AFM image acquisition

For this study we conducted our research on two separate image data sets. For each set, two different image resolutions were captured on overlapping surface areas both at low resolution of 128 × 128 pixels and high resolution of 512 × 512 pixels. The first set is composed of 52 pairs of low- and high-resolution images of a Celgard® 2400 membrane (Celgard, LLC - North Carolina, USA). Images of 5 μm × 5 μm were captured at 8–10 Hz scanning speed, using a fast-scan AFM system, operated by using photothermal off-resonance (at 10 kHz) tapping [35] and small cantilevers, which fit on the base of a commercial MultiMode AFM system (Nanoscope V electronics, Bruker AXS SAS, Santa Barbara, CA). The fast-scanning AFM head and control electronics were designed in-house and built according to the details in [36-38]. Images were acquired using LabView-based software as described in [39]. Scans were made with a silicon tip on a silicon nitride cantilever (FASTSCANC, Bruker). The second set is composed of 25 pairs of low- and high-resolution images of a titanium film, which is used for AFM tip characterization (TipCheck, Aurora Nanodevices, BC, Canada). Images of 5 μm × 5 μm were captured at 1 Hz scanning speed by using a MultiMode AFM with Nanoscope V electronics (Bruker AXS SAS, Santa Barbara, CA) controlled with Nanoscope 9.2 software (Build R2Sr1.130547). Scans were made in PeakForce tapping mode at 2 kHz tapping frequency using a PNP-TRS pyrex-nitride probe formed from silicon nitride (NanoWorld). Images were subject to plane leveling and alignment using Gwyddion 2.62, an open-source software for SPM data analysis [40]. The Gwyddion files were converted to Python .npy files for input to the computational pipeline.

Computational Pipeline

The research aims to apply traditional methods and SR deep learning models on low-resolution images and increase their resolution to a 4× scale. Increasing the resolution to the 4× scale will make the images the same size as the high-resolution GT images gathered by AFM. A computational pipeline was established to take the low-resolution images, prepare them as input for the various traditional methods and deep learning SR models (Image normalization), apply those methods and models (Traditional methods and deep learning super-resolution models), transform the values to a standard form (Image value transformation), perform alignment along all images (Image alignment), and finally assess the quality of the algorithms using reference and no-reference metrics as well as an expert survey (Metrics) followed by statistical analysis (Statistical analysis).

Image normalization

The AFM images had a single height channel in units of nanometers. The values of the low-resolution images were normalized to be in the range between zero and one using min–max normalization and expanded equally across RGB color channels as part of the image preprocessing phase for the SR deep learning models. To prepare the normalized low-resolution images for the traditional methods they were converted to pixel values ranging from 0 to 255.

Traditional methods and deep learning super-resolution models

The choice of SR techniques was aimed at assessing the quality of advanced deep learning approaches and comparing their performance to the traditional methods. Bilinear, bicubic, and Lanczos interpolation were employed using the implementations of Python's openCV library [41].

The SR deep learning models were all part of the torchSR GitHub repository supplied by Gabriel Gouvine. Five distinct model architectures were used, all of which were built using principles of residual neural network (ResNet) architectures as their backbones. Enhanced deep super-resolution networks (EDSR) make some modifications such as removing batch normalization [31]. Residual dense networks (RDN) employ the use of custom residual dense blocks. This sets them apart from prior dense block techniques, which fail to use additional local dense connections across blocks [30]. Another modification is the cascading residual network (CARN), which uses a cascading mechanism at local and global levels to combine features from both levels [29]. Additionally, SR deep learning models leverage attention along feature channels. This attention is incorporated into residual channel attention blocks, which are stacked to make up deep residual channel attention

networks (RCAN) [28]. The torchSR repository also includes a scalable neural network for the SR task, NinaSR [27]. Three different models were supplied (NinaSR-B0, NinaSR-B1, NinaSR-B2), ranging from lighter to heavier sizes. The NinaSR model utilizes local attention blocks and a wide expansion ratio of the residual blocks, and it was initialized using methods adapted from NFNet [27,42].

Image value transformation

Images generated from the deep learning models were RGB images, and the distribution of pixel values reflected those of the input images. The pixel values of the SR images were clamped to be between zero and one and then were converted to values between 0 and 255. The RGB images were then transformed into greyscale images. The high-resolution GT images were also normalized and converted to values ranging from 0 to 255.

Image alignment

During the AFM image capture, the low-resolution and high-resolution GT image pairs were taken sequentially over the same area of the sample, resulting in a high image overlap across image pairs. Nevertheless, the overlap location is not perfect due to typical AFM drift. This is also projected on the corresponding images obtained by the traditional methods and SR deep learning models. Hence, it was necessary to first align the obtained images with respect to their corresponding high-resolution GT images to assess the accuracy and quality of the different methods and models used.

We employed a multistep approach for image alignment using OpenCV. First, the scale-invariant feature transform (SIFT) was utilized to detect and describe local features, ensuring invariance to scale and rotation [43]. These features were then matched across images using a brute force matching algorithm, followed by k-nearest neighbors to refine the matching process based on Euclidean distance [44]. The best corresponding pixel matches were used to compute the homography matrix, allowing for perspective transformation [45]. The borders of the transformed images and the high-resolution GT images were cropped to ensure precise pixel alignment across the image pairs.

Metrics

Assessing the effectiveness of traditional methods and SR deep learning models can be divided into two main domains, namely, reference and no-reference metrics. Reference metrics measure the correctness of a method or model by comparing the images obtained from a given method or model against their corresponding GT images. In this study, the images obtained by the

different methods and models were compared to their experimentally captured GT counterparts.

No-reference metrics measure the quality of the images obtained by different methods and models. Such metrics try to reflect quality as interpreted by human perception. They often extract features from an image and transform them into a calculated metric. For example, calculating the gradients of an image enables the calculation of edge magnitudes in the image and consequently its sharpness. As the domain name suggests, these metrics do not rely on the presence of GT reference images. These metrics can score optimally but do not account for the fidelity of the generated image. For this reason, it is always important to use methods from both domains to first assess the fidelity of an image using reference metrics and then its quality when attempting to quantify the performance upscaling methods and models.

In addition to the use of algorithmic assessments, a blind and subjective evaluation was conducted, polling AFM experts for their opinions on both image fidelity and image quality.

Reference metrics

The first comparison of the SR images to the GT references was to take the peak-signal-to-noise ratio (PSNR). This is done by taking the logarithm of the maximum value of the reference and dividing that by the root-mean squared error between the image and the reference. The PSNR is then multiplied by a coefficient to conveniently scale the metrics output to the decibel scale.

Other methods attempted to avoid pixel-to-pixel differences and instead assess image similarity on a structural basis. This was the motivation for formulating the structural similarity index measure (SSIM) [46]. SSIM has become a widely used reference metric when quantifying image fidelity.

No-reference metrics

One intuitive approach to quantify the quality of an image is calculating the sharpness of that image. In some sense, sharpness quantifies the clearness of an image. Nonetheless, high sharpness values can be due to the spikes typical of noise, and values should be interpreted carefully. One way to determine sharpness is by calculating first-order derivatives (gradients) of pixel values along the horizontal and vertical axes of the image (x, y) and averaging the absolute value of the gradients. A second approach is to transform the image to the frequency domain with the discrete Fourier transform (DFT) when high-frequency regions correspond to the sharp edges. Also here, high-frequency regions may represent noise, and values should be interpreted carefully. Here, we calculated the Fourier sharpness by the mean of the logarithm of the absolute value shifted DFT.
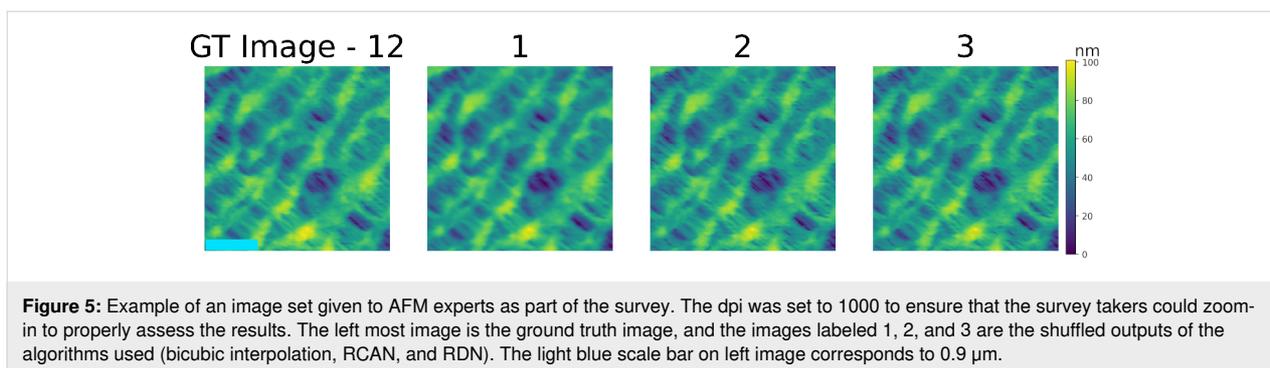
Additionally, there are other no-reference metrics that rely on image features extracted from the images [20-22,33,34]. In this study, the PI, Ma, and NIQE methods were used as no-reference metrics [20-22]. In Ma, low-level statistical features are extracted from super-resolution images in the spatial and frequency domains. The super-resolution images are scored by humans to reflect the human visual perception. Then, a regression model is trained to map between the extracted low-level statistical features and the human scores and is available for inference on new images. NIQE, in contrast, is not based on human scoring and, in that sense, is a completely blind, no-reference, image quality metric. It extracts statistical features in the spatial domain that are associated with image quality from a collection of natural images. A multivariate Gaussian model is fitted to the extracted features and serves as a reference model. Then, the same procedure is applied to new images, resulting in a second fit. The fit is compared to the reference fit, and the deviations from it yield the NIQE score. PI is derived from the combination of Ma and NIQE and is given explicitly by PI = 0.5 × ((10 − Ma) + NIQE).

Experts survey

In addition to the algorithmic approaches, three experts in AFM assessed image fidelity and quality. They were provided with all images in each data set. For each image, a set of images was supplied. Each set contained four images aligned in a row. The left most image was the GT image taken experimentally and was labeled as such. The other three (unlabeled) images were all outputs of traditional methods and SR deep learning models: specifically, those from images generated by bicubic interpolation as well as by two deep-learning models (RCAN and RDN). For each image set, the three images were shuffled and labeled 1, 2, and 3. Figure 5 presents an example image that was shown to the AFM experts. The AFM experts did not have the key and, therefore, did not know which of the algorithms corresponded to which of the labeled images for every set. The experts were asked to rank the SR image fidelity and quality from a discrete scale of 1 (lowest) to 6 (highest).

Statistical analysis

To methodically compare statistical significance between all the various traditional methods and SR deep learning models for each of the metrics listed above, the Tukey's honestly significant difference (HSD) test [47] performed pairwise comparison of means for the set of all methods and models used. Individual methods and models were compared using box plots, and full comparisons were done using adjacency matrices.

Figure 5: Example of an image set given to AFM experts as part of the survey. The dpi was set to 1000 to ensure that the survey takers could zoom-in to properly assess the results. The left most image is the ground truth image, and the images labeled 1, 2, and 3 are the shuffled outputs of the algorithms used (bicubic interpolation, RCAN, and RDN). The light blue scale bar on left image corresponds to 0.9 µm.

Code

In this study, all code was written in the Python programming language [48]. In addition to its common packages, we used, OpenCV (v. 4.7.0) [41], PyTorch (v. 2.1.2) [49], PYIQA (v. 0.1.11) [50], Scikit-Image (v. 0.23.2) [51], SciPy (v. 1.13.1) [52], and torchSR github repository for the pre-trained deep learning models [26].

ORCID® iDs

Samuel Gelman - https://orcid.org/0009-0005-6800-036X
Irit Rosenhek-Goldian - https://orcid.org/0000-0002-4878-5359
Nir Kampf - https://orcid.org/0000-0002-6713-6979
Marek Patočka - https://orcid.org/0000-0003-3898-8600
Maricarmen Rios - https://orcid.org/0000-0001-8020-9709
Marcos Penedo - https://orcid.org/0000-0002-2936-7354
Georg Fantner - https://orcid.org/0000-0001-5889-3022
Sidney R. Cohen - https://orcid.org/0000-0003-4255-3351
Ido Azuri - https://orcid.org/0000-0002-2891-1514

Data Availability Statement

Data generated and analyzed during this study is currently in use in ongoing research and may be available from the corresponding author upon reasonable request.

References

1. Nakamoto, K.; Mooney, C. B.; Iwatsuki, M. *Rev. Sci. Instrum.* **2001,** *72,* 1445–1448. doi:10.1063/1.1342033
2. Li, M.; Xi, N.; Liu, L. *Nanoscale* **2021,** *13,* 8358–8375. doi:10.1039/d1nr01303c
3. Dufrêne, Y. F.; Ando, T.; Garcia, R.; Alsteens, D.; Martinez-Martin, D.; Engel, A.; Gerber, C.; Müller, D. J. *Nat. Nanotechnol.* **2017,** *12,* 295–307. doi:10.1038/nnano.2017.45
4. Lapshin, R. V. *Nanotechnology* **2004,** *15,* 1135–1151. doi:10.1088/0957-4484/15/9/006
5. Jung, H.; Han, G.; Jung, S. J.; Han, S. W. *Micron* **2022,** *161,* 103332. doi:10.1016/j.micron.2022.103332
6. Bonagiri, L. K. S.; Wang, Z.; Zhou, S.; Zhang, Y. *Nano Lett.* **2024,** *24,* 2589–2595. doi:10.1021/acs.nanolett.3c04712
7. Kocur, V.; Hegrová, V.; Patočka, M.; Neuman, J.; Herout, A. *Ultramicroscopy* **2023,** *246,* 113666. doi:10.1016/j.ultramic.2022.113666
8. Wu, Y.; Fan, Z.; Fang, Y.; Liu, C. *IEEE Trans. Instrum. Meas.* **2021,** *70,* 5004212. doi:10.1109/tim.2020.3038007
9. Erickson, B. W.; Coquoz, S.; Adams, J. D.; Burns, D. J.; Fantner, G. E. *Beilstein J. Nanotechnol.* **2012,** *3,* 747–758. doi:10.3762/bjnano.3.84
10. Kubo, S.; Umeda, K.; Kodera, N.; Takada, S. *Biophys. Physicobiol.* **2023,** *20,* e200006. doi:10.2142/biophysico.bppb-v20.0006
11. Azuri, I.; Rosenhek-Goldian, I.; Regev-Rudzki, N.; Fantner, G.; Cohen, S. R. *Beilstein J. Nanotechnol.* **2021,** *12,* 878–901. doi:10.3762/bjnano.12.66
12. Heath, G. R.; Kots, E.; Robertson, J. L.; Lansky, S.; Khelashvili, G.; Weinstein, H.; Scheuring, S. *Nature* **2021,** *594,* 385–390. doi:10.1038/s41586-021-03551-x
13. Villarrubia, J. S. *J. Res. Natl. Inst. Stand. Technol.* **1997,** *102,* 425–454. doi:10.6028/jres.102.030
14. Keller, D. J.; Franke, F. S. *Surf. Sci.* **1993,** *294,* 409–419. doi:10.1016/0039-6028(93)90126-5
15. Matsunaga, Y.; Fuchigami, S.; Ogane, T.; Takada, S. *Sci. Rep.* **2023,** *13,* 129. doi:10.1038/s41598-022-27057-2
16. Liu, Y.; Sun, Q.; Lu, W.; Wang, H.; Sun, Y.; Wang, Z.; Lu, X.; Zeng, K. *Adv. Theory Simul.* **2019,** *2,* 1800137. doi:10.1002/adts.201800137
17. Han, G.; Lv, L.; Yang, G.; Niu, Y. *Appl. Surf. Sci.* **2020,** *508,* 145231. doi:10.1016/j.apsusc.2019.145231
18. Han, G.; Wu, T.; Lv, L.; Li, H.; Lin, H.; Lin, C.; Luo, J. *Nano* **2021,** *16,* 2150147. doi:10.1142/s1793292021501472
19. Wang, J.; Yang, F.; Wang, B.; Liu, M.; Wang, X.; Wang, R.; Song, G.; Wang, Z. *J. Struct. Biol.* **2024,** *216,* 108107. doi:10.1016/j.jsb.2024.108107
20. Blau, Y.; Mechrez, R.; Timofte, R.; Michaeli, T.; Zelnik-Manor, L. The 2018 PIRM Challenge on Perceptual Image Super-Resolution. In *Computer Vision – ECCV 2018 Workshops,* Munich, Germany, Sept 8–14, 2018; Springer: Berlin, Heidelberg, Germany, 2019; pp 334–355. doi:10.1007/978-3-030-11021-5_21
21. Ma, C.; Yang, C.-Y.; Yang, X.; Yang, M.-H. *arXiv* **2016,** 1612.05890. doi:10.48550/arxiv.1612.05890
22. Mittal, A.; Soundararajan, R.; Bovik, A. C. *IEEE Signal Process. Lett.* **2013,** *20,* 209–212. doi:10.1109/lsp.2012.2227726
23. Smith, P. R. *Ultramicroscopy* **1981,** *6,* 201–204. doi:10.1016/s0304-3991(81)80199-4
24. Keys, R. *IEEE Trans. Acoustics, Speech, Signal Process.* **1981,** *29,* 1153–1160. doi:10.1109/tassp.1981.1163711
25. Lanczos, C. *Applied Analysis;* Dover Publications: New York, NY, USA, 1988.
26. torchsr·PyPI. https://pypi.org/project/torchsr/ (accessed July 2, 2025).
27. Coloquinte/torchSR: v1.0.4. https://zenodo.org/records/10427745. doi:10.5281/zenodo.10427745

28. Zhang, Y.; Li, K.; Li, K.; Wang, L.; Zhong, B.; Fu, Y. *arXiv* **2018,** 1807.02758. doi:10.48550/arxiv.1807.02758
29. Ahn, N.; Kang, B.; Sohn, K.-A. *arXiv* **2018,** 1803.08664. doi:10.48550/arxiv.1803.08664
30. Zhang, Y.; Tian, Y.; Kong, Y.; Zhong, B.; Fu, Y. *arXiv* **2018,** 1802.08797. doi:10.48550/arxiv.1802.08797
31. Lim, B.; Son, S.; Kim, H.; Nah, S.; Lee, K. M. *arXiv* **2017,** 1707.02921. doi:10.48550/arxiv.1707.02921
32. Moorthy, A. K.; Bovik, A. C. *IEEE Trans. Image Process.* **2011,** *20,* 3350–3364. doi:10.1109/tip.2011.2147325
33. Mittal, A.; Moorthy, A. K.; Bovik, A. C. *IEEE Trans. Image Process.* **2012,** *21,* 4695–4708. doi:10.1109/tip.2012.2214050
34. Tang, H.; Joshi, N.; Kapoor, A. Learning a Blind Measure of Perceptual Image Quality. In *CVPR 2011,* IEEE: Colorado Springs, CO, USA, 2011; pp 305–312. doi:10.1109/cvpr.2011.5995446
35. Nievergelt, A. P.; Banterle, N.; Andany, S. H.; Gönczy, P.; Fantner, G. E. *Nat. Nanotechnol.* **2018,** *13,* 696–701. doi:10.1038/s41565-018-0149-4
36. Adams, J. D.; Nievergelt, A.; Erickson, B. W.; Yang, C.; Dukic, M.; Fantner, G. E. *Rev. Sci. Instrum.* **2014,** *85,* 093702. doi:10.1063/1.4895460
37. Nievergelt, A. P.; Adams, J. D.; Odermatt, P. D.; Fantner, G. E. *Beilstein J. Nanotechnol.* **2014,** *5,* 2459–2467. doi:10.3762/bjnano.5.255
38. Nievergelt, A. P.; Andany, S. H.; Adams, J. D.; Hannebelle, M. T.; Fantner, G. E. Components for High-Speed Atomic Force Microscopy Optimized for Low Phase-Lag. In *2017 IEEE International Conference on Advanced Intelligent Mechatronics (AIM),* 2017; pp 731–736. doi:10.1109/aim.2017.8014104
39. SPM Controller/Software. https://www.epfl.ch/labs/lbni/spm-controller-software/ (accessed March 2, 2025).
40. Nečas, D.; Klapetek, P. *Cent. Eur. J. Phys.* **2012,** *10,* 181–188. doi:10.2478/s11534-011-0096-2
41. opencv-python·PyPI. https://pypi.org/project/opencv-python/ (accessed July 2, 2025).
42. Brock, A.; De, S.; Smith, S. L.; Simonyan, K. *arXiv* **2021,** 2102.06171. doi:10.48550/arxiv.2102.06171
43. Lowe, D. G. Object Recognition from Local Scale-Invariant Features. In *Proceedings of the Seventh IEEE International Conference on Computer Vision,* 1999; pp 1150–1157. doi:10.1109/iccv.1999.790410
44. Jakubović, A.; Velagić, J. Image Feature Matching and Object Detection Using Brute-Force Matchers. In *2018 International Symposium ELMAR,* 2018; pp 83–86. doi:10.23919/elmar.2018.8534641
45. Richard, H.; Zisserman, A. *Multiple View Geometry in Computer Vision,* 2nd ed.; Cambridge University Press: Cambridge, UK, 2004.
46. Wang, Z.; Bovik, A. C.; Sheikh, H. R.; Simoncelli, E. P. *IEEE Trans. Image Process.* **2004,** *13,* 600–612. doi:10.1109/tip.2003.819861
47. Tukey, J. W. *Biometrics* **1949,** *5,* 99. doi:10.2307/3001913
48. Van Rossum, G.; Drake, F. L. *Python 3 Reference Manual;* CreateSpace: Scotts Valley, CA, USA, 2009.
49. Paszke, A.; Gross, S.; Massa, F.; Lerer, A.; Bradbury, J.; Chanan, G.; Killeen, T.; Lin, Z.; Gimelshein, N.; Antiga, L.; Desmaison, A.; Kopf, A.; Yang, E.; DeVito, Z.; Raison, M.; Tejani, A.; Chilamkurthy, S.; Steiner, B.; Fang, L.; Bai, J.; Chintala, S. PyTorch: An Imperative Style, High-Performance Deep Learning Library. In *Advances in Neural Information Processing Systems,* 33rd Conference on Neural Information Processing Systems (NeurIPS 2019), Vancouver, Canada; Curran Associates, Inc., 2019. https://papers.nips.cc/paper_files/paper/2019/file/bdbca288fee7f92f2bfa9f7012727740-Paper.pdf
50. chaofengc/IQA-PyTorch. https://github.com/chaofengc/IQA-PyTorch (accessed July 2, 2025).
51. van der Walt, S.; Schönberger, J. L.; Nunez-Iglesias, J.; Boulogne, F.; Warner, J. D.; Yager, N.; Gouillart, E.; Yu, T.; the scikit-image contributors. *PeerJ* **2014,** *2,* e453. doi:10.7717/peerj.453
52. Virtanen, P.; Gommers, R.; Oliphant, T. E.; Haberland, M.; Reddy, T.; Cournapeau, D.; Burovski, E.; Peterson, P.; Weckesser, W.; Bright, J.; van der Walt, S. J.; Brett, M.; Wilson, J.; Millman, K. J.; Mayorov, N.; Nelson, A. R. J.; Jones, E.; Kern, R.; Larson, E.; Carey, C. J.; Polat, İ.; Feng, Y.; Moore, E. W.; VanderPlas, J.; Laxalde, D.; Perktold, J.; Cimrman, R.; Henriksen, I.; Quintero, E. A.; Harris, C. R.; Archibald, A. M.; Ribeiro, A. H.; Pedregosa, F.; van Mulbregt, P.; SciPy 1.0 Contributors. *Nat. Methods* **2020,** *17,* 261–272. doi:10.1038/s41592-019-0686-2

License and Terms

Automated collection and categorisation of STM images and STS spectra with and without machine learning

Dylan Stewart Barker[*] and Adam Sweetman[*]

Full Research Paper

Address:
School of Physics and Astronomy, University of Leeds, Leeds LS2 9JT, United Kingdom

Email:
Dylan Stewart Barker[*] - D.S.Barker@leeds.ac.uk; Adam Sweetman[*] - A.M.Sweetman@leeds.ac.uk

* Corresponding author

Abstract

Atomic resolution scanning probe microscopy, and in particular scanning tunnelling microscopy (STM) allows for high-spatial-resolution imaging and also spectroscopic analysis of small organic molecules. However, preparation and characterisation of the probe apex in situ by a human operator is one of the major barriers to high-throughput experimentation and to reproducibility between experiments. Characterisation of the probe apex is usually accomplished via assessment of the imaging quality on the target molecule and also the characteristics of the scanning tunnelling spectra (STS) on clean metal surfaces. Critically for spectroscopic experiments, assessment of the spatial resolution of the image is not sufficient to ensure a high-quality tip for spectroscopic measurements. The ability to automate this process is a key aim in development of high resolution scanning probe materials characterisation. In this paper, we assess the feasibility of automating the assessment of imaging quality, and spectroscopic tip quality, via both machine learning (ML) and deterministic methods (DM) using a prototypical tin phthalocyanine on Au(111) system at 4.7 K. We find that both ML and DM are able to classify images and spectra with high accuracy, with only a small amount of prior surface knowledge. We highlight the practical advantage of DM not requiring large training datasets to implement on new systems and demonstrate a proof-of-principle automated experiment that is able to repeatedly prepare the tip, identify molecules of interest, and perform site-specific STS experiments using DM, in order to produce large numbers of spectra with different tips suitable for statistical analysis. Deterministic methods can be easily implemented to classify the imaging and spectroscopic quality of a STM tip for the purposes of high-resolution STM and STS on small organic molecules. Via automated classification of the tip state, we demonstrate an automated experiment that can collect a high number of spectra on multiple molecules without human intervention. The technique can be easily extended to most metal–adsorbate systems and is promising for the development of automated, high-throughput, STM characterisation of small adsorbate systems.

Introduction

Scanning tunnelling spectroscopy (STS) extends the capability of scanning tunnelling microscopy (STM) beyond topographic imaging, allowing for the direct measurement of the electronic properties of surfaces and molecules with atomic precision. This opens up the ability to map the local density of states (LDOS) of a sample with high spatial resolution [1-3]. Peaks within a map of the LDOS correspond to increases in conductance at specific bias values, revealing the energy levels of key features (e.g. molecular orbitals in the case of molecular samples) within the material.

As for STM imaging, the sharpness and overall tip shape is crucial in optimising the spatial resolution of STS measurements; sharp tips result in localised tunnelling through a single position, whereas blunt or misshaped tips cause averaging of contributions over larger areas, reducing the spatial resolution and potentially blending the electronic features between different sites. However, even for tips with high spatial resolution, different tip structures and probe terminations are known to influence these results [4-7].

STS measurements are the result of an integration over the available density of states (DOS) in both the tip and the sample, with the current measured therefore being proportional to the convolution of two. To isolate the DOS of the sample, it is crucial that the tip has a nominally "flat" DOS, which is typically achieved by using a purely metallic tip. However, most tips do not demonstrate a perfectly flat local density of states (LDOS) as they have a complex electronic structure governed by the geometry of the metallic cluster at the tip apex [8-12]. Non-metallic contaminants can also strongly perturb the electronic structure of the tip.

Methods of optimising the probe state for ideal STS are slow and laborious, involving indentation into a metal surface and bias pulses applied to the tip, manually checking spectra and imaging after each probe shaping attempt. The automation of this process could result in a more rapid and reproducible method for performing spectroscopy measurements.

To classify the state of the probe for STS experiments, spectra are usually taken over bare areas of a metallic substrate. On coinage metal surfaces, these $\frac{dI}{dV}$ spectra typically exhibit a characteristic feature corresponding to the surface state, which appears as a step function around a specific bias value, which for the Au(111) surface appears at around −0.48 V [13,14].

One notable attempt to automate this classification using machine learning (ML) was carried out by Wang et al. [15]. This work aimed to classify the state of a STM tip based on STS measurements of the Au(111) surface. Using a total of 1789 archived $\frac{dI}{dV}$ spectra, a ML model was trained which aimed to classify new spectra into one of five categories, based on the similarity of each the spectrum to an idealised surface state.

This schema achieved final precision in classification of 84% and a recall of 74%. Similarly to image classification in scanning probe microscopy (SPM) [16-18], the availability of such a large amount of data for training is usually very low, making ML-based classifiers troublesome to train. In addition to the lack of data, ML models require careful labelling and a high level of knowledge from the labeller to be able to train such a model. Switching to a new substrate system is likely to require retraining of the model, and furthermore, even after a successful training, it is still often unclear what the model is learning from the input data, a problem which leads to these models being referred to as a "black box". Because of these limitations, there is a strong case to develop methods which do not rely on ML, circumventing these drawbacks whilst still being able to make precise classifications of the tip quality for use in automation.

In the following work, we use the prototypical system of tin phthalocyanine (SnPc) on Au(111) to investigate the feasibility of a DM automated classifier and compare it to ML methods. This molecular system has the advantage that the SnPc adsorbs on the surface in two distinct configurations, one with the tin atom facing up (SnUp), and the other with the tin facing down (SnDown) (Figure 1), providing a variety of molecular configurations to challenge the automated molecular identification.

In addition to the classification of the probe quality based on the surface state, we use a DM-based cross-correlation (CC) feature finding method [19] in order to also assess the imaging quality of the tip, and also automatically locate various molecules on the surface. Combining these methods, it is possible to conduct a fully automated experiment, where a large number of STS measurements can be obtained over various molecules automatically with optimised tips and the quality of the spectra and image assessed automatically.

Methods
Experimental details

We used a third-generation commercial low-temperature (LT) STM NC-AFM instrument (Scienta Omicron GmbH), which was operated using an RC5 Nanonis controller, with all experiments carried out in UHV (base pressure ≤5×10^{-11} mbar) cooled to 5 K. Gold and silver crystals (spl.eu) were prepared via repeated sputter–anneal cycles, sputtering under an argon

Figure 1: (a) Structure of tin phthalocyanine (SnPc). Side-on view of SnPc, illustrating its non-planar nature in the (b) SnUp and (c) SnDown configurations. (d) and (e) show constant-current STM images of the SnUp and SnDown configurations respectively, taken at 5 K, −100 mV, 50 pA.
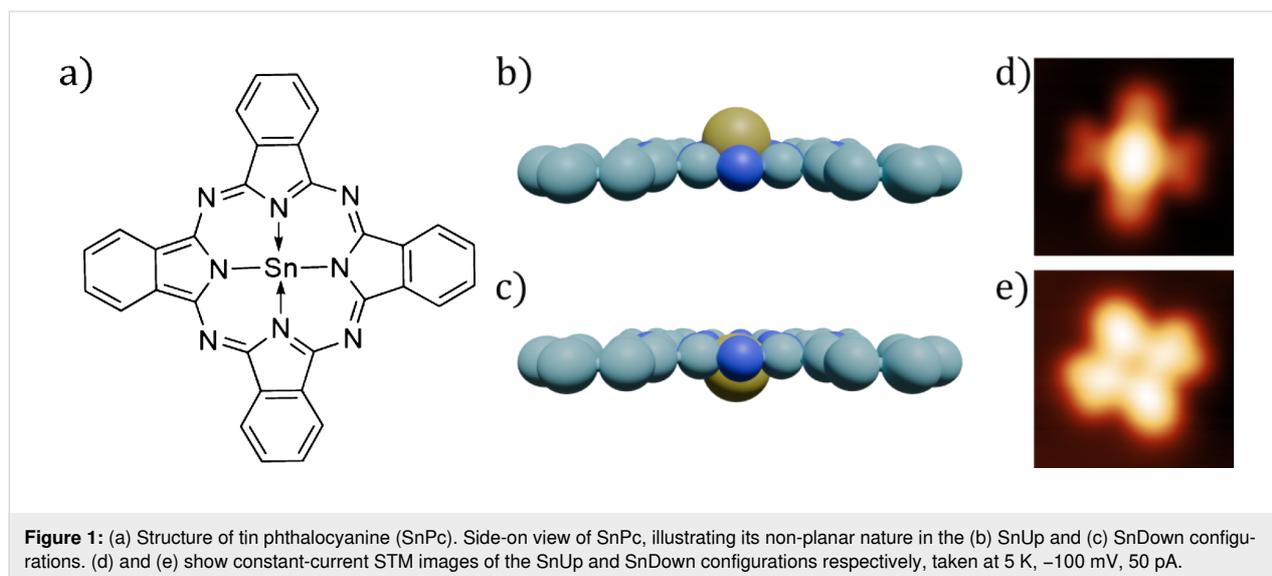
pressure of $\approx 5 \times 10^{-5}$ mbar, with a beam energy of 1.5 kV for 30 min, measuring a drain current of ≈ 7.0 μA, before annealing at 500 °C for 30 min and then placed into the scan head for imaging. Platinum–iridium STM tips were used throughout this work and were prepared by standard STM methods (voltage pulses, controlled contacts with the sample) until good atomic resolution was obtained in STM feedback.

SnPc was deposited onto the Au(111) surface using a custombuilt evaporator, where the powdered source material is contained within a glass crucible using glass wool, around which a coil of tantalum wire is wound, providing a source of heat for the crucible. The target temperature for SnPc deposition was 360 °C; once reached, the cryostat shields were opened for 1 h, before closing and checking the coverage in STM. Once deposited, the sample was cold annealed to room temperature, which has the effect of driving the molecules preferentially to the "elbow" sites of the herringbone structure.

An STS spectrum (differential conductance) can be obtained in practice using one of two methods. Both begin by positioning the STM tip at a desired lateral position on the surface whilst scanning in STM feedback. At this point, the feedback loop is disabled, keeping the tip–sample distance constant throughout the spectroscopy measurement. The voltage is then swept through a range of values whilst measuring the current, which is obtained as a function of the varying voltage, $I(V)$. This curve can then be differentiated with respect to the voltage to obtain the differential conductance, $\frac{dI}{dV}$, spectra.

Alternatively, the derivative signal, $\frac{dI}{dV}$, as a function of voltage, can be directly measured using the lock-in technique. In this method, an AC signal is generated by applying a small

modulation voltage, $V_{\mathrm{M}}\cos(\omega t)$, to the bias. Due to this modulation, the measured current is expressed as
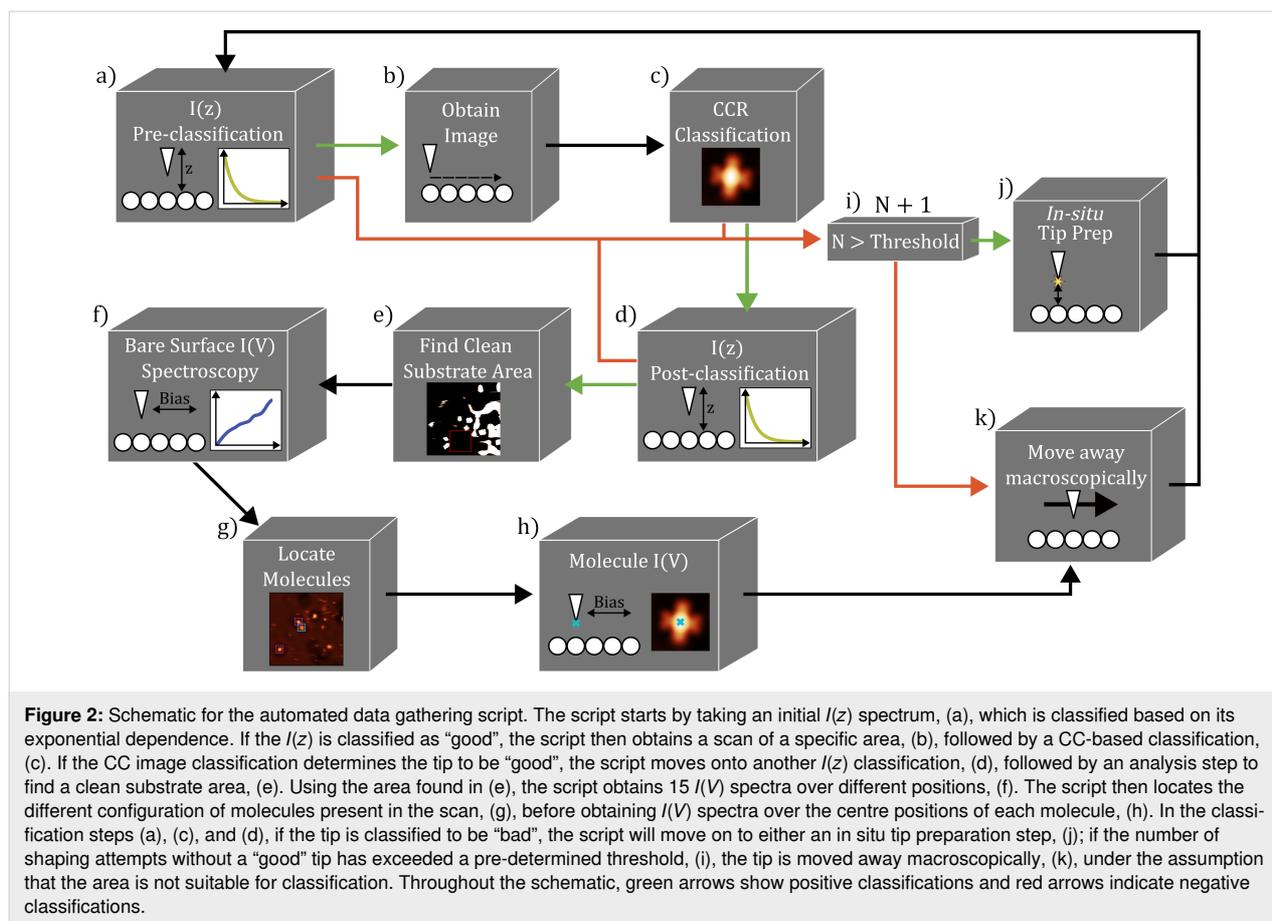
$$ I(t) = f\left(V + V_{\mathrm{M}}\cos(\omega t)\right), \tag{1} $$

where V_{M} is the modulation amplitude and ω is the frequency. Applying this modulation around a central voltage creates a corresponding modulation in the measured tunnel current with an amplitude proportional to the gradient of the $\frac{dI}{dV}$ curve at that bias. Therefore, once the tip is in position, the bias can be swept through a range whilst applying the modulation. The resultant current can then be detected by a lock-in amplifier, where its amplitude for small values of V_{M} is proportional to $\frac{dI}{dV}$, therefore directly measuring the differential conductance of the sample. Throughout the work presented here, the conductance was measured directly using the lock-in technique.

Results

To create the ML-based classification models needed for this work, a large amount of data was needed in the form of STS spectra taken with a variety of different tip shapes and configurations. The dataset generation procedures were created using LabVIEW, which interfaces directly with the Nanonis controller. The process of the dataset generation was performed in a manner similar to that described in Barker et al. [19], with some minor alterations, as described below.

The process of the automated dataset generation is shown in Figure 2. One addition to this method compared to the automated data gathering method described in Barker et al. [19] is the addition of $I(z)$ classifications prior to performing imaging to ensure a tunnelling junction. This acts as a rapid "pre-

Figure 2: Schematic for the automated data gathering script. The script starts by taking an initial *I*(*z*) spectrum, (a), which is classified based on its exponential dependence. If the *I*(*z*) is classified as "good", the script then obtains a scan of a specific area, (b), followed by a CC-based classification, (c). If the CC image classification determines the tip to be "good", the script moves onto another *I*(*z*) classification, (d), followed by an analysis step to find a clean substrate area, (e). Using the area found in (e), the script obtains 15 *I*(*V*) spectra over different positions, (f). The script then locates the different configuration of molecules present in the scan, (g), before obtaining *I*(*V*) spectra over the centre positions of each molecule, (h). In the classification steps (a), (c), and (d), if the tip is classified to be "bad", the script will move on to either an in situ tip preparation step, (j); if the number of shaping attempts without a "good" tip has exceeded a pre-determined threshold, (i), the tip is moved away macroscopically, (k), under the assumption that the area is not suitable for classification. Throughout the schematic, green arrows show positive classifications and red arrows indicate negative classifications.

filtering" step, eliminating tips that do not show a stable tunnelling junction (and hence are not suitable for STS) without the need to perform a complete image to characterise the tip. The classification of the state of the probe based on imaging is performed via the CC method as a key feature of a "good" tip for STS is also the sharpness of the probe, in order to ensure high spatial resolution in the acquired data. Further details on the CC and *I*(*z*) classification as implemented for the SnPc models is provided in the online supporting information.

Once the imaging classification is complete, the *I*(*z*) classification is performed again to check that a tip change did not occur during the scan. The obtained topograph is then analysed to find both a large area of clean metal substrate, over which *I*(*V*) spectra can be obtained, and to find the location of the molecules in various configurations, over which additional *I*(*V*) spectra are taken.

After completing this data gathering step, the tip moves away from the imaging area for a tip preparation event, in order to change the apex substantially before repeating the entire process to collect another dataset with a different tip. Throughout, if the tip is classified as "bad" in either of the *I*(*z*) classifications or

the CC-based imaged classification, the script moves onto a tip preparation event. If the tip fails in being classified as "good" more than a set number of times in a row, the tip is moved away macroscopically, under the assumption that the current area of the surface is not suitable for classification; this typically occurs due to the area being damaged from prior tip preparation, or the absence of an SnUp molecule in the frame which is used in the CC classification of the image.

The CC classification is carried out as described in Barker et al. ([19]), with the reference image used being a cropped image of an SnUp molecule as is shown in Figure 1d. SnUp molecules were chosen for classification as in this configuration, the Sn atom in the molecule presents a higher aspect ratio than in the SnDown configuration, and so is more sensitive to the sharpness of the tip. Using this method with a threshold of >0.98, the model was able to reliably generate and identify sharp tips.

Dataset summary

Using the data generation method described above, we obtained a total of 2604 individual spectra on the bare Au(111) surface, 86 of which were used for our classification models. In order to use this data for training and evaluation of models, the

dataset required labelling. We note that labelling of the dataset is non-trivial as for ML models the model can only attempt to learn to evaluate spectra based on the ground truth provided by the labelling.

Labelling was carried out using a similar process to [19]. A custom Python script was written with a graphical interface. The script would show each spectrum individually, with a choice of four labels depending on the visibility of the surface state (SS): SS "good", SS "step visible", SS "peak visible", and

SS "not visible". When classifying the data, the region around the surface state step was focused on, with the "good" label being attributed to a spectrum where the step was clearly visible at the correct position, showing few features before and after the step.

Whilst it was clear which data fell into each category, we note that even the data with the most visible surface state contained a background slope, as seen in Figure 3c. It is well understood that different suitable STS tips can produce considerable varia-
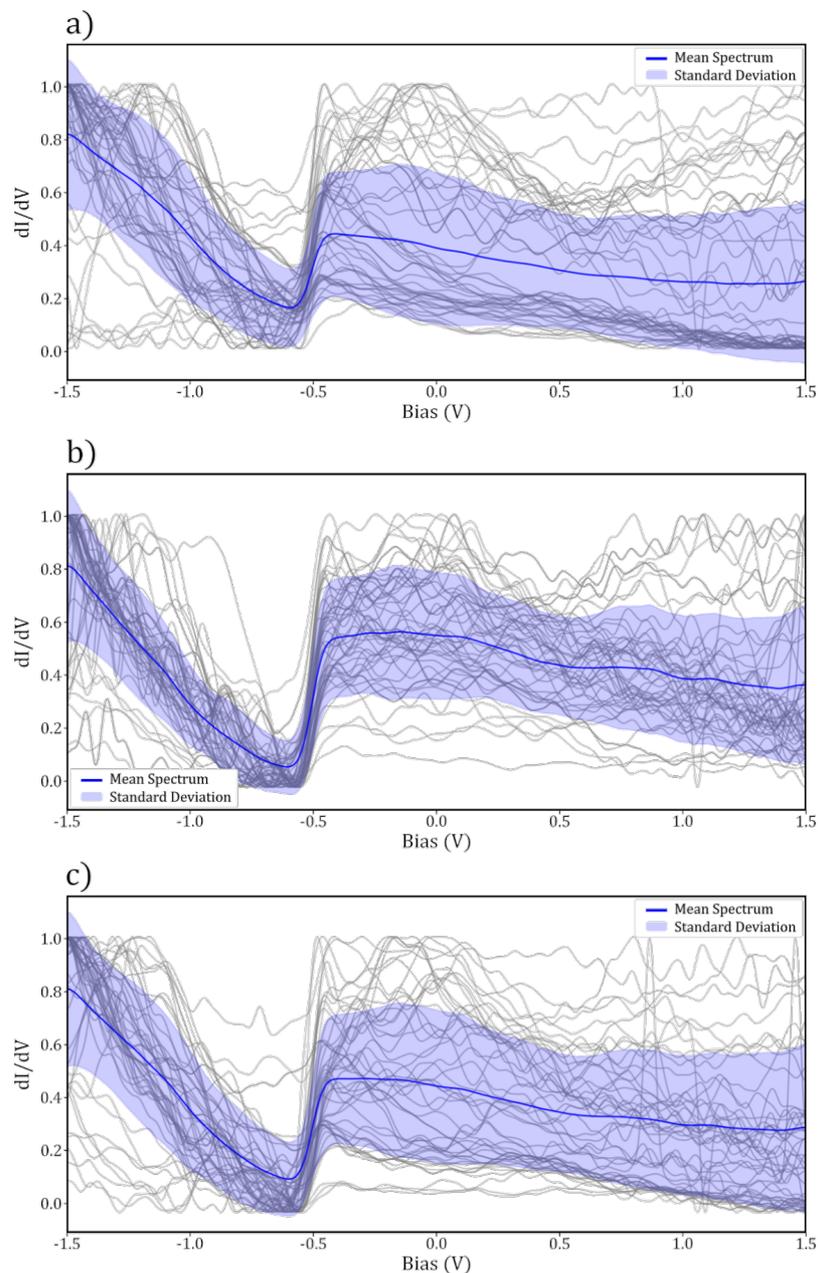
Figure 3: Samples of 50 normalised spectra (grey lines) taken over the clean Au(111) surface, mean (blue line) and standard deviation (shaded area) for (a) surface state "step visible", (b) surface state "good" and (c) binary "good" labels.

tion in the features observed in spectra taken over a bare substrate, including slopes through the bias range [10,20]. Therefore, the classification of what constitutes as a "good" tip is in a sense somewhat arbitrary and dependent on what the end user is interested in investigating. For the purposes of this work, we chose the primary point of interest for classification as the visibility of the surface state step at the correct bias. Our data were therefore classified with this trend in mind, with the final "good" classifications often containing a trend in the region

below −0.5 V. The SS "step visible" label was given to spectra whose curves show the step in the correct position, but where a general trend (slope) was also visible throughout the data. The SS "peak visible" label applied to spectra where there was an apparent feature at the correct position for the step, but not necessarily a step, and the final SS "not visible" label was given to spectra where no feature resembling the surface state could be observed. A representative sampling of spectra from each labelling category are shown in Figure 3 and Figure 4, with all
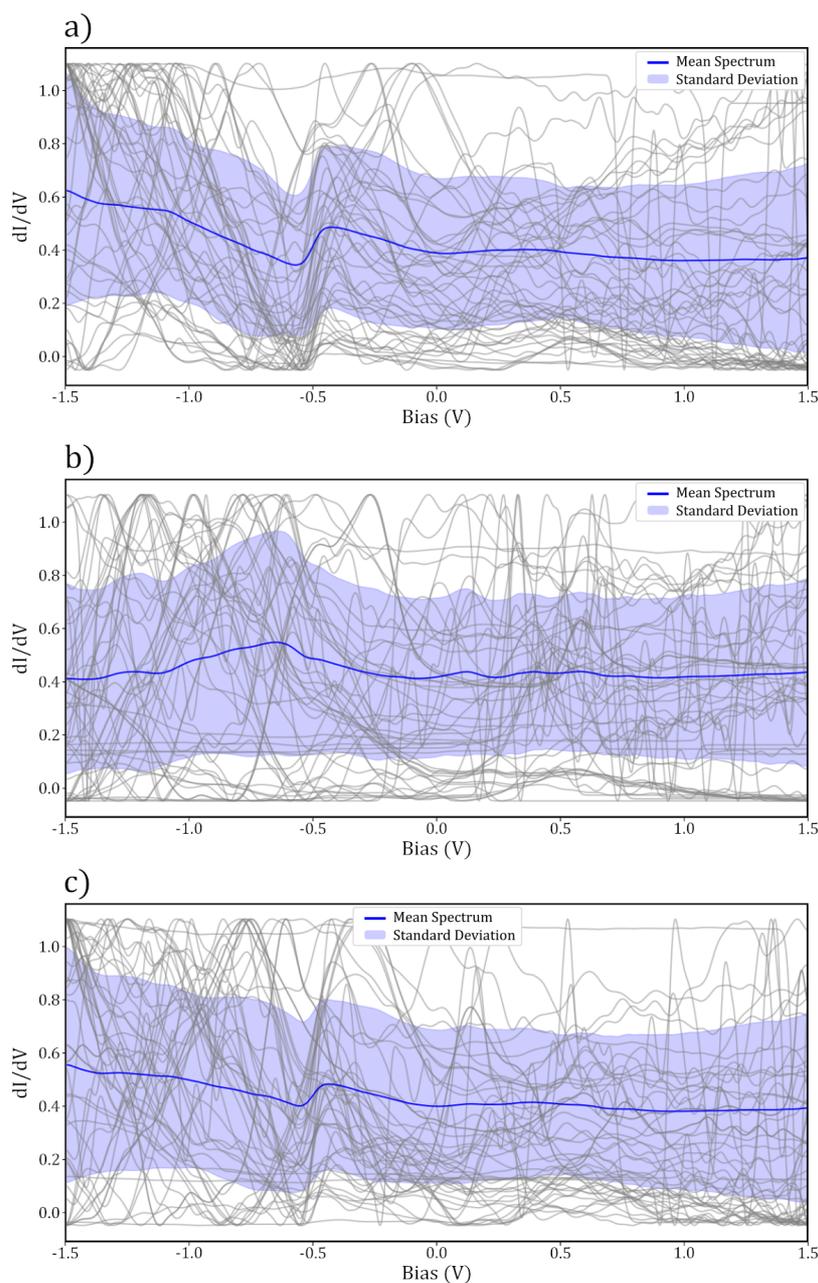
Figure 4: Samples of 50 normalised spectra (grey lines) taken over the clean Au(111) surface, mean (blue line) and standard deviation (shaded area) for (a) surface state "peak visible", b) surface state "not visible" and (c) binary "bad" labels.

spectra obtained shown in Supporting Information File 1, Figure S2.

For the final classification, the SS "good" and SS "step visible" categories were combined into a single "good" category, and the SS "not visible" and SS "peak visible" were combined into a "bad" category. This was done to allow for a simple binary classification on the basis that further distinction between the classes is unlikely to improve the final model and would greatly increase the complexity of the problem.

Table 1 shows the number of spectra in each category after the labelling step. For ML training, the data were split into training, validation, and test sets at a ratio of 70:10:20. This left 1823 spectra for training, 260 for validation, and 521 for final testing.

Table 1: Number of spectra in each category.

Labels	Count
SS "good"	384
SS step visible	482
SS peak visible	1169
SS not visible	569
binary "good"	866
binary "bad"	1738

Classification methods
Machine learning classifier

With the labelling completed, it was possible to train a series of 1D convolutional neural networks (CNNs). In total, 72 models were trained, varying the number of convolutional layers between 1 and 3, the number of dense training layers between 1 and 3, the number of kernels in the first convolutional layer (32 and 64 kernels were used, doubling in successive layers), kernels of sizes 3×3 or 5×5, and dropout layers with rates of either 0.3 or 0.5, including all combinations of these. The training was carried out on the training dataset containing 1823 spectra, validating the model after each epoch on the validation set of 260.

After training, each of these models were evaluated on a test set of 521 spectra, with their final accuracies, precisions, and recalls compared. We note the recall is defined as the percentage of all data labelled as "good", which is then also classified as "good". This metric therefore places more weight on false negatives than the precision metric and is also not as largely skewed by imbalanced datasets as the accuracy metric.

The model which achieved the best balance between the three metrics was one which contained two convolutional layers starting with 5×5 kernels, 32 in the first layer and 64 in the second, a single dense training layer, followed by a dropout rate of 0.3. The architecture of this model is shown schematically in Supporting Information File 1, Figure S1. This achieved an over-all accuracy of 86%, a precision of 85%, and a recall of 70%.
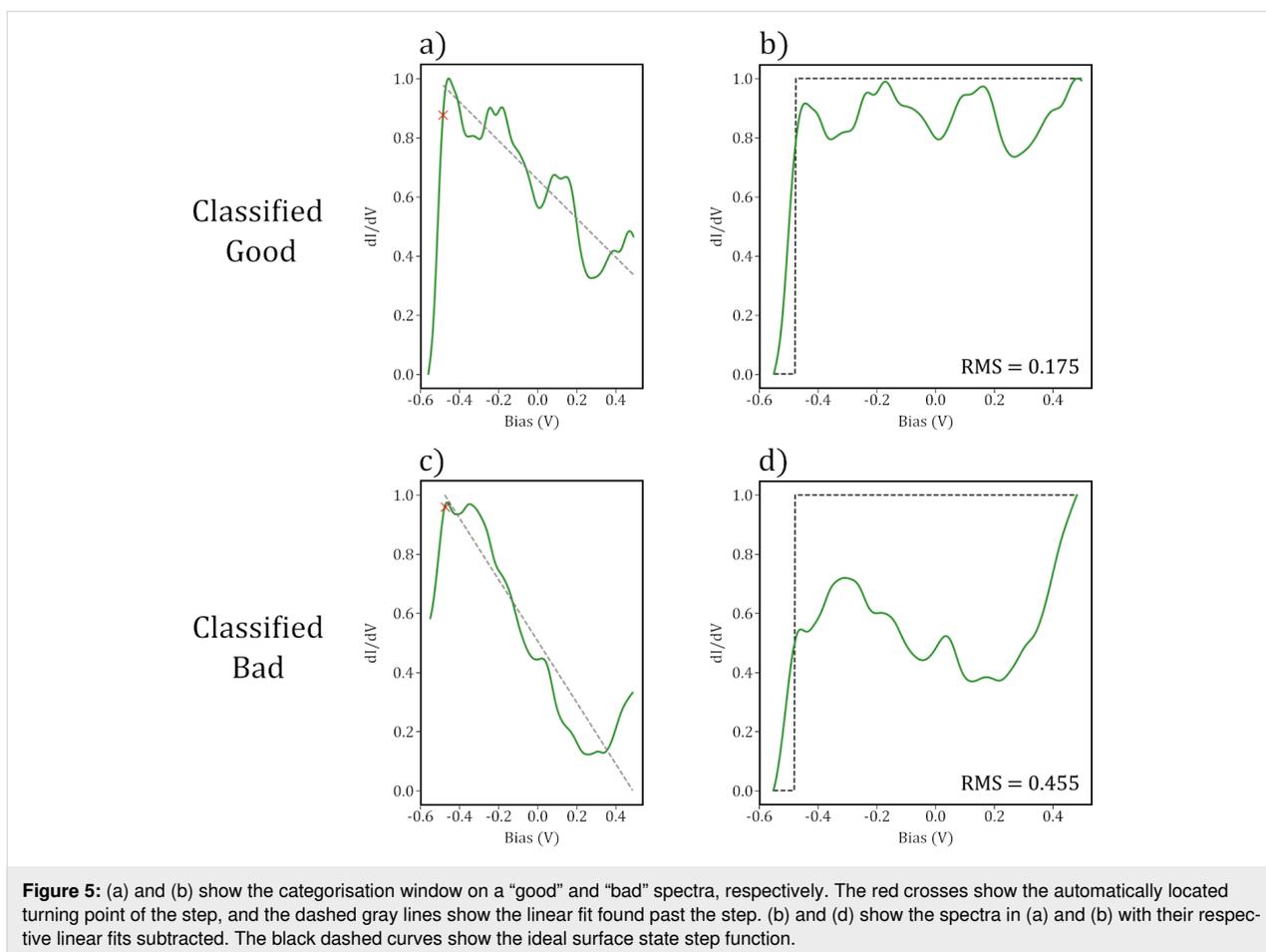
Deterministic classifier

For the deterministic classifier, we required a method which is able to adapt to the entire dataset with a clear set of rules, outputting a metric describing how close any individual spectrum is to an idealised surface state spectrum. To this end, we implemented a simple model to calculate the difference between the surface state step at −0.48 V with a perfect step function, both normalised between 0 and 1.

In principle, for an "ideal" metallic tip, the step function would be clearly visible within the spectrum at the correct bias. However, as noted above, the majority of the data we acquired were not completely flat and showed a noticeable slope even when the SS was clearly visible. Therefore, in order to make a comparison between these tips and the ideal step function, additional processing is needed.

First, the spectra were cropped to remove features outside of the categorisation window, which for this dataset was the bias range from −0.55 to 0.5 V. From here, any general trend/slope visible in the data needs to be found and subtracted from the step. Commonly in our data, it seems that the trend is a linear offset in the $\frac{dI}{dV}$, and hence a linear function after the step can be fit to the data, and then subtracted from the original spectrum. The specific location of the turning point of each spectrum is obtained by finding the minimum of the differential of the curve within a small range around −0.48 V, and the step is assumed to be contained within the categorisation range, following this determined turning point. From this, a linear function is fit to the window, an example of which is shown for both a "good" and "bad" classified tip in Figure 5a and Figure 5c, respectively.

Once the linear trend is found, it is subtracted from the original spectrum, the result of which is shown in Figure 5b and Figure 5d. For a "good" spectrum, the resultant curve should appear roughly as a step function, and so by direct comparison to a perfect step function, starting at the turning point found earlier, a deterministic classification measure can be made. The specific metric output as the difference between these two curves is the root mean squared (RMS) error between the two, which is described by Equation 2:

Figure 5: (a) and (b) show the categorisation window on a "good" and "bad" spectra, respectively. The red crosses show the automatically located turning point of the step, and the dashed gray lines show the linear fit found past the step. (b) and (d) show the spectra in (a) and (b) with their respective linear fits subtracted. The black dashed curves show the ideal surface state step function.

$$\text{RMS} = \sqrt{\sum_{i=1}^{n}\left(\hat{y}_i - y_i\right)^2}. \qquad (2)$$

Here, $\hat{y}$ are the perfect step function data points, and y are the spectra for classification. To evaluate the optimal thresholds for classification, a stacked histogram was plotted, showing the spread of the RMS in each category. This histogram is shown in Figure 6. From this, the final threshold was chosen <0.25, with all spectra resulting in a value within this range classified as "good".
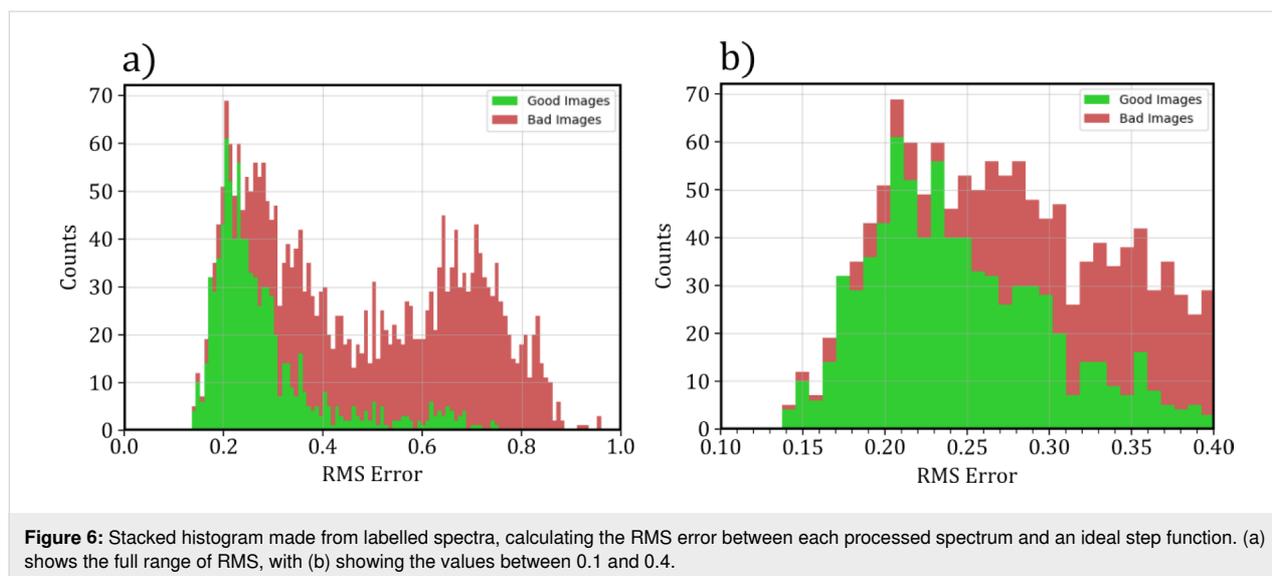
Using this method, the deterministic model was able to achieve an overall accuracy of 82%, a precision of 86%, and a recall of 53% when evaluated on the same test set used for the ML model.

Results and Discussion

Both the deterministic and ML-based models were tested on the same isolated test set of 521 spectra, with the final results as given in Table 2. Both models achieve very similar accuracies

and precisions; however, the recall for the deterministic model is significantly lower than in the ML model. In practise, this lower recall would mean that more tips which a human may classify as "good" would be misclassified as "bad", slowing down the overall tip preparation process. However, since the precisions of both the ML and deterministic models are very similar, the probability of an automated tip preparation script exiting with a "bad" tip would be roughly the same using either model. Since both models show comparable results in the precision of the final classification, the main advantage to using the deterministic model over ML is that the classifier requires much less labelled data for its creation, and hence is easier to apply to a new system.

Our ML accuracies are consistent with the prior work undertaken by Wang and colleagues [15]. Their highest ML-based classifier was able to achieve a precision of 84% and a recall of 74%, whereas our DM-based results are substantially better than the DM approach they trialled, which used correlation-based metrics and only achieved a final precision of 41% and a recall of 53% (no accuracies were given for this work).

Figure 6: Stacked histogram made from labelled spectra, calculating the RMS error between each processed spectrum and an ideal step function. (a) shows the full range of RMS, with (b) showing the values between 0.1 and 0.4.

Table 2: Table showing the accuracy, precision and recall obtained using deterministic and ML models to classify probe tips based on spectroscopy measurements.

	Deterministic	ML
accuracy	82%	86%
precision	86%	85%
recall	53%	70%

It should be noted, however, that Wang et al. attempted to make a classification between five different labels of spectra, whereas our dataset was split into a binary "good" or "bad" before training. In general, binary classifiers are expected to achieve higher accuracies as the differences between the two categories are less subtle.

Automated experiment discussion

In addition to automatically classifying the tip quality via STS on the Au(111) substrate, the script automatically located each SnPc molecule on the Au(111) surface, identified the different configurations of the molecule, and carried out lock-in $\frac{\mathrm{d}I}{\mathrm{d}V}$ measurements over the centre of each. In this section, we will discuss the STS data taken on the molecules, discuss the impact on the STS data quality due to the quality of the tip and highlight the advantages of automated assessment of tip quality and statistical categorisation of the data in STS.

Molecule location and identification

Once a series of Au(111) surface spectra had been obtained for use in the classifier training, the script continued to obtain STS measurements over the centre of each located SnPc molecule, whilst also distinguishing between the two configurations

(SnUp and SnDown) prior to measurement. The identification of each molecular configuration was determined using the CC method with two separate reference images as shown in Figure 1d,e.

For the final distinctions on the Au(111) surface, the CCR thresholds used for the SnUp and SnDown molecules were 0.983 and 0.980, respectively. Using these thresholds on a small test set of 13 images, the script was able to locate the positions of SnUp molecules with 100% accuracy and precision, whereas on the SnDown molecules the accuracy achieved was 95% with a precision of 96%.

Once located, lock-in $\frac{\mathrm{d}I}{\mathrm{d}V}$ curves were obtained over the central atom of each molecule located, using the same range of −1.5 V to 1.5 V as for the bare surface.

Note on SnPc switching instability

The adsorption of SnPc on coinage metal substrates is well studied, and the molecule is known to undergo an irreversible switch from the SnUp to the SnDown state on the Ag(111) surface [21] under hole injection. This is usually carried out intentionally by positioning the tip over the centre of an SnUp molecule, and applying a bias pulse via the tip of less than −1.9 V. On injection, the Sn atom within the molecule is transiently oxidised to Sn^{3+}, which favours a new position closer to the surface, where the atom binds to the Ag(111), at which point charge transfer from the substrate to the molecule will return it to its neutral state [21].

Whilst carrying out bias spectroscopy over these SnPc molecules, it was found that a switch could occasionally be induced, even if the bias range used did not reach −1.9 V. With moder-

ate negative bias (e.g., −1.5 V) a switch would commonly occur, and even with parameter adjustments to reduce the probability of switching (i.e. reduced integration times), there was still a chance that the switch would be induced, as can be seen in Supporting Information File 1, Figure S4.

In the automated experiment, an image would be taken, the molecules located based on this image, and then spectra would be obtained, saving each spectrum with a label indicating which configuration of molecule the spectrum was taken over. Unfortunately, due to this switching occurring over specifically the SnUp molecules, spectra labelled SnUp had the potential to be unreliably labelled. Additionally, it was observed that these switches could occur at the start of the measurement in the initial setting of the bias, or during the bias sweep itself, meaning identifying if a switch had occurred could not be reliably inferred from simple analysis of the STS spectrum. For this reason, the results shown in the next section will only consider spectra taken over the SnDown configuration, as the labelling of these was reliable.

Results

Using our STS spectra surface state classification method as described previously, we were able to process the entire dataset collected and to categorise the spectra taken on molecules as being acquired with either a "good" tip, or with a "bad" tip.
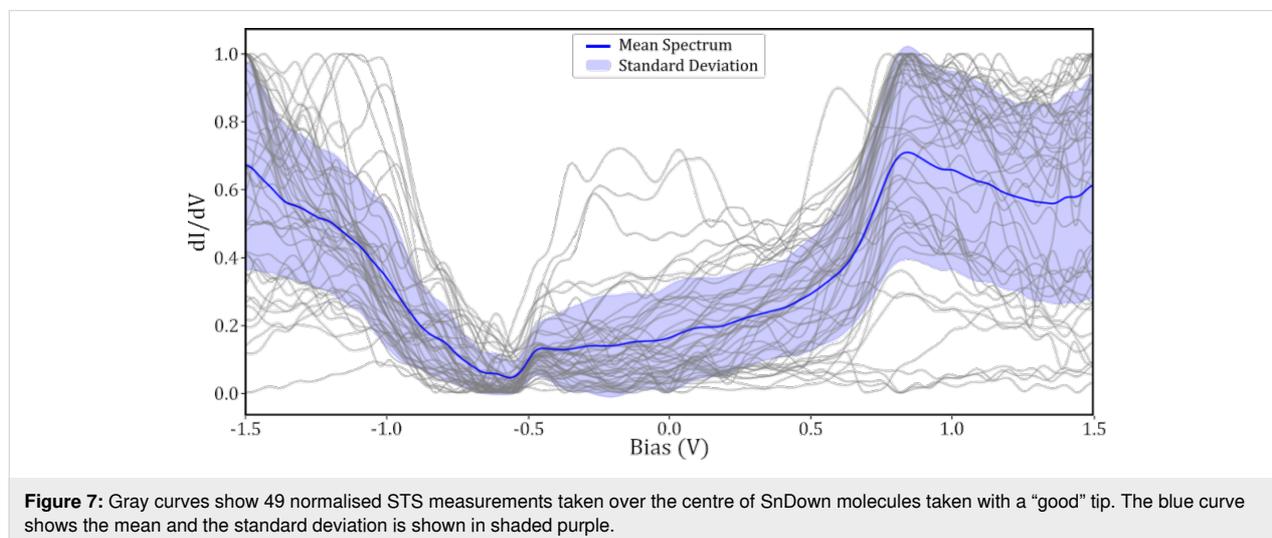
Throughout the data gathering, a total of 86 images (and so probe tips) passed the $I(z)$ and CCR pre-classification steps and were used to obtain molecular STS measurements. Of these 86 tips, 30 were classified as "good" and 56 as "bad", based on the analysis of the final STS spectra on Au(111). These 30 "good" tips were used to obtain spectra over a total of 49 SnDown mol-
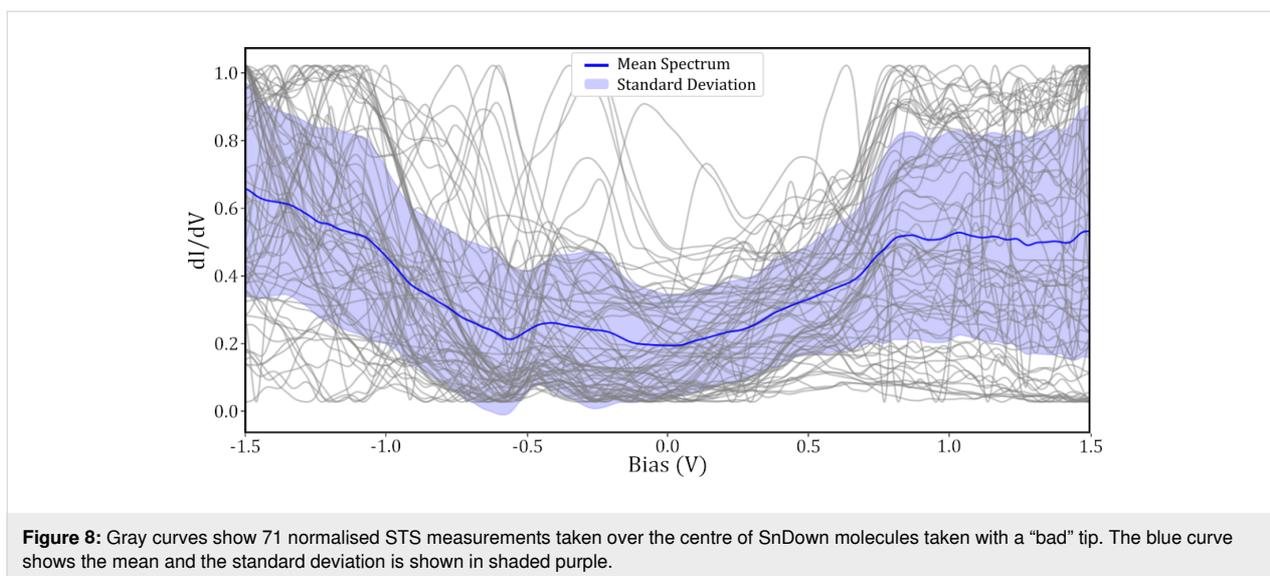
ecules. The mean of these curves is shown in Figure 7, where it can be clearly seen that there is a peak at roughly 0.8 V, which is not present in the bare surface spectra seen in Figure 3c.

Previous STS data of SnDown molecules show a clear increase in conductance at both −0.85 and 0.75 V when imaging at a setpoint of 50 pA [22]. These peaks in conductance correspond to the lowest unoccupied molecular orbital (LUMO) and highest occupied molecular orbital (HOMO), respectively. The cited work, however, was carried out on the Ag(111) surface, as opposed to Au(111) used here, which could explain the slight shift in the position of the HOMO from the literature value of 0.75 V to our consistent measurement of roughly 0.8 V. In addition, the work also suggests a current dependence on the position of the HOMO, which could be a contributing factor to the difference.

When comparing the "good" $\frac{dI}{dV}$ spectra taken over the molecules (Figure 7) to the binary "good" bare surface spectra (Figure 3c), the surface state and general increase in conductance at biases below −0.5 V can be seen in both. However, unlike the HOMO, which is clearly visible in the molecular $\frac{dI}{dV}$, the LUMO is not visible at the expected bias value of −0.85 V. This is possibly due to the peak being obscured by the shoulder in the negative portion of the spectra. Comparing the region between −1.5 and −0.5 V in both spectra, it can be seen that the mean curve for the molecular spectra contains an additional feature which is not present in the mean bare surface state spectrum. The features contained within this could contain the LUMO, but this is difficult to ascertain without completely deconvolving the tip and sample LDOS.

Figure 8 shows the mean and standard deviation of the $\frac{dI}{dV}$ spectra taken over SnDown molecules taken with a "bad" tip.

Figure 7: Gray curves show 49 normalised STS measurements taken over the centre of SnDown molecules taken with a "good" tip. The blue curve shows the mean and the standard deviation is shown in shaded purple.

Figure 8: Gray curves show 71 normalised STS measurements taken over the centre of SnDown molecules taken with a "bad" tip. The blue curve shows the mean and the standard deviation is shown in shaded purple.

By comparing this to Figure 7, it is clear that the HOMO peak at 0.8 V is much less prominent. In addition to this, the features throughout the spectra have become less evident. This clear difference between the molecular STS taken with a "good" and a "bad" tip, with the former showing expected features, reinforces that the tip state classification was successful in producing higher quality spectra, and highlights the importance of appropriately charactering the tip state before STS experiments.

A clear advantage to performing automated experiments with a large number of different tips and over a large number of molecules in different surface positions is that, statistically, variations in the spectra due to the changes in the tip or small changes in the molecular adsorption, will be averaged out, and better approach those from ensemble techniques. As can be seen in both Figure 7 and Figure 8, there is a substantial variation in the individual spectra around the mean curve. This is most likely due to variations in the quality of the tip or slight differences in the molecule itself. However, with a large enough aggregate of different tips, and taking STS measurements over different molecules, when averaged, these small variations should be dominated by the consistent features present in all the data. This can be seen particularly well in Figure 7, where some of the individual molecular spectra (grey curves), which here were all taken with tips classified as "good", show a featureless region around the HOMO, whilst others clearly show a strong peak. With individual spectra, it is possible that specific features in the $\frac{dI}{dV}$ could remain unobserved due to spurious problems with the tip.

For a human operator, taking a large number of spectra, with different, yet still "good" tips, on different instances of the same molecule is extremely time-consuming. However, with the en-

tire process being automated, this can be carried out very simply, and without any need for constant monitoring.

We note that while we collected data using both types of tip in order to highlight the differences in quality, in a real use case data collection would be improved by using the proposed method of classifying the tip based on a $\frac{dI}{dV}$ spectrum taken over the bare surface, such that the script would only take molecular spectra using probes which have been classified as "good" based on the surface state spectra. An example flow diagram with data taken from a generation run where the surface state spectrum was classified as "good" is shown in Figure 9.

Conclusion

We have shown that it is possible to perform a fully automated experiment, carrying out STS measurements over targeted areas of specific organic molecules, including the ability to modify and characterise the state of the tip, by both analysis of its spectroscopic characteristics and imaging quality, without the use of machine learning. This enables the ability to obtain a large number of spectra over various features on a surface, with a variety of characterised tip states, without the need for an operator to be present, and to perform statistical analysis of the spectroscopic data, via the automated labelling of the state and the location of the spectrum.

Importantly, the ability to carry this out without machine learning means that this method can be easily adapted to different adsorbate/substrate systems without the need for extensive data collection to train ML models. This methodology can aid in the rapid characterisation of new materials via automated probing of different features in a system, taking numerous mea-
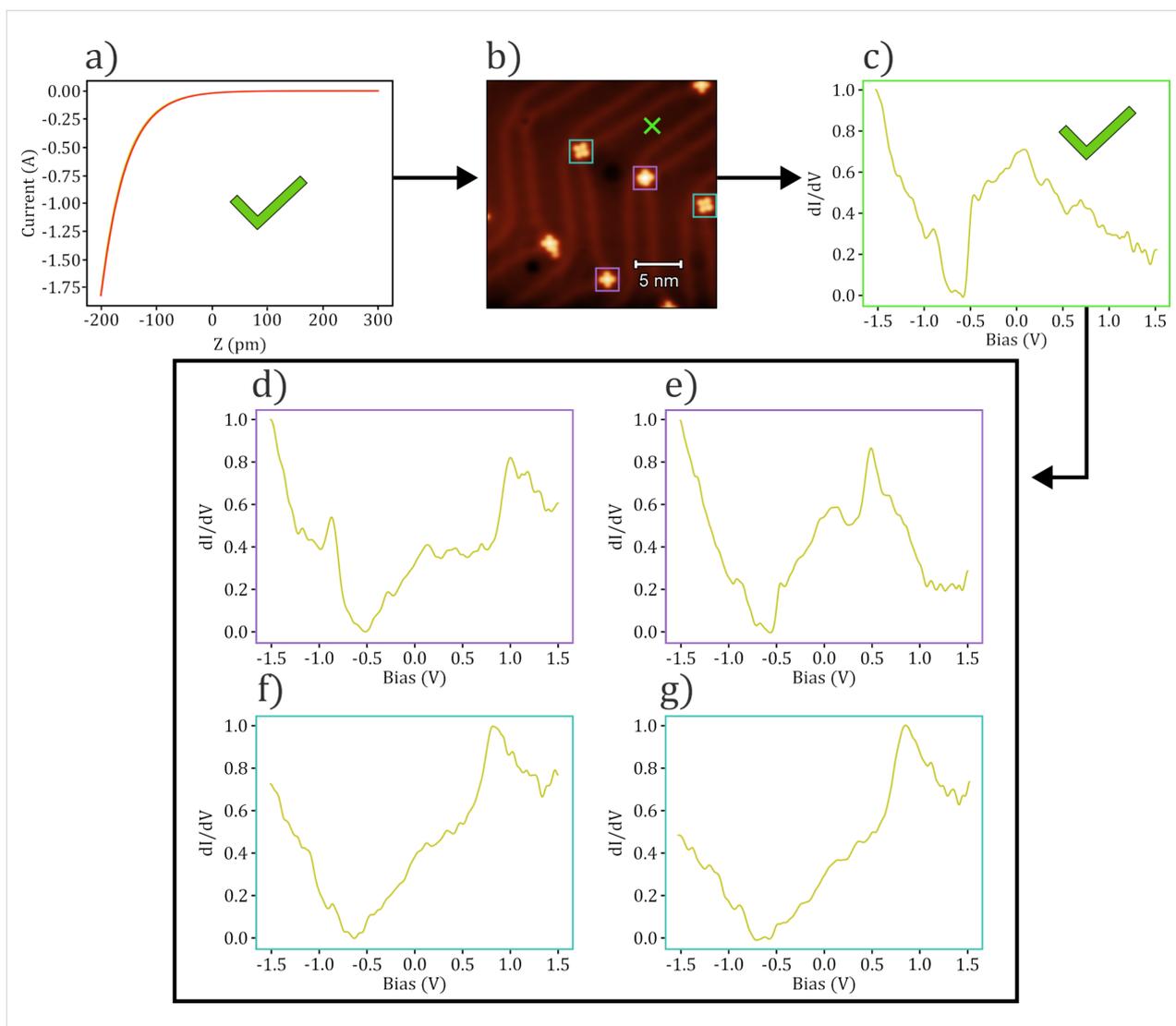
Figure 9: Example flow of an automated spectroscopy experiment taken over various SnPc molecules on the Au(111) surface. (a) An initial *I*(*z*) measurement is taken, where an exponential dependence is observed and so moves onto imaging, (b). The tip is then classified to be "good" based on imaging, and so a clean area of the substrate is located (marked by a green cross), where a surface STS measurement is taken, (c). This is then classified to be "good", at which point the various orientations of SnPc are located (SnUp in pink boxes and SnDown in blue boxes), where STS measurements are taken as shown in (d–g). (d) and (e) correspond to measurements taken over SnUp molecules, while (f) and (g) correspond to SnDown. The script would then change the tip and repeat the steps, over different areas, varying the tip after each set of STS measurements (formed through in situ tip preparation).

surements over different areas, only requiring an operator once the experiment is complete, to process the resultant data for analysis.

Supporting Information

Supporting Information File 1
Additional Information.
[https://www.beilstein-journals.org/bjnano/content/
supplementary/2190-4286-16-99-S1.pdf]

Author Contributions

Dylan Stewart Barker: conceptualization; data curation; formal analysis; investigation; methodology; project administration; resources; software; supervision; validation; visualization; writing – original draft; writing – review & editing. Adam

ORCID® iDs

Dylan Stewart Barker - https://orcid.org/0000-0001-5272-6266
Adam Sweetman - https://orcid.org/0000-0002-7716-9045

Data Availability Statement

Data generated and analyzed during this study is available from the corresponding author upon reasonable request.

Preprint

A non-peer-reviewed version of this article has been previously published as a preprint: https://doi.org/10.3762/bxiv.2025.28.v1

References

1. Rizzo, D. J.; Veber, G.; Cao, T.; Bronner, C.; Chen, T.; Zhao, F.; Rodriguez, H.; Louie, S. G.; Crommie, M. F.; Fischer, F. R. *Nature* **2018,** *560,* 204–208. doi:10.1038/s41586-018-0376-8
2. Gross, L.; Moll, N.; Mohn, F.; Curioni, A.; Meyer, G.; Hanke, F.; Persson, M. *Phys. Rev. Lett.* **2011,** *107,* 086101. doi:10.1103/physrevlett.107.086101
3. Repp, J.; Meyer, G.; Stojković, S. M.; Gourdon, A.; Joachim, C. *Phys. Rev. Lett.* **2005,** *94,* 026803. doi:10.1103/physrevlett.94.026803
4. Repp, J.; Meyer, G.; Paavilainen, S.; Olsson, F. E.; Persson, M. *Science* **2006,** *312,* 1196–1199. doi:10.1126/science.1126073
5. Bartels, L.; Meyer, G.; Rieder, K.-H. *Appl. Phys. Lett.* **1997,** *71,* 213–215. doi:10.1063/1.119503
6. Lagoute, J.; Kanisawa, K.; Fölsch, S. *Phys. Rev. B* **2004,** *70,* 245415. doi:10.1103/physrevb.70.245415
7. Liljeroth, P.; Repp, J.; Meyer, G. *Science* **2007,** *317,* 1203–1206. doi:10.1126/science.1144366
8. Tsukada, M.; Kobayashi, K.; Isshiki, N. *Surf. Sci.* **1991,** *242,* 12–17. doi:10.1016/0039-6028(91)90234-j
9. Kwapiński, T.; Jałochowski, M. *Surf. Sci.* **2010,** *604,* 1752–1756. doi:10.1016/j.susc.2010.06.026
10. Passoni, M.; Donati, F.; Li Bassi, A.; Casari, C. S.; Bottani, C. E. *Phys. Rev. B* **2009,** *79,* 045404. doi:10.1103/physrevb.79.045404
11. Garcia, N.; Binh, V. T.; Purcell, S. T. *Surf. Sci. Lett.* **1993,** *293,* L884–L886. doi:10.1016/0167-2584(93)90226-9
12. Palotás, K.; Hofer, W. A.; Szunyogh, L. *Phys. Rev. B* **2011,** *83,* 214410. doi:10.1103/physrevb.83.214410
13. Andreev, T.; Barke, I.; Hövel, H. *Phys. Rev. B* **2004,** *70,* 205426. doi:10.1103/physrevb.70.205426
14. Thomas, J. C.; Rossi, A.; Smalley, D.; Francaviglia, L.; Yu, Z.; Zhang, T.; Kumari, S.; Robinson, J. A.; Terrones, M.; Ishigami, M.; Rotenberg, E.; Barnard, E. S.; Raja, A.; Wong, E.; Ogletree, D. F.; Noack, M. M.; Weber-Bargioni, A. *npj Comput. Mater.* **2022,** *8,* 99. doi:10.1038/s41524-022-00777-9
15. Wang, S.; Zhu, J.; Blackwell, R.; Fischer, F. R. *J. Phys. Chem. A* **2021,** *125,* 1384–1390. doi:10.1021/acs.jpca.0c10731
16. Rashidi, M.; Wolkow, R. A. *ACS Nano* **2018,** *12,* 5185–5189. doi:10.1021/acsnano.8b02208
17. Gordon, O.; D'Hondt, P.; Knijff, L.; Freeney, S. E.; Junqueira, F.; Moriarty, P.; Swart, I. *Rev. Sci. Instrum.* **2019,** *90,* 103704. doi:10.1063/1.5099590
18. Krull, A.; Hirsch, P.; Rother, C.; Schiffrin, A.; Krull, C. *Commun. Phys.* **2020,** *3,* 54. doi:10.1038/s42005-020-0317-3
19. Barker, D. S.; Blowey, P. J.; Brown, T.; Sweetman, A. *ACS Nano* **2024,** *18,* 2384–2394. doi:10.1021/acsnano.3c10597
20. Hofer, W. A.; Garcia-Lekue, A. *Phys. Rev. B* **2005,** *71,* 085401. doi:10.1103/physrevb.71.085401
21. Wang, Y.; Kröger, J.; Berndt, R.; Hofer, W. A. *J. Am. Chem. Soc.* **2009,** *131,* 3639–3643. doi:10.1021/ja807876c
22. Toader, M.; Hietschold, M. *J. Phys. Chem. C* **2011,** *115,* 3099–3105. doi:10.1021/jp111478v

License and Terms

Mechanical property measurements enabled by short-term Fourier-transform of atomic force microscopy thermal deflection analysis

Thomas Mathias[1], Roland Bennewitz[2] and Philip Egberts[*1]

Abstract

Contact resonance atomic force microscopy (CR-AFM) has been used in many studies to characterize variations in the elastic and viscoelastic constants of materials along a heterogeneous surface. In almost all experimental work, the quantitative modulus of the surface is calculated in reference to a known reference material, rather than calculated directly from the dynamics models of the cantilever. We measured the cantilever displacement with very high sampling frequencies over the course of the experiment and captured its oscillations that result from thermal energy. Using short-term Fourier transformations, it was possible to fit the thermal resonance peak of the normal displacement to track the frequency and Q-factor of the cantilever during an experiment, using a similar process to that used to calibrate the normal bending stiffness of cantilevers. With this quantitative data, we have used the dynamic mechanics models relating the contact stiffness of the tip/cantilever pressing into a surface with the oscillation frequency of the cantilever and show that they did not accurately model the experiment. Several material combinations of tip and sample were examined; tip size and cantilever stiffness demonstrate that existing models cannot capture the physics of this problem. While concrete solutions to use analytical models to interpret CR-AFM data have not been found, a possible solution may include revisiting the analytical model to capture a potentially more complex system than the current model, improved matching the cantilever/sample stiffness to obtain a larger variation in contact stiffness with frequency, or investigating the use of higher-order modes that may achieve this improved match.

Introduction

Atomic force microscopy (AFM) has become an indispensable tool for imaging the surface topography on a variety of surfaces [1]. Since the invention of the AFM [2], several other modes of AFM have been developed, including friction force microscopy [3], tapping mode AFM [4], and contact resonance AFM (CR-AFM) [5], each providing unique advantages or insights into a

surface and the materials that comprise it. Alongside the developments of the experimental technique, there have been a number of modeling techniques created that can be used to bring physical values or interpretation to the data that is collected by the AFM, allowing operators of the technique to compare their measurements across fields [6].

CR-AFM is a technique that was established in 2008, allowing for the measurement of mechanical properties (elastic modulus and viscoelastic modulus) of surfaces [5]. It is particularly useful for the measurement of heterogeneous surfaces, characteristic of composite and biological materials, where understanding the interplay between microstructure and mechanical properties of the constituent materials is critical for the performance of the overall structure. Analytical models for interpreting the vibrational modes of cantilevers were developed prior to the invention of the technique [7,8]. This model or variations of it are often presented in manuscripts to explain the interpretation of experimental data, but are not used to bring physical meaning to the experimental data. Instead, in almost every example in the literature, the frequency variation is normalized to what is measured on a surface having known mechanical properties [5,9,10].

Alongside the development of CR-AFM and the analytical models used to describe the technique, spectral analysis of the thermal motion in the deflection of AFM cantilevers has shown promise as a lower-cost, less equipment-intensive mechanism to access the dynamic and time-evolving oscillatory characteristics of the cantilever [11-16]. In these techniques, the cantilever deflection signal is acquired at rates several times greater than the first normal resonant frequency (typically greater than 1 MHz) for several seconds, as the cantilever is approached, and the tip is pressed against, and finally removed from, a surface. In a significant number of studies, a Fourier transform, or transformation of the time-based AFM deflection into the frequency domain is conducted. In the majority of studies examining the thermal oscillations of AFM cantilevers, the cantilever's displacement is measured for a specific length of time and then converted to frequency space over the entire length of the measurement [14-16]. This calculation results in a single measurement of the cantilever's oscillation frequency and other oscillation parameters, but can also result in high frequency/spectral resolution that can allow for the determination of quantifiable results for parameters such as elastic modulus or viscoelastic properties when the duration of the cantilever's thermal motion was measured for sufficiently long times [15]. However, the drawback of this type of measurement is that, with such infrequent measurements of the cantilever's oscillation characteristics, it is difficult to measure mechanical properties of heterogeneous surfaces as the cantilever is scanned over the surface,

or to measure how mechanical properties of the surface evolve with time as the cantilever is pressed against the surface. Furthermore, the analysis assumes that the cantilever's oscillation characteristics are static over the measurement period, which often is not the case. To solve this issue, wavelet transformations of the AFM cantilever's deflection signal have been conducted, allowing for several frequency spectra at defined time intervals to be calculated over the course of the experiment [11-13].The drawback to most wavelet transforms applied to analyze AFM thermal deflection signals is that these measurements suffer from insufficient spectral resolution, which limits the ability to accurately quantify cantilever oscillation characteristics, as well as making it difficult to obtain quantitative measurements from the frequency of the AFM cantilever's bending mode.

In this manuscript, we bring together the analytical models that describe cantilever oscillations in AFM experiments where a tip is oscillated and pressed into contact with a solid surface [7,8] with the spectral analysis of the thermal motion of the cantilever using short-term Fourier transforms (STFTs). Similar to wavelet transforms, STFTs allow one to calculate the time-varying spectra of the cantilever's deflection signal over the measurement time with a simpler way of controlling the spectral/frequency resolution, supporting the end goal of quantifiable mechanical property data. Here, we observe the thermal oscillations of the AFM cantilever rather than an externally excited cantilever. An advantage to observing and analyzing the thermal oscillations of the cantilever is that the oscillations of the cantilever have sub-angstrom amplitudes regardless of if the tip is in contact with the sample or far from the surface. When the tip is in contact with the surface, these small oscillations of the AFM cantilever are much smaller than atomic bonds in our materials, which then can be interpreted as a small perturbation to the system that is examined. We also avoid disturbance of the medium surrounding the sample, as occurs with piezoacoustic excitation of the cantilever, without requiring expensive modification of our existing AFM system. Finally, by avoiding the use of a phase-locked loop to track the frequency of the cantilever oscillation and rather using STFTs to calculate time-varying frequency spectra, we are able to monitor the oscillation of the cantilever as it transitions from free out-of-contact to in-contact, changing the oscillation mode of the cantilever. Additionally, spectral analysis allows for the measurement and tracking of all resonant modes simultaneously, which would otherwise require a separate phase-locked loop for each mode to be tracked.

To examine and validate the use of spectral analysis of the thermal motion of AFM cantilevers as an alternative approach to CR-AFM, we conducted AFM experiments on well-characterized surfaces, such as highly ordered pyrolytic graphite

(HOPG), using silicon cantilevers with integrated probes. To examine the time evolution of the AFM cantilever's oscillatory modes during an experiment, STFTs, rather than wavelet transforms, of the thermal motion of the AFM cantilever were calculated. Once calculated, the resonant peak corresponding to the cantilever's first oscillatory mode was fit, yielding the time-evolving parameters of the AFM cantilever be to tracked over the course of the experiment, such as the resonant frequency. CR-AFM models were used to determine the size of the tip–sample contact, assuming the relevant material parameters of the system examined. Finally, the same experiment and data analysis was performed with other substrates and AFM tip materials to further explore the analytical CR-AFM models.

Methods
Experimental design
An Agilent Keysight 5500 AFM was used in all experiments with measurements conducted under ambient laboratory conditions of 20–40% humidity. Four samples were analyzed in the experiments, namely, a silicon wafer, freshly-cleaved HOPG, poly(ethylene oxide) (PEO), and polydimethylsiloxane (PDMS). The mechanical properties of these samples are provided in Table 1.

Table 1: Mechanical properties of the examined samples. Values for silicon, HOPG, and platinum are from [17], [18], and [19], respectively. The values for PEO and PDMS were measured using a Hysitron Premier Nanoindenter.

Material	Young's modulus (GPa)	Poisson's ratio
silicon	160	0.3
HOPG	20	0.25
platinum	140	0.38
PEO	*0.22 ± 0.03*	0.5
PDMS	*0.0025 ± 0.0002*	0.45

Silicon wafers were ultrasonicated in acetone and ethanol for 10 min each. HOPG samples were cleaved using the Scotch tape method within 30 min of beginning an experiment. Finally, the PEO and PDMS samples were not surface-treated following their polymerization/deposition. The topography of the surface was measured before acquiring a force-versus-distance measurement to ensure that these measurements were acquired on clean and flat regions of the substrate. To observe how the resonant frequency of the AFM cantilever changes as the attached tip is pressed against a substrate, force-versus-distance measurements were conducted. In these measurements, the sample was moved up and down at a rate of approximately 100 nm·s^{-1} while recording the cantilever deflection over the course of the measurement. In addition to the AFM's own control software

measuring the deflection of the cantilever and moving the sample during the experiment, the cantilever deflection was measured by a National Instruments BNC box (NI-USB-6341) via an unfiltered connection direct from the photodetector at a sampling rate of 2.0 MHz and for a duration of 1 s of the experiment, unless otherwise noted. The data from this instrument will be referred to in the paper as the "high-sample rate" data.

Three types of uncoated cantilevers were used all experiments, that is, soft cantilevers with an integrated tip (Nanosensors PPP-CONT), soft tipless cantilevers (Nanosensors TL-CONT), and harder cantilevers with an integrated tip (Nanosensors PPP-NCL). The soft cantilevers have a nominal stiffness in the normal bending direction of 0.2 N·m^{-1}, and the hard cantilevers have a nominal stiffness of 40 N·m^{-1}. For each cantilever used, the spring constant of the cantilever in the normal bending direction was determined through the Sader method [20], with the plan-view dimensions and the setback of the tip from the end of the cantilever measured in an optical microscope. To convert the voltage signal measured by the photodetector, the slope of the force versus distance curve generated from the manufacturer's software was determined, having a unit of volts per meter. Four different tip materials were used in experiments, namely, conventional silicon cantilevers (Nanosensors PPP-CONT), conductive diamond-coated probes (Nanosensors CDT-CONTR), platinum silicide-coated probes (Nanosensors PtSi-CONT), and borosilicate glass colloids (Sigma-Aldrich 440345-100G) attached to the tipless cantilevers (Nanosensors TL-CONT). The borosilicate glass colloids had a diameter of 8–11 μm and an elastic modulus of 60 GPa.

Data analysis
Following completion of experiments, post processing of the high-sample rate data was performed. This data was windowed into segments of data having lengths of 2^N in number of data points, with N ranging from 10 to 20. These windowed segments were convolved with the Hanning window to reduce spectral leakage. For each window, a Fourier transform was calculated and stored. Subsequently, for each window generated, the resonant peak of the first normal mode was fitted using Equation 1,

$$A(f) = \frac{k_B T f_n^3}{\pi Q_n D_n \left(f^2 - f_n^2\right)^2 + \left(\dfrac{ff_n}{Q_n}\right)^2} \cdot 10^{18} + y_0, \tag{1}$$

where f is the frequency, T is the temperature, $k_B = 1.3806 \times 10^{-23}$ m^2·kg·s^{-2}·K^{-1} is Boltzmann's constant, Q_n is the quality factor of the cantilever for the n-th mode, D_n is the stiffness of the n-th oscillation mode, and y_0 is an offset value

[21]. Fits of these resonant peaks using the non-linear least squares method yielded the parameters f_n, Q_n, and D_n. To ensure accurate fits to the resonance peak, the window size N, impacting the frequency resolution (f_Δ) of the calculated Fourier transform, was carefully chosen to ensure that β in Equation 2 was much larger than 1 [22]:

$$\beta = \frac{\pi}{2Q_n} \frac{f_n}{f_\Delta}. \tag{2}$$

Fitting of the first resonant peak of the cantilever in contact with the surface during the force-versus-distance measurement thus provides the evolution of the f_1, Q_1, and D_1 values as functions of time during the experiments. These values can be related to the displacement of the sample, force, or other parameters that are time-averaged over the window size.

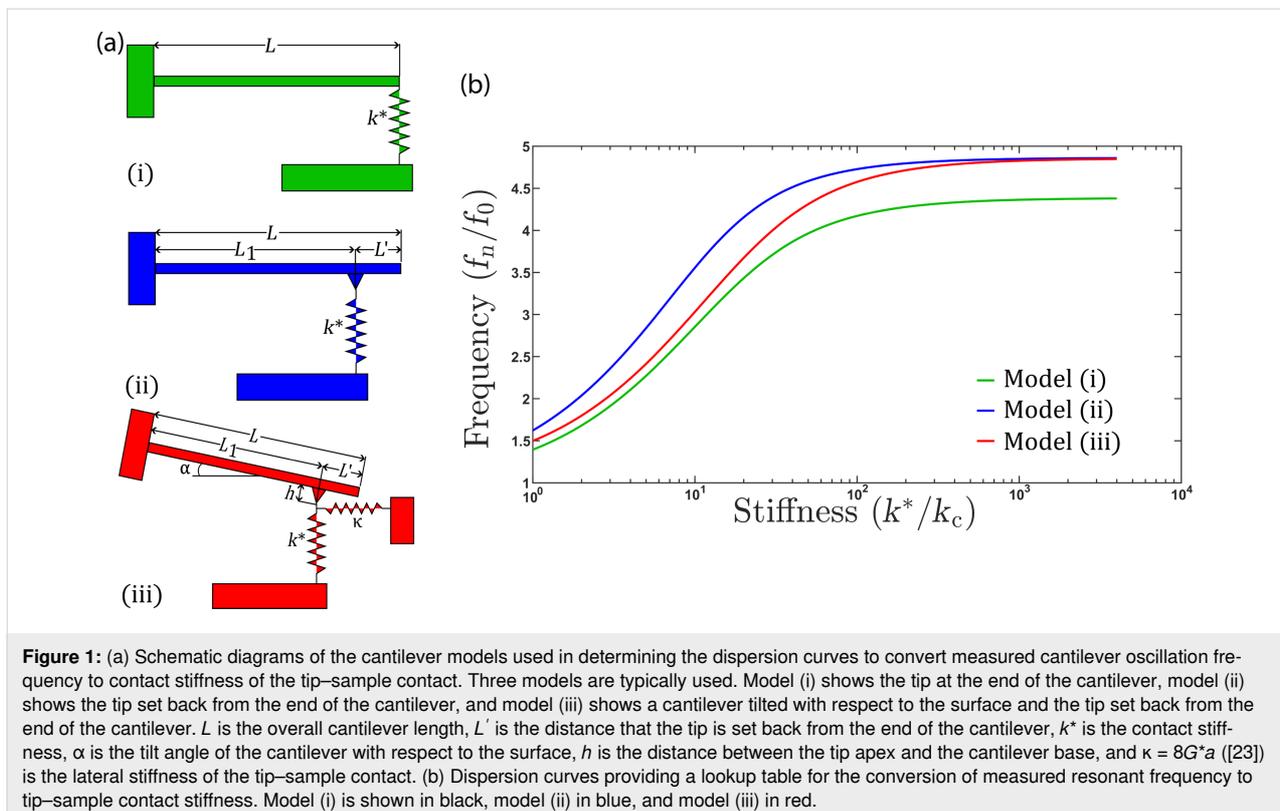## Analytical models of cantilever dynamics

Several analytical models of cantilever dynamics have been developed, with the basis of most models originating from the work by Rabe et al. [7], and are schematically shown in Figure 1a(i) and Figure 1a(ii). More advanced models that include the tilt angle of the cantilever relative to the surface [23], to better reflect the typical 12.5° or 22.5° angles of the cantilever relative to the surface, have been subsequently de-

veloped and are shown in Figure 1a(iii). To relate the oscillation frequency of the cantilever to the contact stiffness, equations of motion for the schematic have been developed in [7,23] and are provided in Supporting Information File 1 for reference. These equations are used to develop the dispersion curve shown in Figure 1b. The dispersion curve shows how the measured frequency changes as the contact becomes stiffer, which occurs in the previously described experiments when the tip is pressed against the surface with a larger normal force. Typically, CR-AFM experiments are conducted at a constant normal force (increasing the tip–sample contact size); thus, changes in the contact stiffness result from variations in the elastic modulus, E, along the surface. The relation between elastic modulus, contact size, and contact stiffness is found in Equation 3 [24],

$$k^* = 2aE^*, \tag{3}$$

$$\frac{1}{E^*} = \frac{1 - \nu_{sample}^2}{E_{sample}} + \frac{1 - \nu_{tip}^2}{E_{tip}^*}, \tag{4}$$

where a is the size of the contact between the tip and sample, E^* is the reduced elastic modulus defined in Equation 4, ν is the Poisson ratio of tip or sample, and E is the elastic modulus of tip or sample.

Figure 1: (a) Schematic diagrams of the cantilever models used in determining the dispersion curves to convert measured cantilever oscillation frequency to contact stiffness of the tip–sample contact. Three models are typically used. Model (i) shows the tip at the end of the cantilever, model (ii) shows the tip set back from the end of the cantilever, and model (iii) shows a cantilever tilted with respect to the surface and the tip set back from the end of the cantilever. L is the overall cantilever length, L' is the distance that the tip is set back from the end of the cantilever, k^* is the contact stiffness, α is the tilt angle of the cantilever with respect to the surface, h is the distance between the tip apex and the cantilever base, and κ = $8G^*a$ ([23]) is the lateral stiffness of the tip–sample contact. (b) Dispersion curves providing a lookup table for the conversion of measured resonant frequency to tip–sample contact stiffness. Model (i) is shown in black, model (ii) in blue, and model (iii) in red.
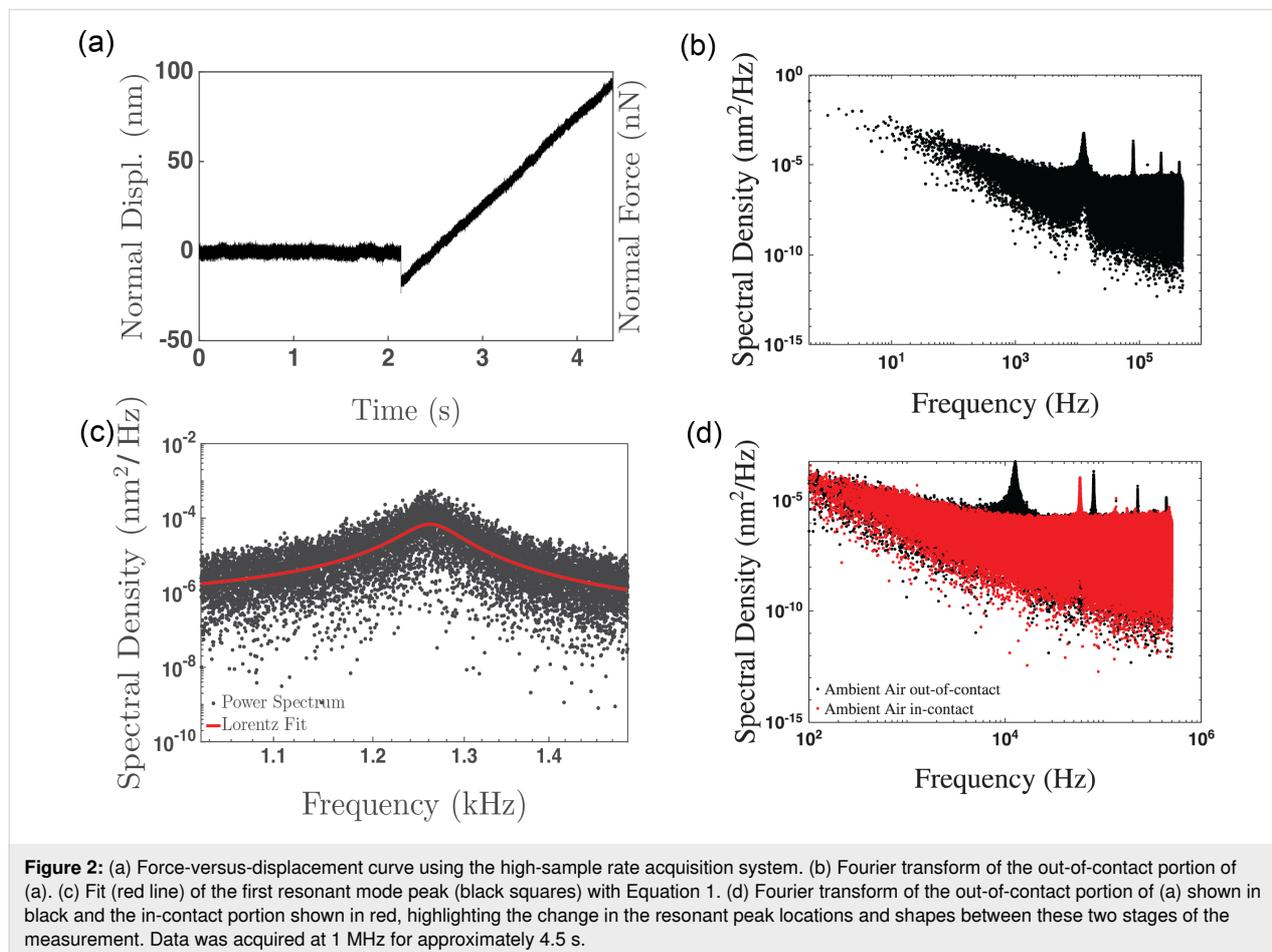
Results and Discussion

Figure 2a shows an exemplary force-versus-distance measurement acquired with the high-sample rate acquisition system for a soft silicon cantilever on a HOPG substrate. Both the normal force and the cantilever displacement values are shown as most AFM studies report normal force values, but the power spectrum calculation requires the cantilever displacement values. Figure 2b shows the calculated Fourier transform/power spectrum of the cantilever displacement in the out-of-contact portion of Figure 2a, that is, the data acquired from approximately 0 to 2 s of the experiment. The power spectrum clearly shows the first four oscillation modes of the cantilever, with the first oscillation mode having the largest amplitude. Figure 2c shows the quality of the fit obtained using Equation 1 to the first oscillation mode, yielding values of $f_1 = 12.627 \pm 0.003$ kHz, $Q_1 = 19.84 \pm 0.20$, and $D_1 = 25.67 \pm 0.02$ mN·m^{-1}. We note that the fit value obtained from Equation 1 is not the same value as the one obtained using the Sader method (74.3 mN·m^{-1} for this cantilever in Figure 2) [20]. Similar observations were made for the other cantilevers used in the experiments conducted within this paper, with the difference between the value of D_1 and the normal spring constant calculated using the Sader method ranging between a factor of 2 and 10. This difference is likely a result of the plan-view dimensions of the cantilevers having dimensions beyond the 10% variation of the manufacturer's specifications, observed in other experiments we have conducted outside this study. Viscous damping from the ambient environment is not accounted for in Equation 1 and may also be responsible for a small percentage of the difference between the two calculations of the spring constants. However, our results highlight that the measurement of the cantilever's plan-view dimensions and using these dimensions in the determination of the Sader spring constant or other calculations of the normal spring constant are important. Finally, it has been demonstrated that the Sader method can consistently show a difference compared with the thermal noise method used above, particularly for soft cantilevers as used in this study [25]. We take the Sader spring constant, which has been widely used in other studies and is less sensitive to variations in the calculated cantilever sensitivity [25], as the spring constant of all cantilevers in the calculations in subsequent sections of this manuscript.

Figure 2d shows two power spectra, the black spectrum calculated from the time ranging from 0 to 2 s, and the second in red

Figure 2: (a) Force-versus-displacement curve using the high-sample rate acquisition system. (b) Fourier transform of the out-of-contact portion of (a). (c) Fit (red line) of the first resonant mode peak (black squares) with Equation 1. (d) Fourier transform of the out-of-contact portion of (a) shown in black and the in-contact portion shown in red, highlighting the change in the resonant peak locations and shapes between these two stages of the measurement. Data was acquired at 1 MHz for approximately 4.5 s.

from the time ranging between 2.5 and 4.5 s. These two spectra highlight the change in the location and shape of the normal resonant peaks for the cantilever from when the cantilever was out of contact to when it was in contact. We are able to estimate the values of the various modes, as Rabe et al. showed that the value of $f_n/(k_nL)^2$ is a constant for the cantilever, which also allows us to distinguish between higher-order oscillatory modes of the cantilever and pinning of the free end of the cantilever [7]. With the first resonant peak out of contact having a center frequency of 12.62 kHz and using model (i) to estimate the location of subsequent resonant peaks, the expected second resonant mode of a free cantilever would be approximately 79.1 kHz, in contrast to an expected frequency of 55.3 kHz in the first resonant mode if the end of the cantilever was completely pinned. The measured value of the cantilever resonant frequency when the tip was pressed into the surface was 58.15 kHz, which is much closer to the expected value of pinned cantilever than the second resonant mode. Beyond identifying and fitting the first pinned mode of oscillation, it is also possible to observe several of the higher modes within the in-contact power spectrum compared with the out-of-contact spectrum. Finally, we note that the full width at half maximum increases slightly for the first oscillation mode when the cantilever makes contact with the surface, but shows significant scatter during the force curve measurement, making a statement regarding the variation of the Q-factor difficult with the present analysis technique.

Figure 3a shows the variation of the frequency of the first normal mode as a function of normal force during the in-contact period of the force curve. A sub-linear variation is observed with increasing applied normal force. Figure 3b shows the variation of the quality factor with normal force, simultaneously determined with the frequency of the first normal oscillatory mode. Here, the variation in the Q-factor is less clear than for the resonant frequency. An initial increase is observed, which plateaus around 0 nN applied force. However, significant scatter in the Q-factor is observed, in particular compared with the variation in the frequency of the first normal oscillatory mode. Significantly more scatter is observed for the last fit parameter, D_1, which, in the case of a free oscillation, represents the spring constant of the single-harmonic-oscillator mode. Additionally, the physical meaning of D_1 is less clear when the tip/cantilever is in contact with the surface than when it is free. Thus, how D_1 varies over the course of the experiment has been included in Supporting Information File 1, Figure S1 for completeness but is not further analyzed within the manuscript.

Figure 4 shows the dispersion curves generated for the three cantilever models, with the data obtained from all material com-
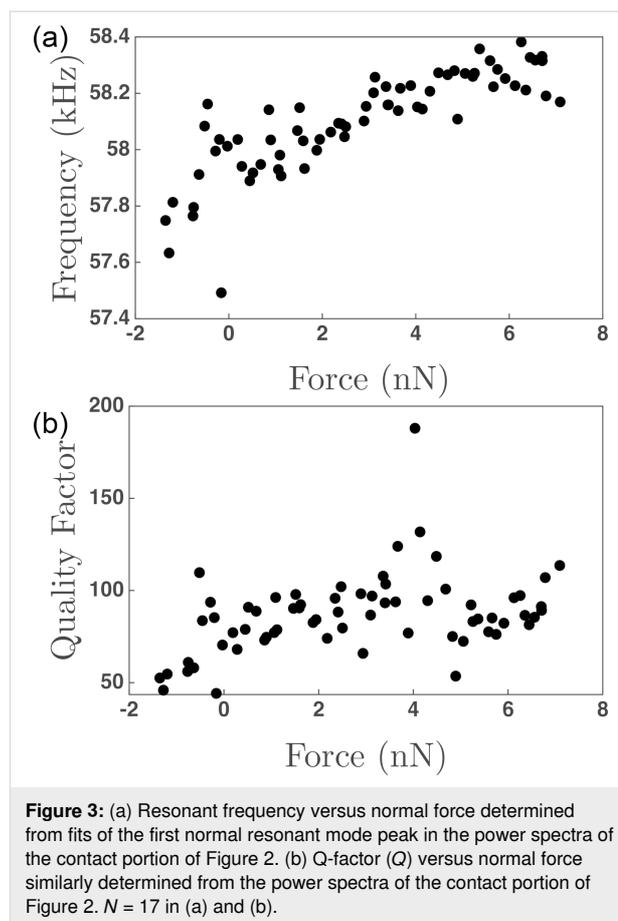
Figure 3: (a) Resonant frequency versus normal force determined from fits of the first normal resonant mode peak in the power spectra of the contact portion of Figure 2. (b) Q-factor (*Q*) versus normal force similarly determined from the power spectra of the contact portion of Figure 2. *N* = 17 in (a) and (b).

binations evaluated in this study in each of the models. For example, Figure 4 shows that for soft materials, such as the Si–PDMS combination (silicon cantilever and PDMS substrate), all three models can be used to translate the oscillation frequency variation into a contact stiffness. However, for harder materials, such as Si–HOPG or diamond–Si, model 1 (Figure 1a(i)) has a frequency response in the dispersion curve that saturates at a reduced frequency (f_1/f_0) that is lower than the measured reduced frequency. We note that the PtSi–PEO combination showed a high frequency response, which is unexpected for a soft material such as PEO. We attribute this to a very high elastic modulus measured a low penetration depths in PEO samples [26]. Model 3 (Figure 1a(iii))) in this case does not saturate as early, but the plateau in the dispersion curve translates into a wide variation in contact stiffness values assigned for very small changes in frequency. Thus, model 3 does not have sufficient accuracy for contact stiffness determination for these material systems. Model 2 (Figure 1a(ii)) slightly improves upon this issue, with the dispersion curve shifted more significantly to lower values of contact stiffness and a higher frequency plateau than model 1, such that improved accuracy in translating the measured cantilever frequency to a stiffness is possible. The additional benefit of model 2
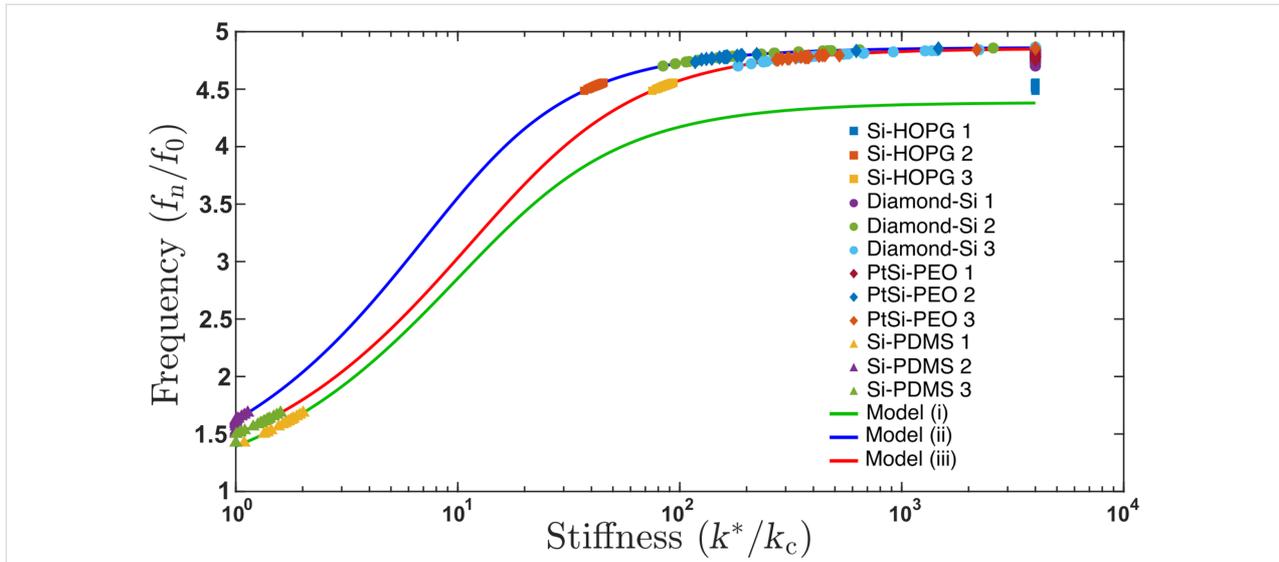
Figure 4: Experimental data for four sample combinations tested (silicon tips on HOPG, diamond-coated tips on silicon, silicon tip on PEO, and silicon tip on PDMS) plotted for the three cantilever models.

over model 3 is that the model is much simpler and a friction coefficient, κ, between the tip/colloid and the substrate does not need to be assumed or calculated to generate the dispersion curve. However, as shown in Figure 1, the value of κ does not significantly change the positioning of the dispersion curve.

It has been suggested that careful selection of the cantilever stiffness is required when performing CR-AFM measurements [27]. Within the context of Figure 1, increasing the value of k_c, while keeping all other material parameters constant, should shift the measured reduced frequency (f_n/f_0) left or to lower values, to a region of the dispersion curve where a more linear variation between frequency and stiffness is expected. In other words, with a very soft cantilever and a very hard sample, the saturated variation of the reduced frequency changes very little with contact stiffness, k^*. We attempted to use cantilevers with a higher k_c value, ranging from 20 to 40 N·m^{-1}, and perform the same analysis as done previously. As shown in Supporting Information File 1, Figure S2, the issue becomes that, with the stiffer cantilever, the magnitude of the resonance peak for the first normal mode, particularly when the tip contacts the surface, is much smaller than for the softer cantilevers. At this time, the base noise of our AFM system and electronic sampling of the deflection signal is too large to automate the fitting of the resonance peak with reasonable successful fits, limiting the application of our method to cantilevers having a lower spring constant.

With the frequency data translated to contact stiffness, the Derjaguin–Muller–Toporov (DMT), Johnson–Kendall–Roberts (JKR), and Carpick-Ogletree-Salmeron (COS) contact

mechanics theories can be used to relate tip size, elastic modulus, and normal force. The relationship between contact stiffness, k^*, and normal force for the DMT, JKR, and COS models are then given by Equation 5, Equation 6, and Equation 7, respectively [24,28]:

$$k^*_{\text{DMT}} = 2E^* \left(\frac{R\left(3F + F_a\right)}{4E^*} \right)^{1/3}, \qquad (5)$$

$$k^*_{\text{JKR}} = 2E^* \left(\frac{3R(3F + 2F_a + \sqrt{4FF_a + 4F_a^2})}{2E^*} \right)^{1/3}, \qquad (6)$$

$$k^*_{\text{COS}} = 2E^* \left(\frac{\hat{a}_o}{\hat{F}_c^{1/3}} \right) \left(\frac{R(3F + F_a)}{4E^*} \right)^{1/3}, \qquad (7)$$

where R is the tip radius and F_a is the adhesive force. In Equation 7, we use the transition parameter λ to bridge the two contact streams. We then denote

$$\hat{a}_o = a \cdot \left(\frac{E^*}{\pi\gamma R^2} \right)^{1/3}$$

and

$$\hat{F}_c = \frac{F}{\pi\gamma R^2},$$

and γ is the work of adhesion, which can be calculated from the pull-off force in experiments. We calculated the Tabor parameter, μ_T, and the transition parameter, λ, for each material pair, which are given in Table 2. Rather than fitting data with Tabor parameters smaller than 0.1 with the DMT model and greater than 5.0 with the JKR model [29], we use the COS model, which has been shown to more accurately fit contacts having material properties between the DMT and JKR extremes. The fits to the experimental data are provided in Figure 5. In each case, all materials for tip and substrate were pure amorphous/ polycrystalline and, thus, had isotropic elastic moduli across the surface. Further, these materials were chosen as they are well characterized in the literature and often used in AFM experiments. Thus, rather than fitting the elastic modulus of the substrate, we took the elastic modulus values from literature for tip

and substrate and fitted the radius of the probes using contact mechanics models. In many cases, the fits did not converge, so we used the best fit values near convergence and plotted the expected model variations for k^* and normal force in Figure 5 with a red dashed line, with the experimental data overlaid in the graph. In each case, as stated previously, either the fits did not converge or yielded unphysical values for the tip radius. More specifically, Figure 5a and Figure 5b show converging fits to the experimental data, resulting in fits of 0.02580 ± 0.00002 nm and 17.42 ± 0.13 nm, respectively. Figure 5c and Figure 5d show results where the fits did not converge, with the experimental results clearly not following the predicted trend for contact stiffness by the MG model. In these cases, the radii estimated for the fits shown in Figure 5c and Figure 5d were 0.0011 and 0.0920 nm, respectively. This is a result of the very

Table 2: Tabor and transition parameters calculated for each material pairing.

| Probe material	Sample material	Tabor parameter μ_T	transition parameter λ
silicon	HOPG	0.4567	0.5284
diamond	silicon	0.1600	0.1851
glass colloid	HOPG	7.1923	8.3214
steel colloid	silicon	1.8955	2.1931
PtSi	PEO	3.1966	3.6985
silicon	PDMS	283.961	328.543
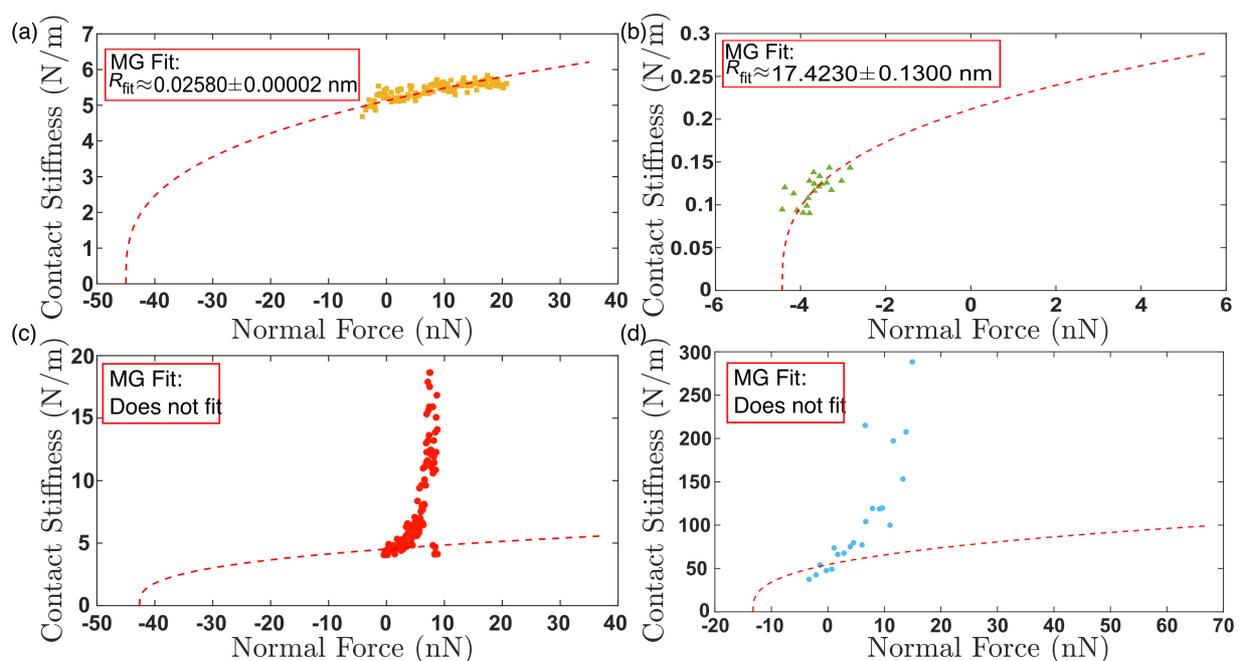
Figure 5: Contact stiffness versus normal force for (a) a silicon probe on HOPG sample (yellow squares) (b) a silicon probe on PDMS sample (green triangles), (c) a borosilicate glass colloid probe on a HOPG sample (red circles), and (d) a diamond-coated silicon on silicon sample (blue circles). A red dashed line in each figure shows a fit to the experimental data using Equation 7.

high stiffness of the contacting materials, which resulted in the reduced frequency having a value near the asymptote of the dispersion curve in models (ii) and (iii). Work by Killgore and Hurley identified that the analysis of stiff materials, or those having an elastic modulus greater than 10 GPa, with soft cantilevers such as those used in this experiment will not provide accurate results [30]. This finding is emphasized by the non-convergent fits observed in Figure 5c,d. However, the convergent fits in Figure 5a,b suggest that the CR-AFM models are valid, yet they result in unphysical values of the fit parameters. Therefore, our findings suggest that the CR-AFM models used are not applicable for a wider range of stiffness than previously thought. Finally, only by processing the cantilever deflection signal with STFT, such as here, or other time–frequency spectral analysis techniques, can sufficient temporal resolution of the oscillatory changes in the AFM cantilever within a single experiment be captured to perform such mechanical analysis

and allow for the limits of the analytical models to be better validated.

Figure 6 shows SEM images of two of the tips used in the study, that is, a borosilicate glass colloid glued onto a tipless silicon cantilever and a PtSi-coated silicon cantilever. In each of these cases, the tip radius was estimated to be much larger than what was fitted in Figure 5. While it is possible that, in particular with the colloidal probe, local surface roughness will yield a much smaller contact radius than the overall probe shape, it is still significantly larger than predicted by the models in Figure 5.

In summary, we have used longstanding analytical models to convert the measured variation in cantilever resonant frequency with applied normal force into contact stiffness. While the measurement process is very similar to what is typically done in
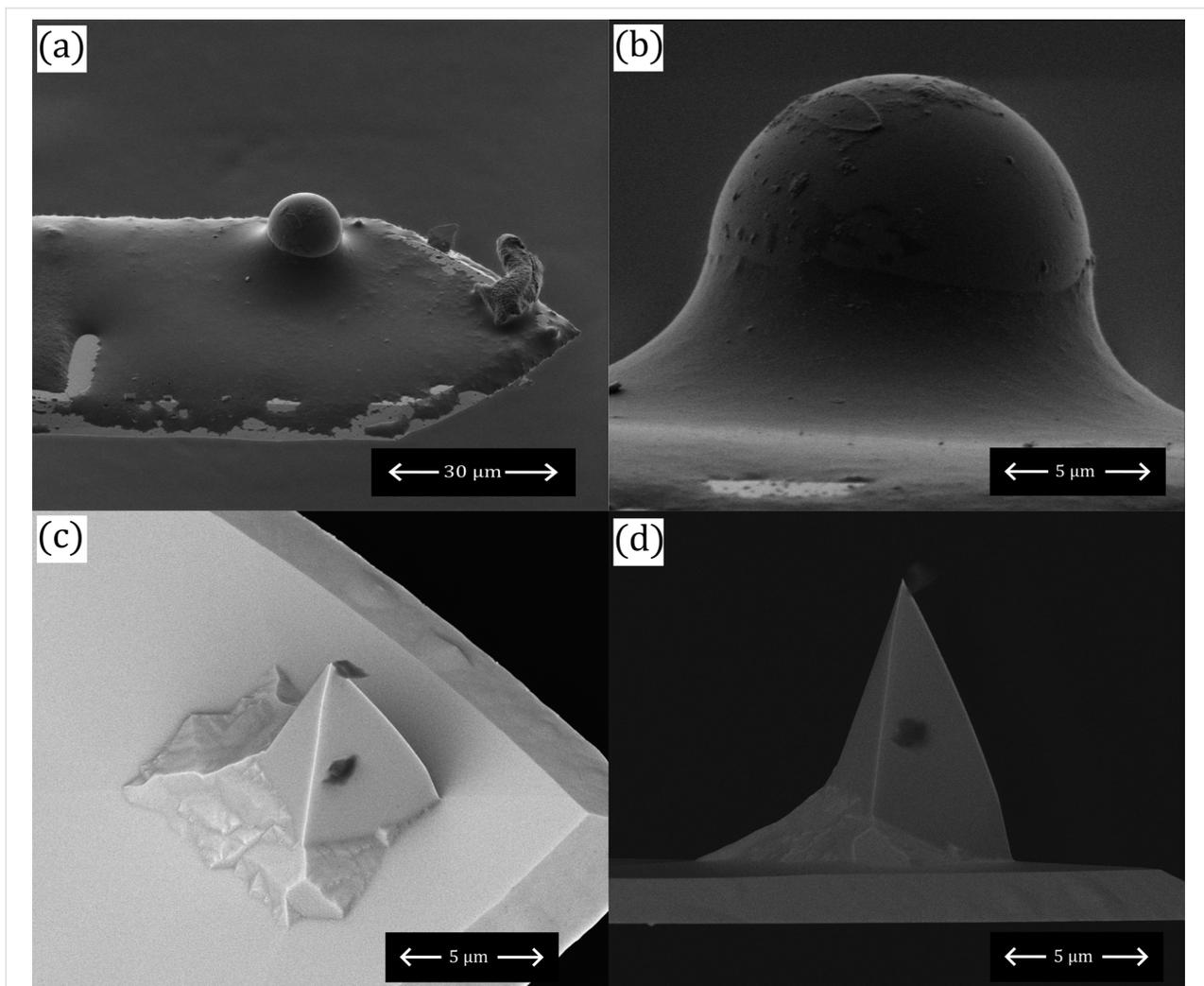
Figure 6: (a, b) Scanning electron microscopy images of the borosilicate glass colloid glued onto the tipless silicon cantilever. (c, d) Scanning electron microscopy images of the PtSi-coated AFM cantilever with integrated tip.

CR-AFM studies, it becomes more clear as to why these studies normalize their results to a section or area of the surface with known mechanical properties: The analytical models that have been developed do not accurately describe the variation of cantilever frequency when the tip is pressed against the surface. At this time, no better models were developed to describe the link between cantilever frequency and contact stiffness, and we believe that normalization of the surface properties is the only method that makes it possible for experimentalists to provide some understanding of a quantitative value of the surface elastic modulus and other mechanical properties.

Conclusion

High-data rate acquisition of the cantilever deflection signal from the photodiode of an AFM allows for the capture of the thermal motion of the AFM cantilever during a force-versus-distance measurement. STFT analysis was used to produce power spectra at regular time intervals during the experiments, with the frequency resolution varied to balance a faster time response of the cantilever's oscillation parameters against the necessary frequency resolution to accurately fit the resonant peak of the first normal oscillation mode of the AFM cantilever. The resonance mode was fitted to a Lorentz peak to extract its center frequency and quality factor at each time point, providing similar information as to what is generated in a CR-AFM experiment. The cantilever resonant frequency was converted into contact stiffness using analytical models of cantilever vibrations, which could then be compared with contact mechanics models relating the applied normal force to contact stiffness. It was shown that those commercially available cantilevers, which provide enough signal for analysis in a standard AFM, push CR-AFM into a regime where small variations in frequency result in large variations of derived contact stiffness. This relationship between frequency and contact stiffness makes correlating experimental contact resonance data with contact stiffness, or other mechanical property assessments, very difficult. Thus, our findings show that, while high-fidelity data of the changing oscillatory behavior of AFM cantilevers can be obtained with high sampling rates and subsequent STFT analysis, quantitative analysis is not possible without measuring a calibration curve or normalizing data on a known material pair. These observations confirm why most CR-AFM studies report normalized data, despite providing information on the analytical models to convert frequency to contact stiffness in most cases, or only show qualitative frequency data. Further, we have been able to produce high-fidelity data that accurately captures the cantilever's oscillation frequency and Q-factor over the course of the experiment, such that it can be compared directly with analytical models of cantilever oscillations and contact mechanics models, which had not been previously captured in the literature. Our study also shows that the current model used

to describe CR-AFM experiments may not be complex enough to capture the physical experiment. However, choosing the cantilever stiffness knowing in advance what the expected material stiffness is may result in larger variations of contact stiffness with frequency than was captured in our study. Analysis of higher-order modes, having higher stiffnesses, may also improve the determination of contact stiffness from the measured resonant frequency.

Supporting Information

Supporting Information File 1
Equations of motion of the cantilever dynamics models and additional experimental data.
[https://www.beilstein-journals.org/bjnano/content/supplementary/2190-4286-16-136-S1.pdf]

Author Contributions
Thomas Mathias: data curation; formal analysis; investigation; methodology; software; writing – original draft. Roland Bennewitz: conceptualization; investigation; supervision; validation; writing – review & editing. Philip Egberts: conceptualization; data curation; formal analysis; funding acquisition; methodology; project administration; software; supervision; validation; writing – original draft; writing – review & editing.

ORCID® iDs
Roland Bennewitz - https://orcid.org/0000-0002-5464-8190
Philip Egberts - https://orcid.org/0000-0002-3353-4493

Data Availability Statement
Data generated and analyzed during this study is available from the corresponding author upon reasonable request.

Preprint

A non-peer-reviewed version of this article has been previously published as a preprint: https://doi.org/10.3762/bxiv.2025.42.v1

References

1. Meyer, E.; Hug, H. J.; Bennewitz, R. *Scanning Probe Microscopy: The Lab on a Tip;* Springer: Berlin, Heidelberg, Germany, 2004.
2. Binnig, G.; Quate, C. F.; Gerber, C. *Phys. Rev. Lett.* **1986,** *56,* 930–933. doi:10.1103/physrevlett.56.930
3. Mate, C. M.; McClelland, G. M.; Erlandsson, R.; Chiang, S. *Phys. Rev. Lett.* **1987,** *59,* 1942–1945. doi:10.1103/physrevlett.59.1942
4. Martin, Y.; Williams, C. C.; Wickramasinghe, H. K. *J. Appl. Phys.* **1987,** *61,* 4723–4729. doi:10.1063/1.338807
5. Yuya, P. A.; Hurley, D. C.; Turner, J. A. *J. Appl. Phys.* **2008,** *104,* 074916. doi:10.1063/1.2996259
6. Szlufarska, I.; Chandross, M.; Carpick, R. W. *J. Phys. D: Appl. Phys.* **2008,** *41,* 123001. doi:10.1088/0022-3727/41/12/123001
7. Rabe, U.; Janser, K.; Arnold, W. *Rev. Sci. Instrum.* **1996,** *67,* 3281–3293. doi:10.1063/1.1147409
8. Yamanaka, K.; Nakano, S. *Appl. Phys. A: Mater. Sci. Process.* **1998,** *66,* S313–S317. doi:10.1007/s003390051153
9. Killgore, J. P.; Yablon, D. G.; Tsou, A. H.; Gannepalli, A.; Yuya, P. A.; Turner, J. A.; Proksch, R.; Hurley, D. C. *Langmuir* **2011,** *27,* 13983–13987. doi:10.1021/la203434w
10. Stan, G.; King, S. W.; Cook, R. F. *Nanotechnology* **2012,** *23,* 215703. doi:10.1088/0957-4484/23/21/215703
11. Malegori, G.; Ferrini, G. *Nanotechnology* **2011,** *22,* 195702. doi:10.1088/0957-4484/22/19/195702
12. Pukhova, V.; Banfi, F.; Ferrini, G. *Nanotechnology* **2013,** *24,* 505716. doi:10.1088/0957-4484/24/50/505716
13. López-Guerra, E. A.; Banfi, F.; Solares, S. D.; Ferrini, G. *Sci. Rep.* **2018,** *8,* 7534. doi:10.1038/s41598-018-25828-4
14. Gonzalez-Martinez, J. F.; Kakar, E.; Erkselius, S.; Rehnberg, N.; Sotres, J. *Langmuir* **2019,** *35,* 6015–6023. doi:10.1021/acs.langmuir.8b04222
15. Tung, R. C.; Killgore, J. P.; Hurley, D. C. *J. Appl. Phys.* **2014,** *115,* 224904. doi:10.1063/1.4882755
16. Gonzalez-Martinez, J. F.; Kakar, E.; Erkselius, S.; Rehnberg, N.; Sotres, J. *Wear* **2019,** *418–419,* 151–159. doi:10.1016/j.wear.2018.11.027
17. Suk, J. W.; Na, S. R.; Stromberg, R. J.; Stauffer, D.; Lee, J.; Ruoff, R. S.; Liechti, K. M. *Carbon* **2016,** *103,* 63–72. doi:10.1016/j.carbon.2016.02.079
18. Suriano, R.; Credi, C.; Levi, M.; Turri, S. *Appl. Surf. Sci.* **2014,** *311,* 558–566. doi:10.1016/j.apsusc.2014.05.108
19. Salvadori, M. C.; Brown, I. G.; Vaz, A. R.; Melo, L. L.; Cattani, M. *Phys. Rev. B* **2003,** *67,* 153404. doi:10.1103/physrevb.67.153404
20. Sader, J. E.; Chon, J. W. M.; Mulvaney, P. *Rev. Sci. Instrum.* **1999,** *70,* 3967–3969. doi:10.1063/1.1150021
21. Pfeiffer, O.; Loppacher, C.; Wattinger, C.; Bammerlin, M.; Gysin, U.; Guggisberg, M.; Rast, S.; Bennewitz, R.; Meyer, E.; Güntherodt, H.-J. *Appl. Surf. Sci.* **2000,** *157,* 337–342. doi:10.1016/s0169-4332(99)00548-6
22. Labuda, A. *Rev. Sci. Instrum.* **2016,** *87,* 033704. doi:10.1063/1.4943292
23. Hurley, D. C. Contact Resonance Force Microscopy Techniques for Nanomechanical Measurements. *Applied Scanning Probe Methods XI: Scanning Probe Microscopy Techniques;* Springer: Berlin, Heidelberg, Germany, 2009; pp 97–138. doi:10.1007/978-3-540-85037-3_5
24. Johnson, K. L. *Contact Mechanics;* Cambridge University Press: Cambridge, UK, 1985. doi:10.1017/cbo9781139171731
25. te Riet, J.; Katan, A. J.; Rankl, C.; Stahl, S. W.; van Buul, A. M.; Phang, I. Y.; Gomez-Casado, A.; Schön, P.; Gerritsen, J. W.; Cambi, A.; Rowan, A. E.; Vancso, G. J.; Jonkheijm, P.; Huskens, J.; Oosterkamp, T. H.; Gaub, H.; Hinterdorfer, P.; Figdor, C. G.; Speller, S. *Ultramicroscopy* **2011,** *111,* 1659–1669. doi:10.1016/j.ultramic.2011.09.012
26. Iqbal, T.; Camargo, S. S., Jr.; Yasin, S.; Farooq, U.; Shakeel, A. *Polymers (Basel, Switz.)* **2020,** *12,* 795. doi:10.3390/polym12040795
27. Friedrich, S.; Cappella, B. *Beilstein J. Nanotechnol.* **2020,** *11,* 1714–1727. doi:10.3762/bjnano.11.154
28. Carpick, R. W.; Ogletree, D. F.; Salmeron, M. *J. Colloid Interface Sci.* **1999,** *211,* 395–400. doi:10.1006/jcis.1998.6027
29. Tabor, D. Surface Forces and Surface Interactions. In *Plenary and Invited Lectures;* Kerker, M.; Zettlemoyer, A. C.; Rowell, R. L., Eds.; Academic Press: New York, NY, USA, 1977; pp 3–14. doi:10.1016/b978-0-12-404501-9.50009-2
30. Killgore, J. P.; Hurley, D. C. *Nanotechnology* **2012,** *23,* 055702. doi:10.1088/0957-4484/23/5/055702

License and Terms

Calibration of piezo actuators and systems by dynamic interferometry

Knarik Khachatryan[*] and Michael Reichling[*]

Open Access

Abstract

To achieve precise measurements of small displacements in non-contact atomic force microscopy, it is crucial to control the position of moving parts with high accuracy. This is commonly accomplished by piezo actuators, for instance, in the form of tube piezos for positioning the tip or optics. For their calibration, we propose an approach based on the dynamic response signal from a fiber interferometer used for cantilever displacement detection. The fine-positioning z-piezo of the fiber is calibrated by the analysis of measurements of the dynamic interferometer response signal recorded for various cantilever oscillation amplitudes and varied distances between the cantilever and the fiber end. Furthermore, we demonstrate the cantilever oscillation amplitude calibration under conditions of various amounts of tube piezo contraction and extension. The merits and limits of accuracy for such type of calibration are discussed.

Introduction

Interferometric displacement detection stands as a cornerstone in high-precision techniques employed in cantilever-based atomic force microscopy (AFM), since its early days [1-6]. This method of cantilever displacement detection is specifically well suited for non-contact atomic force microscopy (NC-AFM) operation in an ultrahigh-vacuum (UHV) environment at low temperature and has been developed tremendously over the last three decades [7-12].

In frequency-modulated NC-AFM, the cantilever is kept at oscillation with constant amplitude, yielding an interferometric signal that is a periodic function of time. However, it is generally not a harmonic oscillation due to the convolution of the (quasi)-harmonic oscillation of the cantilever with the spatially modulated light field in the interferometer cavity [13]. Dynamic interferometric signals have been studied in the context of NC-AFM using the interferometric concepts of Michelson and

Fabry–Perot interferometers [14,15]. Both interferometers rely on the precise alignment of a single-mode optical fiber delivering the light and receiving the optical signal generated in the optical cavity formed by the cantilever and the fiber end. Controlling and stabilizing the fiber–cantilever distance is of principal importance for the accurate operation of the interferometric detection system [16]. Here, we address the aspect of calibrating the *z*-motion of the fiber tube piezo [17,18] with high accuracy to ensure full control over the interferometer cavity. Measurements involve the expansion and contraction of the piezo tube by an amount of the order of 100 nm, raising the issues of piezo nonlinearity [19], hysteresis [20], and creep [21]. Therefore, we address systematic errors in tube piezo calibration and explore to what extent the cantilever amplitude calibration [13] is affected by the actual extension or extension history of the tube piezo.

Experimental

Experiments are performed with a NC-AFM interferometric setup, and the methods of interferometer signal analysis are as described in [13]. The schematic setup of the system electronics and relevant voltages is detailed in Figure 3 of [16]. We investigate the dynamics of the free cantilever excited to oscillation at constant amplitude *A* and frequency f_{exc}, which is always kept at the fundamental cantilever eigenfrequency f_0.

Initially, the interferometer is stabilized so that the working point is the inflection point and center of symmetry of the time-dependent interferometer signal [16], implying that the mean cavity length is $d_0 = m\frac{\lambda}{8}$, where *m* is an odd integer and λ is the vacuum wavelength of the light used for interferometer operation in a UHV environment. As long as the respective stabilization loop of interferometer alignment is active [16], this adjustment is maintained even in the presence of drift or piezo creep by the automatic adjustment of the voltage applied between the fiber tube piezo inner electrode and the common potential of the tube piezo voltage sources $V_{z,f} = V_{z,f}^0$. To contract or expand the tube piezo, the automatic control loop action is frozen and an appropriate voltage $V_{z,f}^{add}$ is added to $V_{z,f}^0$, yielding an incremental change d_{err} of the mean cavity length to $d_0' = d_0 + d_{err}$. This quantity can be extracted from the time-domain interferometric signal by a two-step fit method based on Equation 1 as detailed in [13].

$$V_{sig} = V_{DC} + V_0 \sin\left(\frac{4\pi}{\lambda}\left(d_0' - A\sin\left(2\pi f_{exc}t - \varphi\right)\right) - \frac{\pi}{2}\right). \quad (1)$$

Here, V_{DC} represents the DC part of the interferometer signal voltage, V_0 is the voltage amplitude of the modulated signal, and φ is the phase shift introduced by the electronics in the signal path, which may be determined from the fit. Experiments are performed with laser light of wavelength $\lambda = \lambda_{vac} = 780.41$ nm and the excitation frequency is kept at the cantilever eigenfrequency $f_{exc} = 169.667$ kHz determined at the beginning of the measurements.

The piezoelectric tube (PZT-8, EBL Products Inc., East Hartford, CT, USA) used for fiber positioning is specified with a piezoelectric constant $d_{31} = -0.95$ Å/V [22] at 293 K, according to the manufacturer's data sheet [23]. The extension or contraction of the fiber tube piezo Δ*L* depends on $V_{z,f}$ and the dimensions of the tube [24].

$$\Delta L = d_{31}\frac{L}{h}V_{z,f}, \quad (2)$$

where *L* and *h* are the length of the piezo tube and the wall thickness, respectively. According to the widely used convention, the piezo tube is poled so that a negative potential applied to the inner electrode $V_{z,f} < 0$ results in an extension Δ*L* > 0 that translates into a reduction of the cavity length $\Delta d = d_{err} = -\Delta L < 0$. From d_{31} and the geometry parameters of the tube piezo (*L* = 31.8 mm and *h* = 1.40 mm), we deduce a nominal fiber tube piezo calibration factor of $S_f^{nom} = \frac{\Delta L}{V_{z,f}} = -\frac{\Delta d}{V_{z,f}} = d_{31}\frac{L}{h} = -2.15$ nm/V relating the extension or contraction Δ*L* of the tube piezo to the applied voltage.

Fiber tube piezo calibration

In our measurements, the fiber is mounted at α = 15° so that it is directed perpendicular to the cantilever, which is also mounted at the same angle α to the horizontal [25]. The vertical movement of the fiber in *z*-direction (z_f) changes the cavity length with $\Delta d = \frac{\Delta z_f}{\cos(\alpha)}$. For the measurement of the actual tube piezo calibration factor $S_f = -\frac{\Delta d}{\Delta V_{z,f}} = -\frac{\Delta z_f}{\cos(\alpha)\Delta V_{z,f}}$, we measure the contraction and extension of the tube via the change in cavity length Δ*d* as a function of the change in the added voltage $\Delta V_{z,f}^{add}$. Initially, the control loop is frozen at $V_{z,f} = V_{z,f}^0$, with $d_{err} = 0$ for a long time (many days) to facilitate complete equilibration of the piezo tube. After the start of the measurement, $V_{z,f}^{add}$ is varied in positive and negative directions in steps of 20 V, while an accommodation time of 10 min passes before the extension or contraction is measured. The cantilever excitation voltage is kept constant at $V_{exc} = 3.50$ V, yielding an oscillation amplitude of *A* = 111 nm, facilitating convenient interferometer signal fits.

Results and Discussion

Results are compiled in the four frames of Figure 1, including linear functions that fit the measurement points. Measurements have been performed in the sequence of contraction ($V_{z,f}^{add} = 0 \ldots 120$ V, Figure 1b) and then extension ($V_{z,f}^{add} = 0 \ldots -120$ V, Figure 1a). Note that the contraction measure-
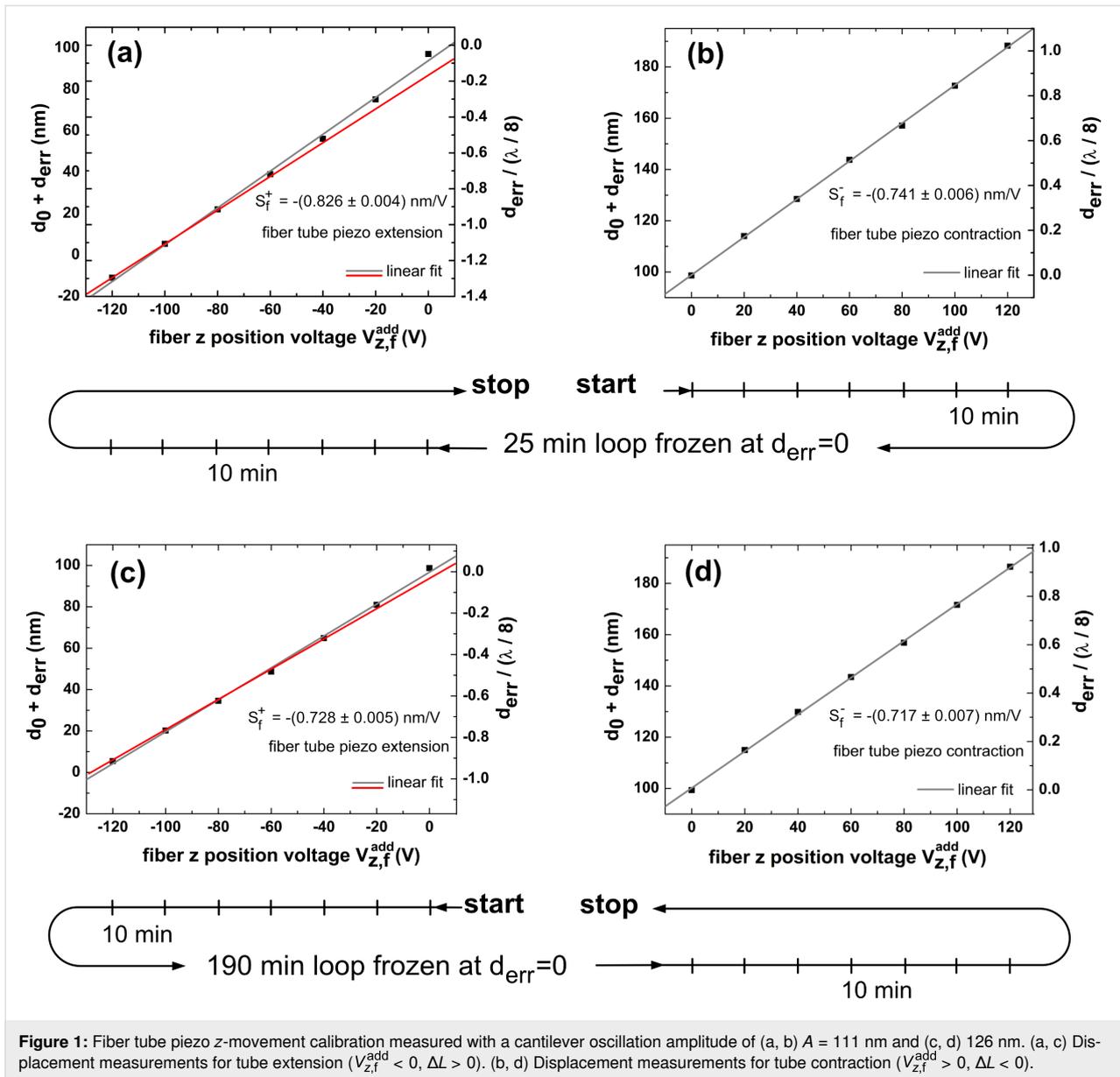
Figure 1: Fiber tube piezo *z*-movement calibration measured with a cantilever oscillation amplitude of (a, b) $A = 111$ nm and (c, d) 126 nm. (a, c) Displacement measurements for tube extension ($V_{z,f}^{add} < 0$, $\Delta L > 0$). (b, d) Displacement measurements for tube contraction ($V_{z,f}^{add} > 0$, $\Delta L < 0$).

ment yields a perfect result with the straight line very well fitting the data and crossing (0,0) in the ($V_{z,f}^{add}$, d_{err}) plane, while the fit for the following expansion measurement (Figure 1a) is less precise and exhibits a systematic trend of approach towards a limiting straight line defined by the last three data points (red line in Figure 1a). We find that the calibration factors for contraction ($V_{z,f}^{add} > 0$) and extension ($V_{z,f}^{add} < 0$) reproducibly differ from each other. From the slope of the straight lines in Figure 1, we determine $S_f^- = -(0.741 \pm 0.006)$ nm/V for the contraction and $\tilde{S}_f^+ = -(0.889 \pm 0.020)$ nm/V for the extension. Evaluating the calibration factor from the red, straight line yields $S_f^+ = -(0.826 \pm 0.004)$ nm/V, a value closer but clearly different from S_f^-. Further, we note that, in Figure 1a, neither the first data point of this measurement nor one of the fit lines

crosses (0,0). We attribute this behavior to piezo creep and hysteresis occurring after switching polarity from positive to negative. Note that we observe this phenomenon although we paused the measurement for 25 min between contraction and extension experiments to give the system time for equilibration. The deviation of data points from a straight line is a systematic effect yielding a bow shape that can qualitatively be explained by the action of creep accumulated over the extension steps. The striking observation that the bow is not observed for the contraction measurement points to a significant difference of the piezo response for contraction and extension.

To clarify if the observation is inherent to the piezo or an artefact of the sequence of measurements or of a lack of accommo-

dation time between measurements, we repeated the measurement in reverse order and with an extended accommodation time of 190 min between extension and contraction. The corresponding results compiled in Figure 1c,d qualitatively yield a perfect reproduction of the previous measurement, while there is a difference in quantitative results slightly beyond the statistical error of individual measurements. Based on the last measurements that we consider to be the most reliable ones, the study yields a calibration factor of $S_f = -0.722$ nm/V without specified error margins. We keep in mind that the response of the tube piezo depends in detail on the direction of the movement and that there are slight differences for the directional calibration factors S_f^+ and S_f^-. Principally, it might be possible to reduce the bow effect observed for the tube piezo extension by leaving more accommodation time between the voltage steps. However, in this case, thermal drift is likely to deteriorate the measurement by similar amounts as the observed creep.
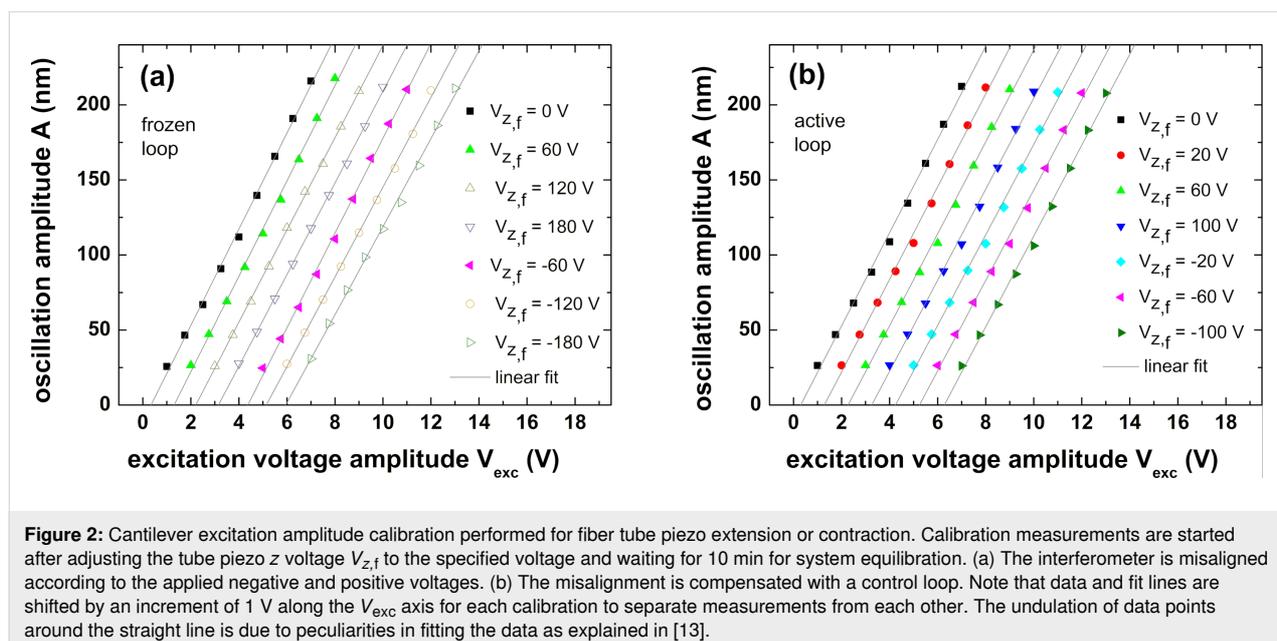
The fact that the measured tube piezo calibration factor differs from the nominal value by more than a factor of two might be due to the manufacturing tolerance; but, more likely, it can be explained by a depolarization of the tube piezo material as it has been subject to many heating cycles for bakeout of the UHV chamber.

Next, we investigate the influence that the extension or extension history of the fiber tube piezo might have on the cantilever excitation. The calibration of the cantilever excitation system comprising the excitation piezo, the cantilever, their mutual coupling, and electrical system parameters, further termed amplitude calibration, is highly accurate when performed with a

perfectly aligned interferometer. A high-precision measurement based on an expanded dataset as described in [13] yields a value of $S^{\mathrm{prec}} = (33.26 \pm 0.27)$ nm/V for the amplitude calibration factor.

For testing the calibration accuracy for the misaligned interferometer, various voltages $V_{z,f}^{\mathrm{add}}$ are applied to the fiber tube piezo, and, after each step of voltage change, the cantilever excitation voltage is varied from 1 V to 7 V in steps. For each step, the interferometer signal is analyzed to extract the oscillation amplitude A corresponding to the respective voltage step. Figure 2 shows plots of A against the cantilever excitation voltage V_{exc}, where the data are fitted by straight lines. Note that all straight lines should coincide; however, they are shifted for each step along the V_{exc} axis for better clarity. The measurements presented in Figure 2a have been performed without activating the fiber piezo control loop. Hence, for each amplitude calibration run, the interferometer is misaligned by an amount defined by the respective voltage $V_{z,f}^{\mathrm{add}}$. For the measurement represented in Figure 2b, the misalignment compensation loop has been activated. Consequently, the interferometer is forced back to the initial condition of perfect alignment before each run of amplitude calibration. To allow for piezo relaxation after significant extension or retraction, a waiting time of 10 min has been applied between the change in $V_{z,f}^{\mathrm{add}}$ and the following calibration measurement.

The amplitude calibration factors determined with the aligned or misaligned interferometer are compiled in Table 1. The weighted mean of the calibration factors for the misaligned interferometer (frozen loop) is determined as $\overline{S}^{\mathrm{fl}} = (30.84 \pm$

Figure 2: Cantilever excitation amplitude calibration performed for fiber tube piezo extension or contraction. Calibration measurements are started after adjusting the tube piezo *z* voltage $V_{z,f}$ to the specified voltage and waiting for 10 min for system equilibration. (a) The interferometer is misaligned according to the applied negative and positive voltages. (b) The misalignment is compensated with a control loop. Note that data and fit lines are shifted by an increment of 1 V along the V_{exc} axis for each calibration to separate measurements from each other. The undulation of data points around the straight line is due to peculiarities in fitting the data as explained in [13].

Table 1: Measured calibration factors for the cantilever oscillation piezo determined for the non-aligned (frozen loop) and well-aligned (active loop) interferometer.

frozen loop		active loop	
$V_{z,\mathrm{f}}^{\mathrm{add}}$	S_i [nm/V]	$V_{z,\mathrm{f}}^{\mathrm{add}}$	S_i [nm/V]
0 V	32.008 ± 0.555	0 V	30.855 ± 0.679
60 V	31.794 ± 0.605	20 V	30.608 ± 0.662
120 V	30.736 ± 0.290	60 V	30.320 ± 0.661
180 V	30.542 ± 0.281	100 V	30.168 ± 0.634
−60 V	31.587 ± 0.537	−20 V	30.135 ± 0.638
−120 V	29.900 ± 0.387	−60 V	30.278 ± 0.672
−180 V	29.325 ± 0.560	−100 V	31.035 ± 0.501

0.15) nm/V, while in the measurements in which misalignment was corrected before each measurement (active loop), the mean of calibration factors is $\overline{S}^{\mathrm{al}} = (30.34 \pm 0.24)$ nm/V.

For the misaligned interferometer (frozen loop), the maximum and minimum S_i^{fl} values for $V_{z,\mathrm{f}}^{\mathrm{add}} \neq 0$ differ by 2.470 nm/V and the $\overline{S}^{\mathrm{fl}}$ value for $V_{z,\mathrm{f}}^{\mathrm{add}} = 0$ differs from the mean $V_{z,\mathrm{f}}^{\mathrm{add}}$ by 1.361 nm/V. Both differences are significantly larger than the standard deviation determined for the individual measurements and the weighted mean of uncertainties. This points to a systematic error in the amplitude calibration factor measurements. Applying the same analysis to the data of the alignment-corrected interferometer (active loop), we find that the respective differences are smaller or close to the relevant standard deviations. We conclude that, in the latter case, the loop action provides the same conditions for each calibration measurement, allowing for a calibration with 2% relative uncertainty in this case.

Above observations clearly demonstrate that the misalignment and the fiber piezo motion history may deteriorate the excitation system calibration. This is probably due to piezo hysteresis and the fit procedure that has been optimized for the perfectly aligned interferometer [13] but not extensively tested for the misaligned interferometer. The slight difference between the S_i values corresponding to $V_{z,\mathrm{f}}^{\mathrm{add}} = 0$ for frozen and active loops is a result of a slight change in the interferometer alignment during about 24 h elapsed between respective measurements. The differences between both values and S^{prec} are even larger as the precision measurement has been performed many weeks earlier. The difference in calibration results for measurements taken with significant time elapsed between can be explained by slight differences in the alignment of the laser spot on the cantilever due to manual adjustment or drift. Although, in our models, light is treated as a plane wave, in reality the light beam exiting the fiber end has a divergence of about 9°. As a conse-

quence, light diffracted at the edges of the cantilever acts back on the reflected light sampled by the fiber. Furthermore, the partially coherent light of the laser produces speckle patterns [26] depending on minute charges in the beam profile or cantilever alignment. Both effects result in a considerable dependence of the lateral intensity distribution in the cantilever plane [25] on details of the alignment and, in turn, have an impact on the amount and interference structure of the reflected light, affecting the amplitude calibration.

Conclusion
Our results demonstrate that a tube piezo, which is part of an interferometer for cantilever displacement detection, can precisely be calibrated by dynamic interferometry. However, care has to be taken in performing and analyzing experiments as piezo non-linearity and creep may have a considerable impact on the calibration results. Therefore, the calibration should be performed under conditions that are as close as possible to the conditions of the experiment the calibration results are used for. Generally, the system should be given much time to relax to avoid the deterioration of results by piezo creep. Also, one has to keep in mind that the piezo as a complex electromechanical system can be characterized by a single parameter S_{f} only in a limited range of system parameters. We find that, provided necessary precautions are applied, a valid amplitude calibration by dynamic interferometry can be performed for the well-aligned interferometer; however, additional care has to be taken for an amplitude calibration performed under conditions of a misaligned interferometer.

Author Contributions
Knarik Khachatryan: conceptualization; data curation; formal analysis; investigation; resources; visualization; writing – original draft. Michael Reichling: formal analysis; investigation; methodology; project administration; supervision; visualization; writing – review & editing.

ORCID® iDs

Knarik Khachatryan - https://orcid.org/0009-0006-8403-7274
Michael Reichling - https://orcid.org/0000-0003-3186-9000

Data Availability Statement

Data generated and analyzed during this study is available from the corresponding author upon reasonable request.

References

1. Martin, Y.; Williams, C. C.; Wickramasinghe, H. K. *J. Appl. Phys.* **1987,** *61,* 4723–4729. doi:10.1063/1.338807
2. Rugar, D.; Mamin, H. J.; Erlandsson, R.; Stern, J. E.; Terris, B. D. *Rev. Sci. Instrum.* **1988,** *59,* 2337–2340. doi:10.1063/1.1139958
3. Erlandsson, R.; McClelland, G. M.; Mate, C. M.; Chiang, S. *J. Vac. Sci. Technol., A* **1988,** *6,* 266–270. doi:10.1116/1.575440
4. Meyer, G.; Amer, N. M. *Appl. Phys. Lett.* **1988,** *53,* 1045–1047. doi:10.1063/1.100061
5. Putman, C. A. J.; de Grooth, B. G.; van Hulst, N. F.; Greve, J. *Ultramicroscopy* **1992,** *42–44,* 1509–1513. doi:10.1016/0304-3991(92)90474-x
6. Fujisawa, S.; Ohta, M.; Konishi, T.; Sugawara, Y.; Morita, S. *Rev. Sci. Instrum.* **1994,** *65,* 644–647. doi:10.1063/1.1145131
7. Albrecht, T. R.; Grütter, P.; Rugar, D.; Smith, D. P. E. *Ultramicroscopy* **1992,** *42–44,* 1638–1646. doi:10.1016/0304-3991(92)90498-9
8. Allers, W.; Schwarz, A.; Schwarz, U. D.; Wiesendanger, R. *Rev. Sci. Instrum.* **1998,** *69,* 221–225. doi:10.1063/1.1148499
9. Hug, H. J.; Stiefel, B.; van Schendel, P. J. A.; Moser, A.; Martin, S.; Güntherodt, H.-J. *Rev. Sci. Instrum.* **1999,** *70,* 3625–3640. doi:10.1063/1.1149970
10. Karcı, Ö.; Dede, M.; Oral, A. *Rev. Sci. Instrum.* **2014,** *85,* 103705. doi:10.1063/1.4897147
11. von Allwörden, H.; Ruschmeier, K.; Köhler, A.; Eelbo, T.; Schwarz, A.; Wiesendanger, R. *Rev. Sci. Instrum.* **2016,** *87,* 073702. doi:10.1063/1.4955448
12. Karc, Ö.; Çelik, Ü.; Oral, A. *Rev. Sci. Instrum.* **2020,** *91,* 013703. doi:10.1063/1.5120007
13. Khachatryan, K.; Anter, S.; Reichling, M.; von Schmidsfeld, A. *Beilstein J. Nanotechnol.* **2024,** *15,* 1070–1076. doi:10.3762/bjnano.15.87
14. von Schmidsfeld, A.; Reichling, M. *Appl. Phys. Lett.* **2015,** *107,* 123111. doi:10.1063/1.4931702
15. Milde, P.; Langenhorst, M.; Hölscher, H.; Rottmann-Matthes, J.; Hundertmark, D.; Eng, L. M.; Hoffmann-Vogel, R. *J. Appl. Phys.* **2021,** *130,* 035303. doi:10.1063/5.0054509
16. von Schmidsfeld, A.; Khachatryan, K.; Reichling, M. *Rev. Sci. Instrum.* **2025,** *96,* 093703. doi:10.1063/5.0269765
17. Vandervoort, K. G.; Zasadzinski, R. K.; Galicia, G. G.; Crabtree, G. W. *Rev. Sci. Instrum.* **1993,** *64,* 896–899. doi:10.1063/1.1144139
18. Chen, F.; Mohideen, U. *Rev. Sci. Instrum.* **2001,** *72,* 3100–3102. doi:10.1063/1.1378341
19. Dürselen, R.; Grunewald, U.; Preuss, W. *Scanning* **1995,** *17,* 91–96. doi:10.1002/sca.4950170205
20. Al Janaideh, M.; Al Saaideh, M.; Rakotondrabe, M. *Mech. Syst. Signal Process.* **2020,** *145,* 106880. doi:10.1016/j.ymssp.2020.106880
21. Jung, H.; Gweon, D.-G. *Rev. Sci. Instrum.* **2000,** *71,* 1896–1900. doi:10.1063/1.1150559
22. Smith, W. F.; Axelrod, B. W. *Rev. Sci. Instrum.* **2000,** *71,* 1772–1775. doi:10.1063/1.1150535
23. Piezocaramic tubes for ultra-precise positioning applications; EBL Productes Inc. (East Hartford, CT, USA), data sheet. https://eblproducts.com/wp-content/uploads/2023/09/piezoceramic-tubes.pdf (accessed Oct 22, 2025).
24. Moheimani, S. O. R. *Rev. Sci. Instrum.* **2008,** *79,* 071101. doi:10.1063/1.2957649
25. von Schmidsfeld, A.; Nörenberg, T.; Temmen, M.; Reichling, M. *Beilstein J. Nanotechnol.* **2016,** *7,* 841–851. doi:10.3762/bjnano.7.76
26. Akkermans, E.; Montambaux, G. *J. Opt. Soc. Am. B* **2004,** *21,* 101–112. doi:10.1364/josab.21.000101

Quantitative estimation of nanoparticle/substrate adhesion by atomic force microscopy

Aydan Çiçek[1], Markus Kratzer[*2], Christian Teichert[2] and Christian Mitterer[*1]

Full Research Paper

Address:
[1]Department of Materials Science, Montanuniversität Leoben, Franz-Josef-Straße 18, 8700 Leoben, Austria and [2]Chair of Physics, Department Physics, Mechanics and Electrical Engineering, Montanuniversität Leoben, Franz-Josef-Straße 18, 8700, Leoben, Austria

Email:
Markus Kratzer[*] - markus.kratzer@unileoben.ac.at;
Christian Mitterer[*] - christian.mitterer@unileoben.ac.at

* Corresponding author

Abstract

Understanding nanoparticle adhesion to substrates is the key for their stability and performance in many applications, including energy systems, nanofabrication, catalysis, and electronic devices. In this study, we present a methodology for examining adhesion of copper nanoparticles to silicon substrates deposited under varying conditions using DC magnetron sputter inert gas condensation. Atomic force microscopy was utilized as a tool for the manipulation of the nanoparticles and to measure lateral forces for their displacement, with cantilever calibration achieved through wedge and diamagnetic lateral force calibrator methods. The work of adhesion was quantified by integrating the obtained lateral forces over the distance moved during manipulation, revealing a non-monotonic dependency on nanoparticle size with maximum adhesion observed for particles between 6 and 12 nm. In addition, an applied positive substrate bias voltage led to more energetic landing conditions and thus to increased adhesion forces. This study underscores the suitability of atomic force microscopy in characterizing adhesion on the nanoscale and offers insights into future strategies for tailoring nanoparticle/substrate interactions.

Introduction

Nanoparticles (NPs) are at the forefront of basic research and technological innovation, captivating researchers and engineers from various fields such as energy storage [1], electronics [2], and catalysis [3]. These tiny particles, with sizes typically ranging from 1 to 100 nm, have fundamentally different properties compared to their bulk counterparts because of their large surface-to-volume ratio [4], as well as unique electronic [5] and physicochemical properties [6]. Among these properties, parti-

cle adhesion (which is determined by the interaction between the NP and the substrate) and the interface formed between NPs and substrate [7,8] play a decisive role. Particularly when the contact area between NPs and the substrate gets large compared to their volume, adhesion forces become predominant. Understanding the adhesion of NPs is expected to provide significant benefits in many applications [9,10]. A prerequisite for their application is the ability to measure and to understand their adhesion to suitable support materials. Low adhesion could be beneficial for movable parts within micro- and nanoelectromechanical systems to eliminate undesired sticking or friction [9]. In contrast, when NPs need to withstand external forces and/or harsh conditions without detachment, for example, in catalytic applications where NPs are immobilized on supports like carbon-based materials or TiO_2 to prevent aggregation and to maintain catalytic activity, strong adhesion is required [11]. To improve adhesion, Au NPs have been stabilized on SiO_2 substrates by embedding them into an organometallic layer, effectively immobilizing the NPs and significantly enhancing their interfacial adhesion. Their mechanical stability was tested utilizing scanning probe microscopy nanomanipulation [12]. Another approach tested for SiO_2 NPs was functionalizing their surfaces for improved adhesion on epoxy film-covered substrate surfaces [13].

In order to develop strategies for improved NP functionality and performance, it is necessary to measure and to quantify their adhesion to the corresponding substrates. With the available highly sensitive force sensors, atomic force microscopy (AFM) is well suited for determining the adhesion between individual NPs and the supporting substrate. Applying controlled forces to manipulate NPs enables precise quantification of adhesion forces [14]. Significant progress in AFM manipulating nanometer-scale objects has been achieved, particularly in the last two decades, enhancing its capabilities and accuracy [15-17]. However, achieving consistently accurate manipulation of NPs has inherent limitations due to limited knowledge of the exact geometry of the AFM tip as well as the complex interactions involving surface contact area and interfacial friction between the AFM tip, NPs, and the substrate [18], similar to friction studies on thin films [19]. Therefore, proper calibration of the normal and lateral force constants of the cantilever is crucial in order to extract quantitative, accurate, reliable, and reproducible lateral force values from AFM manipulation experiments [20].

Overall, manipulating NPs of extremely small size (<20 nm) is still a challenge and consequently limits studies in this area [9,14]. The majority of studies concerning AFM-based NP manipulation focuses on establishing reproducible protocols for the creation of patterns and structures with NPs as building blocks, but often without detailing lateral forces involved in the

experiments [15,21,22]. Rough estimations of the lateral forces were suggested to be two thirds of the applied normal force [23]. In order to assess adhesion properties, there are only a few studies providing quantification attempts of the lateral forces acting during AFM nanomanipulation [24-27]. Thus, there is little information available on the adhesion forces involved, which is critical for understanding the correlation between NPs' positional stability and deposition conditions.

In this study, we have investigated the adhesion between Cu NPs, deposited using different landing conditions, and a Si substrate. Cu NPs were synthesized via magnetron sputter inert gas condensation at different applied substrate bias voltages to vary their kinetic energy during landing at the substrate, thereby influencing their adhesion properties. AFM was utilized as a tool for the manipulation of the NPs in order to determine the adhesion forces. The NPs were pushed in normal direction to the AFM cantilever's long axis by scanning the surface with the AFM tip in contact mode. The corresponding lateral forces necessary to move NPs were determined. The lateral force constant of the AFM probe, comprising the AFM tip mounted on the cantilever, was calibrated based on the modified wedge and the diamagnetic lateral force calibrator (D-LFC) method [20]. Both qualitative and quantitative analyses of the measured force distributions are presented. To provide a reliable measure for adhesion forces, the mechanical work required to manipulate NPs was calculated by determining the area covered by the measured lateral force versus distance curves. The suggested approach provides insight into the complex interplay between the NP landing conditions and resulting adhesion forces.

Experimental
Synthesis of Cu nanoparticles
Before deposition, single-crystalline Si(100) wafer substrates, with a thickness of around 500 μm and covered by a native oxide, were cleaned in an ultrasonic bath for 10 min with ethanol, followed by rinsing with isopropanol. Then, the substrates were plasma-cleaned in a Diener electronic Tetra 30 system at a N_2 pressure of 50 Pa for 20 min. Immediately after plasma cleaning, the substrates were loaded in the NP deposition chamber.

The NP deposition experiments were conducted using DC magnetron sputter inert gas condensation in a Moorfield MiniLab 125 vacuum system equipped with a Nikalyte NL-UHV NP source, described in detail in a previous study [28]. The NP source is mounted at 45° angle to the deposition chamber and consists of two components, namely, the magnetron head and the aggregation zone with an attached quadrupole mass filter (QMF), both with a diameter of 125 mm. In this study, only one of the three water-cooled magnetrons, equipped with a Cu target

(Kurt J. Lesker, 99.999% purity) with 25.8 mm diameter and 3.2 mm thickness, was used. Prior to deposition, the base pressure in the deposition chamber was pumped down to 6×10^{-7} mbar. Ar was introduced as a sputtering gas, keeping a constant flow rate of 40 sccm. Sputtering was carried out at a constant current of 200 mA ($\approx$70 W) applied to the target. The sputtered atoms start to form NPs and to grow in the aggregation zone, where the aggregation length was adjusted to 110 mm and the pressure within the aggregation was held constant at 0.5 mbar. The growth of NPs stops after passing through the orifice, where the pressure difference from the aggregation zone to the QMF causes rapid cooling. The QMF allows one to select charged NPs based on their mass-to-charge ratio. Since it is assumed that NPs are single-charged [5], the QMF can, on the one hand, be used for scanning the NP mass distribution and, under the common assumption of spherical shape and the theoretical density of Cu, the size distribution. On the other hand, the QMF can be also be employed for filtering NPs with desired masses. An AC voltage, $V = \pm250$ V, with a frequency of 4.19 kHz, a DC voltage, $U = +2.5$ V, and a U/V ratio of 0.02 were used. In the filter mode, the QMF was set to a NP diameter of 7 nm. Then, the NPs pass through a mesh grid with +21.7 V grid bias voltage, enabling to determine the flux of the negatively charged NPs. It should be noted that also positively charged and neutral NPs contribute to the NP flux, which could not be detected by the positively charged mesh grid. Subsequently, NPs passing the QMF and the grid are deposited on the Si substrates, which are fixed on the substrate holder rotating at a continuous speed of 10 rpm. The pressure in the deposition chamber was set to 1.8×10^{-3} mbar. The NP deposition time was controlled using a shutter placed in front of the substrate holder. Before opening the shutter to start NP deposition on the substrates, a positive DC substrate bias voltage set to values between 0 V (grounded) and 1000 V was applied to the substrate holder to affect the NP landing conditions.
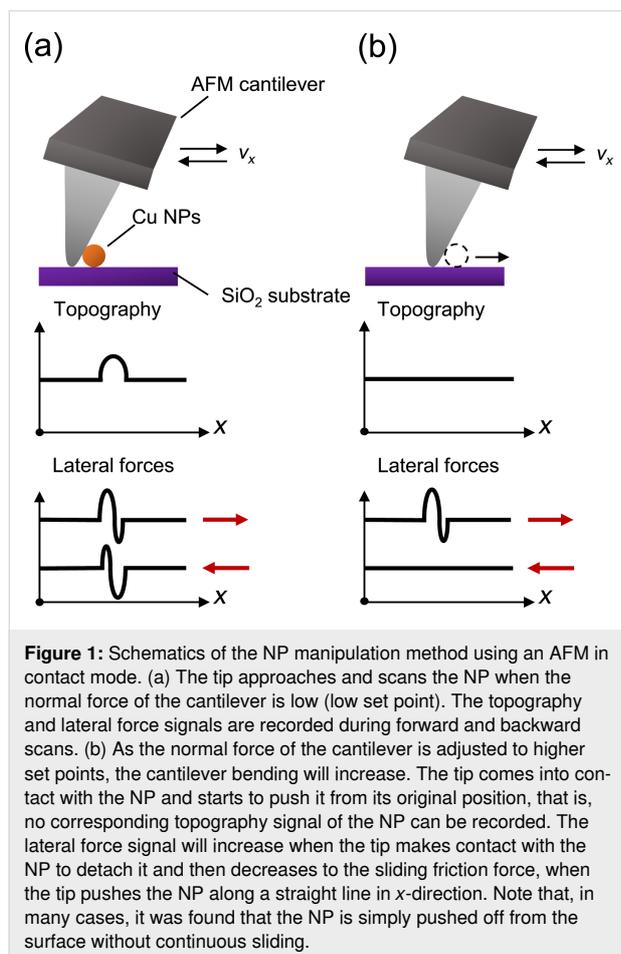
For the AFM measurements, a total of ten samples were prepared. For both wedge and D-LFC calibration, five samples were prepared with bias voltages of 0, 10, 100, 500, and 1000 V and corresponding deposition times of 60, 45, 10, 5, and 3 s, respectively. The deposition time was reduced for higher bias voltages to prevent full surface coverage as higher voltages have been found in our earlier work to increase the deposition rate [29]. To avoid significant oxidation of Cu NPs in ambient air, every sample was kept in a separate vacuum chamber until the AFM measurements.

AFM characterization

After calibrating the cantilever by either the wedge or the D-LFC method, each sample was immediately measured at the same day. It should be noted that using a sufficiently sharp tip,

the AFM investigation can proceed with the next sample without the need for recalibrating the cantilever. All AFM measurements were performed using an Asylum Research MFP 3D microscope at room temperature and under ambient conditions. AFM probes of type qp-CONT-10 provided by Nanosensors were applied in contact mode, with nominal force constants of 0.08–0.15 N·m^{-1} and tip curvature radii smaller than 10 nm. AFM topography images and lateral force data of the samples were processed using the open source software Gwyddion (version 2.63) [30]. For statistical analysis of the measured data, several independent areas were measured on each sample, ranging from 1×1 µm^2 to 10×10 µm^2. To obtain high-quality images, the scan speed was set to 750 nm·s^{-1} with 512 lines per frame, typically taking 30–35 min for a 10×10 µm^2 image. The wedge method measurements were conducted at 60% relative humidity (RH) and a temperature of 25 °C, whereas the D-LFC method measurements were performed at 40% RH and a temperature of 18 °C. All measurements were taken with a scan angle of 90° with respect to the long axis of the cantilever, and the z-scale used in Gwyddion for data analysis was set to 14 nm. Note that consecutively recorded AFM images (see below in Figure 2) usually exhibit a slight thermal drift. However, this does not interfere with the data evaluation. During AFM manipulation, NPs do not always move along straight lines. Small deviations, jumps, or irregular paths can occur, depending on local variations in friction and adhesion between the particle and the surface. Rao et al. studied such behavior and showed that the stability of NP trajectories decreases with lower interfacial friction [31]. Their results support our observations that differences in adhesion and surface conditions influence how Cu NP move and detach during manipulation. Similar trajectories as observed by Rao et al. occurred very rarely in our experiments. In this study, a frequently applied standard protocol for AFM manipulation was used [32]. The protocol consists of a two-step method and is schematically illustrated in Figure 1. First, an arbitrary area with size 5×5 µm^2 or 10×10 µm^2 was scanned in contact mode to identify regions containing a suitable surface coverage with Cu NPs. Subsequently, more detailed scans were conducted on smaller areas of interest, that is, 1×1 µm^2 or 2×2 µm^2, with higher resolution. These scans captured both topography signals from vertical cantilever movement and lateral signals from twisting of the cantilever (Figure 1a). The vertical bending of the cantilever, which is linked to the height of the NPs and to their diameter (assuming spherical NPs), was recorded to provide topography images. Lateral forces were measured by observing the twisting of the cantilever during forward and backward scans. If a higher set point is chosen, that is, a larger normal force is applied to the cantilever (Figure 1b), the respective NP is pushed from its original position (as evidenced by the corresponding topography images), resulting in differences in the measured lateral

forces. During NP manipulation, two primary forces dominate: The lateral force signal will increase when the tip hits the NP to overcome the NP adhesion strength to the substrate (static force) and decrease when the tip pushes the detached NP along a straight line in *x*-direction (sliding force) [16]. This approach shares similarities with manipulation of NPs from the side, known as "tip-on-side" mode [33]. However, in our approach, the tip is not pre-positioned in front of a NP of interest before manipulation; instead, it pushes NPs along the scan path on the substrate.

Figure 1: Schematics of the NP manipulation method using an AFM in contact mode. (a) The tip approaches and scans the NP when the normal force of the cantilever is low (low set point). The topography and lateral force signals are recorded during forward and backward scans. (b) As the normal force of the cantilever is adjusted to higher set points, the cantilever bending will increase. The tip comes into contact with the NP and starts to push it from its original position, that is, no corresponding topography signal of the NP can be recorded. The lateral force signal will increase when the tip makes contact with the NP to detach it and then decreases to the sliding friction force, when the tip pushes the NP along a straight line in *x*-direction. Note that, in many cases, it was found that the NP is simply pushed off from the surface without continuous sliding.

Lateral force calibration methods

In order to quantify NP adhesion and sliding friction, the cantilevers used need to be calibrated. Several calibration methods for AFM lateral force have been developed [34-36]. Among these, the wedge method [37] stands out as the most commonly utilized and, with subsequently suggested modifications [38], widely accepted state-of-the-art procedure. In this study, a TGZ calibration grating from NT-MDT with defined Si slopes of 55° was used for the wedge calibration. The method is based on scanning sloped surfaces to extract lateral force calibration parameters from friction loops. However, achieving precise cali-

bration with this indirect method requires considerable effort and extensive data processing. It relies extensively on the accuracy of the underlying mathematical models, which are based on the ratio of lateral and normal calibration constants. These ratios are obtained from the half-width and offset values of the measured torsion loops (friction loops), which are plots of lateral force vs displacement, showing frictional resistance as the tip scans a surface over a range of applied tip loads in ascending order. In the end, a series of friction loops needs to be measured for each applied tip load to calculate friction coefficients and, consequently, the lateral force calibration factor. This factor depends on the lateral sensitivity of the position-sensitive photodetector (PSPD), which gauges cantilever deflection as well as torsional spring constant [39]. However, errors can arise due to the sensitivity of the PSPD to laser alignment and a few micrometers offset from the tip shear center, leading to erroneous determination of the cantilever torsion loop offset. As a result, there is very low tolerance for measuring lateral forces with experimental errors in the nanonewton (nN) range [20]. That is why an alternative calibration method, utilizing a diamagnetic lateral force calibrator (D-LFC) [20] was developed, allowing for a direct calibration of the cantilever based on the independent calibration of the lateral force constant. In practice, this involves scanning the cantilever tip over the D-LFC surface to directly relate the deflection signal to the applied lateral force constant. Thus, the voltage signals provided by the PSPD are directly related to the lateral force applied on the tip. The sensitivity of both calibration methods is restricted by the radius of curvature of the tip, necessitating very sharp tips for the required high accuracy [20].

In this study, we calibrated the lateral force of the cantilever using either the wedge or the D-LFC method, based on the specific requirements of each experimental setup. The normal spring constant was determined using the thermal sweep method [40] implemented by default in the Asylum Research MFP-3D system. Table 1 summarizes the calibration constants and applied normal forces obtained for both wedge and D-LFC methods, which were used for all samples deposited at substrate bias voltages of 0, 10, 100, 500, and 1000 V.

Results and Discussion

Before manipulating the NPs on each sample, surface areas of $5 \times 5 \ \mu m^2$ or $10 \times 10 \ \mu m^2$ were pre-scanned. A sufficiently low surface coverage of Cu NPs was defined as the criterion for choosing a suitable area of interest because it allows each NP to be pushed independently and accurately, thereby enabling precise determination of the respective lateral force. Then, within these areas, selected $1 \times 1 \ \mu m^2$ areas of interest containing Cu NPs were scanned. The average lateral force required to push a Cu NP increases with increasing bias voltage, as will be

Table 1: Calibration and manipulation parameters determined for different substrate bias voltages and calibration methods.

Substrate bias (V)	Calibration method	Lateral spring constant [N·m^{-1}]	Normal spring constant (k_n) [N·m^{-1}]	Lateral sensitivity [nN·V^{-1}]	Normal sensitivity [nm·V^{-1}]	Applied normal force (F_n) [nN]
0	wedge	0.1	0.1	1	89	2
10	wedge	0.1	0.1	1	89	2
100	wedge	0.1	0.1	1	57	5
500	wedge	0.1	0.5	1	57	5
1000	wedge	0.1	0.1	1	64	3
0	D-LFC	0.2	0.2	2	64	3
10	D-LFC	0.2	0.2	2	72	3
100	D-LFC	0.2	0.1	2	68	2
500	D-LFC	0.2	0.1	2	82	1
1000	D-LFC	0.2	0.1	2	57	9

discussed in this study. Indeed, at bias voltages of 10 V and below, NP pushing already during surface scanning was unavoidable under the applied measuring conditions. Even standard scanning conditions, which were chosen to be "soft" with lower set points, resulted in removal of NPs. An example is demonstrated in Figure 2; Figure 2a–c presents consecutive scans of the same surface area of Cu NPs deposited at a bias voltage of 10 V onto Si. The height (which is identical to the diameter for spherical NPs) of the Cu NP within the green circle in Figure 2a was measured to 7 nm, as evidenced by the corre-

sponding 3D image in Figure 2d. The NP features visible in Figure 2a appear to have uniform shape and size. This indicates that the NPs are smaller than the AFM tip (tip radius ≤ 10 nm), and the tip-convolution effect [41] results in images representing rather the tip shape than the actual NPs. Figure 2b indicates that the number of NPs is reduced after each scan. The streaky features at the lower area of the image, highlighted by red, green, and white circles, represent signatures of pushing events. These streaks indicate where NPs have been displaced, vanishing from one scan line to the other. The corresponding
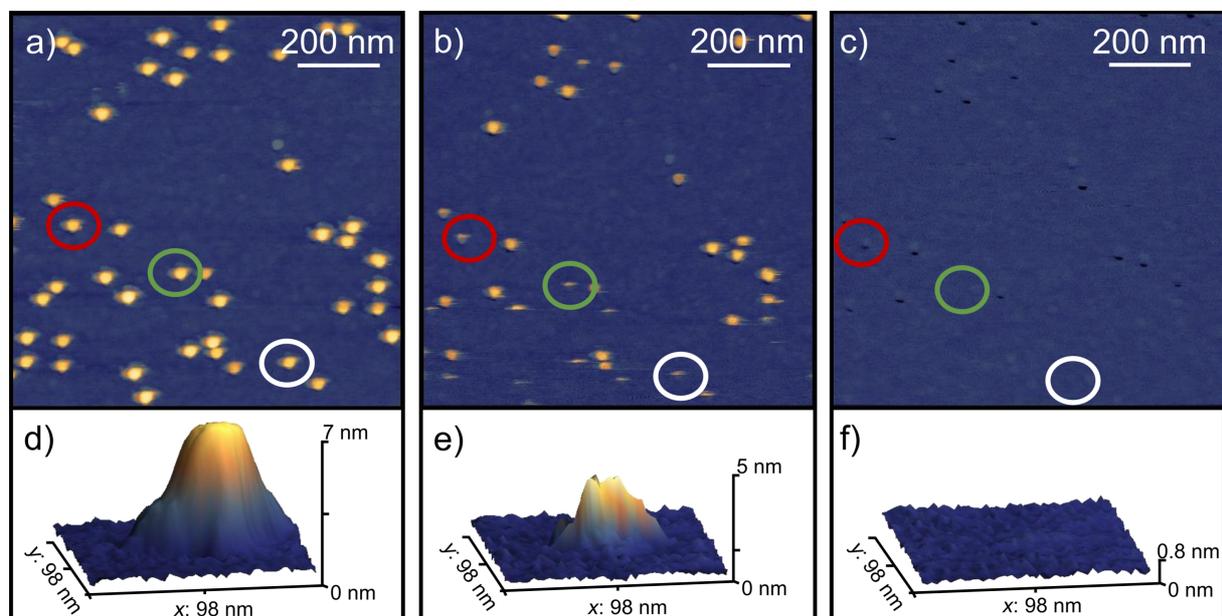
Figure 2: AFM topography images (1 × 1 μm^2) of Cu NPs on Si deposited at a bias voltage of 10 V with a scan angle of 90° and a *z*-scale of 14 nm. The red, green, and white circles highlight three NP manipulation examples: (a) the initial scan for imaging Cu NPs, (b) the second scan where the NPs start to be pushed, and (c) the third scan showing the removal of NPs from the surface area. Corresponding 3D images of the green circles in (a), (b), and (c) are displayed in (d), (e), and (f), respectively. Note that the black dots in (c) are "holes" left by NPs pushed during the scanning process. A cropped AFM topography image (5 × 5 μm^2, *z*-scale of 14 nm) of the same region, demonstrating that the displaced Cu NPs accumulate at the edges of the 1 × 1 μm^2 scan area, is provided in Supporting Information File 1 (Figure S1).

3D image in Figure 2e indicates a change in the NP's position relative to the substrate. The reduction in height from 7 to 5 nm is interpreted as the initial stage of NP displacement, where the particle starts moving before the tip has reached the NP's top. Also tilting and/or deforming of the NP might occur. After the third scan, Figure 2c and the corresponding 3D image in Figure 2f clearly evidence that all NPs were completely removed from the surface area, confirming successful pushing. The black dots in Figure 2c obviously stem from pushed NPs, leaving holes with a depth of up to 7 nm in the Si surface. The origin of these holes still needs to be clarified, but formation during NP impact (at high substrate voltages) due to plastic deformation/tilting, formation of the Cu_3Si intermetallic phase [42], and/or fracturing of the NP/substrate interface [43] might be possible reasons. In addition, since Si(100) substrates are naturally covered by a thin native SiO_2 layer under ambient conditions and may form a mixed SiO_xN_y surface after N_2 plasma cleaning, local modification of this oxide or oxynitride layer by NP impact, such as partial penetration, removal, or reduction cannot be excluded. We did not detect changes in the roughness between pristine and plasma-treated surfaces (RMS < 0.2 nm at 5 × 5 μm area) that would contribute to a change in friction. Interfacial redox reactions between the copper NP and the wafer surface might also contribute to this behavior. However, to the best of the authors' knowledge, no description of such reactions has been published so far. In addition, it should be noted that such pits were only observed in this specific sample.

Binns describes three distinct energy regimes for NP deposition, namely, low, medium, and high energies, corresponding to total energy per atom ranges of 0.1 eV·atom^{-1}, 1–10 eV·atom^{-1}, and more than 10 eV·atom^{-1}, respectively [44]. In our study, size-selected Cu NPs with a diameter of 7 nm (i.e., around 15000 atoms, assuming a spherical NP shape and the theoretical density of Cu) were considered. Assuming an initial velocity of ≈100 m·s^{-1} [45] for 0 V acceleration bias, the total energy per atom increases linearly from 0.003 eV·atom^{-1} at 0 V to 0.068 eV·atom^{-1} at 1000 V, placing the single-charged NPs within the low-energy regime (soft landing) [46]. Note, the term "soft" just means that the kinetic energy carried with the NP, equally distributed over the contained atoms, is insufficient to break the metallic atom–atom bonding in the NP. However, bond breaking cannot be excluded for multiply charged and, thus, much more energetic NPs. Nevertheless, the impact can still result in high forces in the small region at the NP/substrate interface. However, under such low-energetic conditions there is a good chance that NPs deposit "softly" at their landing sites, becoming immobilized with minimal distortion and no significant surface damage.

Figure 3 represents an attempt to quantify the interfacial adhesion of Cu NPs on Si substrates as a function of the applied substrate bias voltage. In Figure 3a, the lateral force values required to push Cu NPs for both wedge and D-LFC methods are compared, and no clear trend emerges as all data points fall within the error bars. The significant scatter in the data, with the exception of the 0 and 500 V biases, prevents establishing a clear relationship between lateral force and substrate bias. Both calibration methods provide similar lateral force values, suggesting that measurement uncertainties are responsible for the observed scatter. Considering the results for a substrate bias

Figure 3: (a) Relationship between the average lateral force necessary to push Cu NPs on Si and the applied bias voltages for wedge and D-LFC calibration. (b) Average lateral force necessary to push NPs with a given diameter deposited at a bias voltage of 0 V, where the individual symbols for wedge and D-LFC calibration each include twelve data points, resulting in a total of 24 data points. Note that some error bars are too small to be visible.

voltage of 0 V in Figure 3b, the wedge and D-LFC results are closely aligned, although the wedge method yields slightly higher values. The NP size dependence of measurement accuracy might be attributed to the variations in contact geometry arising from the difference of the tip's radius of curvature and NP diameter. Further, NP deformation and possible tip-on-NP gliding may result in additional/altered forces. The relative contribution of those additional effects is the stronger the weaker the particle adheres. Environmental factors, such as humidity and temperature, may also have contributed, particularly through enhanced capillary forces between tip and sample during AFM characterization. In general, as the NPs size increases, the lateral force required to push NPs is expected to increase. This expectation is attributed to the larger NP/substrate contact area, which strengthens interfacial adhesion forces and increases resistance to displacement. However, the interfacial forces are not only influenced by NP size but depend on the rather complex interplay of a number of parameters such as impact velocity, impact angle, surface energy, NP surface termination, relative orientation of the NP upon landing, and mechanical properties of NP and substrate [46,47]. However, a very decisive parameter is the impact velocity, which can be controlled by the substrate bias voltage applied during deposition. A higher bias voltage results in more kinetic energy of the NPs, leading to higher impact energy upon landing. The landing energy can enhance interfacial adhesion, as the NPs may embed more deeply into the substrate [29]. For larger NPs, this effect can result in even stronger adhesion; thereby, a higher lateral force is required to push them. However, plotting lateral force versus bias voltage, as done in Figure 3a, does not yield meaningful insights. Thus, we focus on the energy needed to move the NPs, as the energy is a more general and comparable parameter across different samples. Therefore, our next attempt includes the force profile and the distance along which the NPs are pushed, offering a more robust measure of interfacial adhesion.

To provide a reliable and accurate measure of the energy required to manipulate the NPs, the total work of manipulation (W_m) was calculated by taking the integral of lateral force (LF) over the manipulation distance (l_m) in x-direction. The procedure is illustrated in Figure 4. For each NP pushing event, W_m was calculated using Equation 1:

$$W_m = \int_0^{l_m} \text{LF} \, dx. \qquad (1)$$

The area under the lateral force versus manipulation distance curve, as indicated by points 1 to 3 in Figure 4b, corresponds to the total work of manipulation. It should be noted that the derived values for the total work of manipulation include both the actual work of separation W_{sep} and the dissipated work W_{diss}, which does not contribute to the separation. The relationship can be expressed as:
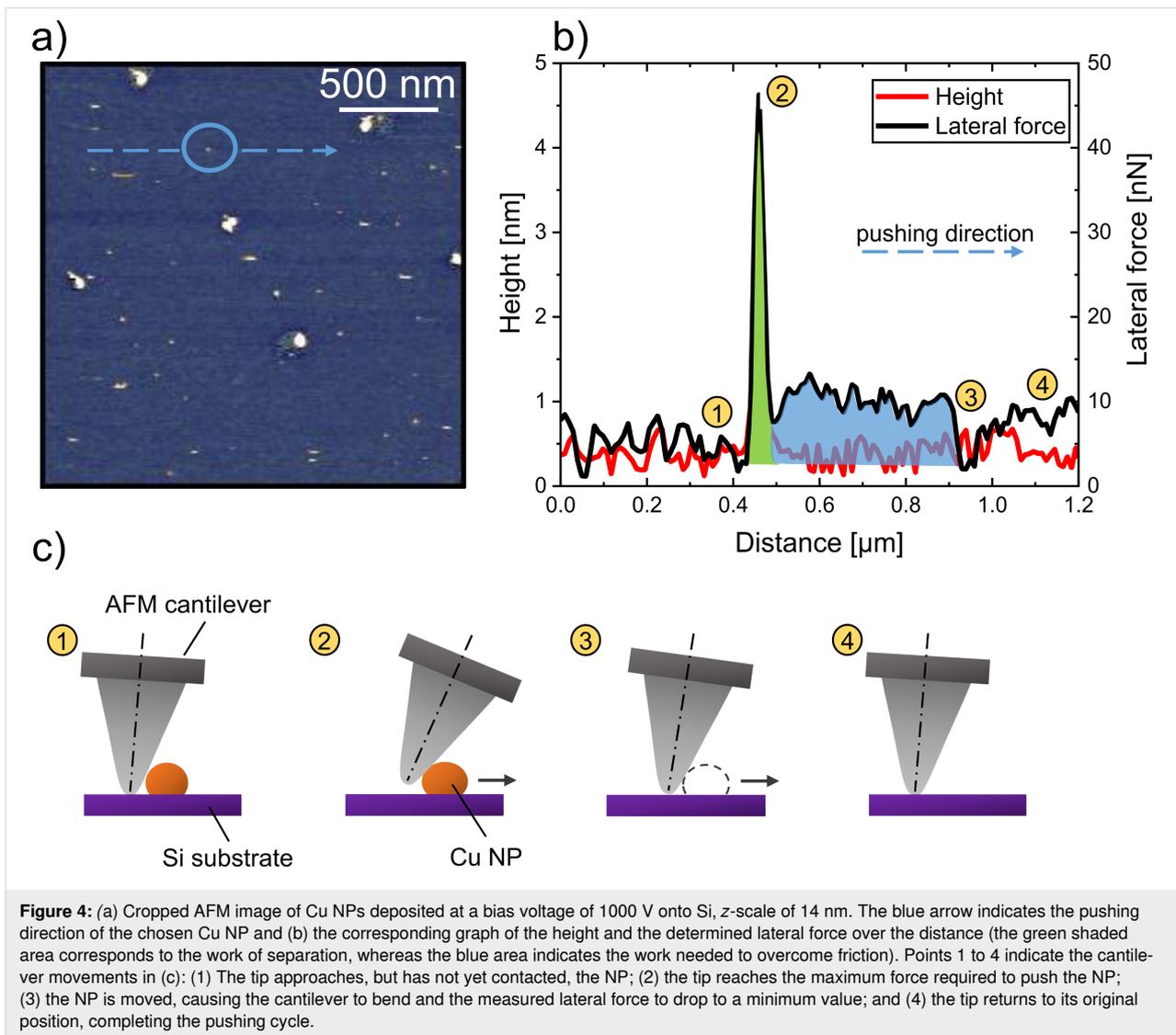
$$W_m = W_{sep} + W_{diss}. \qquad (2)$$

NP motion on a surface may not necessarily proceed as an ideal lateral sliding path. Depending on the local contact geometry, the displacement may also include a rolling component. According to Tafazzoli et al., sliding motion sets in first and is dominant over rolling motion [48]. When the force exceeds a critical threshold, rolling and sliding can occur simultaneously. However, since the maximum forces remain below 40 nN, a rolling contribution is highly unlikely. In addition, the presented formalism would not change if rolling motion was present, as it can be expressed analogously by the product of normal force and (rolling) friction coefficient. Thus, the overall NP displacement is described as a translation, covering both sliding- and rolling-like contributions [16]. The work extracted from the lateral force–distance integral therefore represents the effective energy required to translate a NP on the surface. For simplicity, we calculate the work of manipulation as a first approximation for the work of adhesion as the details in the process of manipulation are rather complex including adhesion, static and dynamic friction, and humidity [49]. Due to the challenges in direct calculation of the dissipated work, the work of separation is approximated using the following equation:

$$W_{sep} \approx \frac{\left[F_{static} - \left(F_{cap} \cdot \mu + F_n \cdot \mu \right) \right] \cdot l_s}{2}, \qquad (3)$$

where F_{static} is the maximum static lateral force, F_{cap} represents the capillary force, and F_n is the normal force applied by the cantilever. μ is the coefficient of friction and l_s the separation distance given by the distance between the first tip/NP contact and the position with the maximum lateral force needed to separate the NP from the substrate surface [50]. Both F_{static} and F_{cap} are typically very small in magnitude, contributing only minimally to the overall force. The factor 1/2 accounts for the relevant part of the lateral force vs distance curve, which is to a good approximation triangular (see green shaded part of Figure 4b.

An exemplary calculation is provided for the NP marked by the blue arrow in Figure 4a, where the corresponding lateral force and height profiles are plotted in Figure 4b. The separation distance l_s is the x-separation between points 1 and 2 indicated in Figure 4b. A corresponding scheme is provided in Figure 4c. For the sake of brevity, from now on, we will use the term "dis-
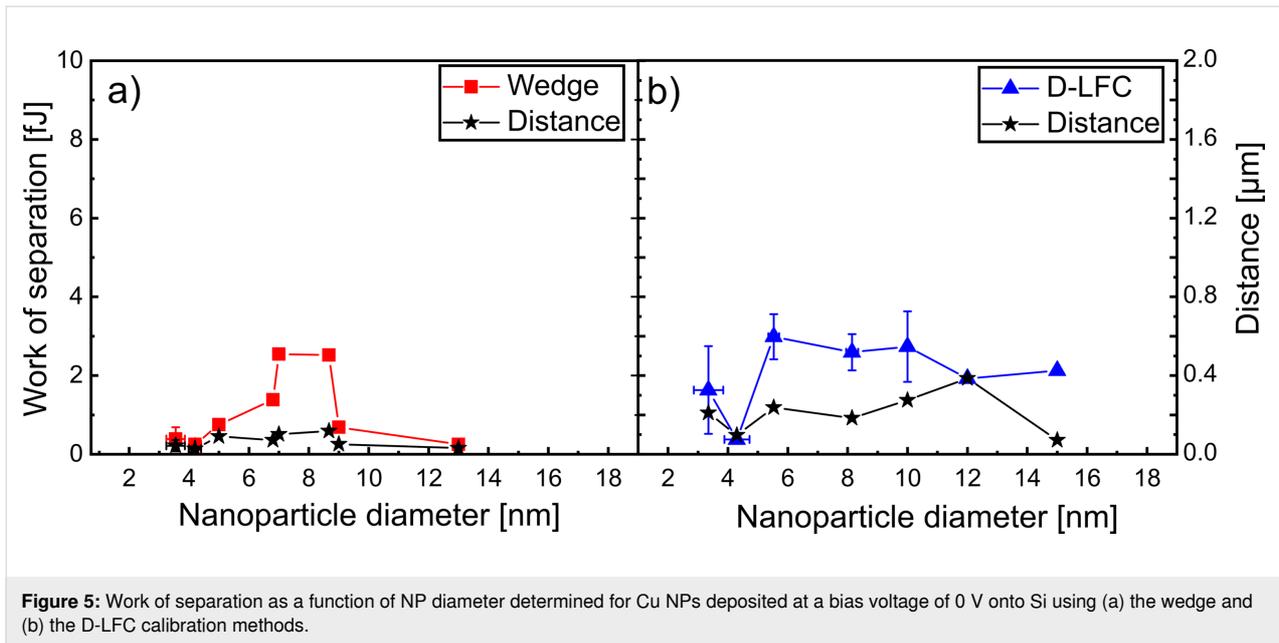
Figure 4: *(a)* Cropped AFM image of Cu NPs deposited at a bias voltage of 1000 V onto Si, *z*-scale of 14 nm. The blue arrow indicates the pushing direction of the chosen Cu NP and (b) the corresponding graph of the height and the determined lateral force over the distance (the green shaded area corresponds to the work of separation, whereas the blue area indicates the work needed to overcome friction). Points 1 to 4 indicate the cantilever movements in (c): (1) The tip approaches, but has not yet contacted, the NP; (2) the tip reaches the maximum force required to push the NP; (3) the NP is moved, causing the cantilever to bend and the measured lateral force to drop to a minimum value; and (4) the tip returns to its original position, completing the pushing cycle.

tance" synonymously with "separation distance" as used in Equation 3. In more detail, at point 1, the cantilever approaches the NP on the Si substrate. Point 2 corresponds to the maximum lateral force required to initiate NP displacement, as shown by the green-shaded area, which represents the work of separation. Beyond this, at points 3 and 4, the NP is already pushed out of the intimate contact with the surface [49] and, thus, has overcome the adhesion strength. The blue-shaded area represents the work dissipated due to sliding friction, which is not included in the calculation. The approximation of work of separation assumes a linear NP translation along the scan direction. Minor deviations from this ideal path may occur, but they remain within the scatter of the presented data.

While an increase in the work of separation with NP diameter was expected, the lateral force versus NP diameter in Figure 3b does not show a clearly increasing trend. Instead, the results

presented in Figure 5 show a different behavior, as exemplified for a substrate bias voltage of 0 V. Specifically, both work of separation and distance reach maximum values for NP diameters between 6 and 10 nm. NPs outside this size range exhibited lower work of separation values as well as shorter distances. With an AFM tip diameter smaller than 10 nm, it has to be assumed that the behavior shown in Figure 5 is affected by the interaction between tip and NPs. This could also explain why both calibration methods show peak values at certain NP sizes, suggesting that each method has certain particle ranges where it performs most reliably.

The relationship between work of separation and distance for the different NP diameter size ranges and substrate bias voltages is summarized in Figure 6. As the applied voltage increases, the peak values for both work of separation and distance shift from the 6–10 nm range to 10–12 nm. This indicates

Figure 5: Work of separation as a function of NP diameter determined for Cu NPs deposited at a bias voltage of 0 V onto Si using (a) the wedge and (b) the D-LFC calibration methods.

that a larger lateral force, and consequently a higher work of separation, is required to manipulate NPs in this size range. In our approach, the work of separation includes both the work of adhesion and the dissipated energy that is lost via different channels during the pushing experiment (e.g., deformation energy of NP and/or surface). Despite this, we consider the results to still reflect the work of adhesion between the NP and the surface reasonably well.

As generally expected, the typical work of adhesion increases with higher substrate bias voltage. For instance, although the total kinetic energy for 2 nm NPs increases by a factor of ≈390 between 0 and 1000 V bias, the energy per atom (≈2.8 eV·atom^{-1}) is still clearly below the binding strength of a bulk Cu–Cu bond (≈3.5 eV·atom^{-1}) [51]. This energy per atom remains near the upper limit of the soft-landing regime, but approaches the threshold of the intermediate regime [46]. Larger NPs (10–12 nm) require higher values of work of separation, as particularly evident at 100 and 1000 V. This may be due to increased adhesion, although interaction of the tip simultaneously with several NPs at once cannot be excluded.

Nevertheless, we observed a trend towards increasing overall translation distances (up to ≈2 μm at 1000 V) at higher acceleration voltages (Figure 6). Even though the work of separation invested to detach the NPs from their resting positions has no clear dependence on acceleration bias or NP size, the longer transition distances might be indicative for stronger NP/substrate adhesion. This is in line with the short translation distances and smallest work of separation values for the 500 V case.

Although the dataset shows considerable scatter, the size-dependent behavior can still be discussed on a qualitative level. In order to deliver a plausibility argument for our observation, we refer to the approach of Weir and McGavin [8], who developed an analytic model for describing the coefficient of restitution of NPs rebounding from an ideally flat and rigid surface. Note that it delivers just a semi-quantitative trend and is not a rigorous description of the process. Their model provides a criterion to determine whether an NP escapes or is captured upon impact. This condition is expressed as:

$$
\begin{aligned}
F_0 > 6\pi R\gamma \quad &\text{(NP escape)} \\
F_0 < 6\pi R\gamma \quad &\text{(NP capture),}
\end{aligned}
\tag{4}
$$

where F_0 is the force acting to detach the NP from the surface, and $6\pi R\gamma$ is the adhesive force trying to hold the NP on the surface. R represents the radius of curvature defining the NP contact region with the surface, and γ is the interface/surface energy. As previously discussed, the NP/substrate adhesion represents a complex system involving many parameters, most of which can only be approximated.

For the calculation, the substrate is treated as ideally flat, perfectly smooth, and infinitely rigid, and its properties are therefore not considered in the model. The total velocity of a NP, v_i, can be expressed as follows:

$$
v_i = A \cdot d^{-b} + \sqrt{\frac{12e \cdot V}{\rho \cdot \pi \cdot d^3}},
\tag{5}
$$
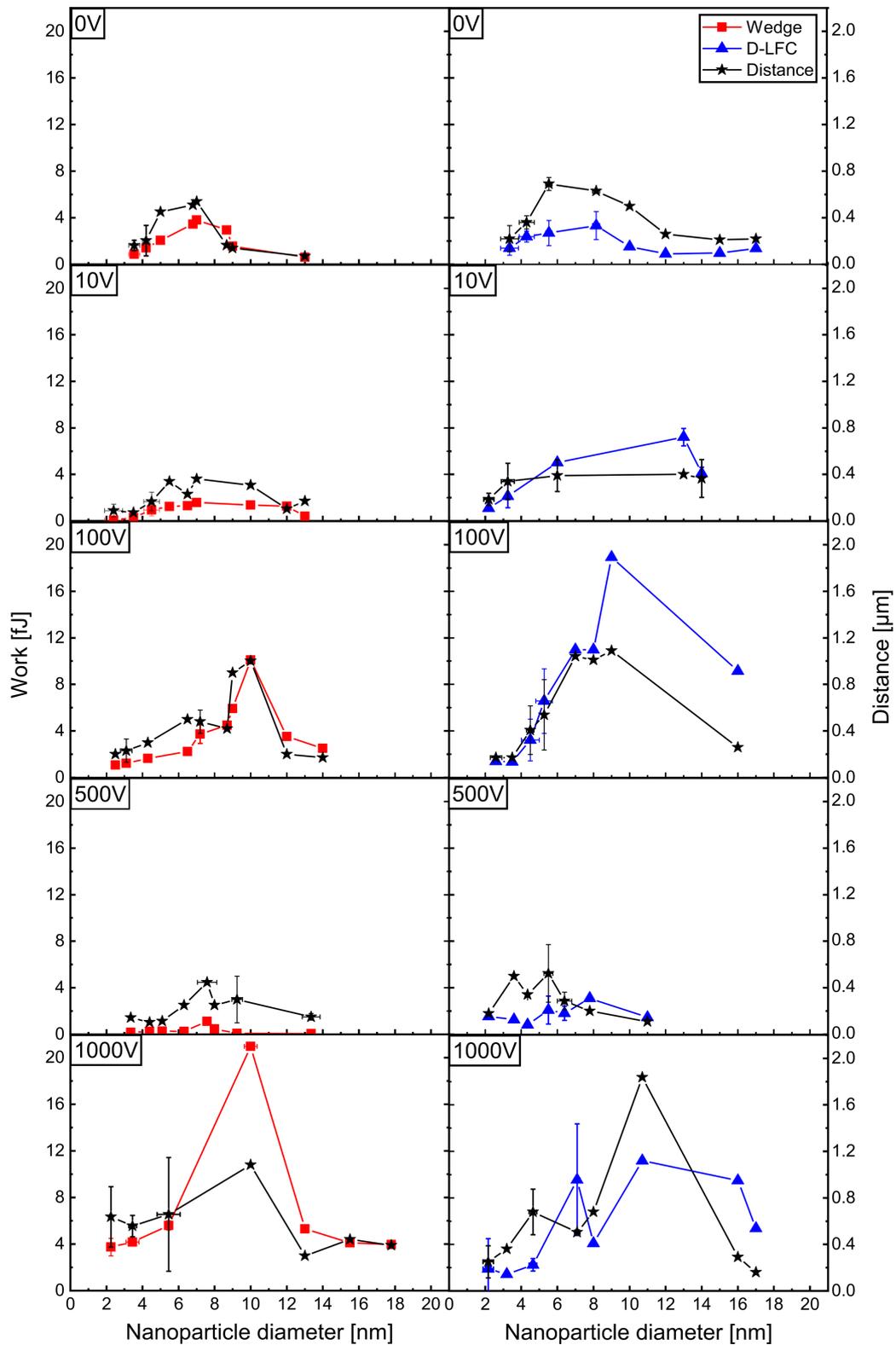
Figure 6: Relationship between work of separation and NP diameter at different substrate bias voltages. In addition, the distance (black stars) moved by the NPs is also indicated. For comparison, two sets of experiments with different lateral force calibration methods are shown (left column: wedge method; right column: D-LFC method). Each work of separation symbol represents the average of twelve data points. Note that some error bars are too small to be visible.

where the first term corresponds to the initial NP velocity as it exits the NP source orifice, and the second term is the velocity added due to the substrate bias V. The density ρ was assumed to be the room-temperature bulk density of Cu with 8935 kg·m^{-3} [52]. The parameters A and b, taken from the literature, are 188 m$^{1.35}$·s^{-1} and 0.35, respectively [45], and d represents the NP diameter. NP charge states may vary as neutral, single, or multiple, while only at 0 V substrate bias of all them may arrive at the substrate. For simplicity, we assumed a single elementary charge e having a value of 1.6×10^{-19} A·s [53]. Choosing the mechanical properties of the NPs is not straightforward as their internal structure is unknown. Nevertheless, the following parameters were used for the model: γ was taken as 2.3 J·m^{-2} [54], the Young's modulus E of copper as 150 MPa [4], and the yield strength Y of Cu NPs with a diameter of ≈ 20 nm as 11 GPa [55]. While E and Y are not explicitly included in Equation 5, both parameters are essential for the model. Y affects the NP/substrate contact area and the plastic deformation, which determine F_0 and whether the NP will rebound or stick to the substrate. A high Y limits deformation, reducing F_0; a low Y increases deformation and adhesion. E is applied in the calculation of the elastic energy, which contributes to the deformation behavior model and the energy balance used to describe the NP/substrate interaction in the model. For a high E, more elastic energy is stored, promoting rebound, while at a low E, less energy is stored, favoring sticking. The values might seem high compared to bulk or polycrystalline Cu materials, but such values are common for single-crystalline Cu. In Figure 7 the theoretical adhesion threshold, $F_0 - 6\pi R\gamma$, values are plotted as a function of the NP diameter. Negative values indicate the sticking regime, and positive values correspond to NP rebound (compare Equation 4). As shown in Figure 7, these calculated values reach their minimum between 6 and 10 nm across all voltages, suggesting a transition point in NP behavior. Notably, lower values of $F_0 - 6\pi R\gamma$ mean a higher probability of sticking. This theoretical behavior matches well with our experimental observations, particularly with the stronger adhesion measured for particles in the 6–12 nm range with increasing substrate bias.

Interestingly, the model predicts a rebound for all NP diameters at a substrate bias voltage of 1000 V, which appears rather counterintuitive. This result stems from the oversimplifications within the model. In reality, the NPs are unlikely to be perfectly spherical; they likely possess facetted surfaces due to their crystalline nature. Consequently, both the interface energy and the mechanical properties can vary depending on the particle orientation and contacting facet, such as (001) and (111), as shown in [4]. Further, the yield strength effects are also entirely omitted. In addition, neither chemical interactions with the substrate nor its mechanical response are considered. For small NP diameters
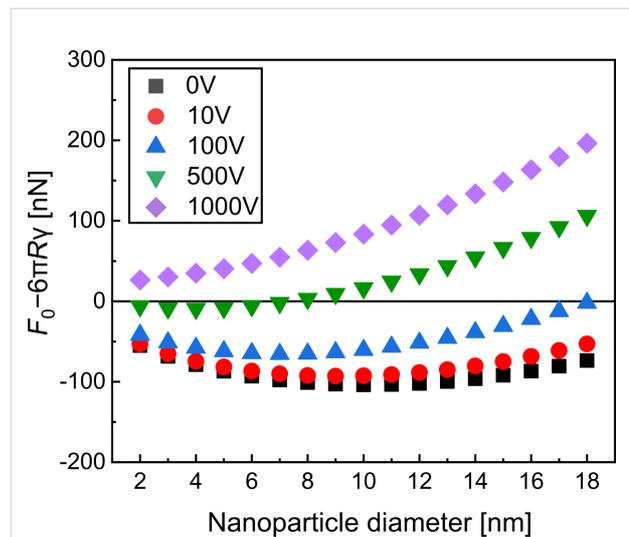
Figure 7: Deviation from the adhesion threshold $F_0 - 6\pi R\gamma$ as a function of NP diameter under varying substrate bias voltages.

(2–4 nm), the predicted deformation seems clearly overestimated, as the theoretical contact radius exceeds the NP size, suggesting full flattening of the particle into a disk, which was not observed experimentally. However, it should be noted that the AFM tip radius was 7–10 nm, meaning that features smaller than this remain unresolved, and the true NP shape remains unknown.

An attempt to recalculate the specific interface energies from the measured work of adhesion, using theoretically calculated contact areas, yields values in the range of 6 ± 2 J·m^{-2} at 500 V to 30 ± 30 J·m^{-2} at 0–100 V and 150 ± 150 J·m^{-2} at 1000 V. The deviation from the input value of 2.3 J·m^2 indicates the limitations of the model in capturing the full complexity of the interaction. While the case from 0 to 500 V is in fair agreement with interface energies of sputter-deposited Cu films grown on SiO$_2$/Si substrates at temperatures of 100–120 °C [56], the 1000 V case deviates substantially. This is most likely to due to the high impact velocities, which also include a rapid and strong temperature increase upon impact. Thus, the validity range of the Weir and McGavin model, which does not include temperature effects, is exceeded. Such effects could include massive dislocation activity at the interface and formation of the Cu$_3$Si intermetallic phase, both leading to interface strengthening. Future research on local interface formation between substrates and NPs with different kinetic energies would be necessary to establish a comprehensive understanding of NP adhesion. Despite the deviations between theoretically predicted and measured adhesion energies, the model still highlights a key point: A higher impact energy does not necessarily lead to stronger NP adhesion.

Conclusion

In this study, we examined the adhesion properties of Cu nanoparticles (NPs) on Si substrates, with a focus on varying landing conditions affected by the applied substrate bias voltages during NP deposition. The examined NP sizes ranged from 1 to 18 nm. AFM was utilized to measure the lateral forces required for NP manipulation, and we explored both lateral force–distance curves and work of separation as characteristic values to evaluate NP adhesion. Lateral force–distance curves alone did not provide comprehensive understanding of NP/substrate adhesion, and no clear trends were observed when correlating lateral forces with bias voltages. In contrast, the work of separation calculated as the integral of lateral force over the distance offered more accurate and insightful characteristics for NP adhesion.

The proposed method highlights the interplay between NP landing conditions governed by deposition parameters and NP-specific values like their diameter, surface energy, Young's modulus, yield strength, as well as their crystallography-related anisotropies. Higher bias voltages and increased NP sizes did not automatically result in stronger adhesion. Typically, the adhesion was the strongest for NP diameters between 6 and 12 nm and reduced for larger NPs. A simple analytical model showed qualitative agreement with the AFM-based results, confirming that the adhesion is not a monotonic function of the sample bias voltage.

AFM-based manipulation was shown to be a reliable and reproducible method for quantifying NP adhesion, yielding consistent results across different calibration methods. The observed relationship between deposition parameters and adhesion strength provides a practical framework for characterizing NP/substrate interactions. Such understanding is essential for developing reliable NP coatings, where adhesion directly influences coating stability, uniformity, and functional performance under varying environmental and mechanical stress conditions during the use of functional devices or surfaces. Future studies should focus on the effects of environmental factors, such as humidity and temperature, and the exploration of alternative NP/substrate combinations to expand the understanding of the adhesion mechanisms at the nanoscale.

Supporting Information

Supporting Information File 1

AFM topography of manipulated Cu nanoparticles.
[https://www.beilstein-journals.org/bjnano/content/
supplementary/2190-4286-17-1-S1.pdf]

Author Contributions

Aydan Çiçek: conceptualization; formal analysis; investigation; methodology; visualization; writing – original draft. Markus Kratzer: formal analysis; investigation; methodology; resources; writing – review & editing. Christian Teichert: resources; supervision; writing – review & editing. Christian Mitterer: conceptualization; resources; supervision; writing – review & editing.

ORCID® iDs

Aydan Çiçek - https://orcid.org/0009-0001-4942-2795
Markus Kratzer - https://orcid.org/0000-0001-5181-6796
Christian Teichert - https://orcid.org/0000-0002-0796-2355
Christian Mitterer - https://orcid.org/0000-0002-7768-7926

Data Availability Statement

Data generated and analyzed during this study is available from the corresponding author upon reasonable request.

References

1. Al Mahmud, M. Z. *J. Nanomater.* **2023,** *2023,* 5432099.
   doi:10.1155/2023/5432099
2. Matsui, I. *J. Chem. Eng. Jpn.* **2005,** *38,* 535–546.
   doi:10.1252/jcej.38.535
3. Wu, B.; Miraghaee, S.; Handa, S.; Gallou, F.
   Curr. Opin. Green Sustainable Chem. **2022,** *38,* 100691.
   doi:10.1016/j.cogsc.2022.100691
4. Erbì, M.; Amara, H.; Gatti, R. *Small* **2023,** *19,* 2302116.
   doi:10.1002/smll.202302116
5. Popok, V. N.; Gurevich, L. *J. Nanopart. Res.* **2019,** *21,* 171.
   doi:10.1007/s11051-019-4615-1
6. Johnston, L. J.; Mansfield, E.; Smallwood, G. J. Physicochemical
   Properties of Engineered Nanomaterials. In *Metrology and
   Standardization of Nanotechnology: Protocols and Industrial
   Innovations;* Mansfield, E.; Kaiser, D. L.; Fujita, D.; Van de Voorde, M.,
   Eds.; Wiley-VCH: Weinheim, Germany, 2017; pp 99–114.
   doi:10.1002/9783527800308.ch5
7. Lehtinen, K. E. J.; Zachariah, M. R. *Phys. Rev. B* **2001,** *63,* 205402.
   doi:10.1103/physrevb.63.205402
8. Weir, G.; McGavin, P. *Proc. R. Soc. A* **2008,** *464,* 1295–1307.
   doi:10.1098/rspa.2007.0289
9. Oras, S.; Vlassov, S.; Berholts, M.; Lõhmus, R.; Mougin, K.
   Beilstein J. Nanotechnol. **2018,** *9,* 660–670. doi:10.3762/bjnano.9.61
10. Xiao, Z.; Zhao, Q.; Niu, Y.; Zhao, D. *Soft Matter* **2022,** *18,* 3447–3464.
    doi:10.1039/d2sm00265e
11. Sorenson, A. H. T. N. Immobilization of Copper Nanoparticles onto
    Various Supports Applications in Catalysis. Ph.D. Thesis, Brigham
    Young University, Proto, UT, USA, 2020.
12. Resch, R.; Meltzer, S.; Vallant, T.; Hoffmann, H.; Koel, B. E.;
    Madhukar, A.; Requicha, A. A. G.; Will, P. *Langmuir* **2001,** *17,*
    5666–5670. doi:10.1021/la001296p

13. Ming, W.; Wu, D.; van Benthem, R.; de With, G. *Nano Lett.* **2005,** *5,* 2298–2301. doi:10.1021/nl0517363

14. Kim, S.; Shafiei, F.; Ratchford, D.; Li, X. *Nanotechnology* **2011,** *22,* 115301. doi:10.1088/0957-4484/22/11/115301

15. Junno, T.; Deppert, K.; Montelius, L.; Samuelson, L. *Appl. Phys. Lett.* **1995,** *66,* 3627–3629. doi:10.1063/1.113809

16. Dietzel, D.; Schwarz, U. D.; Schirmeisen, A. *Friction* **2014,** *2,* 114–139. doi:10.1007/s40544-014-0054-2

17. Vasić, B.; Stanković, I.; Matković, A.; Kratzer, M.; Ganser, C.; Gajić, R.; Teichert, C. *Nanoscale* **2018,** *10,* 18835–18845. doi:10.1039/c8nr04865g

18. Dietzel, D.; Mönninghoff, T.; Herding, C.; Feldmann, M.; Fuchs, H.; Stegemann, B.; Ritter, C.; Schwarz, U. D.; Schirmeisen, A. *Phys. Rev. B: Condens. Matter Mater. Phys.* **2010,** *82,* 035401. doi:10.1103/physrevb.82.035401

19. Klünsner, T.; Shen, Q.; Hlawacek, G.; Teichert, C.; Fateh, N.; Fontalvo, G. A.; Mitterer, C. *Thin Solid Films* **2010,** *519,* 1416–1420. doi:10.1016/j.tsf.2010.09.040

20. Li, Q.; Kim, K.-S.; Rydberg, A. *Rev. Sci. Instrum.* **2006,** *77,* 065105. doi:10.1063/1.2209953

21. Baur, C.; Bugacov, A.; Koel, B. E.; Madhukar, A.; Montoya, N.; Ramachandran, T. R.; Requicha, A. A. G.; Resch, R.; Will, P. *Nanotechnology* **1998,** *9,* 360–364. doi:10.1088/0957-4484/9/4/011

22. Hlawacek, G.; Shen, Q.; Teichert, C.; Lex, A.; Trimmel, G.; Kern, W. *J. Chem. Phys.* **2009,** *130,* 044703. doi:10.1063/1.3062841

23. Eppler, A. S.; Rupprechter, G.; Anderson, E. A.; Somorjai, G. A. *J. Phys. Chem. B* **2000,** *104,* 7286–7292. doi:10.1021/jp0006429

24. Dietzel, D.; Mönninghoff, T.; Jansen, L.; Fuchs, H.; Ritter, C.; Schwarz, U. D.; Schirmeisen, A. *J. Appl. Phys.* **2007,** *102,* 084306. doi:10.1063/1.2798628

25. Sümer, B.; Sitti, M. *J. Adhes. Sci. Technol.* **2008,** *22,* 481–506. doi:10.1163/156856108x295527

26. Hartmuth, F.; Dietzel, D.; de Wijn, A. S.; Schirmeisen, A. *Lubricants* **2019,** *7,* 66. doi:10.3390/lubricants7080066

27. Cihan, E.; Dietzel, D.; Jany, B. R.; Schirmeisen, A. *Phys. Rev. Lett.* **2023,** *130,* 126205. doi:10.1103/physrevlett.130.126205

28. Knabl, F.; Bandl, C.; Griesser, T.; Mitterer, C. *J. Vac. Sci. Technol., A* **2024,** *42,* 023201. doi:10.1116/6.0003283

29. Knabl, F.; Gutnik, D.; Patil, P.; Bandl, C.; Vermeij, T.; Pichler, C. M.; Putz, B.; Mitterer, C. *Vacuum* **2024,** *230,* 113724. doi:10.1016/j.vacuum.2024.113724

30. Nečas, D.; Klapetek, P. *Cent. Eur. J. Phys.* **2012,** *10,* 181–188. doi:10.2478/s11534-011-0096-2

31. Rao, A.; Wille, M.-L.; Gnecco, E.; Mougin, K.; Meyer, E. *Phys. Rev. B* **2009,** *80,* 193405. doi:10.1103/physrevb.80.193405

32. Requicha, A. A. G.; Meltzer, S.; Arce, F. T.; Makaliwe, J. H.; Sikén, H.; Hsieh, S.; Lewis, D.; Koel, B. E.; Thompson, M. E. Manipulation of nanoscale components with the AFM: principles and applications. In *Proceedings of the 2001 1st IEEE Conference on Nanotechnology. IEEE-NANO 2001,* Maui, HI, U.S.A., Oct 28–30, 2001; IEEE: Piscataway, NJ,, 2001; pp 81–86. doi:10.1109/nano.2001.966398

33. Dietzel, D.; Feldmann, M.; Herding, C.; Schwarz, U. D.; Schirmeisen, A. *Tribol. Lett.* **2010,** *39,* 273–281. doi:10.1007/s11249-010-9643-z

34. Liu, E.; Blanpain, B.; Celis, J. P. *Wear* **1996,** *192,* 141–150. doi:10.1016/0043-1648(95)06784-1

35. Cain, R. G.; Biggs, S.; Page, N. W. *J. Colloid Interface Sci.* **2000,** *227,* 55–65. doi:10.1006/jcis.2000.6840

36. Ogletree, D. F.; Carpick, R. W.; Salmeron, M. *Rev. Sci. Instrum.* **1996,** *67,* 3298–3306. doi:10.1063/1.1147411

37. Varenberg, M.; Etsion, I.; Halperin, G. *Rev. Sci. Instrum.* **2003,** *74,* 3362–3367. doi:10.1063/1.1584082

38. Khare, H. S.; Burris, D. L. *Rev. Sci. Instrum.* **2013,** *84,* 055108. doi:10.1063/1.4804163

39. Wang, H.; Gee, M. L. *Ultramicroscopy* **2014,** *136,* 193–200. doi:10.1016/j.ultramic.2013.10.012

40. Walters, D. A.; Cleveland, J. P.; Thomson, N. H.; Hansma, P. K.; Wendman, M. A.; Gurley, G.; Elings, V. *Rev. Sci. Instrum.* **1996,** *67,* 3583–3590. doi:10.1063/1.1147177

41. Shen, J.; Zhang, D.; Zhang, F.-H.; Gan, Y. *Appl. Surf. Sci.* **2017,** *422,* 482–491. doi:10.1016/j.apsusc.2017.06.053

42. Souli, I.; Terziyska, V. L.; Keckes, J.; Robl, W.; Zechner, J.; Mitterer, C. *J. Vac. Sci. Technol., B: Nanotechnol. Microelectron.: Mater., Process., Meas., Phenom.* **2017,** *35,* 022201. doi:10.1116/1.4975805

43. Wanjura, C. C.; Geiger, D.; Schrezenmeier, I.; Roos, M.; Marti, O. *arXiv* **2019,** 1902.04494. doi:10.48550/arxiv.1902.04494

44. Binns, C. *Surf. Sci. Rep.* **2001,** *44,* 1–49. doi:10.1016/s0167-5729(01)00015-2

45. Solař, P.; Škorvánková, K.; Kuzminova, A.; Kousal, J.; Kylián, O. *Vacuum* **2022,** *202,* 111114. doi:10.1016/j.vacuum.2022.111114

46. Popok, V. N.; Barke, I.; Campbell, E. E. B.; Meiwes-Broer, K.-H. *Surf. Sci. Rep.* **2011,** *66,* 347–377. doi:10.1016/j.surfrep.2011.05.002

47. Schöner, C.; Pöschel, T. *Phys. Rev. E* **2018,** *98,* 022902. doi:10.1103/physreve.98.022902

48. Tafazzoli, A.; Sitti, M. Dynamic Modes of nanoparticle motion during nanoprobe-based manipulation. In *4th IEEE Conference on Nanotechnology, 2004,* Munich, Germany, Aug 16–19, 2004; IEEE: Piscataway, NJ, USA, 2004; pp 35–37. doi:10.1109/nano.2004.1392241

49. Israelachvili, J. N.; Chen, Y.-L.; Yoshizawa, H. *J. Adhes. Sci. Technol.* **1994,** *8,* 1231–1249. doi:10.1163/156856194x00582

50. Bhushan, B., Ed. *Handbook of Micro /Nanotribology,* 2nd ed.; CRC Press: Boca Raton, FL, USA, 1998.

51. Delley, B.; Ellis, D. E.; Freeman, A. J.; Baerends, E. J.; Post, D. *Phys. Rev. B* **1983,** *27,* 2132–2144. doi:10.1103/physrevb.27.2132

52. Arblaster, J. W. *Selected Values of the Crystallographic Properties of the Elements;* ASM International: Materials Park, OH, USA, 2018.

53. Gao, X.; Xie, L.; Zhou, J. *Sci. Rep.* **2022,** *12,* 10117. doi:10.1038/s41598-022-13251-9

54. Tafreshi, S. S.; Roldan, A.; de Leeuw, N. H. *J. Phys. Chem. C* **2014,** *118,* 26103–26114. doi:10.1021/jp5078664

55. Liang, Z.; Magar, N. T.; Koju, R. K.; Chesser, I.; Zimmerman, J.; Mishin, Y.; Rabkin, E. *Acta Mater.* **2024,** *276,* 120101. doi:10.1016/j.actamat.2024.120101

56. Kriese, M. D.; Moody, N. R.; Gerberich, W. W. *Acta Mater.* **1998,** *46,* 6623–6630. doi:10.1016/s1359-6454(98)00277-8

Advancing nanolithography: a comprehensive review of materials for local anodic oxidation with AFM

Matteo Lorenzoni[§]

Abstract

Local anodic oxidation (LAO), also known as local oxidation nanolithography or oxidation scanning probe lithography has emerged as a versatile technique for nanoscale patterning, leveraging the precision of scanning probe microscopy, relying specifically on atomic force microscopy. This review explores the materials utilized in LAO experiments, including semiconductors, metals, insulators, two-dimensional (2D) materials, and emerging heterostructures. Semiconductors such as silicon and silicon carbide remain foundational due to their controllable oxidation kinetics, while metals like titanium and aluminum offer opportunities for plasmonic and optical applications. 2D materials, including graphene, graphene oxide, and transition metal dichalcogenides, demonstrate unique oxidation behaviors, enabling high-resolution applications in electronics and quantum devices. Recent advancements, such as electrode-free LAO, have expanded the range of applicable materials and improved the precision and scalability of the process. This paper also aims to provide a comprehensive understanding of material selection in LAO and its implications for advancing nanotechnology.

Review

1 Introduction

Advancements in nanotechnology have led to the development of numerous nanoscale fabrication techniques, with scanning probe lithography (SPL) [1] gaining prominence as a versatile method for high-resolution patterning, particularly in the early 2000s. SPL encompasses multiple methods, including nanomechanical processing [2], AFM bias-induced lithography [3], dip-

pen nanolithography [4] and thermal scanning probe lithography [5], each catering to unique fabrication requirements. Among the bias-driven techniques, local anodic oxidation (LAO) stands out due to its precise, resist-free process and the compatibility with a wide range of materials [6-9]. LAO uniquely provides maskless patterning under ambient condi-

tions with sub-10 nm lateral resolution, enabling direct oxide formation or material removal with nanoscale precision, capabilities not readily achievable with conventional lithographic approaches. AFM-based LAO originated from earlier STM local oxidation studies [10-12], which first demonstrated tip-induced electrochemical modification of semiconductor surfaces and even early device structures [13]. These STM works established the fundamental mechanism later adopted and expanded by AFM-based approaches. LAO utilizes an AFM to generate localized oxidation patterns through a biased conductive tip. The process relies on the formation of a nanoscale water meniscus [14] at the tip–sample interface, enabling electrochemical reactions that oxidize the substrate, creating protruding nanostructures mainly composed of oxide. Unlike other techniques requiring complex preparation steps, LAO enables direct chemical modification, with precise control of the tip–sample separation during the writing process. This is typically achieved in contact mode, where the tip apex is in direct contact with the substrate, ensuring capillary condensation and the formation of a stable water bridge. However, this approach increases the likelihood of tip wear and plastic deformation of the sharp AFM tip apex. An alternative involves using AFM dynamic mode [15,16], where the electric field induces the formation of the bridge that then stretches and adapts to the tip's motion. This can be implemented through a dual-pass technique or by controlling the electronic and ionic contributions to the total current [17,18]. While dynamic mode LAO does not eliminate tip wear [19], it significantly reduces its impact.

As new materials continue to emerge in the field of nanotechnology, this review also aims to highlight the capability of LAO to pattern two-dimensional (2D) materials such as graphene [20-22], hexagonal boron nitride [23] (hBN), transition metal dichalcogenides (TMDs) [21,24-27], metals [18,28,29], as well as traditional semiconductors such as silicon (Si) [6,10,30,31], gallium arsenide (GaAs) [32,33] and silicon carbide (SiC) [34], meaning that SPL has still the potential to revolutionize nanolithography. In the context of 2D materials, LAO facilitates the fabrication of intricate structures such as nanoribbons and transistors, granting proper operation of the fabricated device and preserving the intrinsic material properties [35,36]. For semiconductors, the method allows for precise control over oxide thickness, critical for applications in microelectronics and sensor technology. Oxide thickness can be precisely controlled, enabling the formation of layers as thin as sub-nanometer for SiO_2 [37] and extending to tens of nanometers for materials such as SiO_xC_y [34], TiO_x, and MoO_x [38]. In contrast, atomic layer deposition (ALD) provides exceptional conformality and atomic-scale thickness control, typically depositing films at 0.1–0.2 nm per cycle [39], making it the preferred technique for large-scale, uniform coatings. However, LAO remains advanta-

geous for high-resolution, direct-write patterning at the nanoscale, despite its limited scalability. Furthermore, the resulting LAO oxide can be easily etched by mild acid solutions [40] or water [24]. A layer of a few nanometers of insulating material (e.g., native oxide, fabricated oxide, or silicon nitride masks [41]) does not represent an obstacle to the LAO process, while bulk insulating materials still represent a major challenge. Figure 1a summarizes the content of this review, showing the materials considered and illustrating a comparison between conventional and electrode-free LAO (EFLAO).

2 Principles of local anodic oxidation (LAO)

As already said, LAO is a nanoscale fabrication technique that utilizes an AFM to generate precise oxidation patterns on a substrate. The process is based on the application of a voltage bias between a conductive AFM tip and the sample surface, resulting in localized electrochemical reactions. This section delves into the fundamental principles governing LAO, including its mechanisms, controlling factors, fabrication metrics and advancements in the technique.

2.1 Mechanism of LAO

The key to LAO lies in the formation of a nanoscale water meniscus between the AFM tip and the sample surface, as depicted in Figure 1b. Under ambient humidity, the water layer serves as an electrolyte, enabling electrochemical reactions. When a positive voltage is applied to the AFM tip relative to the substrate, the intense electric field ($E > 10^7$ V·m^{-1}) [23] within the water meniscus drives oxygen-containing ions (e.g., OH^- and O^{2-}) towards the substrate surface. This triggers the oxidation reaction. At the substrate, the ions react with the material, forming newly grown oxide. Specifically, on Si, LAO-derived oxide exhibits a density of 2.05 g·cm^{-3}, lower than the 2.27 g·cm^{-3} density of thermally oxidized silicon [43]. In the case of Si surfaces the chemical reaction leading to SiO_2 formation is:

$$Si + 2OH^- \rightarrow SiO_2 + H_2O.$$
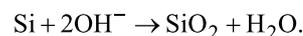
In the case of SiC, carbon atoms are eliminated in the form of carbon dioxide:

$$SiC + 8h^+ + 4OH^- \rightarrow SiO_2 + 4H^+ + CO_2.$$
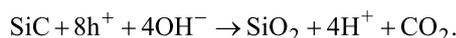
The oxides fabricated on MoX_2 materials (MoS_2, $MoSe_2$, and $MoTe_2$) are instead soluble in water, indicating that the product of the reaction is MoO_3 [21]:

$$MoS_2 + 2OH^- \rightarrow MoO_3 + H_2O.$$
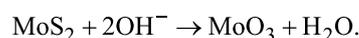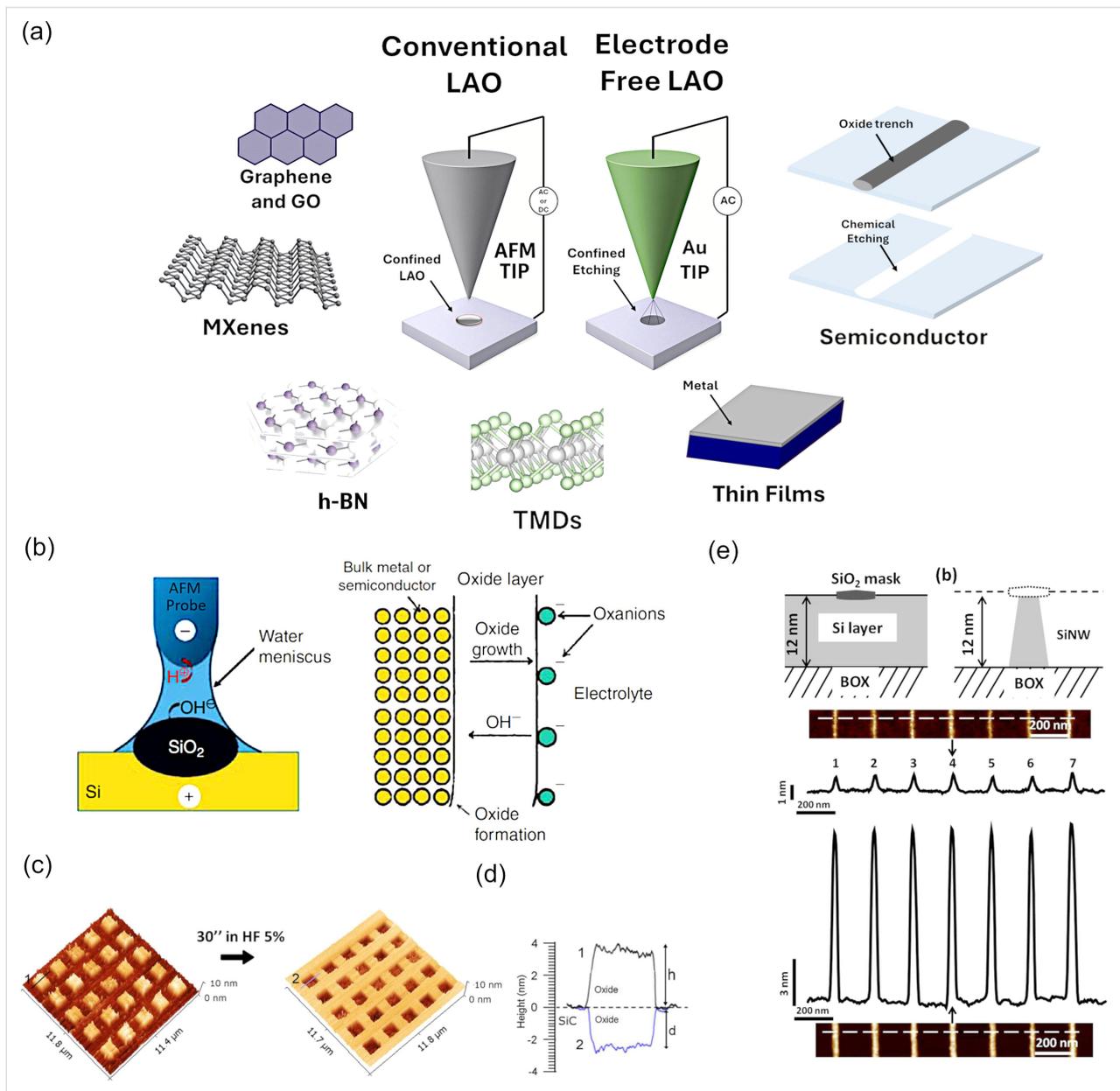
Figure 1: Overview of the local anodic oxidation process and resulting oxide structures. (a) Schematic summary of the main materials addressed in this review and comparison between conventional LAO and electrode-free LAO. (b) Mechanism of oxide growth on a silicon surface during LAO, illustrating the formation of a protruding oxide feature and the corresponding buried oxide volume. Reproduced from [8], M. Lorenzoni and F. Pérez-Murano, "Conductive Atomic Force Microscopy for Nanolithography Based on Local Anodic Oxidation," in *Conductive Atomic Force Microscopy: Applications in Nanomaterials*, with permission from John Wiley and Sons. Copyright © 2017 Wiley-VCH GmbH. This content is not subject to CC BY 4.0. (c) AFM images of square oxide patterns fabricated by LAO on SiC before and after wet etching. (d) Height profile of the top left corner feature, before (black solid line) and after etching (blue solid line), showing the ratio between protruding and buried oxide. Panels (c and d) adapted from [34], with the permission of AIP Publishing. This content is not subject to CC BY4.0. (e) Schematic of the fabrication process together with AFM topography and cross-sectional views of an array of oxide masks (top) and their corresponding etched silicon nanowires (bottom). Panel (e) adapted from [42], with the permission of AIP Publishing. This content is not subject to CC BY4.0.

Similarly, LAO on WSe_2 produces WO_3 features that have been etched in water [24]. If we consider semiconductors and metals, most authors agree with an oxidation kinetic consistent with the Cabrera–Mott model [44,45]. As an electrochemical process, LAO is inherently current-dependent. Early studies showed that oxide growth evolves from an initial electronic tunneling regime to ionic transport as the film develops [46]. Dagata and coworkers further demonstrated that charge accumulation within the growing oxide leads to space-charge-limited behavior, reinforcing the self-limiting character of LAO [47]. As the oxide thickens, the local electric field weakens, the supply of reactive species at the water–oxide interface decreases, and

stress and trapped charges hinder further ion transport. Together, these effects progressively slow oxidation and ultimately halt growth [48]. This explains why local oxidation experiments on Si report maximum features below 10 nm, while oxide features grown on SiC (with different stoichiometry and density) can reach up to 100 nm height [34]. The protruding oxide observed by AFM represents only part of the total oxide

volume. Because oxidation proceeds into the substrate and the formed oxide is less dense than the parent material, a comparable portion (typically 40–60%) develops beneath the surface. This buried component is a general feature of LAO and must be considered when interpreting feature height and oxide thickness [10,48]. This is illustrated in Figure 1c,d, taking into consideration LAO experiments on SiC (Figure 2a).

Figure 2: Examples of oxide nanostructures fabricated by local anodic oxidation. (a) AFM topography of an array of single oxide dots produced on a 6H-SiC surface at 40% relative humidity using voltage pulses from 0.1 to 30 s at 10 V. Adapted from [34], with the permission of AIP Publishing. This content is not subject to CC BY4.0. (b) Cross-sectional profile and AFM topography of a single silicon oxide line patterned using a carbon nanofiber (CNF)-functionalized AFM tip. Adapted from [49] ("Boosting the local anodic oxidation of silicon through carbon nanofiber atomic force microscopy probes", © 2015 G. Rius et al., published by Beilstein-Institut, distributed under the terms of the Creative Commons Attribution 2.0 Generic License, https://creativecommons.org/licenses/by/2.0). (c) Multilevel silicon nanowire transistor fabricated through sequential LAO steps. AFM topography after etching and corresponding device micrograph. Adapted with permission from [50], Copyright 2008 American Chemical Society. This content is not subject to CC BY 4.0.
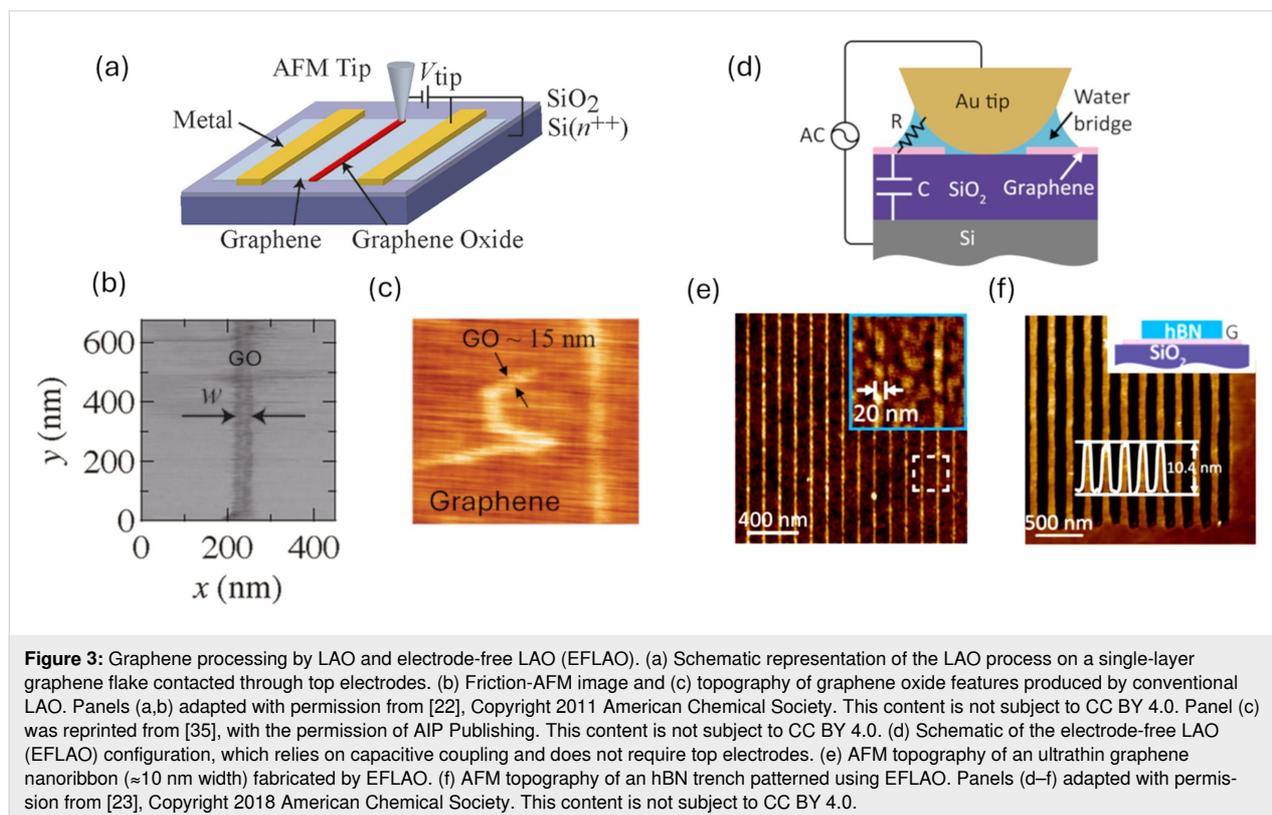
Beyond the chosen substrate, the thickness and lateral dimensions of the oxide features are governed mainly by the applied voltage, pulse duration, and tip movement speed. This controlled oxidation process is highly effective for fabricating high-resolution patterns, with numerous examples demonstrating the successful creation of silicon oxide nanostructures featuring lateral dimensions well below 100 nm and heights ranging from 1 to 10 nm. The electrochemical reaction in LAO progresses relatively slowly with the water bridge forming rapidly ($\approx$10 µs), but it is the subsequent growth process that may last several seconds. This kind of patterning capability is widespread, and most commercial AFM nowadays implement some interface enabling LAO lithography. Often, the oxide features are used as masks to amplify the pattern depth, as shown in Figure 1e, where silicon nanowires (SiNWs) are created by patterning a SOI wafer [42]. In Figure 2b,c, we show some outcome of LAO experiments aimed to fabricate narrow oxide lines on Si. In one case (Figure 2b), the aspect ratio was enhanced by using a carbon nanofiber (CNF)-functionalized AFM tip [51]; Figure 2c illustrates the scale of a multilevel SiNW transistor, serving as proof that LAO is compatible with performing multiple oxidation steps at the same location during device fabrication [52].

The common experimental setup of LAO on 2D materials flakes is depicted in Figure 3a, where top electrodes are necessary due to the insulating SiO$_2$ layer. The nanometer sized GO features obtained are shown in Figure 3b,c. The description of the fabrication steps to enhance the aspect ratio of such features is out of the scope of this work. But it is worth mentioning that most oxides exhibit good selectivity against many common etchants used for dry etching, including reactive ion etching with fluorine- or chlorine-based plasmas, allowing for precise pattern transfer [50,52].

The use of a single probe remains a significant limitation for all SPL methods. In LAO experiments, scanning probes mounted on commercial AFMs typically operate at processing speeds of tens of micrometers per second, restricting the ability to create fast patterns over large areas. Unfortunately, the current state of the art for oxidation scanning probe lithography in terms of subsequent of resolution and throughput has not changed significantly in the last years [53]. The lateral resolution of modified features is usually set around tens on nanometers, with remarkable exceptions of single narrow lines reaching sub-10 nm full width at half maximum [21,50] and machined gaps on 2D materials as narrow as 20 nm [21,23]. The typical throughput of LAO is around a few square millimeters per hour [53]. In comparison, thermal scanning probe lithography (t-SPL), the fastest SPL technique, can reach writing speeds of up to 1 mm·s^{-1}, enabling patterning rates of the order of 10–100 mm^2·h^{-1} under optimal conditions [5]. This puts it in a similar throughput range

Figure 3: Graphene processing by LAO and electrode-free LAO (EFLAO). (a) Schematic representation of the LAO process on a single-layer graphene flake contacted through top electrodes. (b) Friction-AFM image and (c) topography of graphene oxide features produced by conventional LAO. Panels (a,b) adapted with permission from [22], Copyright 2011 American Chemical Society. This content is not subject to CC BY 4.0. Panel (c) was reprinted from [35], with the permission of AIP Publishing. This content is not subject to CC BY 4.0. (d) Schematic of the electrode-free LAO (EFLAO) configuration, which relies on capacitive coupling and does not require top electrodes. (e) AFM topography of an ultrathin graphene nanoribbon ($\approx$10 nm width) fabricated by EFLAO. (f) AFM topography of an hBN trench patterned using EFLAO. Panels (d–f) adapted with permission from [23], Copyright 2018 American Chemical Society. This content is not subject to CC BY 4.0.

to electron beam lithography (EBL), which, depending on beam current and pattern complexity, typically achieves 1–$100\ mm^2 \cdot h^{-1}$ for high-resolution writing [54,55]. Table 1 incorporates t-SPL, field-emission lithography (FEL), and EBL to provide reference benchmarks against which the capabilities of LAO can be evaluated. t-SPL is the fastest tip-based method, using a heated cantilever to induce thermochemical changes in an ultrathin resist, and is therefore an important comparator for writing speed and patterning rate. FEL, based on the emission of low-energy electrons from an AFM tip, provides sub-10 nm resolution in ultrathin molecular resists and thus represents the upper limit of tip-based spatial precision. EBL, although not a scanning probe technique, remains the industrial standard for high-resolution patterning and sets the baseline for assessing scalability and throughput. Their inclusion highlights where LAO stands relative to established nanolithography methods and clarifies its unique advantages and limitations.

2.2 Factors influencing oxidation

The effectiveness and precision of LAO depend strongly on ambient humidity, which governs formation and size of the water meniscus. Optimal relative humidity (RH) between 35% and 55% ensures reproducible oxidation, while higher humidity enlarges the meniscus and broadens oxide lines. Conversely, lower humidity reduces meniscus volume and enables narrower, better-defined features. Although RH of 35–55% is widely used for Si and other common substrates, the optimal range can shift depending on the substrate surface chemistry, hydrophilicity,

and the tip material or coating. Studies such as Garcia et al. [15] and Snow et al. [58] systematically demonstrate this dependence, showing a strong correlation between humidity control and achievable resolution in LAO. Voltage and pulse time also play an important role, when the voltage pulse applied is fixed (i.e., tens of milliseconds) oxide size increases linearly with pulse amplitude but logarithmically with pulse width [59]. As expected, higher voltages and longer oxidation times increase oxide thickness but may lead to tip wear and reduced lateral resolution. During LAO, the tip morphologically and chemically degrades; therefore, the choice of tip material (e.g., n^+-doped silicon, metal coating, or solid alloy) affects oxidation efficiency, with solid tips performing better than coated tips in terms of durability. Tip shape and sharpness play also a crucial role as a main regulator of minimum feature size. Carbon nanotube (CNT)-functionalized AFM tips have been explored for LAO [49,60,61] because their high aspect ratio and good conductivity can, in principle, enable sharper and more controlled oxidation. However, their practical performance is limited by mechanical fragility and variability in CNT integration. For this reason, CNT tips may show excellent results in specific cases [62] but do not consistently outperform robust commercial Si tips. Conductive or semiconductive substrates facilitate the process, while insulating substrates may require additional surface treatments [63] or modified LAO setups. Topography also plays a significant role: While low-roughness surfaces facilitate the process, RMS roughness above roughly 1–2 nm can distort the meniscus and induce lateral broadening

Table 1: Comparison of metrics: LAO vs t-SPL, FEL and EBL.[a]

Metric	Local anodic oxidation (LAO)	Thermal scanning probe lithography (t-SPL)	Field-emission lithography (FEL)	Electron beam lithography (EBL)
throughput	1–$10\ \mu m^2 \cdot h^{-1}$	10–$100\ mm^2 \cdot h^{-1}$ [5]	1–$10\ \mu m^2 \cdot h^{-1}$	10–$100\ mm^2 \cdot h^{-1}$ [5]
writing speed	micrometers per second to tens micrometers per second	up to 1 mm/s [5]	similar to EBL: nanometers per second to micrometers per second	tens of millimeters per second (limited by dose requirements)
etch selectivity	moderate (thin oxide mask, limited selectivity)	moderate (thin thermal resist layer)	high (depends on resist; PMMA commonly used)	high (i.e., hydrogen silsesquioxane (HSQ) and PMMA)
aspect ratio	low; typically, <2:1 due to shallow oxide features	moderate; aspect ratios up to 4:1 achievable with optimized processes	similar to EBL	high; aspect ratios exceeding 10:1 possible with appropriate resists and etching techniques
resist/mask material	native oxide formed (e.g., SiO_x and TiO_x)	thermal resist (no development needed)	PMMA, HSQ, and calixarene [56]	wide selection (e.g., PMMA and HSQ)
scalability	low (serial tip-based, though arrayed LAO emerging)	moderate (parallel tip arrays under development)	low (self-actuated tip array is possible)	moderate to high (especially with multibeam systems)
resolution	<10 nm [50]	10–20 nm (lateral) [5]; sub-10 nm possible; single-digit nanometer resolution demonstrated [57]	<10 nm (industry standard)	–

[a]Where not explicitly stated, the quantitative data have been derived from sources included in the reference list.

of the oxide features. Notably, Ryu et al. demonstrated that oxygen plasma pretreatment of MoS_2 flakes can spatially confine the oxidation process, enabling the formation of well-controlled dot-shaped features [21].

2.3 Advanced techniques

Recent advancements have expanded the capabilities of LAO to the electrode-free EFLAO [23]. This technique employs high-frequency AC fields to induce oxidation, removing the need for contacted electrodes and broadening the range of usable substrates as shown in Figure 3d. It is important to notice that this technique can be labeled as an anodic oxidation etching. Using AC rather than DC voltage for local anodic oxidation through capacitive coupling, it can be applied to any sample, even those without electrodes or electrical contacts. This method simplifies sample preparation, broadens the range of compatible materials, and enhances the reliability and quality of lithographic cuts, all without the need for additional AFM equipment. If applied to graphene or boron nitride, authors of [23] have shown how reaction by-products are efficiently removed, escaping as gas (i.e., CO_2 in the case of graphene). The resulting patterns exhibit excellent quality with minimal defects (Figure 3e,f). However, a potential drawback is the use of Au-coated tips under contact-mode conditions with applied forces around 1500 nN, which may lead to tip coating wear if the ohmic contact is not facilitated by the presence of a water meniscus. Despite this, the authors demonstrate consistent and reproducible patterning over hundreds of micrometers, achieved at writing speeds typical for LAO experiments.

In a recent study, Shilov et al. [64] proposed a similar approach to EFLAO, demonstrating efficient patterning on multilayer heterostructures composed of graphene, graphite, hexagonal boron nitride (hBN), $NbSe_2$, and WSe_2. Their method leverages the enhancement of the electric field, achieved by assembling the heterostructures on conductive graphite flakes. They suggest that the mechanism of electrical breakdown may play a more significant role than previously assumed, potentially overshadowing the electrochemical reactions traditionally attributed to the process. Although field-induced breakdown may contribute in some electrode-free geometries, current evidence does not rule out a significant anodic oxidation component; therefore, the term EFLAO is retained to describe processes in which electrochemical oxidation remains operative alongside possible breakdown-assisted effects.

For comparison, it is worth mentioning the non-oxidative SPL technique FEL [57], which has recently proven its efficiency and reliability. It exploits a Fowler–Nordheim-type emission of low-energy electrons from a conductive AFM tip. This beam of low-energy electrons can induce highly confined positive and

negative tone as well as self-development reactions within ultrathin molecular resist layers [56,65,66], with resolutions reaching sub-10 nm scales [67]. As demonstrated by Prof. Ivo W. Rangelov and colleagues, FEL relies on the high-intensity electric fields generated at the sharp AFM tip, mounted on an active cantilever, which induces local modifications in the substrate material, such as desorption or structural changes. This approach is particularly advantageous for its simplicity and ability to pattern on a wide range of materials [68] without the need for additional processing steps. It is worth highlighting that FEL serves as an alternative to EBL, particularly excelling in low-sensitivity EBL resists. However, FEL has yet to achieve the capability of locally etching or removing a target substrate, as demonstrated by EFLAO. Additionally, most successful FEL patterning experiments have utilized non-commercial probes equipped with integrated piezoresistive read-out and thermomechanical actuation (active cantilevers). Despite these challenges, Behzadirad et al. demonstrated that using sharp gallium nitride nanowires (GaN NWs) as tips enables atomic-scale patterning [67] (<1 nm) on a molecular resist under vacuum conditions.

2.4 Applications of the LAO process

The fact that LAO can be performed with an inexpensive AFM setup makes it invaluable for the prototyping of nanoelectronics devices such as metal–insulator–metal diodes [69] and field-effect transistors (FETs) based on silicon nanowires [42,70-73]. Usually, a narrow oxide mask is patterned on top of the active layer of a silicon-on-insulator (SOI) substrate; further etching removes the excess silicon, leaving a free-standing silicon nanowire matching the shape and size of the original oxide mask. The nanowire is then contacted by micrometer-sized metal contacts by either photolithography or EBL. By a similar approach, it was possible to fabricate nanoscale FETs on thin-layer TMDs [21,24,36]. Graphene-based nanoelectronics devices present a further challenge, single- or few-layer graphene flakes have been preferentially "removed" [23] (as mentioned before describing EFLAO), mechanically cleaved [74], or thermally etched [75] rather than chemically modified [22,35,76,77]. This was done mainly to preserve the electrical characteristics of pristine graphene. The unique capacity of LAO to build ultranarrow dielectric barriers in a 2D fashion has been also exploited to fabricate quantum devices on semiconductors [71,78].

2.5 Materials used in LAO

A diverse range of materials has been utilized in LAO, leveraging their distinct oxidation behaviors, structural characteristics, and applications. This review focuses on metallic, semiconducting, and 2D materials, while excluding significant efforts on organic semiconductors [79] and functionalized substrates [80-82] (like self-assembled monolayers [83]), which fall

beyond the scope of this work. Nevertheless, it is worth mentioning that tip-induced electrochemical oxidation has also been demonstrated on organic monolayers, most notably in the seminal work of Sagiv and coworkers. They showed that alkylsilane monolayers can be patterned nondestructively by converting terminal –CH_3 groups into –COOH functions [84], enabling chemical templating and subsequent selective self-assembly of organic or inorganic species [85]. Follow-up work further demonstrated that such patterned monolayers can even support single-layer ionic conduction along predefined nanoscale paths [86]. These studies extend LAO-type surface modification to molecular films and highlight its relevance beyond inorganic substrates. Table 2 presents a comparative analysis of the key materials that have been successfully utilized for LAO experiments and device fabrication.

2.5.1 Semiconductors. Semiconductors like silicon have been widely studied for LAO due to their extensive use in microelectronics, the predictable oxidation behavior, and compatibility with microfabrication processes. The formation of SiO_2 enables high-resolution patterning, often achieving feature sizes below 10 nm, making it invaluable for applications like insulating

layers in transistors. Additionally, the stability and integration of SiO_2 within semiconductor workflows make it a reliable choice for robust electronic devices. However, silicon's limitations include dependence on stringent surface preparation, Si crystal orientation (higher reaction rate on the (111) surface than on the other surfaces), and environmental factors, such as humidity, which can impact reproducibility. LAO-grown oxide is less dense than thermally grown oxide, and mechanical stress between the substrate and oxide layer may lead to defects. In addition, the insulating nature of SiO_2 limits its versatility compared to materials that allow for tunable electronic or structural features. While silicon is ideal for standard electronic applications, its constraints highlight the need for alternative materials in more diverse or multifunctional nanoscale devices. LAO has likewise been demonstrated on III–V semiconductors, most notably GaAs and related heterostructures, where the patterned oxide lines were used as templates for nanoscale device fabrication [90].

Silicon carbide (SiC) is an interesting material for LAO, offering unique advantages over silicon due to its high thermal conductivity, chemical inertness, and suitability for high-tem-

Table 2: Overview of materials processed by local anodic oxidation and recent experimental outcomes.[a]

Material	Key experimental results	Applications	Min. feature size (lateral)	By-product/oxide	Key challenges
silicon	precise SiO_2 layer growth with nanometer control	transistors, dielectric isolation layers, and SiNWs	4 nm [50]	SiO_2	limited features height and 20–80% relative humidity
silicon carbide (SiC)	high oxide thickness with SiO_xC_y composition	high-temperature electronics	50 nm [34]	SiO_xC_y	residual charges and mixed oxides
graphene	generate GO features within a graphene channel of a FET	flexible electronics and quantum devices	20 nm [22]	GO	semiconducting GO features and oxidation confinement
graphene oxide	reduction to graphene nanoribbons with sub-20 nm widths	flexible electronics and quantum devices	65 nm [87]	rGO	controlling reduction and reproducibility
MoS_2, $MoSe_2$, and WSe_2	plasma-enhanced oxidation	optoelectronics and transistors	sub-10 nm constrictions [21]; 10 nm precision (EFLAO) [23]	MoO_3 or WO_3	humidity sensitivity and oxidation confinement
titanium	TiO_2 layers for optical and catalytic applications	photocatalysis and sensors	n.a. (conventionally sub-μm)	TiO_2 [88]	sputtered Ti layer and controlling uniformity
aluminum	thin, uniform oxide layers	optical devices and plasmonics	n.a. (conventionally sub-μm)	Al_2O_3 [89]	sputtered Al layer and requires strict voltage control
hBN/graphene	no electrode, AC-driven trench patterns with smooth edges	quantum heterostructures	10 nm precision (EFLAO) [23]	none	n.a.

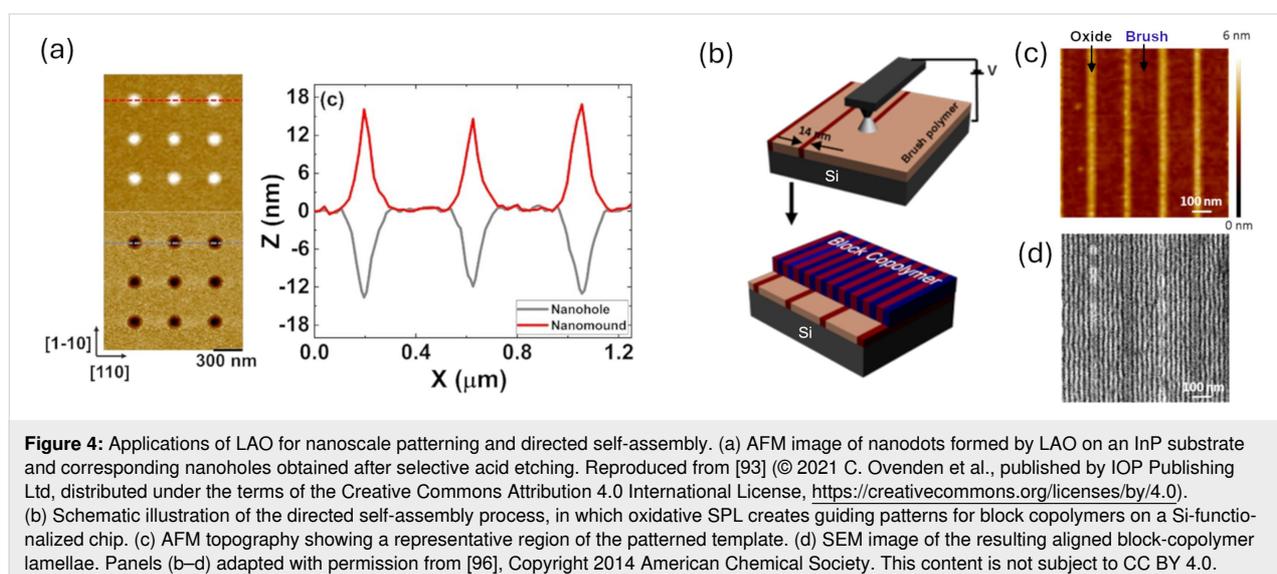[a]Typical LAO operating conditions: voltage: 5–20 V; humidity: 35–55% RH; tip speed: 0.1–10 μm·s^{-1}; pulse duration: 1 ms to 1 s.

perature environments. The formation of mixed oxides [91] (SiO_xC_y) during LAO provides opportunities for tailoring electrical properties, making SiC valuable for robust microelectronic and power devices. Its self-limiting oxide growth allows for precise control of layer thickness, which is critical for nanoscale patterning. Experimental observations report self-limiting oxide growth exceeding 100 nm [34]. As crystal orientation affects LAO on Si, the oxidation rate on c-plane 4H-SiC is higher than on other planes [92]. Challenges with SiC include the incorporation of residual charges in the oxide layer, which can affect electrical performance. Yet, SiC's superior durability and unique properties make it a promising material for applications in harsh and demanding environments, though it is less versatile than newer 2D materials or heterostructures. Recently Ovenden et al. demonstrated conventional LAO on InP [93] intending to obtain quantum dot arrays [94]. Nanohole and nano-oxide mound radius and depth were controlled independently by altering tip bias and humidity, with a maximum nanohole depth of ≈15 nm after acid etching. The obtained nanoholes are shown in Figure 4a. The silicon surface can be functionalized and subsequently patterned through local oxidation [95], as illustrated by a method for generating guiding patterns for the directed self-assembly of block copolymers (BCPs) [96]. By integrating chemical and topographic modifications, these guiding patterns efficiently align BCPs into an ordered parallel lamellar arrangement, as depicted in Figure 4b–d.

2.5.2 Metals. Metals like titanium and aluminum are frequently utilized for plasmonic devices and nanoscale sensors. Oxidation of titanium during LAO forms TiO_2 [69,88], a process highly dependent on relative humidity and applied voltage. Patterns on titanium exhibit uniform thickness, making it well-suited for applications in nanoelectronics devices, memristive memory elements, and lithographic masks. Typically, the titanium layer is deposited on semiconducting or insulating substrates, such as SiO_2, to facilitate effective LAO. A study by Tominov et al. [18] introduced forming-free titanium oxide-based memristive nanostructures created through AFM-assisted local oxidation. This work demonstrates the fabrication of nanoscale resistive switching devices while eliminating the need for the electroforming step, which often requires high voltages that can compromise stability. The study revealed that thinner titanium oxide layers enhance resistive switching performance by providing higher resistance ratios and more uniform switching behavior. Furthermore, compositional analysis showed that TiO_2 dominates the oxide structure, while deeper regions exhibit increased contributions of Ti_2O_3 and TiO. The authors claim that the precise control of oxygen vacancies during LAO would enable the reproducible and scalable production of high-performance ReRAM devices.

Aluminum oxidation by AFM LAO is well suited for forming thin protective layers. The high reflectivity of Al patterns offers applications in optical devices. Successful LAO experiments were performed on a thin Al layer sputtered on SOI substrates [89]. Similarly, oxidation of a 10 nm thick Nb layer was successfully achieved by Heidelberg and colleagues [29].

A more recent study demonstrates the use of LAO to nanostructure thin amorphous vanadium oxide (VO_x) films [97], converting them locally to vanadium pentoxide (V_2O_5) for selective removal. Achieving sub-50 nm lateral precision and sub-0.3 nm depths, the process is influenced by humidity, film thickness, and voltage, following the Cabrera–Mott model. This clean, precise approach highlights LAO's potential for photonic

Figure 4: Applications of LAO for nanoscale patterning and directed self-assembly. (a) AFM image of nanodots formed by LAO on an InP substrate and corresponding nanoholes obtained after selective acid etching. Reproduced from [93] (© 2021 C. Ovenden et al., published by IOP Publishing Ltd, distributed under the terms of the Creative Commons Attribution 4.0 International License, https://creativecommons.org/licenses/by/4.0). (b) Schematic illustration of the directed self-assembly process, in which oxidative SPL creates guiding patterns for block copolymers on a Si-functionalized chip. (c) AFM topography showing a representative region of the patterned template. (d) SEM image of the resulting aligned block-copolymer lamellae. Panels (b–d) adapted with permission from [96], Copyright 2014 American Chemical Society. This content is not subject to CC BY 4.0.

and nanoelectronics applications, aligning with advances in LAO research.

### 2.5.3 Two-dimensional materials.

2D materials are at the forefront of LAO research, owing to their exceptional structural and electronic properties, and have undoubtedly become a major focus for experts in scanning probe lithography. They exhibit oxidation behaviors that differ fundamentally from those of bulk semiconductors and metals. Graphene, TMDs, and their heterostructures each follow distinct reaction pathways under LAO, leading to markedly different feature geometries and device possibilities. LAO can define ultranarrow dielectric barriers, constrictions, and etched channels directly on the active material with nanometer precision and without resist contamination. In 2D materials, this allows for the fabrication of graphene nanoribbons, quantum point contacts, and TMD nanotransistors by locally modulating conductivity or selectively removing material.

2.5.4 Graphene and graphene oxide.

Interest in graphene peaked in the last decades, with several attempts to couple LAO with single/few-layer graphene flakes [22,98,99], epitaxial graphene [20,100], graphene grown by thermal decomposition of SiC [77], and graphite [101]. By applying local oxidation in a humid environment, the resulting reactive oxygen species, such as OH^- and $O_2^{\bullet-}$, oxidize the graphene surface, forming graphene oxide (GO) or trenches, depending on the applied voltage and process conditions. Key experimental findings highlight that the type and size of features depend on several factors, including the magnitude of the tip voltage, relative humidity, and writing speed [22]. For instance, voltages below a threshold of −5 to −10 V led to the formation of GO. Beyond −16 V, ablation occurs, resulting in the formation of trenches where the carbon atoms are removed [98,102]. Feature dimensions are also affected by the tip speed; slower speeds result in wider features, while faster speeds narrow the oxidized lines. The degree of oxidation increases with higher RH, which enhances the size and reactivity of the water meniscus. The structural and electronic behavior of graphene during LAO is influenced by its layer stacking. As pointed out by Liou and coworkers [20], the inherently 2D nature of these materials influences the outcomes of LAO processes. For instance, oxidation can lead to local protrusions significantly taller than the thickness of a single atomic layer due to the formation of an oxide bump in the conductive substrate beneath the 2D material. When a layered material is placed on an insulating substrate (such as SiO_2) and contacted from the top, oxidation can disrupt lateral conductivity, effectively isolating the 2D material and leading to unwanted defects. Bernal-stacked graphene allows for uniform oxidation across layers, while non-Bernal stacked graphene limits oxidation to the topmost layer due to reduced electronic interactions between layers. Raman spectroscopy and micro-XPS studies confirm these effects, revealing oxygen incorporation patterns and changes in chemical composition. In summary, the versatility in achieving selective oxidation or ablation expands the potential for device fabrication, including resistive switching elements and nanosensors, highlighting its importance in advanced graphene-based technologies.

As already mentioned, Li et al. [23] developed EFLAO, a novel technique driven by high-frequency AC voltage, enabling precise and high-quality nanoscale patterning of low-dimensional materials without the need for prefabricated microelectrodes. This method overcomes the limitations of conventional LAO, such as dependency on conductive substrates and residue formation. Key contributions include the successful fabrication of graphene nanoribbons with smooth edges and widths as small as 10 nm, demonstrating superior etching quality comparable to natural edges. Figure 3e shows the topography of an ultrathin graphene nanoribbon with width of ≈10 nm and edge roughness of ≈2 nm. As an etching method that operates without the need for an external electrode, once parameters such as AC frequency and voltage are properly optimized, the technique enables the formation of clean, residue-free patterns while maintaining consistent and reliable oxidation. The study also extends to heterostructures, such as graphene/hexagonal boron nitride (hBN) as presented in Figure 3f, achieving uniform etching and demonstrating that heterostructures consisting of two different materials can also be tailored by EFLAO. The approach relies on capacitive coupling through dielectric substrates to generate localized electric fields and supports patterning at varying frequencies, with optimal performance at frequencies above 10 kHz. Additionally, the technique avoids common issues of oxide residues and ensures scalability with high reproducibility. This breakthrough positions EFLAO as a promising tool for next-generation nanolithography, offering flexibility and simplicity for fabricating ultraclean nanodevices.

Reduced graphene oxide (rGO) resembles graphene but with some residual oxygen and structural defects. rGO comprises ordered sp^2 domains with nanosized dimensions interspersed between highly disordered sp^3 domains with oxygen-containing functional groups. This indeed limits the film's conductivity and mobility. Reversing the bias in a standard LAO setup enables the restoration of conductivity in GO layers or flakes through a localized reduction reaction [87,103] or a localized catalytic reaction [104]. In Figure 5a,b, we show a conductive AFM image of a single restored rGO feature [87] obtained after local reduction by SPL, with a lateral size below 100 nm. Even better results on GO, in terms of lateral resolution, have been achieved by thermochemical nanolithography [105]. The electrical properties of rGO patterns obtained in both ways (electro-
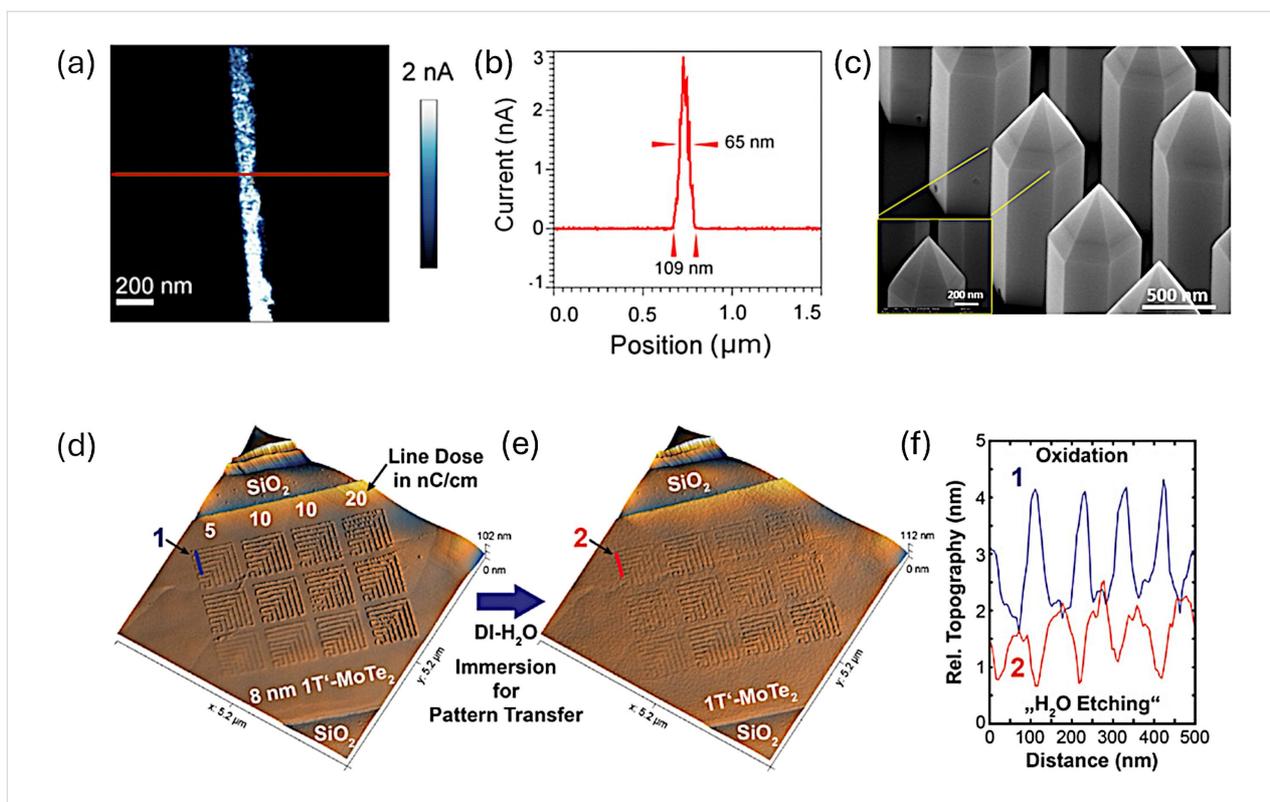
Figure 5: Examples of advanced SPL-based patterning on graphene oxide and MoTe$_2$. (a) Conductive-AFM image of a single reduced graphene oxide (rGO) line fabricated by localized electrochemical reduction. (b) Corresponding current profile demonstrating restored conductivity within the nanoscale rGO feature. Panels (a,b) used with permission from [87] ("Nanoscale reduction of graphene oxide thin films and its characterization", by M. Lorenzoni et al., *Nanotechnology*, Vol. 26, Article No. 285301, published on 29 June 2015; DOI 10.1088/0957-4484/26/28/285301); © 2015 IOP Publishing; permission conveyed through Copyright Clearance Center, Inc.). This content is not subject to CC BY 4.0. (c) Array of GaN nanowires used as ultrasharp, mechanically robust AFM tips for high-resolution SPL. Adapted with permission from [67], Copyright 2021 American Chemical Society. This content is not subject to CC BY 4.0. (d) AFM topography showing nanoscale oxidation patterns created on a 1T′-MoTe$_2$ nanoribbon. (e) Resulting surface morphology after selective removal of the oxide in deionized water. (f) Cross-sectional profiles extracted from panels (d) and (e). Panels (d–f) adapted from [36] (© 2023 C. Reuter et al., *Advanced Materials* published by Wiley-VCH GmbH, distributed under the terms of the Creative Commons Attribution 4.0 International License, https://creativecommons.org/licenses/by/4.0).

chemically and thermochemically) are excellent, with rGO presenting a bulk conductivity that is comparable to the values reported for chemically reduced GO ($>10^4$ S·m^{-1}).

2.5.5 Transition metal dichalcogenides. TMDs, such as MoS$_2$, MoSe$_2$, WSe$_2$, and MoTe$_2$, have emerged as highly promising materials for LAO due to their unique electronic, structural, and chemical properties. LAO on TMDs leverages their atomically thin layers and tunable band structures to create high-resolution nanoscale features, including nanoribbons, trenches, and transistor channels. The oxidation process typically involves converting the metal component of TMDs into higher oxidation states, such as MoO$_3$ or WO$_3$, which can be selectively etched or retained depending on the desired application. Studies have demonstrated that LAO can achieve sub-20 nm patterning resolution on MoS$_2$ [21] and WSe$_2$ [24], enabling the fabrication of nanoribbon-based FETs. Oxygen plasma-assisted LAO has been employed to enhance the precision and reduce defects in the resulting patterns [21], making the process highly suitable

for device applications requiring nanoscale control. In fact, LAO patterning of both MoS$_2$ and WSe$_2$ is enhanced by an initial oxygen plasma treatment, which forms a uniform oxide layer of approximately 3 to 4 nm on the surface of the flake. This pre-treatment not only reduces the flake thickness but also minimizes the impact of the underlying dichalcogenide crystal lattice on the quality of the LAO patterns, surpassing previously reported results [26]. One example of such pattering capabilities is reported in Figure 6 showing a 35 nm constriction fabricated on few-layer WSe$_2$, before and after etching in water.

Additionally, the environmental sensitivity of TMDs, such as the anisotropic oxidation of 1T′ MoTe$_2$ under humid conditions, has been exploited to achieve unique etching profiles and selective modifications. In a study by Reuter et al., low-energy electrons emitted from the tip have been used to induce nanoscale oxidation on a MoTe$_2$ nanosheet surface under ambient conditions [36]. The study demonstrates a novel, resist-free method for nanoscale patterning of MoTe$_2$ in both its semiconducting
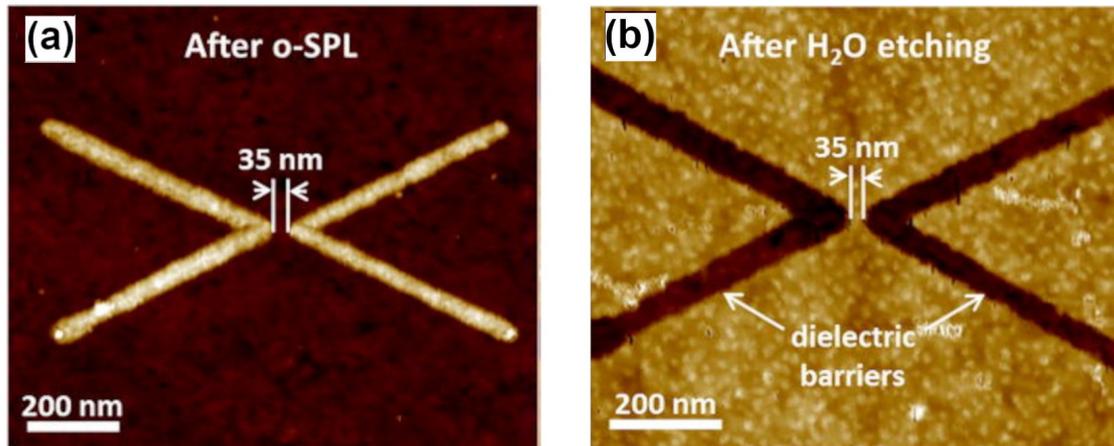
Figure 6: High-resolution patterning of transition metal dichalcogenides by LAO. (a) AFM topography of a ≈35 nm constriction patterned on few-layer WSe$_2$ prior to etching. (b) AFM topography of the same constriction after selective dissolution of the oxide in deionized water, revealing the etched trench. Panels (a,b) adapted from [24] (© 2016 A. I. Dago et al., published by AIP Publishing, distributed under the terms of the Creative Commons Attribution 4.0 International License, https://creativecommons.org/licenses/by/4.0).

(2H) and semi-metallic (1T′) phases using a tip-based lithographic approach; examples of such patterns are shown in Figure 5d–f. The method does not induce measurable phase transitions, preserving the intrinsic material properties and is, therefore, suitable for exploring fundamental behaviors of MoTe$_2$ at the nanoscale. Interestingly, increasing either the relative humidity or the line dose promotes greater oxide formation, resulting in deeper structuring of MoTe$_2$ after oxide removal (i.e., etching depths of up to 6 nm have been observed following water etching). In contrast, raising the bias voltage primarily broadens the lateral growth of the oxide without significantly impacting its height. The authors demonstrated that the hybrid approach (combining electron emission with oxidation) effectively addresses common limitations observed in 2D samples contacted via a top electrode. By regulating current peaks and operating within a controlled field-emission regime, this method suppresses uncontrolled oxidation and minimizes the formation of line defects. The findings suggest broader applicability of such techniques to other tellurium-containing TMDs, emphasizing scalability and environmental considerations. This precise control has significant implications for applications in photonics, nanoelectronics, and quantum computing. However, challenges remain, including the influence of humidity on patterning reproducibility and the need to mitigate structural degradation during the oxidation process. Transitioning to t-SPL would ultimately enable operation in a dry nitrogen environment, thereby preventing oxidation, a capability recently demonstrated by Liu and coworkers [106].

It is to mention that also Shilov and coworkers focused on electrode-free nanopatterning of thick multilayer van der Waals

(vdW) heterostructures [64]. This approach, which relies on applying a low-frequency (10 kHz) AC voltage between the AFM tip in contact mode and the grounded substrate, achieves high-resolution etching (down to ≈100 nm) without the need for a humid environment. The technique demonstrates its effectiveness across a wide range of heterostructures, including those composed of hBN, graphene, WSe$_2$, and NbSe$_2$, with patterns such as trenches, constrictions, and dots created at nanoscale precision. The method capitalizes on electric field enhancement, facilitated by assembling vdW heterostructures on conductive graphite slabs, which localize and amplify the electric field. This enhancement enables the breakdown of dielectric materials, such as hBN, initiating chemical reactions that drive the etching process. Notably, the method is robust under low humidity (RH ≈ 20%). This study emphasizes precise control, reproducibility, and compatibility with complex vdW heterostructures, similar to the previously discussed work on EFLAO, while also asserting the advantage of functioning effectively in a less humid environment.

3 Remaining challenges and perspectives
This section briefly highlights future directions to address current limitations and expand the scope of LAO.

3.1 Novel materials
While semiconductors, metals, and 2D materials have been extensively studied, LAO should be further explored for materials like black phosphorus (BP) and 2D transition metal carbides (MXenes) that may introduce new oxidation dynamics. Regrettably, key factors such as oxygen, humidity, and light, which contribute to the ambient degradation of few-layer BP [107],

may present significant challenges for the application of LAO. The conductive properties of MXenes range from metallic to semiconductor-like [108], making them promising candidates for LAO experiments (see Section 3.2.3). Delaminated individual flakes, reaching lateral sizes of up to 40 μm [109], are already available and can be utilized for patterning multiple contacts and fabricating FETs, like earlier approaches with single graphene flakes. However, their susceptibility to degradation in the presence of water and oxygen remains a significant challenge [110]. Yet, for both materials, an ultrathin casing layer of oxide or polymer resist might not represent an obstacle to LAO processing, as already demonstrated [41,63].

Polymers remain an underexploited material domain for LAO experiments. Suitable polymeric materials with electrochemical patterning capabilities are rare. With few exceptions, like the organic semiconductor [111] or organometallic multilayers [112], polymers, with their markedly insulating nature, tend to pose serious challenges to current-driven local oxidation by the scanning probe. Nevertheless, it is indeed possible to cross-link a thin molecular resist layer by LAO to induce local cross-linking [113].

Expanding LAO to organic and biocompatible materials holds significant potential for creating functional surfaces tailored for medical applications [114]. By leveraging LAO's precise patterning capabilities, researchers can develop surfaces with nanoscale features that promote specific interactions with biological systems. For instance, functionalized surfaces could enhance cell adhesion, guide tissue growth, or enable selective biomolecule immobilization. As an example, Martínez et al. [115] combined top-down oxidative nanolithography techniques and bottom-up electrostatic interactions to pattern single molecules of ferritin on silicon surfaces. Furthermore, biocompatible materials such as polymers can be selectively oxidized to create hydrophilic regions or chemically reactive sites, enabling controlled interactions with proteins, cells, or other biomolecules. However, challenges remain in ensuring that the LAO process does not degrade the material's biocompatibility or structural integrity, particularly for sensitive organic substrates.

3.2 Enhancing process precision

3.2.1 Advanced tip design.
Developing tips with improved durability and conductivity (e.g., multilayer coatings or adaptive tip shapes) could mitigate wear and maintain precision over extended use. Selecting an appropriate tip material is crucial for achieving high image and pattern resolution during LAO. A suitable tip must meet three key criteria: (i) high electrical conductivity, (ii) strong mechanical stability (durability), and (iii) an optimal geometry characterized by a sharp apex and appropriate cone angle. Traditional materials used in LAO ex-

periments are highly doped Si or metals including W, Pt, Au, and Ir. Si-based tips are cheap but lack mechanical durability, frequently suffering from deformation or damage during imaging and patterning. Metal-coated tips all offer excellent electrical conductivity and improved mechanical stability. However, these coatings can degrade over time due to mechanical wear and electrochemical reactions, especially under high contact forces (1000–1500 nN) and elevated bias voltages (10–25 V). This degradation can lead to tip blunting or delamination, reducing resolution and altering oxide feature dimensions. Recently, GaN NWs have demonstrated exceptional mechanical properties [67], making them promising candidates for SPL-related applications (Figure 5c). Diamond carbon-coated tips offer exceptional mechanical properties but are limited by their relatively large minimum tip radius. Solid platinum silicide (PtSi) tips provide a strong alternative [116], combining durability with consistent conductivity, even when the external coating peels off.

3.2.2 Substrate surface engineering.
The substrate plays a critical role in determining the precision and quality of features produced by LAO. Pre-treatment techniques, such as oxygen plasma cleaning, ensure that the substrate surface is free of contaminants and uniform, providing a consistent environment for the oxidation reaction. Similarly, applying thin surface coatings, like hydrophilic layers, can enhance the formation and stability of the water meniscus, which is crucial for consistent oxidation. Engineering the substrate's surface energy is another promising avenue. Substrates with controlled hydrophilic or hydrophobic properties can help localize the oxidation process, reducing lateral spreading and improving feature sharpness. Advanced techniques, such as ALD to create ultrasmooth and defect-free surfaces, further enhance the precision and reproducibility of LAO.

3.2.3 Material-specific approaches.
Tailoring LAO parameters to the specific properties of the material being patterned is essential for achieving high-resolution and uniform features. Different materials exhibit varying oxidation kinetics, conductivity, and susceptibility to environmental conditions. For example, TMDs such as MoS_2 and WSe_2 are especially sensitive to phonon scattering, which significantly influences their thermal conductivity, electrical transport properties, and carrier mobility. As a result, precise control over oxidation depth and lateral diffusion during processing may require the use of lower voltages and carefully optimized humidity conditions. Hybrid approaches, which combine LAO with complementary techniques such as chemical vapor deposition or thermal oxidation, can further improve feature resolution and reduce defects. In the context of biocompatible materials, the direct application of LAO for surface oxidation or modification on biological sub-

strates or tissues remains largely unexplored. A promising strategy could involve the patterning of poly-L-lysine (PLL) thin films, a well-established material in biotechnology [117]. Following LAO patterning, protein-resistant polymers like polyethylene glycol can be selectively grafted onto the patterned areas, forming a copolymer with PLL that faithfully replicates the design. This approach has potential for advancing protein patterning, tissue engineering, biomedical implants, and biosensor development.

LAO offers a promising route for fabricating superconducting quantum devices by enabling direct, nanoscale patterning of Josephson junctions without conventional lithography. Using a biased AFM tip, ultrathin oxide barriers can be written locally on superconducting films such as Nb [29,118], TiN [119], or Al, transforming selected regions into insulating junctions that act as weak links for Cooper pair tunneling. This technique allows for the precise creation of Josephson junctions or SQUID loops with tunable critical currents, minimal contamination, and sub-10 nm spatial control. Extending LAO to 2D superconductors like $NbSe_2$ [120] or Mo_2C [121] could further enable atomically clean, reconfigurable qubit architectures, merging nanolithography and quantum engineering into a single scalable process.

3.2.4 Multitip and parallelized systems. Scaling and automation, such as parallelized LAO, have been proposed as key solutions to compete with standard optical lithography processes. Multitip AFM setups or arrays could enable scalable fabrication while preserving nanoscale resolution. Currently, thermal SPL technologies utilizing active cantilevers appear more likely to advance toward parallel operations [122,123], as illustrated by the recently introduced Decapede system from Heidelberg Instruments, a commercial multicantilever NanoFrazor platform that demonstrates scalable parallel t-SPL. By contrast, LAO remains primarily a prototyping technique best suited for laboratory-scale setups. It is worth noting that recently developed cantilever-free scanning probe technologies [124] address the scalability challenge by employing large arrays of polymer pens, effectively overcoming the inherently low throughput of traditional SPL.

3.2.5 Machine learning. Optimizing LAO process parameters (such as pulse amplitude, width, and tip–sample interaction) remains a complex challenge. Recent developments in numerical simulation and machine learning (ML) offer promising avenues to address these complexities and might reduce dependency on trial-and-error methodologies. For example, numerical simulations can be employed to explore complex reaction mechanisms involved in nanomanufacturing processes at the nanoscale. This approach has recently been used to clarify the

anisotropic effects observed during the LAO process on silicon [125]. Supervised learning models can be trained on experimental data to predict feature geometries, enabling more precise control over the oxidation process. Additionally, reinforcement learning approaches can facilitate real-time adaptive control of pulse parameters to achieve desired nanostructures. Notably, a study by Zhang et al. [126] introduced a semantic segmentation framework that automates the evaluation of nanolithography results, significantly accelerating the optimization of process conditions and parameters. By integrating such ML-based frameworks, LAO nanolithography can transition from empirical methodologies to more deterministic and efficient fabrication processes, paving the way for advancements in nanoelectronics and photonics.

Conclusion

The continued development of LAO will rely on interdisciplinary efforts to innovate materials, processes, and applications. Advances in tip design, dynamic operation modes, and environmental control have significantly enhanced its precision and reproducibility, while substrate engineering and material-specific approaches might expand its applicability to complex systems like TMDs, other 2D layered materials and biocompatible surfaces. Despite challenges like tip wear and environmental sensitivity, innovations such as electrode-free local anodic oxidation are extending the potential of LAO toward scalable and industrially viable solutions. By addressing these challenges and leveraging its strengths, LAO could eventually become a cornerstone technique in next-generation nanofabrication.

Acknowledgements

Conflict of Interest

The author has no conflicts to disclose.

Author Contributions

Matteo Lorenzoni: conceptualization; data curation; formal analysis; funding acquisition; investigation; methodology; project administration; resources; software; supervision; validation; visualization; writing – original draft; writing – review & editing.

ORCID® iDs

Matteo Lorenzoni - https://orcid.org/0000-0001-5287-8761

Data Availability Statement

Data sharing is not applicable as no new data was generated or analyzed in this study.

References

1. Garcia, R.; Knoll, A. W.; Riedo, E. *Nat. Nanotechnol.* **2014,** *9,* 577–587. doi:10.1038/nnano.2014.157

2. Pellegrino, P.; Farella, I.; Cascione, M.; De Matteis, V.; Bramanti, A. P.; Vincenti, L.; Della Torre, A.; Quaranta, F.; Rinaldi, R. *Micromachines* **2022,** *13,* 1982. doi:10.3390/mi13111982

3. Yang, Y.; Lin, J. *Scanning* **2016,** *38,* 412–420. doi:10.1002/sca.21287

4. Liu, G.; Petrosko, S. H.; Zheng, Z.; Mirkin, C. A. *Chem. Rev.* **2020,** *120,* 6009–6047. doi:10.1021/acs.chemrev.9b00725

5. Howell, S. T.; Grushina, A.; Holzner, F.; Brugger, J. *Microsyst. Nanoeng.* **2020,** *6,* 21. doi:10.1038/s41378-019-0124-8

6. Dagata, J. A. *Science* **1995,** *270,* 1625. doi:10.1126/science.270.5242.1625

7. Tseng, A. A., Ed. *Tip-Based Nanofabrication: Fundamentals and Applications,* 1st ed.; Springer: New York, NY, 2011. doi:10.1007/978-1-4419-9899-6

8. Lorenzoni, M.; Pérez-Murano, F. Conductive Atomic Force Microscopy for Nanolithography Based on Local Anodic Oxidation. In *Conductive Atomic Force Microscopy;* Lanza, M., Ed.; Wiley-VCH Verlag GmbH & Co. KGaA, 2017; pp 211–223. doi:10.1002/9783527699773.ch9

9. García, R.; Calleja, M.; Pérez-Murano, F. *Appl. Phys. Lett.* **1998,** *72,* 2295–2297. doi:10.1063/1.121340

10. Dagata, J. A.; Schneir, J.; Harary, H. H.; Evans, C. J.; Postek, M. T.; Bennett, J. *Appl. Phys. Lett.* **1990,** *56,* 2001–2003. doi:10.1063/1.102999

11. Nagahara, L. A.; Thundat, T.; Lindsay, S. M. *Appl. Phys. Lett.* **1990,** *57,* 270–272. doi:10.1063/1.103711

12. Barniol, N.; Pérez-Murano, F.; Aymerich, X. *Appl. Phys. Lett.* **1992,** *61,* 462–464. doi:10.1063/1.107885

13. Minne, S. C.; Soh, H. T.; Flueckiger, P.; Quate, C. F. *Appl. Phys. Lett.* **1995,** *66,* 703–705. doi:10.1063/1.114105

14. Bartošík, M.; Škoda, D.; Tomanec, O.; Kalousek, R.; Jánský, P.; Zlámal, J.; Spousta, J.; Dub, P.; Šikola, T. *Phys. Rev. B* **2009,** *79,* 195406. doi:10.1103/physrevb.79.195406

15. Calleja, M.; Tello, M.; García, R. *J. Appl. Phys.* **2002,** *92,* 5539–5542. doi:10.1063/1.1510171

16. Servat, J.; Gorostiza, P.; Sanz, F.; Pérez-Murano, F.; Barniol, N.; Abadal, G.; Aymerich, X. *J. Vac. Sci. Technol., A* **1996,** *14,* 1208–1212. doi:10.1116/1.580268

17. Dagata, J. A.; Perez-Murano, F.; Martin, C.; Kuramochi, H.; Yokoyama, H. *J. Appl. Phys.* **2004,** *96,* 2393–2399. doi:10.1063/1.1771821

18. Tominov, R.; Avilov, V.; Vakulov, Z.; Khakhulin, D.; Ageev, O.; Valov, I.; Smirnov, V. *Adv. Electron. Mater.* **2022,** *8,* 2200215. doi:10.1002/aelm.202200215

19. He, Y.; Zhang, L.; Cui, J.; Hu, J. *Wear* **2023,** *522,* 204694. doi:10.1016/j.wear.2023.204694

20. Liou, J.-W.; Woon, W.-Y. *J. Phys. Chem. C* **2019,** *123,* 25422–25427. doi:10.1021/acs.jpcc.9b04175

21. Ryu, Y. K.; Dago, A. I.; He, Y.; Espinosa, F. M.; López-Elvira, E.; Munuera, C.; Garcia, R. *Appl. Surf. Sci.* **2021,** *539,* 148231. doi:10.1016/j.apsusc.2020.148231

22. Masubuchi, S.; Arai, M.; Machida, T. *Nano Lett.* **2011,** *11,* 4542–4546. doi:10.1021/nl201448q

23. Li, H.; Ying, Z.; Lyu, B.; Deng, A.; Wang, L.; Taniguchi, T.; Watanabe, K.; Shi, Z. *Nano Lett.* **2018,** *18,* 8011–8015. doi:10.1021/acs.nanolett.8b04166

24. Dago, A. I.; Ryu, Y. K.; Garcia, R. *Appl. Phys. Lett.* **2016,** *109,* 163103. doi:10.1063/1.4965840

25. Espinosa, F. M.; Ryu, Y. K.; Marinov, K.; Dumcenco, D.; Kis, A.; Garcia, R. *Appl. Phys. Lett.* **2015,** *106,* 103503. doi:10.1063/1.4914349

26. Borodin, B. R.; Benimetskiy, F. A.; Alekseev, P. A. *Nanotechnology* **2021,** *32,* 155304. doi:10.1088/1361-6528/abd817

27. Pinilla-Cienfuegos, E.; Mañas-Valero, S.; Navarro-Moratalla, E.; Tatay, S.; Forment-Aliaga, A.; Coronado, E. *Appl. Sci.* **2016,** *6,* 250. doi:10.3390/app6090250

28. Held, R.; Heinzel, T.; Studerus, P.; Ensslin, K. *Phys. E (Amsterdam, Neth.)* **1998,** *2,* 748–752. doi:10.1016/s1386-9477(98)00153-2

29. Heidelberg, A.; Rozenkranz, C.; Schultze, J. W.; Schäpers, T.; Staikov, G. *Surf. Sci.* **2005,** *597,* 173–180. doi:10.1016/j.susc.2004.10.056

30. Avouris, P.; Hertel, T.; Martel, R. *Appl. Phys. Lett.* **1997,** *71,* 285–287. doi:10.1063/1.119521

31. Avouris, P.; Martel, R.; Hertel, T.; Sandstrom, R. *Appl. Phys. A: Mater. Sci. Process.* **1998,** *66,* S659–S667. doi:10.1007/s003390051218

32. Červenka, J.; Kalousek, R.; Bartošík, M.; Škoda, D.; Tomanec, O.; Šikola, T. *Appl. Surf. Sci.* **2006,** *253,* 2373–2378. doi:10.1016/j.apsusc.2006.03.095

33. Gasser, U.; Sigrist, M.; Gustavsson, S.; Ensslin, K.; Ihn, T. Double Layer Local Anodic Oxidation Using Atomic Force Microscopy. In *Tip-Based Nanofabrication;* Tseng, A. A., Ed.; Springer: New York, 2011; pp 91–127. doi:10.1007/978-1-4419-9899-6_3

34. Lorenzoni, M.; Torre, B. *Appl. Phys. Lett.* **2013,** *103,* 163109. doi:10.1063/1.4825265

35. Puddy, R. K.; Chua, C. J.; Buitelaar, M. R. *Appl. Phys. Lett.* **2013,** *103,* 183117. doi:10.1063/1.4828663

36. Reuter, C.; Ecke, G.; Strehle, S. *Adv. Mater. (Weinheim, Ger.)* **2024,** *36,* 2310887. doi:10.1002/adma.202310887

37. Polyakova, V. V.; Kots, I. N.; Smirnov, V. A.; Ageev, O. A. *Russ. Microelectron.* **2019,** *48,* 66–71. doi:10.1134/s1063739719020082

38. Archanjo, B. S.; Siles, P. F.; Oliveira, C. K. B. Q. M.; Baptista, D. L.; Neves, B. R. A. *Adv. Mater. Sci. Eng.* **2013,** *2013,* 898565. doi:10.1155/2013/898565

39. Li, J.; Chai, G.; Wang, X. *Int. J. Extreme Manuf.* **2023,** *5,* 032003. doi:10.1088/2631-7990/acd88e

40. Lorenzoni, M.; Giugni, A.; Torre, B. *Nanoscale Res. Lett.* **2013,** *8,* 75. doi:10.1186/1556-276x-8-75

41. Fernandez-Cuesta, I.; Borrisé, X.; Pérez-Murano, F. *Nanotechnology* **2005,** *16,* 2731–2737. doi:10.1088/0957-4484/16/11/045

42. Kyoung Ryu, Y.; Aitor Postigo, P.; Garcia, F.; Garcia, R. *Appl. Phys. Lett.* **2014,** *104,* 223112. doi:10.1063/1.4881977

43. Morimoto, K.; Pérez-Murano, F.; Dagata, J. A. *Appl. Surf. Sci.* **2000,** *158,* 205–216. doi:10.1016/s0169-4332(00)00017-9

44. Cabrera, N.; Mott, N. F. *Rep. Prog. Phys.* **1949,** *12,* 163–184. doi:10.1088/0034-4885/12/1/308

45. Kinser, C. R.; Schmitz, M. J.; Hersam, M. C. *Adv. Mater. (Weinheim, Ger.)* **2006,** *18,* 1377–1380. doi:10.1002/adma.200501231

46. Pérez-Murano, F.; Martín, C.; Barniol, N.; Kuramochi, H.; Yokoyama, H.; Dagata, J. A. *Appl. Phys. Lett.* **2003,** *82,* 3086–3088. doi:10.1063/1.1572480

47. Dagata, J. A.; Inoue, T.; Itoh, J.; Matsumoto, K.; Yokoyama, H. *J. Appl. Phys.* **1998,** *84,* 6891–6900. doi:10.1063/1.368986

48. Dubois, E.; Bubendorff, J.-L. *J. Appl. Phys.* **2000,** *87,* 8148–8154. doi:10.1063/1.373510

49. Rius, G.; Lorenzoni, M.; Matsui, S.; Tanemura, M.; Perez-Murano, F. *Beilstein J. Nanotechnol.* **2015,** *6,* 215–222. doi:10.3762/bjnano.6.20

50. Martinez, J.; Martínez, R. V.; Garcia, R. *Nano Lett.* **2008,** *8,* 3636–3639. doi:10.1021/nl801599k

51. Rius, G.; Matsui, S.; Tanemura, M.; Lorenzoni, M.; Pérez-Murano, F. Properties and applications of carbon nanofibers for atomic force microscopy. In *2015 IEEE 10th International Conference on Nano/Micro Engineered and Molecular Systems, NEMS 2015,* 2015; pp 571–574. doi:10.1109/nems.2015.7147494

52. Martínez, R. V.; Martínez, J.; Garcia, R. *Nanotechnology* **2010,** *21,* 245301. doi:10.1088/0957-4484/21/24/245301

53. Fan, P.; Gao, J.; Mao, H.; Geng, Y.; Yan, Y.; Wang, Y.; Goel, S.; Luo, X. *Micromachines* **2022,** *13,* 228. doi:10.3390/mi13020228

54. Zhu, C.; Ekinci, H.; Pan, A.; Cui, B.; Zhu, X. *Microsyst. Nanoeng.* **2024,** *10,* 52. doi:10.1038/s41378-024-00682-9

55. Oehrlein, G. S.; Brandstadter, S. M.; Bruce, R. L.; Chang, J. P.; DeMott, J. C.; Donnelly, V. M.; Dussart, R.; Fischer, A.; Gottscho, R. A.; Hamaguchi, S.; Honda, M.; Hori, M.; Ishikawa, K.; Jaloviar, S. G.; Kanarik, K. J.; Karahashi, K.; Ko, A.; Kothari, H.; Kuboi, N.; Kushner, M. J.; Lill, T.; Luan, P.; Mesbah, A.; Miller, E.; Nath, S.; Ohya, Y.; Omura, M.; Park, C.; Poulose, J.; Rauf, S.; Sekine, M.; Smith, T. G.; Stafford, N.; Standaert, T.; Ventzek, P. L. G. *J. Vac. Sci. Technol., B: Nanotechnol. Microelectron.: Mater., Process ., Meas., Phenom.* **2024,** *42,* 041501. doi:10.1116/6.0003579

56. Kaestner, M.; Rangelow, I. W. *Microelectron. Eng.* **2012,** *97,* 96–99. doi:10.1016/j.mee.2012.05.042

57. Kaestner, M.; Rangelow, I. W. *Int. J. Extreme Manuf.* **2020,** *2,* 032005. doi:10.1088/2631-7990/aba2d8

58. Snow, E. S.; Campbell, P. M.; Perkins, F. K. *Appl. Phys. Lett.* **1999,** *75,* 1476–1478. doi:10.1063/1.124730

59. Luo, X.; Gao, J.; Xie, W.; Hasan, R. M. M.; Qin, Y. *CIRP Ann.* **2023,** *72,* 177–180. doi:10.1016/j.cirp.2023.04.030

60. Dai, H.; Franklin, N.; Han, J. *Appl. Phys. Lett.* **1998,** *73,* 1508–1510. doi:10.1063/1.122188

61. Kumar, K.; Sul, O.; Strauf, S.; Choi, D. S.; Fisher, F.; Prasad, M. G.; Yang, E.-H. *IEEE Trans. Nanotechnol.* **2011,** *10,* 849–854. doi:10.1109/tnano.2010.2086474

62. Kuramochi, H.; Tokizaki, T.; Yokoyama, H.; Dagata, J. A. *Nanotechnology* **2007,** *18,* 135703. doi:10.1088/0957-4484/18/13/135703

63. Martin-Olmos, C.; Villanueva, L. G.; van der Wal, P. D.; Llobera, A.; de Rooij, N. F.; Brugger, J.; Perez-Murano, F. *Adv. Funct. Mater.* **2012,** *22,* 1482–1488. doi:10.1002/adfm.201102789

64. Shilov, A. L.; Elesin, L.; Grebenko, A.; Kleshch, V. I.; Kashchenko, M. A.; Mazurenko, I.; Titova, E.; Zharkova, E.; Yakovlev, D. S.; Novoselov, K. S.; Ghazaryan, D. A.; Dremov, V.; Bandurin, D. A. *arXiv* **2024,** No. 2406.16354. doi:10.48550/arxiv.2406.16354

65. Krivoshapkina, Y.; Kaestner, M.; Lenk, C.; Lenk, S.; Rangelow, I. W. *Microelectron. Eng.* **2017,** *177,* 78–86. doi:10.1016/j.mee.2017.02.021

66. Rangelow, I. W.; Ivanov, T.; Ahmad, A.; Kaestner, M.; Lenk, C.; Bozchalooi, I. S.; Xia, F.; Youcef-Toumi, K.; Holz, M.; Reum, A. *J. Vac. Sci. Technol., B: Nanotechnol. Microelectron.: Mater., Process ., Meas., Phenom.* **2017,** *35,* 06G101. doi:10.1116/1.4992073

67. Behzadirad, M.; Mecholdt, S.; Randall, J. N.; Ballard, J. B.; Owen, J.; Rishinaramangalam, A. K.; Reum, A.; Gotszalk, T.; Feezell, D. F.; Rangelow, I. W.; Busani, T. *Nano Lett.* **2021,** *21,* 5493–5499. doi:10.1021/acs.nanolett.1c00127

68. Bicer, M.; Kumar, B. G.; Melikov, R.; Bakis Dogru, I.; Sadeghi, S.; Rangelow, I. W.; Alaca, B. E.; Nizamoglu, S. *Nanotechnology* **2020,** *31,* 435303. doi:10.1088/1361-6528/ab99f5

69. Hu, W.; Bain, J.; Ricketts, D. *Micro Nano Lett.* **2013,** *8,* 43–46. doi:10.1049/mnl.2012.0859

70. Sigrist, M.; Fuhrer, A.; Ihn, T.; Ensslin, K.; Driscoll, D. C.; Gossard, A. C. *Appl. Phys. Lett.* **2004,** *85,* 3558–3560. doi:10.1063/1.1809273

71. Komijani, Y.; Csontos, M.; Ihn, T.; Ensslin, K.; Meir, Y.; Reuter, D.; Wieck, A. D. *Phys. Rev. B* **2013,** *87,* 245406. doi:10.1103/physrevb.87.245406

72. Chiesa, M.; Cardenas, P. P.; Otón, F.; Martinez, J.; Mas-Torrent, M.; Garcia, F.; Alonso, J. C.; Rovira, C.; Garcia, R. *Nano Lett.* **2012,** *12,* 1275–1281. doi:10.1021/nl2037547

73. Alias, N. N.; Mohammad Haniff, M. A. S.; Yaacob, K. A. *Sci. Rep.* **2025,** *15,* 32902. doi:10.1038/s41598-025-18100-z

74. Kun, P.; Fülöp, B.; Dobrik, G.; Nemes-Incze, P.; Lukács, I. E.; Csonka, S.; Hwang, C.; Tapasztó, L. *npj 2D Mater. Appl.* **2020,** *4,* 43. doi:10.1038/s41699-020-00177-x

75. Liu, X.; Huang, Z.; Zheng, X.; Shahrjerdi, D.; Riedo, E. *APL Mater.* **2021,** *9,* 011107. doi:10.1063/5.0026159

76. Colangelo, F.; Piazza, V.; Coletti, C.; Roddaro, S.; Beltram, F.; Pingue, P. *Nanotechnology* **2017,** *28,* 105709. doi:10.1088/1361-6528/aa59c7

77. Weng, L.; Zhang, L.; Chen, Y. P.; Rokhinson, L. P. *Appl. Phys. Lett.* **2008,** *93,* 093107. doi:10.1063/1.2976429

78. Heine, A. W.; Tutuc, D.; Zwicknagl, G.; Haug, R. J. *Phys. Rev. Lett.* **2016,** *116,* 096802. doi:10.1103/physrevlett.116.096802

79. Brown, B. P.; Picco, L.; Miles, M. J.; Faul, C. F. J. *Small* **2015,** *11,* 5054–5058. doi:10.1002/smll.201501779

80. Yang, M.; Wouters, D.; Giesbers, M.; Schubert, U. S.; Zuilhof, H. *ACS Nano* **2009,** *3,* 2887–2900. doi:10.1021/nn9007059

81. Yoshinobu, T.; Suzuki, J.; Kurooka, H.; Moon, W. C.; Iwasaki, H. *Electrochim. Acta* **2003,** *48,* 3131–3135. doi:10.1016/s0013-4686(03)00342-6

82. Li, Z.; Sadowski, J. T.; Dolocan, A.; Mangolini, F. *Adv. Funct. Mater.* **2023,** *33,* 2306660. doi:10.1002/adfm.202306660

83. Wang, P.; Okamoto, K.; Tamada, K. *Adv. Mater. Interfaces* **2014,** *1,* 1400268. doi:10.1002/admi.201400268

84. Maoz, R.; Frydman, E.; Cohen, S. R.; Sagiv, J. *Adv. Mater. (Weinheim, Ger.)* **2000,** *12,* 725–731. doi:10.1002/(sici)1521-4095(200005)12:10<725::aid-adma725>3.0.co; 2-z

85. Zeira, A.; Berson, J.; Feldman, I.; Maoz, R.; Sagiv, J. *Langmuir* **2011,** *27,* 8562–8575. doi:10.1021/la2009946

86. Berson, J.; Burshtain, D.; Zeira, A.; Yoffe, A.; Maoz, R.; Sagiv, J. *Nat. Mater.* **2015,** *14,* 613–621. doi:10.1038/nmat4254

87. Lorenzoni, M.; Giugni, A.; Di Fabrizio, E.; Pérez-Murano, F.; Mescola, A.; Torre, B. *Nanotechnology* **2015,** *26,* 285301. doi:10.1088/0957-4484/26/28/285301

88. Polyakova, V. V.; Savenko, A. V. *Tech. Phys.* **2022,** *67,* 423–428. doi:10.1134/s1063784222060068

89. Jiao, Z.; Zhang, H.; Wu, M.; Guo, H.; Wang, J.; Zhao, B.; Ding, G. *J. Mater. Sci.: Mater. Electron.* **2009,** *20,* 177–180. doi:10.1007/s10854-008-9678-1

90. Lüscher, S.; Fuhrer, A.; Held, R.; Heinzel, T.; Ensslin, K.; Wegscheider, W. *Appl. Phys. Lett.* **1999,** *75,* 2452–2454. doi:10.1063/1.125045

91. Dhar, S.; Seitz, O.; Halls, M. D.; Choi, S.; Chabal, Y. J.; Feldman, L. C. *J. Am. Chem. Soc.* **2009,** *131,* 16808–16813. doi:10.1021/ja9053465

92. Ahn, J.-J.; Jo, Y.-D.; Kim, S.-C.; Lee, J.-H.; Koo, S.-M. *Nanoscale Res. Lett.* **2011,** *6,* 235. doi:10.1186/1556-276x-6-235

93. Ovenden, C.; Farrer, I.; Skolnick, M. S.; Heffernan, J. *Semicond. Sci. Technol.* **2022,** *37,* 025001. doi:10.1088/1361-6641/ac3f20

94. Kumar, A.; Chen, C.-S.; Maroudas, D. *J. Appl. Phys.* **2019,** *125,* 045303. doi:10.1063/1.5064807

95. Fabre, B.; Herrier, C. *RSC Adv.* **2012,** *2,* 168–175. doi:10.1039/c1ra00450f

96. Fernández-Regúlez, M.; Evangelio, L.; Lorenzoni, M.; Fraxedas, J.; Pérez-Murano, F. *ACS Appl. Mater. Interfaces* **2014,** *6,* 21596–21602. doi:10.1021/am506600m

97. Komonov, A. I.; Mantsurov, N. D.; Voloshin, B. V.; Seleznev, V. A.; Mutilin, S. V. *Appl. Surf. Sci.* **2024,** *658,* 159869. doi:10.1016/j.apsusc.2024.159869

98. Giesbers, A. J. M.; Zeitler, U.; Neubeck, S.; Freitag, F.; Novoselov, K. S.; Maan, J. C. *Solid State Commun.* **2008,** *147,* 366–369. doi:10.1016/j.ssc.2008.06.027

99. Masubuchi, S.; Ono, M.; Yoshida, K.; Hirakawa, K.; Machida, T. *Appl. Phys. Lett.* **2009,** *94,* 082107. doi:10.1063/1.3089693

100. Dago, A. I.; Sangiao, S.; Fernández-Pacheco, R.; De Teresa, J. M.; Garcia, R. *Carbon* **2018,** *129,* 281–285. doi:10.1016/j.carbon.2017.12.033

101. Cohen, L. A.; Samuelson, N. L.; Wang, T.; Klocke, K.; Reeves, C. C.; Taniguchi, T.; Watanabe, K.; Vijay, S.; Zaletel, M. P.; Young, A. F. *Nat. Phys.* **2023,** *19,* 1502–1508. doi:10.1038/s41567-023-02114-3

102. Rani, E.; Wong, L. S. *Adv. Mater. Technol. (Weinheim, Ger.)* **2019,** *4,* 1900181. doi:10.1002/admt.201900181

103. Mativetsky, J. M.; Liscio, A.; Treossi, E.; Orgiu, E.; Zanelli, A.; Samorì, P.; Palermo, V. *J. Am. Chem. Soc.* **2011,** *133,* 14320–14326. doi:10.1021/ja202371h

104. Zhang, K.; Fu, Q.; Pan, N.; Yu, X.; Liu, J.; Luo, Y.; Wang, X.; Yang, J.; Hou, J. *Nat. Commun.* **2012,** *3,* 1194. doi:10.1038/ncomms2200

105. Wei, Z.; Wang, D.; Kim, S.; Kim, S.-Y.; Hu, Y.; Yakes, M. K.; Laracuente, A. R.; Dai, Z.; Marder, S. R.; Berger, C.; King, W. P.; de Heer, W. A.; Sheehan, P. E.; Riedo, E. *Science* **2010,** *328,* 1373–1376. doi:10.1126/science.1188119

106. Liu, X.; Howell, S. T.; Conde-Rubio, A.; Boero, G.; Brugger, J. *Adv. Mater. (Weinheim, Ger.)* **2020,** *32,* 2001232. doi:10.1002/adma.202001232

107. Zhang, X.; Zhang, W. *Mater. Today Phys.* **2024,** *43,* 101396. doi:10.1016/j.mtphys.2024.101396

108. Zhang, Y.-Z.; Wang, Y.; Jiang, Q.; El-Demellawi, J. K.; Kim, H.; Alshareef, H. N. *Adv. Mater. (Weinheim, Ger.)* **2020,** *32,* 1908486. doi:10.1002/adma.201908486

109. Shekhirev, M.; Busa, J.; Shuck, C. E.; Torres, A.; Bagheri, S.; Sinitskii, A.; Gogotsi, Y. *ACS Nano* **2022,** *16,* 13695–13703. doi:10.1021/acsnano.2c04506

110. Anasori, B.; Naguib, M.; Guest Editors. *MRS Bull.* **2023,** *48,* 238–244. doi:10.1557/s43577-023-00500-z

111. Fenwick, O.; Bozec, L.; Credgington, D.; Hammiche, A.; Lazzerini, G. M.; Silberberg, Y. R.; Cacialli, F. *Nat. Nanotechnol.* **2009,** *4,* 664–668. doi:10.1038/nnano.2009.254

112. Song, J.; Hempenius, M. A.; Jing Chung, H.; Julius Vancso, G. *Nanoscale* **2015,** *7,* 9970–9974. doi:10.1039/c5nr01206f

113. Lorenzoni, M.; Wagner, D.; Neuber, C.; Schmidt, H.-W.; Perez-Murano, F. *Appl. Surf. Sci.* **2018,** *442,* 106–113. doi:10.1016/j.apsusc.2018.02.096

114. Marrese, M.; Guarino, V.; Ambrosio, L. *J. Funct. Biomater.* **2017,** *8,* 7. doi:10.3390/jfb8010007

115. Martínez, R. V.; Martínez, J.; Chiesa, M.; Garcia, R.; Coronado, E.; Pinilla-Cienfuegos, E.; Tatay, S. *Adv. Mater. (Weinheim, Ger.)* **2010,** *22,* 588–591. doi:10.1002/adma.200902568

116. Liu, M.; Zhu, Y.; Zhao, J.; Wang, L.; Yang, J.; Yang, F. *Micromachines* **2021,** *12,* 1326. doi:10.3390/mi12111326

117. Rossetti, F. F.; Reviakine, I.; Csúcs, G.; Assi, F.; Vörös, J.; Textor, M. *Biophys. J.* **2004,** *87,* 1711–1721. doi:10.1529/biophysj.104.041780

118. Faucher, M.; Fournier, T.; Pannetier, B.; Thirion, C.; Wernsdorfer, W.; Villegier, J. C.; Bouchiat, V. *Phys. C (Amsterdam, Neth.)* **2002,** *368,* 211–217. doi:10.1016/s0921-4534(01)01168-6

119. Gwo, S.; Yeh, C.-L.; Chen, P.-F.; Chou, Y.-C.; Chen, T. T.; Chao, T.-S.; Hu, S.-F.; Huang, T.-Y. *Appl. Phys. Lett.* **1999,** *74,* 1090–1092. doi:10.1063/1.123491

120. Yabuki, N.; Moriya, R.; Arai, M.; Sata, Y.; Morikawa, S.; Masubuchi, S.; Machida, T. *Nat. Commun.* **2016,** *7,* 10616. doi:10.1038/ncomms10616

121. Lei, J.; Kutana, A.; Yakobson, B. I. *J. Mater. Chem. C* **2017,** *5,* 3438–3444. doi:10.1039/c7tc00789b

122. Carroll, K. M.; Lu, X.; Kim, S.; Gao, Y.; Kim, H.-J.; Somnath, S.; Polloni, L.; Sordan, R.; King, W. P.; Curtis, J. E.; Riedo, E. *Nanoscale* **2014,** *6,* 1299–1304. doi:10.1039/c3nr05696a

123. Chaaban, J.; Könemann, F.; Bonnani, S.; Buddha, K.; Cagin, E. *Proc. SPIE* **2024,** *PC12956,* PC129560L. doi:10.1117/12.3009852

124. He, Q.; Tan, C.; Zhang, H. *ACS Nano* **2017,** *11,* 4381–4386. doi:10.1021/acsnano.7b03143

125. Gao, J.; Xie, W.; Luo, X.; Qin, Y.; Zhao, Z. *Langmuir* **2024,** *40,* 15530–15540. doi:10.1021/acs.langmuir.4c01129

126. Liu, Y.; Li, X.; Pei, B.; Ge, L.; Xiong, Z.; Zhang, Z. *Microsyst. Nanoeng.* **2023,** *9,* 128. doi:10.1038/s41378-023-00587-z

Calculation of the dynamic stiffness of a cantilever under torsional oscillation

Keita Nishida, Yuuki Yasui and Yoshiaki Sugimoto[*]

Abstract

Atomic force microscopy using Si cantilevers provides an effective means for investigating both conservative and dissipative interactions in the vertical and lateral directions between the tip and the sample. An accurate evaluation of the dynamic stiffness of the cantilever is indispensable in the quantitative analyses of the interactions. We calculated the dynamic stiffness of cantilevers under torsional oscillation based on the strain energy. Without tips, the torsional dynamic stiffness is approximately 23% larger than the static stiffness. The modification decreases to 21–23% with tips. Applying the present correction is essential for achieving quantitatively accurate stiffness values in dynamic measurements.

Introduction

Friction serves as a fundamental mechanism of energy dissipation [1]. While friction typically arises from direct mechanical contact between surfaces, energy dissipation can also occur even in the absence of physical contact, and this dissipation is called non-contact friction [2]. Its origins have been investigated down to the nanometer scale [3-5]. In particular, the origin of non-contact friction is attributed to electromagnetic interactions between the two bodies, although its detailed mechanisms remain not fully understood [5].

Non-contact atomic force microscopy (nc-AFM) is widely employed to investigate non-contact friction through its dissipation channel. Common techniques include pendulum AFM, bimodal AFM, and quartz tuning fork AFM [6-8]. Pendulum AFM uses cantilevers with small stiffness and provides exceptional sensitivity to conservative and dissipative forces owing to the small stiffness [2,9-11]. Non-contact friction measurements with pendulum AFM on a Nb film across the superconducting transition indicate that friction is electronic in the metallic state,

whereas phononic dissipation dominates in the superconducting state [10]. The cantilever in bimodal AFM oscillates in two modes, typically, the first flexural and first torsional modes [2]. The flexural mode is used for vertical tip-position control via its frequency shift, and the torsional mode detects the lateral interactions [7,12-14]. The torsional oscillation modes of AFM cantilevers are sensitive to in-plane interaction [15-17]. This method enabled highly accurate imaging of the in-plane crystalline orientation by utilizing friction information [14]. Quartz tuning fork AFM is useful as it can electrically detect energy dissipations [8]. Lateral force microscopy with quartz tuning fork AFM, using a CO-terminated tip, enabled the detection of energy dissipation over the chemical bonds of a PTCDA (3,4,9,10-perylenetetracarboxylic dianhydride) molecule, with a vertical decay length of 4 pm [18].

Quantitative interpretation of the conservative interaction energy and the energy dissipation requires the stiffness of the oscillators [19-21]. The oscillator exhibits different stiffnesses in dynamic and static cases [22-24]. While the static stiffness is easily obtained from the geometrical structure [2], an accurate evaluation of dynamic stiffness requires detailed analyses of the oscillator dynamics. The modification from static to dynamic stiffness depends on the oscillation mode because each mode is governed by a different equation of motion reflecting the underlying deformation mechanism.

Here, we calculated the dynamic stiffness of cantilevers with tips in torsional oscillation using the equivalent spring-moment of inertia model. Then we found that the dynamic stiffness should be modified by 21–23% when the tip is considered.

Dissipated energy is derived from the excitation amplitude through a proportionality coefficient that depends on the dynamic stiffness [21]. Thus, the present correction for the dynamic stiffness should be adopted for friction analyses with torsional oscillations in nc-AFM.
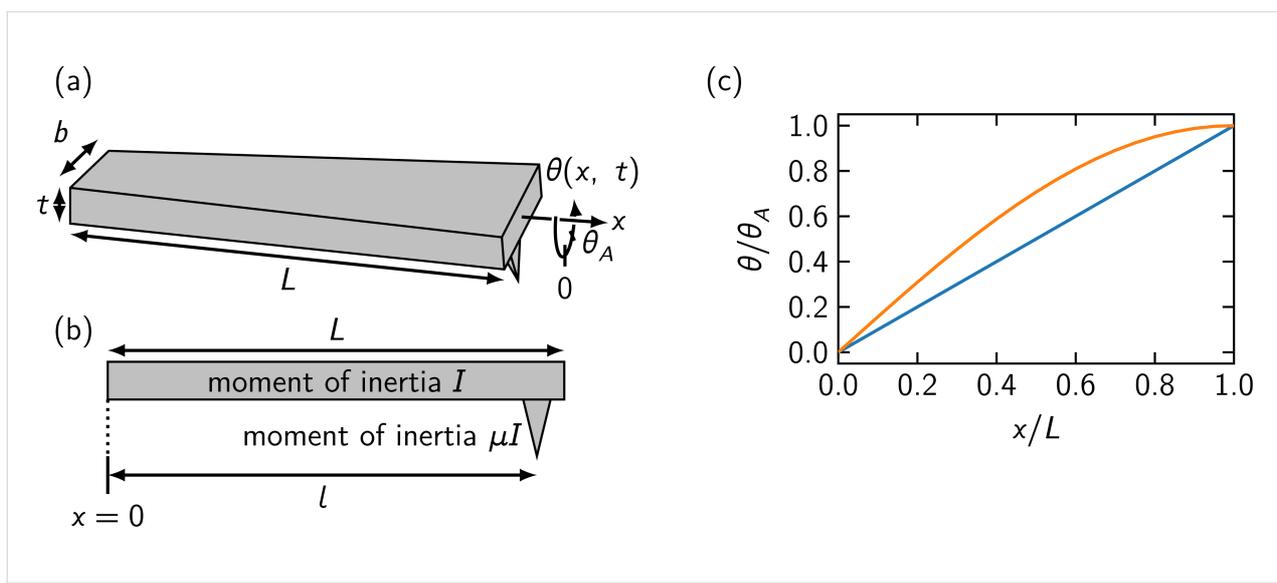
Model

We consider a cantilever with the dimensions length L, width b, and thickness t with $L, b \gg t$ as shown in Figure 1a. The corresponding moment of inertia along the x axis is $I = \rho b^3 t L / 12$, where ρ is the mass density and is uniform in the cantilever. The angle of the torsional displacement is denoted by $\theta(x, t)$ at the position x and the time t, and the angle for the oscillation amplitude is represented by θ_A. The cantilever is fixed at $x = 0$ and is free at $x = L$. A tip is attached at $x = l$, and the moment of inertia of the tip along the x axis is μI with $\mu \ll 1$, as illustrated in Figure 1b. Note that the geometric contribution of the tip is included in the deduced moment of inertia.

The oscillator is modelled as an equivalent spring-moment of inertia model [22,24], and the static stiffness and the dynamic stiffness under torsional oscillation are calculated. The equation of motion of the oscillator under the torsional oscillation is given by

$$\rho I_p \frac{\partial^2 \theta}{\partial t^2} = C_t \frac{\partial^2 \theta}{\partial x^2}, \tag{1}$$

where $I_p = b^3 t / 12$ is the polar moment of inertia, and C_t is the torsional rigidity [25,26].

Figure 1: (a) Schematic image of a model cantilever. (b) Side view of the cantilever. A tip with a moment of inertia μI is at $x = l$. (c) Displacement in the torsional direction for the static deformation (blue) and the dynamic deformation in fundamental mode (orange) for $\mu = 0$ and $l = L$.

Results

First, we consider a static torsion. The solution to Equation 1 is

$$\theta_0\left(x, t\right) = \theta_A \frac{x}{l} \tag{2}$$

under the boundary conditions of $\theta(0, t) = 0$ and $\theta(l, t) = \theta_A$.

Next, we consider dynamic oscillations with a specific tip configuration, where the tip has a negligible moment of inertia ($\mu = 0$) and is at $x = L$. The boundary conditions are $\theta(0, t) = 0$ (no torsion) and $C_t\theta'(L, t) = 0$ (no torque) [27]. With these conditions, we obtain

$$\theta_n\left(x, t\right) = \theta_A \sin\left(\frac{2n-1}{2L}\pi x\right)\cos\left(\omega_n t\right), \tag{3}$$

where $\omega_n = \sqrt{C_t / \rho I_p}(2n-1)\pi / 2L$ is the resonance angular frequency for the n-th eigenmode [28,29]. Figure 1c shows the deformation of the cantilever for the fundamental oscillation mode $\theta_1(x, 0)$ and for the static displacement $\theta_0(x, 0)$. In the dynamic case, the local torsion is concentrated to the range near the fixed end of the cantilever compared with the static case.

We then treat the torsional oscillations using the spring-moment of inertia model and derive the formula for the dynamic stiffness by assuming that the kinetic energy and the strain energy of the cantilever are equivalent to those of the model [22,30]. Specifically, for the kinetic energy $T = \rho I_p \int_0^L \dot{\theta}_n^2 dx / 2 = I_n^* \dot{\theta}_n(l, t)^2 / 2$, and for the strain energy $V = C_t \int_0^L \theta_n'^2 dx / 2 = k_n^{\text{dynamic}}\theta_n(l, t)^2 / 2$, where k_n^{dynamic} is the dynamic stiffness for the n-th oscillation mode, and I_n^* is the effective moment of inertia. The dynamic stiffness and the effective moment of inertia are then given by

$$k_n^{\text{dynamic}} = \frac{k^{\text{static}}}{2}\left(\frac{2n-1}{2}\pi\right)^2, \tag{4}$$

$$I_n^* = \frac{I}{2}, \tag{5}$$

where k^{static} is the static stiffness defined by $k^{\text{static}} = C_t/L$. The resonance angular frequencies obtained as $\omega_n = \sqrt{k_n^{\text{dynamic}} / I_n^*}$ are equal to those defined for Equation 3. Dynamic stiffness differs from static stiffness for all modes. For the fundamental mode, $k_1^{\text{dynamic}} = \pi^2 k^{\text{static}} / 8$, and thus the dynamic stiffness is approximately 23% larger than the static stiffness. The effective moment of inertia is equal to half the moment of inertia of the cantilever for any oscillation modes.

Now, more general configurations are considered, where the tip is at an arbitrary position and has a finite moment of inertia. The boundary conditions should be modified as both the position and the moment of inertia of the tip affect the conditions. The cantilever is divided into two parts; the deformation is described as $\theta_{\text{left}}(x, t)$ for $0 \leq x \leq l$ and $\theta_{\text{right}}(x, t)$ for $l < x \leq L$. The boundary conditions [25] are

$$\theta_{\text{left}}\left(l, 0\right) = \theta_A \quad \text{(amplitude at the tip)},$$
$$\theta_{\text{left}}\left(0, t\right) = 0 \quad \text{(no torsion)},$$
$$\theta_{\text{left}}\left(l, t\right) = \theta_{\text{right}}\left(l, t\right)$$
$$\text{(the same torsion)}, \tag{6}$$
$$C_t\left[\theta_{\text{right}}'\left(l, t\right) - \theta_{\text{left}}'\left(l, t\right)\right] = \mu I\ddot{\theta}\left(l, t\right)$$
$$\text{(torque equilibrium)},$$
$$\theta_{\text{right}}'\left(L, t\right) = 0 \quad \text{(no torque)}.$$

The equation of motion yields

$$\theta_n\left(x, t\right) = \theta_A \cos\left(\omega_n t\right)$$
$$\cdot \begin{cases} \dfrac{\sin\left(\alpha_n x\right)}{\sin\left(\alpha_n l\right)} & \left(0 \leq x \leq l\right) \\[3mm] \dfrac{\cos\left[\alpha_n\left(L-x\right)\right]}{\cos\left[\alpha_n\left(L-l\right)\right]} & \left(l < x \leq L\right) \end{cases}, \tag{7}$$

where the parameters $\alpha_n(l, \mu)$ are the positive solutions of

$$\mu\alpha_n L \sin\left(\alpha_n l\right)\cos\left[\alpha_n\left(L-l\right)\right] - \cos\left(\alpha_n L\right) = 0 \tag{8}$$

in ascending order, and $\omega_n\left(l, \mu\right) = \sqrt{C_t / \rho I_p}\,\alpha_n$ is the resonance angular frequency for the n-th eigenmode. The resonance angular frequency becomes lower when a tip with larger moment of inertia is attached, consistent with previous research [31].

Figure 2 illustrates the deformation of the cantilevers with tips with various moments of inertia at $l/L = 0.95$ in the fundamental oscillation mode. As the tip with larger moment of inertia lowers the resonance angular frequency, the cantilever torsion becomes similar to the situation in the static case. The gradient of the deformation for $l < x \leq L$ is smaller than that of the displacement for $0 \leq x \leq l$ due to the effect of the tip as shown in the boundary conditions in Equation 6. Figure 3 shows the displacement of the cantilever with a tip of a moment

of inertia μ = 0.05 at various positions under the fundamental mode. When the tip is attached closer to the inner part of the cantilever, the local torsion of the cantilever becomes larger for $0 \le x \le l$ to maintain the amplitude at $x = l$, and the gradients of the deformation become smaller for $l < x \le L$.
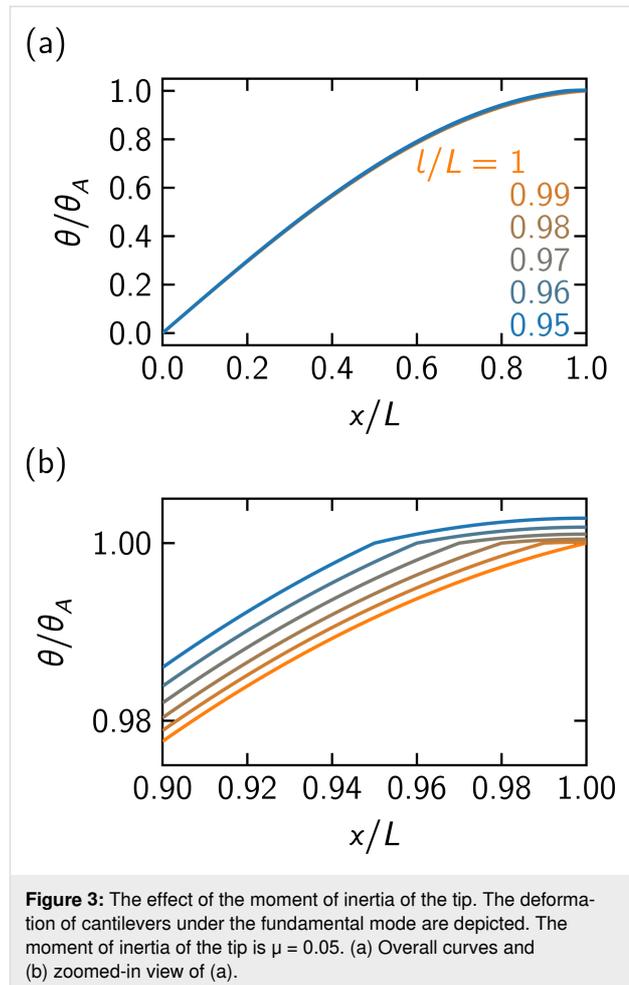

(a)

(b)
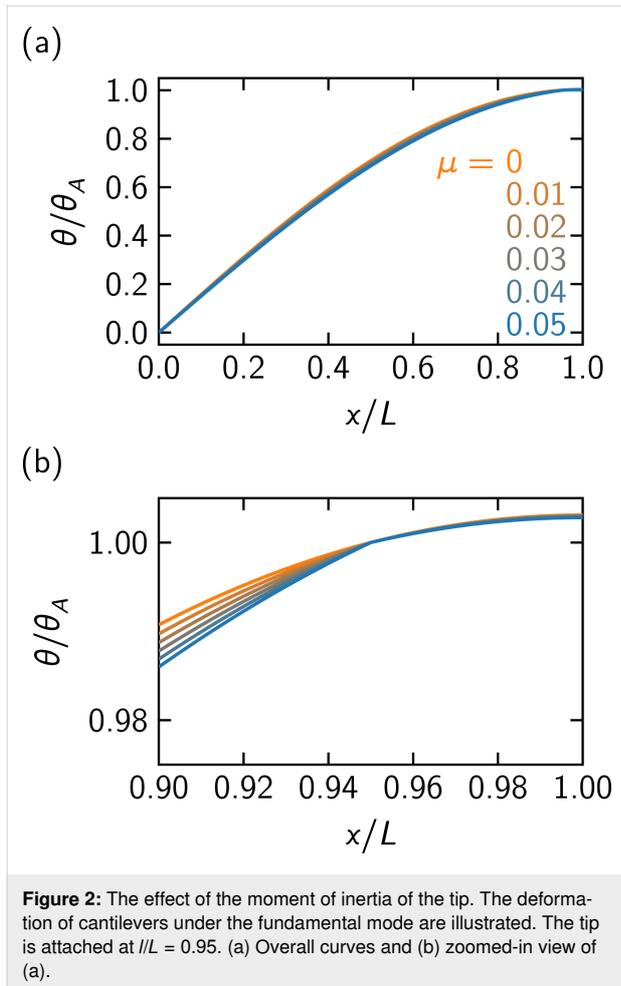
Figure 2: The effect of the moment of inertia of the tip. The deformation of cantilevers under the fundamental mode are illustrated. The tip is attached at *l/L* = 0.95. (a) Overall curves and (b) zoomed-in view of (a).

The dynamic stiffness and the effective moment of inertia with a tip are also calculated. The kinetic energy is now modified to be $T = \rho I_\mathrm{p} \int_0^L \dot{\theta}_n^2 \mathrm{d}x / 2 + \mu I \dot{\theta}_n(l, t)^2 / 2$, while the strain energy $V = C_\mathrm{t} \int_0^L \theta'^2_n \mathrm{d}x / 2$ remains the same [22,30]. The dynamic stiffness $k_n^\mathrm{dynamic}(l, \mu)$ and the effective moment of inertia $I_n^*(l, \mu)$ are derived as

$$k_n^\mathrm{dynamic}(l, \mu) = \frac{k^\mathrm{static}}{2}(\alpha_n L)^2 \frac{P(l, \mu)}{Q(l, \mu)}, \tag{9}$$

$$I_n^*(l, \mu) = \frac{I}{2}\frac{P(l, \mu)}{Q(l, \mu)}, \tag{10}$$

(a)

(b)

Figure 3: The effect of the moment of inertia of the tip. The deformation of cantilevers under the fundamental mode are depicted. The moment of inertia of the tip is μ = 0.05. (a) Overall curves and (b) zoomed-in view of (a).

where $P(l, \mu)$ and $Q(l, \mu)$ are

$$\begin{aligned}P(l, \mu) =\ & \alpha_n L \sin^2(\alpha_n l) \\ & + \alpha_n l \cos(\alpha_n L)\cos\left[\alpha_n(L - 2l)\right] \\ & + \cos(\alpha_n L)\sin(\alpha_n l)\cos\left[\alpha_n(L - l)\right],\end{aligned} \tag{11}$$

$$Q(l, \mu) = \alpha_n L \sin^2(\alpha_n l)\cos^2\left[\alpha_n(L - l)\right]. \tag{12}$$

The dynamic stiffness, the effective moment of inertia, and the resonance angular frequency in the fundamental oscillation mode are plotted in Figure 4. As μ increases, the dynamic stiffness decreases. In contrast, the dynamic stiffness increases as the tip is positioned away from the cantilever end since this configuration leads to larger local torsion of the cantilever. The effective moment of inertia is influenced by the oscillation mode when the tip is attached. It increases as the tip with larger moment of inertia is positioned closer to the inner part of the cantilever. The resonance angular frequencies calculated with

$\omega_n = \sqrt{k_n^{\text{dynamic}} / I_n^*}$ are consistent with the values defined for Equation 7. For the fundamental mode, the resonance frequency is only minimally affected by attaching the tip with small moment of inertia near the free end of the cantilever. It becomes lower with the tip with larger moment of inertia, while it grows higher when the tip is positioned away from the free end of the cantilever.
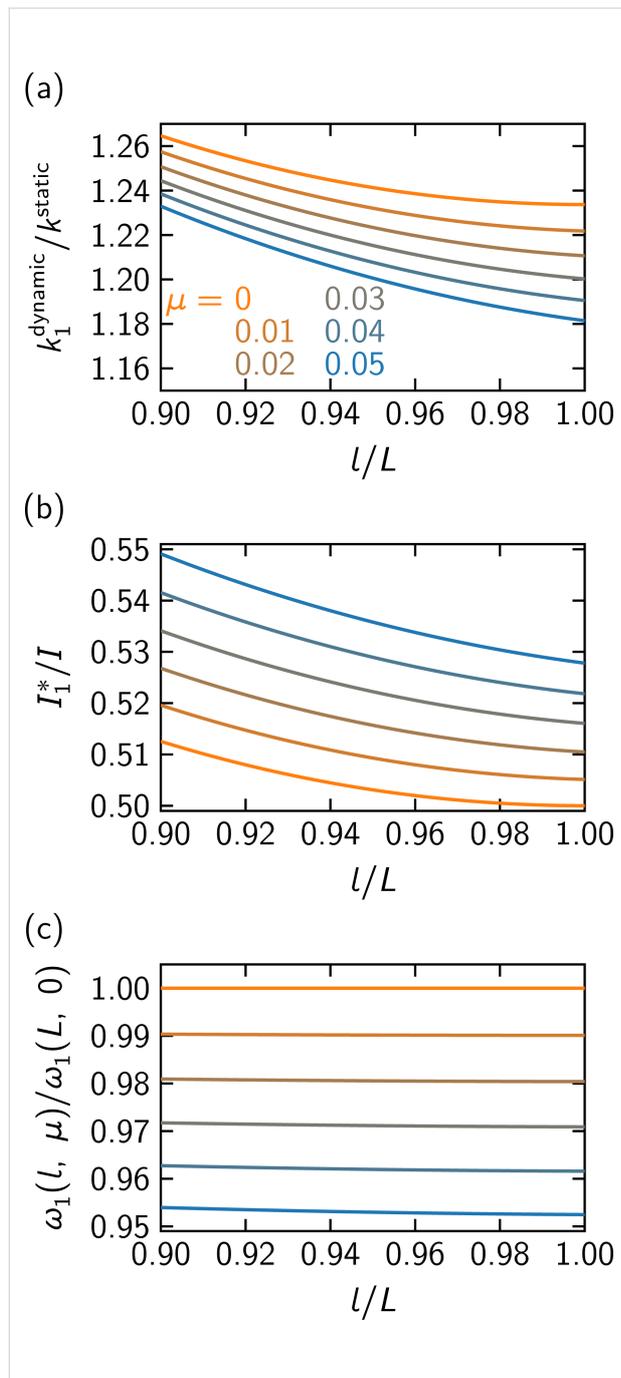
Figure 4: (a) The dynamic stiffness, (b) the effective moment of inertia, and (c) the fundamental resonance angular frequency when a tip of a moment of inertia μl is attached to the cantilever at $x = l$.

Discussion

To know the practical effect of the tip to the oscillating cantilever, we consider two specific cantilever configurations, namely, a long cantilever and a short cantilever. The cantilever geometries are shown in Table 1. The tips in the configurations are assumed to have the same cone shape with the height $h = 17$ μm and the base radius $r = 8$ μm and to be positioned at $l/L = 0.97$ and $l/L = 0.94$ for the long cantilever and the short cantilever, respectively. The ratio of the dynamic stiffness to the static stiffness for the fundamental mode is also shown in Table 1. The dynamic stiffness is larger by 23% for the long cantilever and by 21% for the short cantilever. This implies that the non-contact friction is underestimated by around 20% if the present correction is not adopted.

Table 1: Dynamic stiffness for two cantilever configurations.

	long cantilever	short cantilever
L [μm]	225	125
b [μm]	38	30
t [μm]	7	4
l/L	0.97	0.94
μ	0.008	0.043
$\dfrac{k_1^{\text{dynamic}}}{k^{\text{static}}}$	1.23	1.21

In conclusion, we derived formulae for the dynamic stiffness of the cantilever in torsional oscillation through a comparison of the oscillating cantilever and the equivalent spring-moment of inertia model. The dynamic stiffness is 21% and 23% larger than the static stiffness for specific configurations of cantilevers and tips, implying the importance of the present corrections for accurate measurements of non-contact friction. The present modification can be experimentally evaluated by comparing the lateral force measured with the torsional oscillation mode and that from three-dimensional force maps obtained using vertical oscillation.

ORCID® iDs

Keita Nishida - https://orcid.org/0009-0002-9224-3490
Yuuki Yasui - https://orcid.org/0000-0001-5774-0147
Yoshiaki Sugimoto - https://orcid.org/0000-0003-3346-1586

Data Availability Statement

Data generated and analyzed during this study is available from the corresponding author upon reasonable request.

References

1. Persson, B. N. J. *Sliding Friction: Physical Principles and Applications,* 2nd ed.; NanoScience and Technology; Springer-Verlag: Berlin, Germany, 1998. doi:10.1007/978-3-662-04283-0

2. Meyer, E.; Bennewitz, R.; Hug, H. J. *Scanning Probe Microscopy;* Graduate Texts in Physics; Springer Nature: Cham, Switzerland, 2021. doi:10.1007/978-3-030-37089-3

3. Pawlak, R.; Kawai, S.; Meier, T.; Glatzel, T.; Baratoff, A.; Meyer, E. *J. Phys. D: Appl. Phys.* **2017,** *50,* 113003. doi:10.1088/1361-6463/aa599d

4. Vanossi, A.; Manini, N.; Urbakh, M.; Zapperi, S.; Tosatti, E. *Rev. Mod. Phys.* **2013,** *85,* 529–552. doi:10.1103/revmodphys.85.529

5. Volokitin, A. I.; Persson, B. N. J. *Phys. Rev. Lett.* **2005,** *94,* 086104. doi:10.1103/physrevlett.94.086104

6. Stipe, B. C.; Mamin, H. J.; Stowe, T. D.; Kenny, T. W.; Rugar, D. *Phys. Rev. Lett.* **2001,** *87,* 096801. doi:10.1103/physrevlett.87.096801

7. Kunstmann, T.; Schlarb, A.; Fendrich, M.; Paulkowski, D.; Wagner, T.; Möller, R. *Appl. Phys. Lett.* **2006,** *88,* 153112. doi:10.1063/1.2194367

8. Giessibl, F. J.; Herz, M.; Mannhart, J. *Proc. Natl. Acad. Sci. U. S. A.* **2002,** *99,* 12006–12010. doi:10.1073/pnas.182160599

9. Yildiz, D.; Kisiel, M.; Gysin, U.; Gürlü, O.; Meyer, E. *Nat. Mater.* **2019,** *18,* 1201–1206. doi:10.1038/s41563-019-0492-3

10. Kisiel, M.; Gnecco, E.; Gysin, U.; Marot, L.; Rast, S.; Meyer, E. *Nat. Mater.* **2011,** *10,* 119–122. doi:10.1038/nmat2936

11. Gysin, U.; Rast, S.; Kisiel, M.; Werle, C.; Meyer, E. *Rev. Sci. Instrum.* **2011,** *82,* 023705. doi:10.1063/1.3551603

12. Kawai, S.; Glatzel, T.; Koch, S.; Such, B.; Baratoff, A.; Meyer, E. *Phys. Rev. B* **2010,** *81,* 085420. doi:10.1103/physrevb.81.085420

13. Federici Canova, F.; Kawai, S.; de Capitani, C.; Kan'no, K.-i.; Glatzel, T.; Such, B.; Foster, A. S.; Meyer, E. *Phys. Rev. Lett.* **2013,** *110,* 203203. doi:10.1103/physrevlett.110.203203

14. Arilla, R.; Barrena, E.; Ocal, C.; Martin-Jimenez, D. *Nano Lett.* **2025,** *25,* 3597–3604. doi:10.1021/acs.nanolett.4c06499

15. Yurtsever, A.; Gigler, A. M.; Macias, E.; Stark, R. W. *Appl. Phys. Lett.* **2007,** *91,* 253120. doi:10.1063/1.2826285

16. Pfeiffer, O.; Bennewitz, R.; Baratoff, A.; Meyer, E.; Grütter, P. *Phys. Rev. B* **2002,** *65,* 161403. doi:10.1103/physrevb.65.161403

17. Kawai, S.; Kitamura, S.-i.; Kobayashi, D.; Kawakatsu, H. *Appl. Phys. Lett.* **2005,** *87,* 173105. doi:10.1063/1.2112203

18. Weymouth, A. J.; Riegel, E.; Gretz, O.; Giessibl, F. J. *Phys. Rev. Lett.* **2020,** *124,* 196101. doi:10.1103/physrevlett.124.196101

19. Sader, J. E.; Jarvis, S. P. *Appl. Phys. Lett.* **2004,** *84,* 1801–1803. doi:10.1063/1.1667267

20. Seeholzer, T.; Gretz, O.; Giessibl, F. J.; Weymouth, A. J. *New J. Phys.* **2019,** *21,* 083007. doi:10.1088/1367-2630/ab3353

21. Cleveland, J. P.; Anczykowski, B.; Schmid, A. E.; Elings, V. B. *Appl. Phys. Lett.* **1998,** *72,* 2613–2615. doi:10.1063/1.121434

22. Melcher, J.; Hu, S.; Raman, A. *Appl. Phys. Lett.* **2007,** *91,* 053101. doi:10.1063/1.2767173

23. Labuda, A.; Cao, C.; Walsh, T.; Meinhold, J.; Proksch, R.; Sun, Y.; Filleter, T. *Rev. Sci. Instrum.* **2018,** *89,* 093701. doi:10.1063/1.5045679

24. Sugimoto, Y.; Onoda, J. *Appl. Phys. Lett.* **2019,** *115,* 173104. doi:10.1063/1.5112062

25. Yamanaka, K.; Nakano, S. *Appl. Phys. A: Mater. Sci. Process.* **1998,** *66,* S313–S317. doi:10.1007/s003390051153

26. Timoshenko, S. P.; Goodier, J. N. *Theory of elasticity;* McGraw-Hill: New York, 1970.

27. Reinstaedtler, M.; Rabe, U.; Scherer, V.; Turner, J. A.; Arnold, W. *Surf. Sci.* **2003,** *532-535,* 1152–1158. doi:10.1016/s0039-6028(03)00183-3

28. Rabe, U.; Janser, K.; Arnold, W. *Rev. Sci. Instrum.* **1996,** *67,* 3281–3293. doi:10.1063/1.1147409

29. Song, Y.; Bhushan, B. *Microsyst. Technol.* **2006,** *12,* 219–230. doi:10.1007/s00542-005-0070-2

30. Timoshenko, S. P.; Gere, J. G. *Theory of elastic stability;* Dover Publications: Mineola, 2009.

31. Mokhtari-Nezhad, F.; Saidi, A. R.; Ziaei-Rad, S. *Ultramicroscopy* **2009,** *109,* 1193–1202. doi:10.1016/j.ultramic.2009.05.016

afspm: A framework for manufacturer-agnostic automation in scanning probe microscopy

Nicholas J. Sullivan[*1,2], Julio J. Valdés[3], Kirk H. Bevan[1,2] and Peter Grutter[*2]

Full Research Paper

Address:
[1]Division of Materials Engineering, Faculty of Engineering, McGill University, Montreal H3A 2T8, Canada, [2]Department of Physics, McGill University, Montreal H3A 2T8, Canada and [3]National Research Council Canada, Digital Technologies Research Centre, Ottawa ON K4A 0S2, Canada

Email:
Nicholas J. Sullivan[*] - nicholas.sullivan@mail.mcgill.ca;
Peter Grutter[*] - peter.grutter@mcgill.ca

* Corresponding author

Abstract

Scanning probe microscopy (SPM) is a valuable technique by which one can investigate the physical characteristics of the surfaces of materials. However, its throughput is hampered by the time-consuming nature of running an experiment and the significant domain knowledge required. Recent studies have shown the value of multiple forms of automation in improving this, but their use is limited due to the difficulty of integrating them with SPMs other than the one it was developed for. We have built a framework that allows for tasks written with it to be run on multiple SPM systems. Our framework defines generic commands and data structures that are passed among separate software processes, with the final SPM commands sent to the microscope after passing through an SPM-specific translator. The use of configuration files allows automation logic to be further decoupled from experiment specifics. A mediation layer permits background tasks to intermittently control the microscope, fixing detected experiment problems. Our framework has been tested on various SPM controllers, validating that it can integrate with all existing scripting interfaces types. An automated experiment was run to ensure overall running beyond integration testing.

Introduction

In scanning probe microscopy (SPM), an atomically sharp tip is scanned above a surface of interest while measuring one or more properties. This process allows for atomic-level imaging of properties, spectroscopic analysis, and even manipulation of a sample toward atomic-scale manufacturing [1]. However, a number of factors limit higher throughput of these techniques. First, running an experiment traditionally involves constant user attention, requiring frequent monitoring and manipulation of

SPM parameters. Second, limiting the decision-making of an experiment to the choices of a single researcher constrains the statistical understanding of what is being analyzed. Last, preparing, running, and analyzing such experiments requires significant domain knowledge and expertise.

Dozens of works over the past decade have investigated SPM automation. Some have shown probe tip conditioning to ensure proper surface characterization and/or manipulation [2-4]. Others have classified surface structure, detecting atoms [5], molecules [6], or defects of interest [7,8]. Even the design of experiments has been researched, using statistics to drive decisions during the experiment [9-12]. Active learning, where a machine learning algorithm's internal model is updated during the experiment, has been used in SPM for 2D scan efficiency [10] as well as in SPM spectroscopy [11]. Furthermore, investigators have used hypothesis learning, where a model chooses between a number of hypotheses by testing them during the experiment [12]. As an example of a complete autonomous system, we highlight [13], where atomic-level characterization is achieved via, among other processes, a thermal drift correction approach first described in [14].

Despite promising results, a lingering issue common to all these techniques is reusability. In most cases, the source code is written for a specific SPM controller's commands and data structures; adapting the code to a different controller is a time-consuming and non-trivial task. Some work has been done in this regard: In [15], a software ecosystem was developed to simplify reading and analyzing data from various scientific instruments. While a generalized approach to data handling solves part of the problem, it does nothing to address the control needs posed across the various SPM controllers. Another contribution was made in [16], where a hardware–software framework enables automated experimentation. This framework focuses on the design of low-level particulars, to give researchers finer control on aspects of an experiment (e.g., scanning trajectories and excitation waveforms); while useful, it requires a separate hardware component. These developments complement ours.

Outside of nanoscience, the particle accelerator community have developed Bluesky [17], a suite of Python packages centered around defining and running multiple instrument experiments in a hardware-abstracted manner, while maintaining format-independent data and metadata storage. Outside of many-instrument orchestration, this suite provides various abstractions that may be suitable to other scientific fields. Bluesky does not solve the reusability issues described above, but may prove suitable as an interface to coordinate an SPM among other instruments.

We have developed a software framework for SPM to write reusable and shareable automation scripts, named afspm (after Automation Framework for SPM). This framework serves as a manufacturer-agnostic foundation with which automation processes can be developed; for example, the system developed in [13], a specific application demonstrated on a single SPM, can – once implemented in this framework – be more easily utilized on other SPMs. In what follows, we present an overview of the framework, showing how reusability is achieved by decoupling the various script specificities from the overarching algorithm. Afterward, we validate that our approach should support any microscope controller by integrating and testing translators for each possible scripting interface type. We show the framework functioning beyond integration testing by running an automated experiment; specifically, we implement a drift estimation approach similar to that in [14]. In doing so, we enable easier reuse of this specific application (drift correction) on other SPMs. We conclude by highlighting the value of some of our design decisions for other experimental fields.

Framework Design Overview

Scripting aims to automate some of the user's decisions during an experiment. As illustrated in Figure 1, this level of automation tries to replace a user's manual interaction (Figure 1a) with
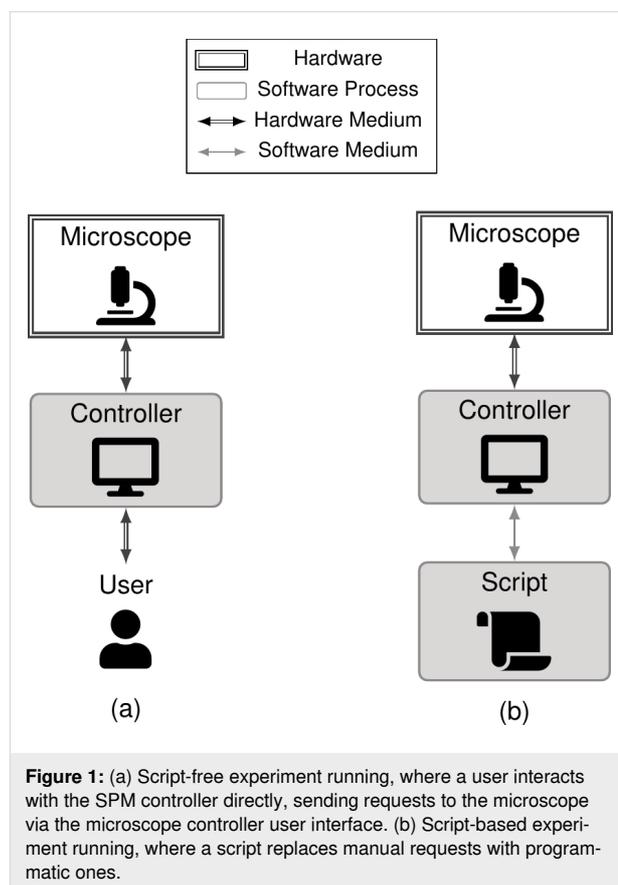
Figure 1: (a) Script-free experiment running, where a user interacts with the SPM controller directly, sending requests to the microscope via the microscope controller user interface. (b) Script-based experiment running, where a script replaces manual requests with programmatic ones.

equivalent programmatic commands sent to a microscope controller (Figure 1b). Note that here we refer to the software controller when we discuss the microscope controller; this software application is responsible for managing the programmatic instructions (e.g., start a scan) that are sent to the hardware controller, which handles real-time control of the microscope (e.g., sending the raster-scanning and *z*-height signals).

A script is an algorithm, or set of specific instructions, for performing some task (our definition here is broad, disregarding the usage of a typeless, interpreted language [18]). We delineate the various aspects of a script with an exemplary one (Figure 2), where we regularly scan a fixed region of a sample and then run spectroscopies on a set of positions we have deemed interesting from analyzing said scan. A subset of a script's instructions are direct instructions to be sent to the microscope (delineated "Microscope Instruction" in Figure 2); these are manufacturer-specific. Another subset of the instructions have predefined parameters associated to them (in this example, "time_has_passed" and "set_scan_params") that are experiment-specific as they are sample- or system-dependent. Last, a single script is often written for performing a composite task, that is, one comprising multiple interdependent subtasks. In this example, we have two tasks, namely, one performing the experimental loop (Task A) and one determining where to run spectroscopies based on the latest scan (Task B). Unless tasks are well decoupled, bundling them makes running them independently difficult. In all three cases, reuse becomes more difficult due their intermixing; any approach toward higher reusability would minimize this. Our approach was to develop a software framework, that is, a reusable architecture providing prebuilt functionality for writing scripts [19]. Figure 3 visualizes some of its features.

As seen in Figure 3a, scripts using manufacturer-specific instructions restrict themselves to said manufacturer; reuse

requires a rewrite. Our framework decouples the manufacturer-specific instructions sent in a traditional script by defining a subset of generic commands and data structures, which are translated to those of a given microscope controller via a translator (Figure 3b). Experiment-specific parameters are decoupled from algorithmic logic via the usage of configuration files: the algorithmic logic resides in scripts, while the predefined parameters reside in a configuration file. The configuration file also defines the various scripts to be instantiated for a given experiment and the mechanism by which they communicate with each other. For experiments where multiple scripts may need to communicate with the microscope, a mediation layer has been developed (Figure 3c), which provides a mechanism (declaring experiment problems) by which a secondary script can temporarily take control of the microscope. This permits background tasks to monitor the experiment and intermittently take over to fix detected problems, decoupling the main experiment from various background tasks.

Our software framework has been developed in Python [20], giving users access to the existing Python ecosystem for scientific computing. While we have defined a subset of microscope commands and data structures, the framework can be adapted as needed. Furthermore, the mechanism by which scripts communicate allows individual scripts to be written in other languages. More information can be found in sections "Communication Protocol" and "Implementing Components in Other Languages" of Supporting Information File 1.

Decoupling manufacturer specifics

In practice, controller interfaces differ not just in the commands and data structures used, but also in the programming language supported and the interfacing mechanism itself. In this section, we classify the various interfacing mechanisms and show how one may implement translators for each. As we will see, the proposed solutions allow instruction set and programming lan-

```
duration =  # [...]          } Experiment-Specific Parameters
scan_params =  # [...]        }

                                    --> Microscope Instruction
while not time_has_passed(duration):
    set_scan_params(scan_params)
    scan = run_scan()
    positions = where_to_run_spect(scan) > Task B   } Task A
    for pos in positions:
        set_probe_pos(pos)
        spect = run_spect()
```

Figure 2: Sample script delineating various aspects of a script. Here, we see that for the set of instructions we have experiment-specific parameters, which are likely to vary from one experiment to another, and instructions that are aimed at the microscope. Additionally, a script may comprise multiple tasks.

Figure 3: (a) Today, SPM scripts are usually written using manufacturer-specific software interfaces, requiring a complete rewrite to port to another system. (b) Usage of a similar script in afspm involves sending generic commands to a microscope translator, which translates these to manufacturer-specific commands. (c) For more involved experiments, a microscope mediator manages control to the microscope, allowing monitoring processes to intermittently take control and correct detected experiment problems. The main experiment script can then be written focused solely on the main experimental loop.
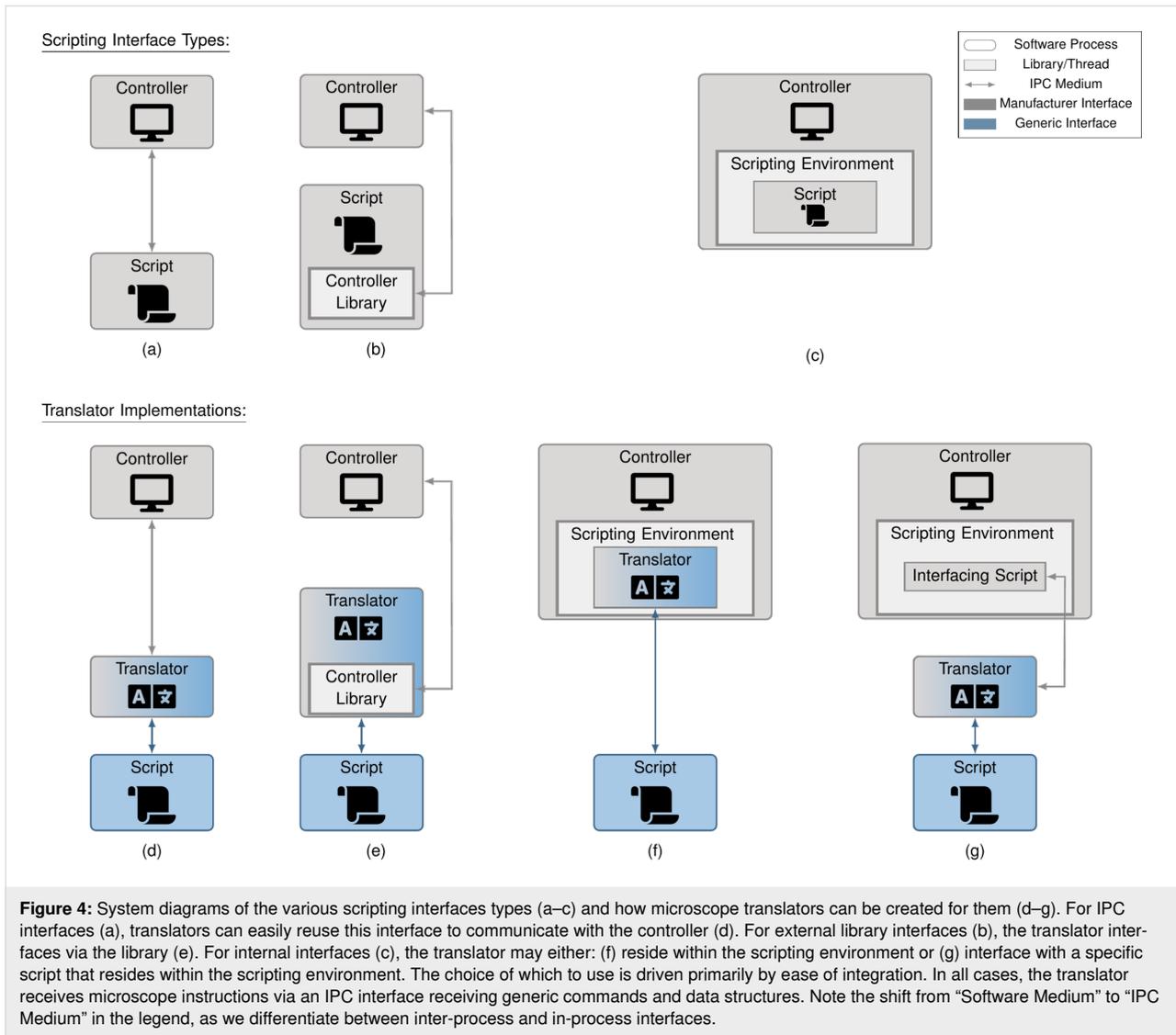
guage differences to be circumvented. The various scripting mechanisms are visualized in Figure 4a–c along with translator implementations in Figure 4d–g. In Table 1, we list a sampling of controllers from various manufacturers and the scripting interfaces they expose.

With inter-process communication (IPC) interfaces (Figure 4a), scripts are run as separate processes from the microscope controller. An IPC interface allows different processes on the computer to communicate with each other; they differ from in-process communication in their generality (being language-agnostic) and their added timing delays (which could be limiting in high-frequency applications). Because this complicates scripts, some manufacturers expose a language-restricted controller library, that is, an external library interface (Figure 4b), which makes communication with the microscope easier, but restricts the script to a single, or subset of, programming languages. Other manufacturers expose an internal interface (Figure 4c), where a provided script is run within the controller process; here, a single programming language is supported and timing delays are minimized due to in-process communication.

Both the internal and external library interfaces impose programming language constraints. From Table 1, there is no

common programming language among our sample of manufacturers; a change in programming language is thus required for at least some systems. This cross-language communication can be achieved via an IPC interface with each language in its own process.

Our implementation treats the script and the translator as independent processes communicating over an IPC interface via generic commands and data structures. This is most easily implemented for the IPC interface type (Figure 4d), where the script sends generic instructions over IPC to the translator, which in turn sends the translated manufacturer-specific instructions over IPC to the controller. In the case of external library interfaces, the controller library resides in the translator process (Figure 4e), with the script-translator communication involving generic instructions over IPC and the translator-controller communication occurring via the library. Last, internal library interfaces can be implemented in one of two ways: the translator logic may reside directly in the scripting environment (Figure 4f), or it may reside in a separate process (Figure 4g). In the former case, the translator-controller communication is embedded in the scripting environment. In the latter case, the translator-controller communication involves manufacturer-specific instructions over IPC, where an interfacing script is run in the scripting environment. By following the translator implementa-

Figure 4: System diagrams of the various scripting interfaces types (a–c) and how microscope translators can be created for them (d–g). For IPC interfaces (a), translators can easily reuse this interface to communicate with the controller (d). For external library interfaces (b), the translator interfaces via the library (e). For internal interfaces (c), the translator may either: (f) reside within the scripting environment or (g) interface with a specific script that resides within the scripting environment. The choice of which to use is driven primarily by ease of integration. In all cases, the translator receives microscope instructions via an IPC interface receiving generic commands and data structures. Note the shift from "Software Medium" to "IPC Medium" in the legend, as we differentiate between inter-process and in-process interfaces.

Table 1: Listing of the programming interfaces of a selection of SPM controllers from various manufacturers. If "all" is indicated, all hardware controllers by this manufacturer should support this interface. All information was obtained via manufacturer datasheets or marketing documents and is therefore not guaranteed to be accurate.

Manufacturer	Supported Controller	Interface type	Language(s)
Asylum Research[a]	all	internal	IGOR
Bruker Nano	Nanoscope	internal	"Recipes"[b]
		external library	C
		external IPC	N/A
Createc	SC6711	external IPC	N/A
EPFL LBNI AFM	N/A	internal	LabVIEW[c]
GXSM	all	internal	Python
SPECS Nanonis[d]	Mimea BP5e/Tramea Base	internal	LabVIEW
		external IPC	N/A
Nanosurf	all	internal	VBScript
	all	external IPC	N/A
	all	external library	Python

Table 1: Listing of the programming interfaces of a selection of SPM controllers from various manufacturers. If "all" is indicated, all hardware controllers by this manufacturer should support this interface. All information was obtained via manufacturer datasheets or marketing documents and is therefore not guaranteed to be accurate. (continued)

Park Systems	SmartScan	internal	Javascript
RHK Tech	R9+	External IPC	N/A
Scienta Omicron	SXM	internal	PASCAL-like
		external library	Python
		external IPC	N/A
	MATRIX	internal	MATE
Unisoku	SPC-STG	internal	LabVIEW

[a]Oxford Instruments Asylum Research Inc., referred to as Asylum Research for convenience. [b]A custom visual programming language for defining internal scripts. [c]All LabVIEW Virtual Instruments (VIs) expose front panel attributes via an External IPC interface. We do not explicit this for these instruments as it is not guaranteed that all desired settings are part of the front panel. [d]SPECS Surface Nano Analysis GmbH Nanonis, referred to as SPECS Nanonis for convenience.

tions of Figure 4d–g and utilizing generic commands and data structures, we can decouple manufacturer specifics from our scripts for any scripting interface type.

Experiment configuration

By using configuration files, afspm allows algorithmic logic to be separated from experiment-specific parameters and split up into subtasks as needed. The potential benefits are best demonstrated via variations of our earlier sample script. In Figure 5, we see pseudocode (Figure 5a) and a system diagram (Figure 5b) for a script including experiment-specific parame-

ters within it. In coupling the algorithmic logic and experiment-specific parameters, we force a new copy of the base script for each new experiment. Imagine running the experiment with the same system and sample twice: The only likely change is the region of the sample we wish to scan ("scan_params" here), due to particulars of sample placement during setup. Even in this case, we would need to duplicate (or modify) our script, indicating the parameter change. Any bug fixes or improvements to our base script would need to be tracked among the various copies we maintained – a time-consuming and error-prone process.

```
duration = # [...]
scan_params = # [...]
ipc_params = # [...]

def run_experiment(scan_params: ScanParameters2d,
                   duration: datetime.timedelta,
                   ipc_params: dict[Any, Any]):
    start_timer()
    while not time_has_passed(duration):
        set_scan_params(ipc_params, scan_params)
        scan = run_scan(ipc_params)
        positions = where_to_run_spect(scan)
        for pos in positions:
            set_probe_pos(ipc_params, pos)
            spect = run_spect(ipc_params)

def main():
    run_experiment(duration, scan_params,
                   ipc_params)
```
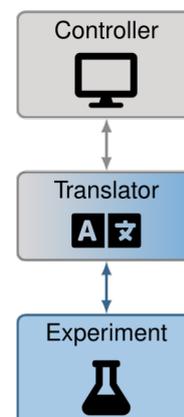
(a)   (b)

Figure 5: Pseudocode (a) and system diagram (b) for an experiment script talking to a translator without a configuration file. Here, experiment-specific parameters (e.g., the scan parameters), as well as communication parameters (e.g., how we talk to the translator) are included in the single script file. To run the same experiment with different experimental setup, one would modify the source file itself.
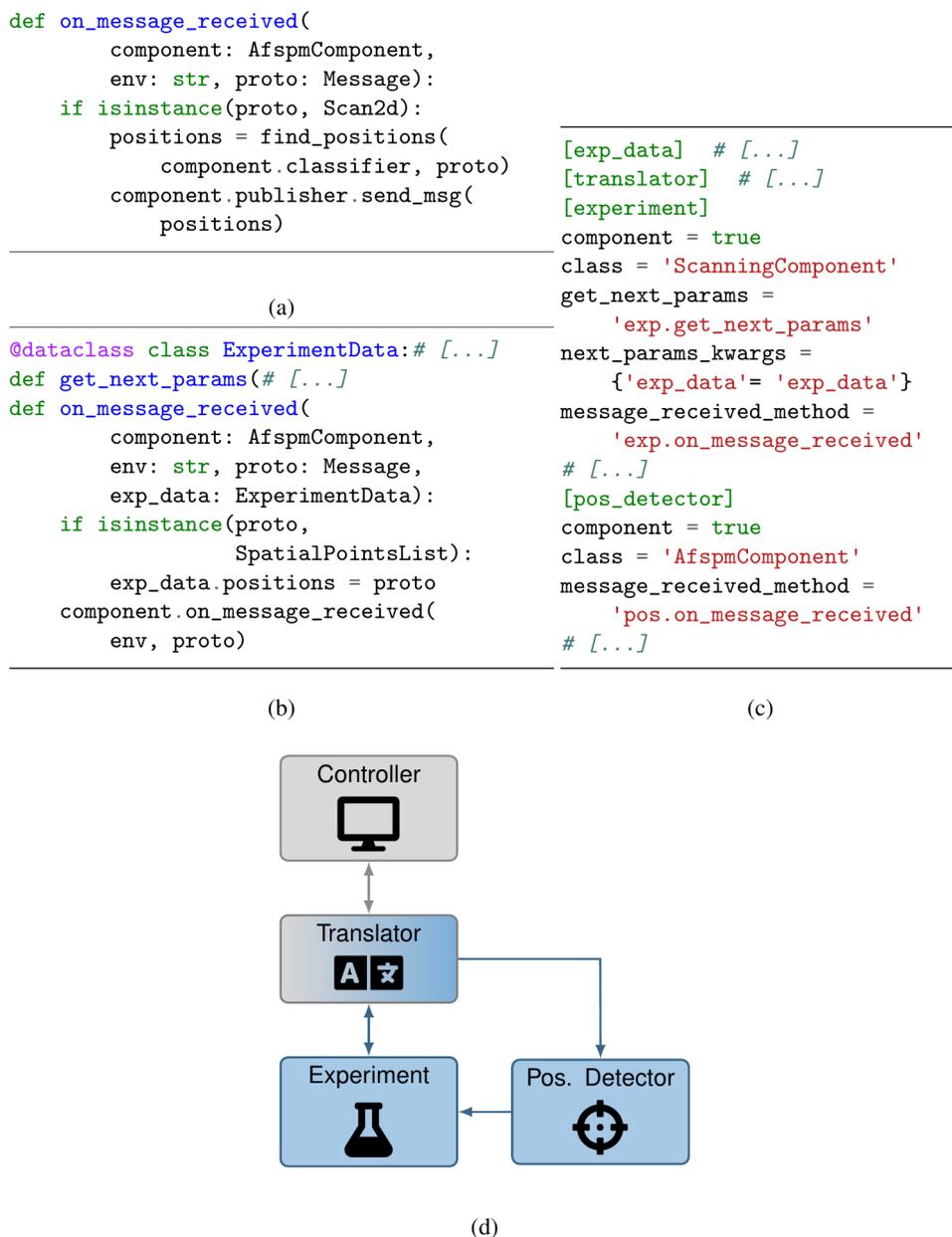
We can avoid this by defining the type of parameters our script expects in the script itself, and declaring them per-experiment in a separate configuration file; the script loads the parameters on startup by parsing the configuration file. This is the approach taken in afspm, as exemplified in Figure 6. In the pseudocode (Figure 6a), we see that the expected parameter types are defined in a data structure (here, "ExperimentData"), which is used by the "get_next_params" method to determine the next action to perform (scanning or running spectroscopies). The method "on_message_received" is run whenever a message is received by the script; in this case, it is used to determine where to run spectroscopies by analyzing each received scan ("Scan2d"). Both of these methods are method callbacks defined within the software framework and are called when certain events occur (i.e., event-driven logic). From the configuration file (Figure 6b), we see that in addition to defining experiment-specific parameters ("[exp_data]"), the various scripts to run are also explicited ("[translator]" and "[experiment]").

When a configuration file is loaded on startup, afspm will instantiate a new process for each indicated script and set up their communication mechanisms as defined by the configuration. Note that the communication mechanisms are hidden in this example; see section "Communication Protocol" of Supporting Information File 1 for more information.

The use of a configuration file also simplifies separating a composite task into subtasks, as seen in Figure 7. This example performs the same logic as that shown in Figure 6, but with the logic split in two tasks, that is, determination of where to run spectroscopies (Figure 7a) and general experimental logic (Figure 7b). The position detector script ("[pos_detector]" in Figure 7c) concerns itself only with analyzing received 2D scans to decide where spectroscopies should be run. One could imagine the method "find_positions" invoking a pre-trained machine learning classifier, or predefined image processing logic. The determined positions are sent over IPC to the experi-

```python
@dataclass
class ExperimentData:
    scan_params = # [...]
    positions = # [...]
    duration = # [...]
    start_ts = time.now()
    scan_idx = len(positions)

def get_next_params(component: AfspmComponent,
                    exp_data: ExperimentData
                    ) -> (ScanParameters2d |
                          ProbePosition | None):
    if time_has_passed(exp_data)
        component.control_client.end_experiment()
    if time_for_scan(exp_data)
        params = exp_data.scan_params
    else:
        params = pop_position(exp_data)
    return params

def on_message_received(component: AfspmComponent,
                        env: str, proto: Message,
                        exp_data: ExperimentData):
    if isinstance(proto, Scan2d):
        exp_data.positions = where_to_run_spect(
            component.classifier, proto)
```

```ini
[exp_data]
class = 'exp.ExperimentData'
# [...]

[translator]
component = true
class = 'trans.MyTranslator'
# [...]

[experiment]
component = true
class = 'ScannningComponent'
get_next_params =
    'exp.get_next_params'
next_params_kwargs =
    {'exp_data'= 'exp_data'}
message_received_method =
    'exp.on_message_received'
# [...]
```

(a)   (b)

Figure 6: Pseudocode (a) and configuration file (b) for an experiment with system diagram matching Figure 5 using a configuration file. In the source file (a), a data structure holding experiment-specific parameters is defined ("ExperimentData"), and the logic of what action to take once a prior action has finished is described ("get_next_params"). The logic for determining where to run spectroscopies is run whenever a new scan is received ("on_message_received"). In the configuration file (b), the experimental parameters for a specific experiment and the two software processes to be instantiated are defined ("[translator]" and "[experiment]"). Note the usage of a variable "component" to indicate to the parser that this is a script to be instantiated. Additionally, how the two scripts communicate is defined (not shown here).

```
def on_message_received(
        component: AfspmComponent,
        env: str, proto: Message):
    if isinstance(proto, Scan2d):
        positions = find_positions(
            component.classifier, proto)
        component.publisher.send_msg(
            positions)
```

(a)

```
@dataclass class ExperimentData:# [...]
def get_next_params(# [...]
def on_message_received(
        component: AfspmComponent,
        env: str, proto: Message,
        exp_data: ExperimentData):
    if isinstance(proto,
                SpatialPointsList):
        exp_data.positions = proto
component.on_message_received(
    env, proto)
```

(b)

```
[exp_data]  # [...]
[translator]  # [...]
[experiment]
component = true
class = 'ScanningComponent'
get_next_params =
    'exp.get_next_params'
next_params_kwargs =
    {'exp_data'= 'exp_data'}
message_received_method =
    'exp.on_message_received'
# [...]
[pos_detector]
component = true
class = 'AfspmComponent'
message_received_method =
    'pos.on_message_received'
# [...]
```

(c)

(d)

Figure 7: Pseudocode (a, b), configuration file (c), and system diagram (d) for an experiment involving two dependent scripts. A classifier-based position detector (a) receives scans and detects positions to perform spectroscopies. These are sent to the experiment script (b), which sends scan and spectroscopy requests to the microscope. Note that this script contains equivalent logic to that of Figure 6a, with changed logic to handle the received spectroscopy positions. The configuration file (c) differs from Figure 6c in the definition of the position detector and its input parameters.

ment script ("[experiment]" in Figure 7c), which, upon receipt, stores them in an internal data structure for later use. This script runs the overarching experimental logic, namely, alternating between 2D scans and spectroscopies for a predetermined duration.

Mediation logic
Thus far, we have considered experiments where only one script communicates with the microscope. However, one can envision experiments where multiple separate tasks may require microscope control. This is notably the case for tasks that involve monitoring and fixing issues detected during an experiment: Correcting for thermal drift, characterizing the tip, and optimization feedback parameters all fit within this category. To simplify automation of this kind, we have added mediation logic determining control of the microscope, managed by a microscope mediator that sits between the translator and all other running scripts (see Figure 3c). This mediation assumes a

"primary" script that is principally communicating with the microscope and various "background" scripts that monitor and fix issues in an intermittent fashion.

Tied to mediation is the concept of experiment problems, predefined issues that may be flagged or removed throughout an experiment. The mediator maintains a list of currently logged experiment problems and a record of the current script in control along with the enumerated problem it resolves (an enumeration exists for "standard" scripts that do not resolve a problem). Control can only be given when it has not been granted and is determined in a greedy fashion, that is, to the first "suitable" script requesting control, either one that resolves a flagged problem if problems have been flagged or a standard script otherwise.

The mediation logic is best demonstrated via the mediator's state machine (Figure 8), starting from top and following clockwise. We begin with no problems flagged and no script in control ("No Problem, No Control"). At this point, a standard script can request and gain control of the microscope ("No Problem, In Control"). If there are no other scripts monitoring for experiment problems, the whole experiment may reside in this state. If a monitoring script exists and a problem is detected, it may flag it to the mediator, causing the in-control script to lose control ("Problem, No Control"). Any number of further problems may be flagged or removed in this state, as long as a single problem remains flagged. At this point, a script capable of fixing a flagged problem can request control ("Problem, In Control"). Following this, the in-control problem can be removed (or the in-control script releases control), transitioning back to "Problem, No Control"; or all flagged problems can be removed, causing the mediator to remove control and transition to "No Problem, No Control". As indicated by the vertical transitions, any script may flag a problem and transition the mediator from "No Problem, No Control" to "Problem, No Control"; transitioning back requires all flagged problems to be removed.

In the current implementation, there is no hierarchy between experiment problems. Race conditions may thus occur whenever two suitable scripts request control. Given our assumption of a single "primary" script, this is mainly problematic if certain experiment problems are interdependent and the resolution order is important. This can be avoided by extending the mediator to accept a problem hierarchy on startup; subsequent versions of the framework may support this.
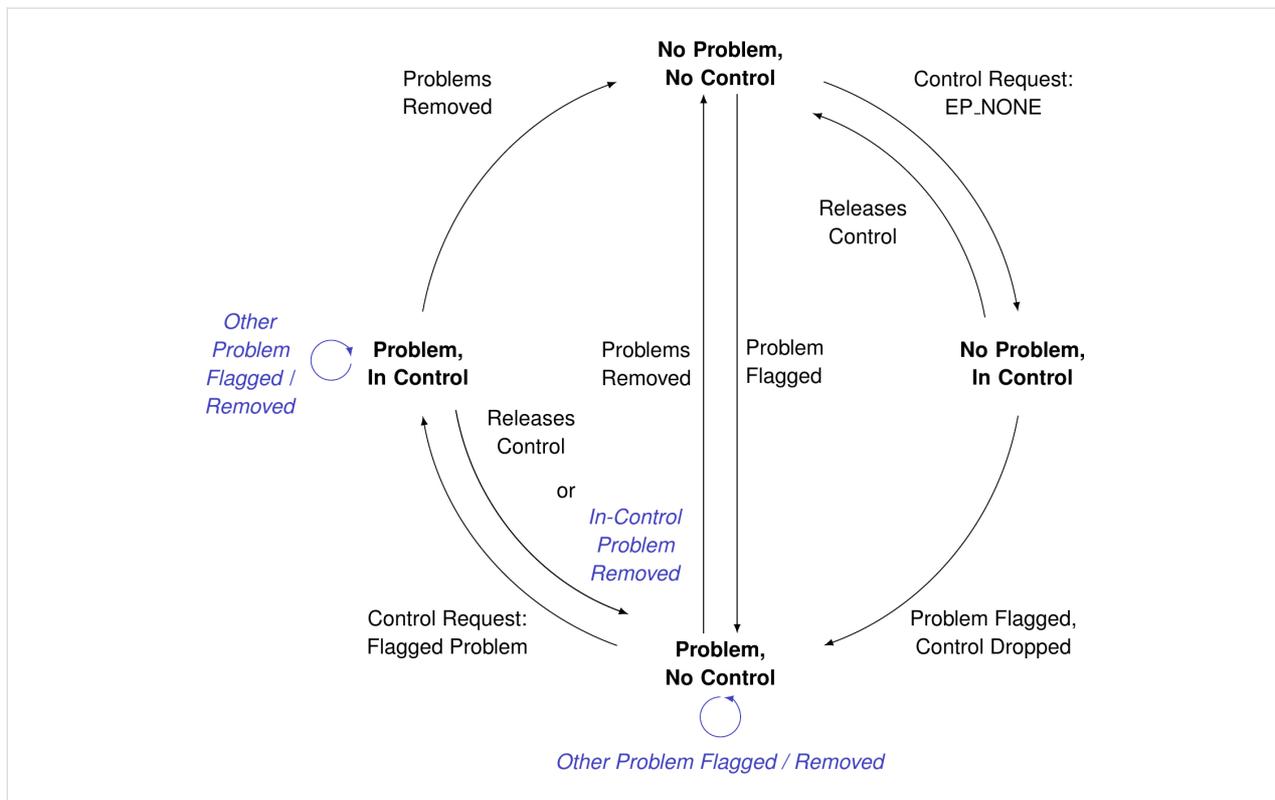
Figure 8: Mediation logic state machine. Here, we transition from the default "No Problem, No Control" state to "No Problem, In Control" when a script solving no specific problem requests control. If a problem is flagged, control is dropped and we transition to "Problem, No Control". A script able to resolve the flagged problem can gain control, transitioning to "Problem, In Control", and we return to the default state when the problem has been removed.

Base microscope actions and parameters

When defining this framework, we attempted to define some minimum set of commands and data structures that we believe form a "base" set to run automation tasks. Such a definition is arbitrary; however, the high volume of controls available in most SPM controllers make the task of creating a fully comprehensive framework impractical. We chose to focus on the most common actions and parameters (Table 2); these are running and configuring scans (the physical region and data resolution), running and configuring spectroscopies (the physical position where it is to be run), and configuring the z-height feedback (the proportional and integral gain parameters and setpoint value).

Table 2: Table listing generic requests expected from all translators.

Grouping	Request	Notes
actions	start/stop 2D scan	begin or override currently configured scan
	start/stop 1D spectroscopy	begin or override currently configured spectroscopy
parameters	set scan parameters	spatial rectangle and digital resolution
	set probe position	xy position for 1D spectroscopy
	set z-control parameters	proportional / integral gain weights

Table 3 lists the generic data structures all microscope translators are expected to publish to connected processes and their source (i.e., where a translator obtains them). Here, the scan parameters, probe position, and z-control parameters match what is settable and described above. The scope state indicates the current state the microscope is in (e.g., scanning, moving, or free). The 2D scans structure holds the one or more 2D scans collected during a single scanning event, where each scan corresponds to a channel saved. The 1D spectroscopy structure holds a one-dimensional array of values collected at a single xy position within the scan region. Both the scan and spectroscopy data structures are expected to be read directly from the computer hard drive, which simplifies the translator logic as it does not need to monitor data live (which is accessible for only some controllers).

The exposed level of control assumes the user has pre-configured their "operating mode" (e.g., amplitude-modulated atomic force microscopy (AM-AFM) or frequency-modulated atomic force microscopy (FM-AFM)) and spectroscopic mode (e.g., *IV* curves or force spectroscopy), which we believe is justifiable as part of the experimental setup. This base set of operations gives

Table 3: Table listing generic data structures expected from all translators and where a translator may source each from.

Data structure	Source
1D spectroscopy	saved files
2D scans	saved files
probe position	microscope controller
scan parameters	microscope controller
scope state	microscope controller
z-control parameters	microscope controller

the user a reasonable degree of flexibility: One could design an image analysis script to analyze 2D scans for defects of interest; an experiment could then regularly alternate between performing 2D scans and running local spectroscopies on the detected defects. A user of the framework is not restricted to this subset of controls; generic actions and generic parameters can be added as needed (e.g., adding actions to swap between operating modes or adding parameters to control additional feedback loops).

Framework Validation Methodology

To validate interfacing feasibility, we developed a translator for each solution illustrated in Figure 4. In order to ensure a given translator behaves as the framework expects, an automated test suite was created that validates each of the base parameters and actions, ensuring that scripts written in our generic fashion can be run on a specific microscope. It can be easily invoked via command-line, allowing a user to run an automated sanity check before beginning an experiment. As this test suite validates correct interaction between controller and translator, the actual data recorded during a test is unimportant. We therefore consider it a best practice to run these with the tip disengaged, to avoid unnecessary risk to tip or sample.

The translator test suite exists alongside a comprehensive test suite that validates the framework and available scripts for expected functionality. At any point while the framework is installed, its general functioning, and that of all existing scripts, can be validated quickly. By providing both of these, we allow for quick automated testing, paving the way for continuous integration practices to be run on all supported microscopes. If widely adopted, nightly tests could be run to ensure all integrated microscopes remain supported as the framework evolves.

Next, we aimed to validate full functioning of the framework by developing and running an automated experiment. We chose to run a drift correction system under conditions where correction

was merited. The particular drift estimation method chosen is a feature tracking one similar to that reported in [14] (we direct readers here for estimation specifics). Further information on our implementation may be found in section "Drift Correction" of Supporting Information File 1.

Results and Discussion
System interfacing results

We developed translators for a SPECS Nanonis controller, a system using a Scienta Omicron SXM controller, one using the Gnome X Scanning Microscopy project (GXSM, an open-source software and hardware controller system), and an Asylum Research system. Using the translator test suite, we were able to validate that all translators supported all of our base microscope operations (with the temporary exception of the Scienta Omicron system, as described below). Videos showing these in action can be found in Supporting Information File 2. System diagrams of the implemented translators may be seen in Figure 9.

SPECS Nanonis Integration

We interfaced with a SPECS Nanonis STM Simulator, simulating a Nanonis Mimea BP5 SPM system. This software simulator mimics the hardware and software controller in a one-to-one fashion at the interface-level; to a connected translator, it is equivalent to a real system. The associated software controller provides a LabVIEW-specific library interface, and a transmis-

sion control protocol (TCP)-based IPC interface. Our translator connects via the IPC interface, as seen in Figure 9d and matching the design in Figure 4d. It translates generic commands and data structures into TCP messages as defined in the Nanonis specification, and unpacks the received responses according to said specification. For reading SPECS Nanonis scans and spectroscopies, the Python package SciFiReaders was used [21].

Scienta Omicron SXM Integration

Our Scienta Omicron system was the Infinity UHV SPM Lab using an SXM controller. The SXM controller provides an internal Pascal-like scripting language interface, a dynamic data exchange (DDE) IPC interface, and a series of Python scripts functioning as an external library interface. We chose to have our translator interface via the external library interface, as seen in Figure 9c and matching the design in Figure 4e. Our current implementation interfaces with an earlier version of the programming interface and software controller (version 28.8). This version is more limited in the available controls and notably does not allow for stopping scans or spectroscopies. Because of this, our implementation does not pass two of the tests in our translator test suite. We note that this is a versioning limitation and unrelated to the feasibility of interfacing with an external library interface type. A future version of our translator will interface with a later software controller version, enabling all controls validated by the test suite.
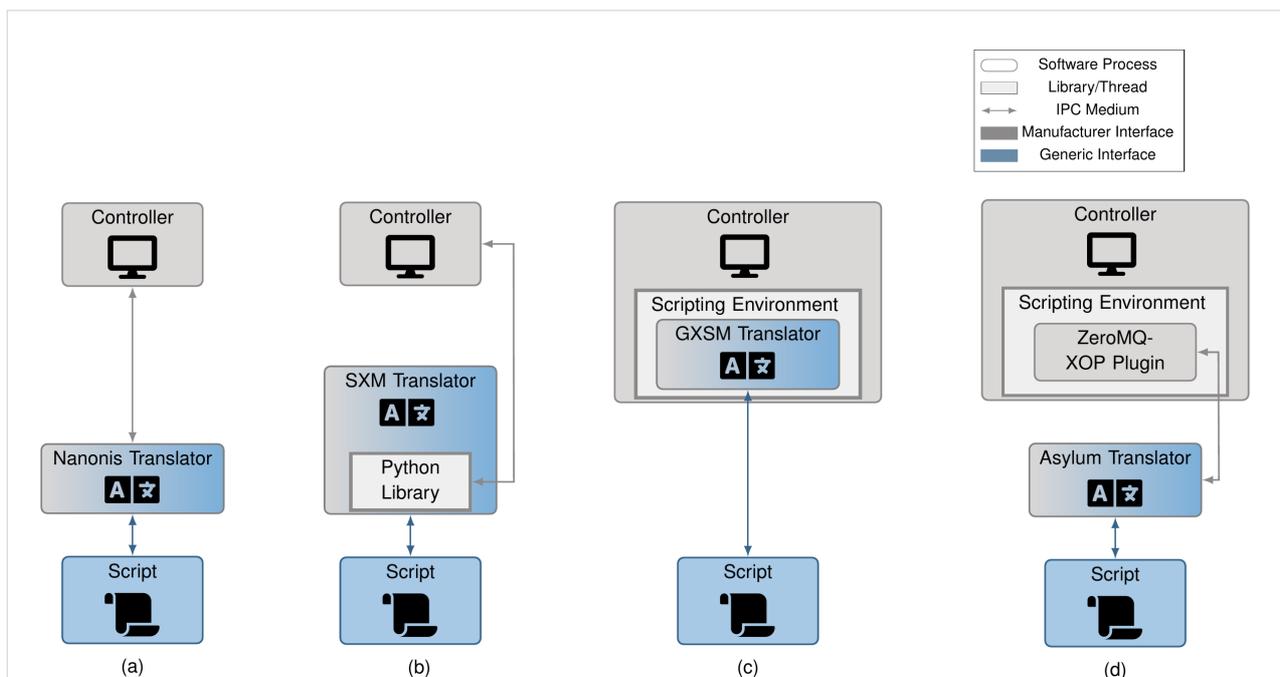
Figure 9: System diagrams of the translators for various integrated microscope controllers: (a) SPECS Nanonis, (b) Scienta Omicron SXM, (c) GXSM, and (d) Oxford Instruments Asylum Research.

We made modifications to the provided Python script to function optimally for our translator. This modified script is included in our software framework with permission from the manufacturer. For reading SXM scans and spectroscopies, custom Python readers were written.

GXSM Integration

For our GXSM-controlled system, our hardware controller was a soft dB Signal Ranger MK2-810, connected to a custom non-commercial SPM system. The GXSM controller provides a Python-based internal scripting interface. In order to integrate with our framework, we designed the translator to run within the scripting environment, communicating with other scripts via our IPC interface (see Figure 9a, matching the design of Figure 4f). Minor changes were made to GXSM's Python programming interface to simplify cancelling and restarting scripts, pushed to GXSM's main development branch. Since a pre-existing Python package for reading GXSM scans and spectroscopies did not exist, one was written called gxsmread [22].

Asylum Research Integration

Our Asylum Research system was an MFP-3D-BIO, which provides an IGOR-based internal scripting interface. Due to the non-Python scripting language, we chose to use a third-party tool, "ZeroMQ-XOP" [23], to function as the interfacing script and allow for communication with the controller (see Figure 9b, matching the design in Figure 4g). This tool installs a custom plugin in the Asylum Research computer software, allowing it to receive IGOR commands packaged into a JSON message format and passed over an IPC interface. Our Asylum Translator thus translates our generic commands and data structures into IGOR commands as represented by this JSON message format, which are sent to the custom plugin using the IPC interface of "ZeroMQ-XOP", where they are parsed and called directly inside the scripting environment.

We made minor modifications to this tool in order to support the underlying data analysis software used by Asylum Research, an earlier version of Igor PRO. These changes were pushed to "ZeroMQ-XOP"'s main development branch. For reading Asylum Research scans and spectroscopies, the Python package SciFiReaders was used [21].

Running an automated experiment

In order to validate the functioning of our drift correction logic, we ran experiments with it on the Asylum Research MFP-3D-BIO AFM system, scanning a CD stamper as a test sample using a MikroMasch HQ:NSC15/Al AFM probe (40 N/m force constant, 325 kHz resonant frequency). These experiments were run under ambient conditions in an AM-AFM mode. Prior to engaging with the sample, we performed an auto-tuning opera-

tion to optimize the cantilever frequency and manually optimized the *z*-height feedback parameters for reasonable imaging quality. In the experiment, we attempted to scan the same region of our sample over a long period of time (~16 h). For our drift estimation, we chose to track a channel representative of the topographic variation on the sample. For this operating mode and microscope setup, this corresponded to the "Height Retrace" channel. We used the instrument's internal "Flatten1" scan pre-processing step, which fits an average line to each scanline and removes it.

We decoupled our drift correction experiments into two phases, that is, scanning with our correction disabled and with it enabled. By scanning with our correction disabled, we were able to roughly characterize the thermal drift. This is useful in order to ensure our experiment configuration and reasonable drift correction parameters. For our test, we requested to scan a specific region over ~2 h with the correction logic off. For a second experimental run, we again scanned a specific region over ~16 h, this time with the correction logic on. To analyze the data, we visualized the measured drift offset $\mathbf{x}_{tot}$ for the case where correction was on in Figure 10. Here, we see that the tracked drift follows a non-linear trajectory, similar to the results in [14]. In contrast with that paper, we did not evaluate the ultimate precision and stability of our corrector; rather, we focused on validating that it tracked correctly and minimized drift between scans. A sample of images collected over the duration of the experiment can be found in Figure 11. The collected experimental data and configuration file used for this experiment can be found in Supporting Information File 3.

Conclusion

afspm is a software framework for writing automated experiments in SPM, using generic commands and data structures and translating them for a microscope only as they are sent out to the microscope controller. afspm also has configuration file support to encourage reusable scripts, which decouples experiment-specifics from algorithmic logic. A mediation layer has additionally been developed, allowing for background tasks to intermittently take control of the microscope. This permits various "monitoring and fixing" automation tasks showcased in prior articles (e.g., tip functionalization) to be integrated in a straightforward manner. We demonstrated the ability to write and run generic code by testing the functionality on microscope controllers that expose each of the scripting interface types. We further validated its usage for running experiments via a drift correction experiment that successfully tracked drift over a reasonable time duration.

Some of afspm's design decisions are worth highlighting. Its usage of a network-based IPC protocol and their definition in a
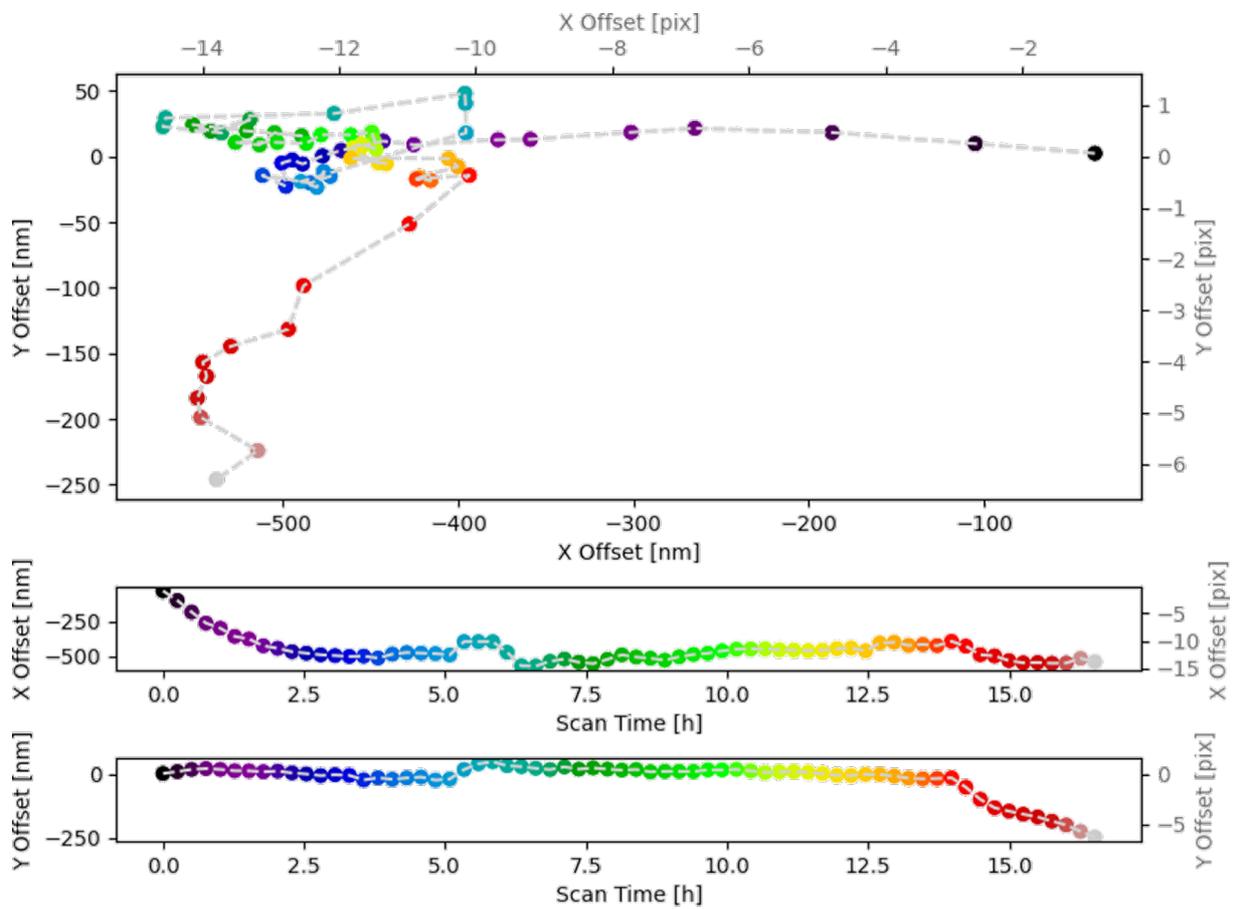
Figure 10: Drift offset $\mathbf{x}_{tot}$ tracked over time during the experiment (i.e., online) with drift correction enabled. The top graph shows the drift offset in *x* and *y* directions, with the bottom two graphs showing the individual dimensions on one axis and time on the other. The color coding of the data points in all three graphs indicates time.
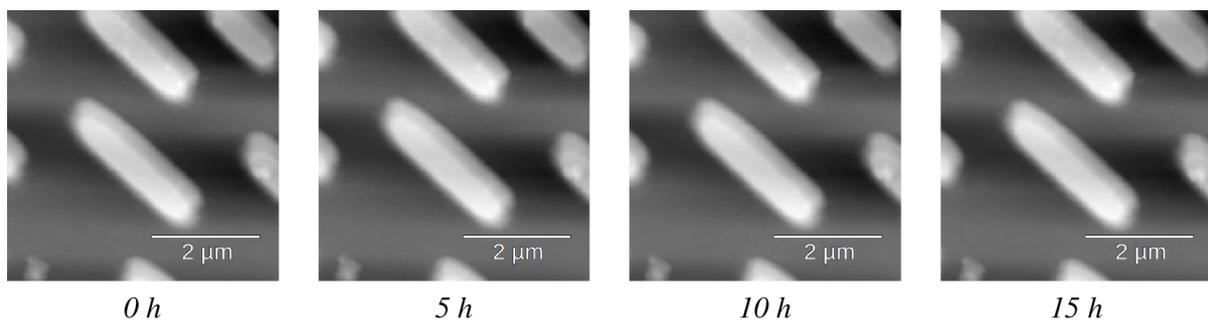
Figure 11: Sample scans collected over the duration of the experiment, at (a) 0 h, (b) 5 h, (c) 10 h, and (d) 15 h, respectively.

configuration file allows experiments to be split up among multiple computers. This helps distribute computing resources, minimizing hardware constraints on experiments. In using a language-flexible data format and communication interface, users can use algorithms or programs that do not integrate with

Python. We should highlight, however, that this flexibility is constrained to the communication protocol supported by our framework; framework features (such as configuration file parsing and some pre-existing software logic) will not be accessible.

We also highlight that the design decisions made here – encapsulating manufacturer-specific logic away from the main code, communicating between scripts over IPC interfaces, and configuration file parsing and instantiation via standalone processes – have broader appeal than just for SPM. Indeed, many experimental fields of study are hampered by a lack of standardization in their instruments' communication interfaces, and may benefit from similar frameworks. We particularly highlight optical and electron microscopy as these instruments share common experimental workflows (e.g., searching a wider region to determine where to image) and may benefit from direct repurposing of automation logic developed for SPM.

In the future, our presented framework may benefit from integration with (or adaptation to) the Bluesky suite of Python packages [17]. That project's focus on interoperability and coordination for multi-instrument experiments may prove useful as afspm progresses. Furthermore, the Bluesky data model may serve as a useful approach for organizing experimental data and metadata for later search and retrieval.

The development of automated tasks within a manufacturer-agnostic framework enables code sharing among the SPM community. This framework is a reasonable first step toward developing generic automation in SPM; as automation tasks are developed and integrated, it will make more experiments accessible to the community at large. We hope afspm encourages this collaboration and would be delighted to assist others in writing reusable automated scripts.

Our developed framework is available for free under an open source license from the Grutter Group Github and can be accessed at [24].

Acknowledgements

Funding

Supporting Information

Supporting Information File 1
Additional description of the framework.
[https://www.beilstein-journals.org/bjnano/content/supplementary/2190-4286-17-45-S1.pdf]

Supporting Information File 2
Videos of the translator validation testing, performed on the various microscope controllers.
[https://www.beilstein-journals.org/bjnano/content/supplementary/2190-4286-17-45-S2.zip]

Supporting Information File 3
Data collected during experimental runs and the configuration file of these. The data folder contains the experimental scans as saved during the experiment. Config.toml contains the afspm configuration file as run. scan_metadata.csv holds the metadata file created by ScanMetadataWriter. drift_correction.csv contains the logged drift correction information created by the CSCorrectedScheduler (the legacy internal name for Drift Compensated Mediator). log.txt holds all logs sent out during the experiment.
[https://www.beilstein-journals.org/bjnano/content/supplementary/2190-4286-17-45-S3.zip]

Author Contributions

Nicholas J. Sullivan: conceptualization; investigation; methodology; software; validation; visualization; writing – original draft; writing – review & editing. Julio J. Valdés: conceptualization; writing – review & editing. Kirk H. Bevan: conceptualization; funding acquisition; supervision; writing – review & editing. Peter Grutter: conceptualization; funding acquisition; resources; supervision; writing – review & editing.

ORCID® iDs

Nicholas J. Sullivan - https://orcid.org/0009-0007-7402-8902
Julio J. Valdés - https://orcid.org/0000-0003-2930-0325
Kirk H. Bevan - https://orcid.org/0000-0001-9884-1403
Peter Grutter - https://orcid.org/0000-0003-1719-8239

Data Availability Statement

All data that supports the findings of this study is available in the published article and/or the supporting information of this article.

Preprint

A non-peer-reviewed version of this article has been previously published as a preprint: https://arxiv.org/abs/2509.00113

References

1. Voigtländer, B. *Scanning probe microscopy: Atomic force microscopy and scanning tunneling microscopy;* Springer: Berlin, Heidelberg, 2015. doi:10.1007/978-3-662-45240-0
2. Rashidi, M.; Wolkow, R. A. *ACS Nano* **2018,** *12,* 5185–5189. doi:10.1021/acsnano.8b02208
3. Krull, A.; Hirsch, P.; Rother, C.; Schiffrin, A.; Krull, C. *Commun. Phys.* **2020,** *3,* 54. doi:10.1038/s42005-020-0317-3
4. Gordon, O. M.; Junqueira, F. L. Q.; Moriarty, P. J. *Mach. Learn.: Sci. Technol.* **2020,** *1,* 015001. doi:10.1088/2632-2153/ab42ec
5. Roccapriore, K. M.; Zou, Q.; Zhang, L.; Xue, R.; Yan, J.; Ziatdinov, M.; Fu, M.; Mandrus, D. G.; Yoon, M.; Sumpter, B. G.; Gai, Z.; Kalinin, S. V. *ACS Nano* **2021,** *15,* 11806–11816. doi:10.1021/acsnano.1c02902
6. Sotres, J.; Boyd, H.; Gonzalez-Martinez, J. F. *Nanoscale* **2021,** *13,* 9193–9203. doi:10.1039/d1nr01109j
7. Ziatdinov, M.; Dyck, O.; Li, X.; Sumpter, B. G.; Jesse, S.; Vasudevan, R. K.; Kalinin, S. V. *Sci. Adv.* **2019,** *5,* eaaw8989. doi:10.1126/sciadv.aaw8989
8. Rashidi, M.; Croshaw, J.; Mastel, K.; Tamura, M.; Hosseinzadeh, H.; Wolkow, R. A. *Mach. Learn.: Sci. Technol.* **2020,** *1,* 025001. doi:10.1088/2632-2153/ab6d5e
9. Noack, M. M.; Zwart, P. H.; Ushizima, D. M.; Fukuto, M.; Yager, K. G.; Elbert, K. C.; Murray, C. B.; Stein, A.; Doerk, G. S.; Tsai, E. H. R.; Li, R.; Freychet, G.; Zhernenkov, M.; Holman, H.-Y. N.; Lee, S.; Chen, L.; Rotenberg, E.; Weber, T.; Goc, Y. L.; Boehm, M.; Steffens, P.; Mutti, P.; Sethian, J. A. *Nat. Rev. Phys.* **2021,** *3,* 685–697. doi:10.1038/s42254-021-00345-y
10. Kelley, K. P.; Ziatdinov, M.; Collins, L.; Susner, M. A.; Vasudevan, R. K.; Balke, N.; Kalinin, S. V.; Jesse, S. *Small* **2020,** *16,* 2002878. doi:10.1002/smll.202002878
11. Thomas, J. C.; Rossi, A.; Smalley, D.; Francaviglia, L.; Yu, Z.; Zhang, T.; Kumari, S.; Robinson, J. A.; Terrones, M.; Ishigami, M.; Rotenberg, E.; Barnard, E. S.; Raja, A.; Wong, E.; Ogletree, D. F.; Noack, M. M.; Weber-Bargioni, A. *npj Comput. Mater.* **2022,** *8,* 99. doi:10.1038/s41524-022-00777-9
12. Liu, Y.; Morozovska, A. N.; Eliseev, E. A.; Kelley, K. P.; Vasudevan, R.; Ziatdinov, M.; Kalinin, S. V. *Patterns* **2023,** *4,* 100704. doi:10.1016/j.patter.2023.100704
13. Diao, Z.; Ueda, K.; Hou, L.; Li, F.; Yamashita, H.; Abe, M. *Small Methods* **2025,** *9,* 2400813. doi:10.1002/smtd.202400813
14. Diao, Z.; Ueda, K.; Hou, L.; Yamashita, H.; Custance, O.; Abe, M. *Appl. Phys. Lett.* **2023,** *122,* 121601. doi:10.1063/5.0139330
15. Vasudevan, R. K.; Valleti, S. M.; Ziatdinov, M.; Duscher, G.; Somnath, S. *Adv. Theory Simul.* **2023,** *6,* 2300247. doi:10.1002/adts.202300247
16. Liu, Y.; Roccapriore, K.; Checa, M.; Valleti, S. M.; Yang, J.-C.; Jesse, S.; Vasudevan, R. K. *Small Methods* **2024,** *8,* 2301740. doi:10.1002/smtd.202301740
17. Allan, D.; Caswell, T.; Campbell, S.; Rakitin, M. *Synchrotron Radiat. News* **2019,** *32,* 19–22. doi:10.1080/08940886.2019.1608121
18. Ousterhout, J. K. *Computer* **1998,** *31,* 23–30. doi:10.1109/2.660187
19. Pree, W. Meta patterns—A means for capturing the essentials of reusable object-oriented design. *European Conference on Object-Oriented Programming (ECOOP 1994);* Lecture Notes in Computer Science., Vol. 821; Springer: Berlin, Heidelberg, 1994; pp 150–162. doi:10.1007/bfb0052181
20. Welcome to Python.org. https://www.python.org/ (accessed Jan 13, 2025).
21. GitHub - pycroscopy/SciFiReaders: Tools for extracting data and metadata from scientific data files · GitHub. https://github.com/pycroscopy/SciFiReaders (accessed Aug 9, 2025).
22. GitHub - grutter-spm-group/gxsmread · GitHub. https://github.com/grutter-spm-group/gxsmread (accessed Aug 9, 2025).
23. GitHub - AllenInstitute/ZeroMQ-XOP: The ZeroMQ XOP enables Igor Pro to interface over the network using a ZeroMQ messaging layer and JSON as message format · GitHub. https://github.com/AllenInstitute/ZeroMQ-XOP (accessed Aug 9, 2025).
24. Sullivan, N. J. GitHub - grutter-spm-group/afspm · GitHub. https://github.com/grutter-spm-group/afspm (accessed Aug 9, 2025).

License and Terms